Computational Approaches and Models for Ovarian Ageing: From 2D to 4D

Angelos A. Skodras

Institute of Reproductive and Developmental Biology

Department of Surgery and Cancer

Imperial College London

Submitted for the degree of Doctor of Philosophy to

Imperial College London

I dedicate this work to my parents, Athanassios Skodras and Gioulie Giovrie

Acknowledgements

First of all, I would like to formally thank my supervisors, Professors Kate Hardy, Stephen Franks and Jaroslav Stark, for always giving me insightful advice and comments, and supported me during the course of this project. Additionally, I would like to express my gratitude to my supervisors for providing the opportunity for me to work on this interdisciplinary project, during which I had the pleasure of working with people from different scientific fields, and acquired new practical skills in the biological laboratory.

A big thanks to all people in the IRDB, and specifically those on the 5th floor. It has been a delight working (and socializing) with you. Especially, I would like to thank Dr Mark Fenwick for his help with most of the biological methods in this project, and for being a good friend. Special thanks goes to Dr Sharron Stubbs for keeping the lab organized and for conducting some of the biological tasks for my project, and to Ms Jossie Mora for always being helpful and getting me out of trouble in the lab. Special thanks go to Dr Martin Spitaler of the imaging facility (FILM) in South Kensington, for introducing me to the world of light microscopy.

I would like to express my gratitude especially to Dr Gianluca Marcelli. Luca has been a mentor to me, supporting my work, debugging my programs and proofreading my documents; he is a good friend, a good teacher and one of the most unselfish persons I had the privilege to meet during this project. A very sincere “thank you”.

Finally, I would like to thank my parents for supporting me in all means possible. A big thank you to my girl, Roula, for her invaluable and selfless moral support, being the person sharing my joys and enduring all my whining for almost four years.

Declaration

This is to certify that:

- The present thesis comprises my original work towards the Ph. D. except where indicated
- Appropriate acknowledgement and/or reference has been made in the text to all other material used
- The thesis is less than 100,000 words in length, inclusive of tables, figure legends footnotes and bibliography

Angelos Skodras

Abstract

The theme of the work presented in this multi-disciplinary PhD is the development of new computational tools and techniques to study and understand spatio-temporal follicle growth in neonatal mouse ovaries. The female ovary is endowed at birth with a finite, non-renewable supply of oocytes, each enclosed in a layer of supporting somatic (granulosa) cells to form a quiescent follicle. From birth, a steady trickle of follicles initiate growth to maintain a supply of mature oocytes for regular ovulation. Disruption in the regulation of initiation of follicle growth can result in various pathologies, such as premature ovarian failure and polycystic ovary syndrome.

The mechanism of regulation of the initiation of follicle growth remains unclear, but may involve inter-follicle signaling via paracrine growth factors. To investigate this hypothesis, a new technique for quantifying and analyzing spatial distributions of quiescent and growing follicles in the adult human has been developed, as an extension of a novel technique previously developed in neonatal mice in our laboratory. As in the mouse study, we have found evidence that in the human ovary neighbouring quiescent follicles inhibit follicle growth, at a small range. This approach has been further extended to cultured neonatal mouse ovaries, which in vitro lack a systemic blood supply, to investigate the relative contributions of inter-follicle paracrine signaling and endocrine growth factor/nutrient signaling to the regulation of initiation of follicle growth.

Accurate counts of the numbers of follicles in ovaries are important for a wide variety of studies of ovarian physiology, including investigating the effects of age, toxins, chemotherapeutics, endocrine disruptors and specific genes (knock out/transgenic studies) on follicle formation, endowment and development. Many published studies use frequent sampling of a small number of ovaries (often as few as three) to obtain estimates of the number of follicles. We have tested the validity of this approach by generating 3D spherical simulated ovaries which contain realistic numbers of follicles at different stages and which are realistically positioned within these ovaries. The number and position of follicles is based on real biological data. This model enables us to rapidly ‘virtually’ section the ovary *in silico* and obtain computer-generated counts of the numbers of follicles in sections at different frequencies, such as one every fifth section (1/5), 1/20 or 1/50. As we know precisely

how many follicles each simulated ovary contains, we can compare the accuracy using different sampling frequencies of varying numbers of ovaries. This has enabled us to demonstrate that the error is smaller when infrequent sampling of a large number of ovaries (≥ 8) is carried out, and that this actually involves analyzing fewer sections overall. We have gone on to generate simulated ovaries from knockout mice, with more or fewer follicles, and can predict how many ovaries are required to make robust comparisons between knockout and control animals. This has shown that biological variability contributes more to counting error than the method of sampling. These simulated ovaries provide a unique resource to model large studies.

Currently follicle counts are obtained by fixing and serially sectioning ovaries, and manually counting the follicles in sections. This is laborious and time-consuming. Faster methods of obtaining follicle estimates are required. With the use of confocal microscopy and immunohistochemistry for an oocyte-specific protein, we were able to establish a protocol that allows us to image and computationally reconstruct a whole neonatal mouse ovary in 3D. Follicle number can be estimated rapidly using a stereologic method. The stereologic technique error was estimated using the simulated ovary model, leading to the conclusion that the method can be safely used to obtain rapid estimates of follicle number. The time required can be further reduced by using image processing to detect the stained follicles on the sections. We have developed an algorithmic technique that can instantaneously identify stained oocytes, count them, and calculate their spatial distribution.

A fundamental unanswered question is whether follicles move in the ovary, particularly as they grow. This question has arisen from the observation that small follicles tend to be situated close to the ovarian surface, while large ones are closer to the medulla. This question has implications for interfollicle signaling. We have developed a protocol to image the ovary while in culture using timelapse confocal and live lipid stains to visualize the follicles. Results show that small follicles are not moving significantly over a period of 12h. This project can be extended in the future with the use of transgenic mice for GFP tagging, to accurately monitor changes in structures of interest within cultured ovaries.

Publications

During the course of this project, a number of public presentations have been made which are based on the work presented in this thesis. They are listed here for reference.

Society for Endocrinology BES 2010 meeting: 15-18 March 2010, Manchester, UK

"GLUT4 expression and translocation in immortalised mouse granulosa cells"

Jalini Joharatnam, **Angelos Skodras**, Kate Hardy and Sthephen Franks

Society for Reproduction and Fertility Conference: 12-14 July 2009, Oxford, UK.

"Assessing the Effects of Biological Variability on Follicle Counting, using Computer Generated Virtual Ovaries".

Angelos Skodras, Gianluca Marcelli, Mark Fenwick, Stephen Franks, Jaroslav Stark and Kate Hardy.

16th International Conference on Digital Signal Processing: 5-7 July 2009, Santorini, Greece.

"Object Recognition in the Ovary: Quantification of Oocytes from Microscopic Images".

Angelos Skodras, Stamatia Giannarou, Mark Fenwick, Stephen Franks, Jaroslav Stark and Kate Hardy.

Contents

LIST OF TABLES **11**

LIST OF FIGURES **12**

ABBREVIATIONS **16**

CHAPTER 1 ..... **18**

INTRODUCTION **18**

1.1 THE OVARY AND ITS ROLE 18
1.2 OVARIAN PHYSIOLOGY AND FOLLICLE FORMATION 18
1.3 FOLLICLE GROWTH AND DEVELOPMENT 21
1.3.1 Initiation of follicle growth: Markers and order of events *22*
1.4 FOLLICLE STAGES OF GROWTH 23
1.5 ACTIVATION OF THE PRIMORDIAL FOLLICLE 27
1.5.1 Molecular regulation of growth factors *35*
1.6 HORMONAL REGULATION OF FOLLICLE GROWTH 37
1.7 REGULATION OF FOLLICLE GROWTH 41
1.7.1 Post natal oogenesis *43*
1.8 OVARIAN CULTURES 44
1.9 ASSESSING THE NUMBER OF FOLLICLES IN THE OVARY 46
1.9.1 Approaches to estimating follicle numbers *48*
1.9.2 Biological variability *52*
1.10 SPATIAL DISTRIBUTIONS 53
1.11 IMAGING 56
1.11.1 Tissue preparation *56*
1.11.2 Imaging approaches *59*
1.11.3 Optical instruments for fluorescent microscopy *61*
1.12 OBJECT RECOGNITION 69

1.13 OVERVIEW, AIMS AND HYPOTHESES **75**

CHAPTER 2 ..... **79**

PREDICTION OF LOCAL MECHANISMS REGULATING INITIATION OF FOLLICLE DEVELOPMENT IN THE HUMAN OVARY BY APPLICATION OF SPATIAL ANALYSIS **79**

2.1 INTRODUCTION TO OVARIAN LOCAL SIGNALING 79
2.1.2 Control of initiation of follicle growth and hypotheses *80*
2.2 APPROACH 82
2.3 RESULTS 83
2.4 DISCUSSION 91

CHAPTER 3 ..... **96**

SPATIAL ANALYSIS OF JUVENILE CULTURED MOUSE OVARIES **96**

3.1 INTRODUCTION 96
3.2 APPROACH 99
3.3 RESULTS 101
3.4 DISCUSSION 109

CHAPTER 4 113

COMPUTER-GENERATED OVARIES FOR ASSESSING THE EFFECT OF BIOLOGICAL VARIABILITY ON NUMBER OF FOLLICLES IN THE JUVENILE MOUSE OVARY 113

4.1 INTRODUCTION 113
4.1.1 Aim of our study 116
4.2 APPROACH 117
4.2.1 Generating the simulated ovaries 117
4.2.2 Application of the unbiased stereological technique 122
4.2.3 FOLLICLE ESTIMATES AND THE ASSOCIATED ERROR 124
4.2.4 Comparing follicle numbers for control and knockout mice 127
4.3 RESULTS 128
4.3.1 Calculations of Standard Error of the Mean (SEM) 128
4.3.2 Normal – mutant comparison 130
4.3.3 Planning experiments to detect differences in follicle number distributions 133
4.4 DISCUSSION 138

CHAPTER 5 142

IMAGING OF WHOLE TISSUE: NEW METHODS FOR 3D-MORPHOLOGY INVESTIGATION AND RAPID FOLLICLE NUMBER ESTIMATION 142

5.1 INTRODUCTION 142
5.1.1 Aims 145
5.2 MATERIALS AND THE PROPOSED EXPERIMENTAL APPROACH 146
5.3 RESULTS 148
5.3.1 OPTICAL SLICES, VOLUME RENDERINGS, CLARITY OF TECHNIQUE 148
5.3.2 Limitations of the technique 158
5.3.3 Comparison with Optical Projection Tomography images 160
5.3.4 Trials using two-photon laser scanning confocal microscopy 162
5.4 FOLLICLE COUNTING AND STEREOLOGY 163
5.4.1 Estimating total number of follicles 163
5.4.2 Use of Simulated Ovaries to corroborate experimental follicle counts 168
5.5 DISCUSSION 169

CHAPTER 6 175

IMAGE PROCESSING TECHNIQUE FOR FOLLICLE QUANTIFICATION FROM MICROSCOPIC IMAGES 175

6.1 INTRODUCTION 175
6.1.1 Automatic follicle detection: preliminary remarks 176
6.2 THE PROPOSED METHOD 179
6.2.1 Pre-processing 181
6.2.2 Image Segmentation 183
6.2.3 Morphological and Spatial Information Extraction 186
6.3 EXPERIMENTAL RESULTS 190
6.3.1 Follicle stage estimation 194
6.3.2 Spatial Analysis 197
6.4 DISCUSSION 199

CHAPTER 7 202

TIME-LAPSE IMAGING OF A WHOLE JUVENILE MOUSE OVARY: A STUDY FOR FOLLICLE MOTILITY 202

7.1 INTRODUCTION 202
7.2 MATERIALS AND EXPERIMENTAL DESIGN 204
7.3 RESULTS 204
7.3.1 Observing live follicle morphology and behaviour 209
7.3.2 Follicle motility 215
7.4 DISCUSSION AND FUTURE RESEARCH POTENTIAL DIRECTIONS 216
7.4.1 Live imaging and GFP tagging 218
7.4.2 Modeling using the Simulated Ovary 221
7.4.3 Conclusions 222

CHAPTER 8 224

DISCUSSION 224

8.1 SYNOPSIS OF THE RESULTS AND DISCUSSION 224
8.2 NOVELTIES, CAVEATS AND FUTURE DIRECTIONS 227
8.3 CONCLUSIONS 230

CHAPTER 9 232

MATERIALS, METHODS AND ALGORITHMS 232

9.1 HUMAN OVARIAN TISSUE COLLECTION (†) 233
9.2 SAMPLE EXAMINATION AND DATA COLLECTION 234
9.3 HUMAN HISTOLOGICAL SECTION IMAGING BY LIGHT MICROSCOPY 237
9.4 FOLLICLE XY COORDINATES 239
9.4.1 Transforming image Coordinates 240
9.5 EUCLIDIAN DISTANCES 244
9.5.1 Inter-follicular distances 244
9.5.2 Euclidian distances of follicles from the ovarian surface 244
9.6 FOLLICLE PROPORTIONS 245
9.6.1 Follicle proportions calculation using Logistic Regression 245
9.6.2 Testing for statistical significance 246
9.6.3 Example of proportion calculation in Stata 8 246
9.7 NEONATAL MOUSE OVARY COLLECTION (†) 248
9.8 CULTURE CONDITIONS FOR NEONATAL MOUSE OVARIES (†) 248
9.9 OVARIAN HISTOLOGY FOR NEONATAL MOUSE (†) 249
9.10 MORPHOLOGICAL ANALYSIS OF MOUSE FOLLICLES (†) 249
9.11 DATA COLLECTION FOR SPATIAL ANALYSIS (†) 250
9.12 NEONATAL MOUSE OVARY COLLECTION FOR FIXATION OR CULTURE (††) 250
9.13 WHOLE OVARY IMMUNOHISTOCHEMISTRY 251
9.14 WHOLE TISSUE MOUNTING AND CHEMICAL CLEARING 252
9.15 WHOLE TISSUE IMAGING USING LASER SCANNING CONFOCAL MICROSCOPY 253
9.16 LIVE IMAGING OF NEONATAL MOUSE OVARIES IN CULTURE 256
9.16.1 Culture media 256
9.16.2 Culture set-up 258
9.16.3 Time-lapse imaging 259
9.17 THE SIMULATED OVARY ALGORITHM 259

REFERENCES 266

List of tables

Table 2.1: Number of follicles analysed on human histological sections from normal and PCO ovaries……..……86

Table 3.1: Follicles counted on the largest ovarian cross-section…..……105

Table 4.1: Primordial follicle numbers reported in the literature……115

Table 5.1: Oocyte number estimates of two day 12 ovaries, using the stereologic technique……..168

Table 5.2: Standard deviations of the *10,000* simulated follicle number estimations and experimental estimates for both resting and growing follicles…….169

Table 6.1: Algorithm oocyte counts compared to experimentalist counts on each section of figure 6.15……...……..193

Table 6.2: Oocyte diameters of primordial follicles of day 4, day 8 and day 12 ovarian sections……..196

Table 9.1: Clinical details of subjects donated the ovaries used for MCM-2 immunohistochemistry, used in this project…….234

Table 9.2: Culture media solution components……..256

Table 9.3: Follicle *diameter* data from neonatal mouse ovarian section analysis…….…….…….260

Table 9.4: Ratios between oocyte, nucleus and nucleolus diameter and the follicle diameter…….260

Table 9.5: Follicle *distance* to ovarian wall……261

Table 9.6: Follicle numbers in whole neonatal mouse ovaries: data reported by Kerr *et al* (2006)……..261

Table 9.7: Profile density, $r_{profile}$, calculated from the actual ovarian sections and volume proportion, *a*, used to generate simulated ovaries……..…..263

Table 9.8: Mean and standard deviation of the various Gaussian distributions used to generate the follicle numbers for each stage and age…….…….263

List of figures

Figure 1.1: Adult human ovarian sections……..19

Figure 1.2: Mouse ovarian section and primordial follicles, and human primordial follicle…….21

Figure 1.3: Micrographs of human primordial and transitional follicles……24

Figure 1.4: Micrographs of human secondary follicles……..25

Figure 1.5: Micrograph of a human antral follicle……..27

Figure 1.6: Diagram of ovarian growth factor signaling……35

Figure 1.7: ***a)*** Illustration of the negative feedback female reproductive endocrine system, responsible for follicle maturation and ovulation, ***b)*** Detail of the theca-granulosa cell interaction……38-39

Figure 1.8: The human menstrual cycle……..40

Figure 1.9: Power model of human non-growing follicle decline with age……...41

Figure 1.10: Logarithmic scale of the resolution power of various imaging systems...……..60

Figure 1.11: The fluorescent (widefield) microscope……...61

Figure 1.12: The confocal microscope……63

Figure 1.13: Illustration of imaging a point light source……..64

Figure 1.14: Convolution of image with point spread function……65

Figure 1.15: Schematic diagram of electronic transitions for multi-photon excitation……..66

Figure 1.16: Optical projection tomography system……68

Figure 1.17: A computer algorithm can't recognize the house in both cases……..70

Figure 1.18: Effects of contrast enhancement on blot images……72

Figure 1.19: Watershed segmentation……..73

Figure 1.20: Diagrammatic illustration of follicle developmental stages in human……...75

Figure 2.1: Human ovarian section with follicles mapped……..…84

Figure 2.2: Part of human ovarian section showing local arrangement of small follicles and signal radii……..…..…85

Figure 2.3: Plot of the proportion of the follicles that are growing vs number of primordial neighbours……..87

Figure 2.4: Proportion of growing follicles vs closest primordial neighbour……88

Figure 2.5: Proportion MCM-2 positive follicles vs closest primordial neighbour…….……90

Figure 3.1: Simulated concentration map of a putative inhibitory factor which is produced and consumed by primordial follicles……..…98

Figure 3.2: Juvenile mouse ovaries allocated for the culturing experiments……100

Figure 3.3: Largest cross sections and details of *in vitro* and *in vivo* mouse ovaries…….....102

Figure 3.4: Proportion of growing follicles vs minimum distance from ovarian surface……103

Figure 3.5: Proportion of follicles of each developmental stage for *in vitro* and *in vivo* ovarian sections…….……..105

Figure 3.6: Proportion of growing follicles vs number of primordial neighbours……..107

Figure 3.7: Proportion of atretic follicles vs distance from ovarian surface…….109

Figure 4.1: Schematic representation of the algorithm that produces a simulated ovary...……...119

Figure 4.2: 3-D renderings of a day 7 and a day 12 simulated ovary, created using POV-Ray……..120

Figure 4.3: Equatorial cross sections of the day 7 and day 12 simulated ovaries shown in figure 4.2…….121

Figure 4.4: Two sections of an object containing spherical particles…..……..…123

Figure 4.5: Schematic representation the 350 ovaries sampling, using the bootstrapping approach……..125

Figure 4.6: *SEM*s of primordial and primary follicle numbers, for different sample sizes and sampling frequencies, for day 7 ovaries……..128

Figure 4.7: *SEM*s of primordial and primary follicle numbers, for different sample sizes and sampling frequencies, for day 12 ovaries…..……..130

Figure 4.8: *SEM*s of primordial follicle numbers, for different sample sizes and sampling frequencies, for day 7 knockout ovaries……..131

Figure 4.9: Proportion of the 10^3 *t*-student tests with a *p-value* ≤ 0.05……132

Figure 4.10: Proportion of the 10^3 *t*-student tests with a *p-value* ≤ 0.01……132

Figure 4.11: Proportion of the 10^3 *t*-student tests with a *p-value* ≤ 0.005……..133

Figure 4.12: Proportion of the 10^4 *t*-tests that detect the difference in each group with significance of 0.05, for various sampling frequencies……..135

Figure 4.13: Proportion of the 10^4 *t*-tests that detect the difference in each group with significance of 0.01, for various sampling frequencies……..136

Figure 5.1: Part of simulated ovary showing the 3D arrangement of follicles, and corresponding 2D section……145

Figure 5.2: Optical planes and volume reconstructions of whole juvenile mouse oviduct……150-151

Figure 5.3: Three optical slices of a juvenile mouse gut slab and a reconstructed volume render…….....…….152

Figure 5.4: Three optical slices of a juvenile mouse kidney and a reconstructed volume render…….153

Figure 5.5: Three optical planes and a detail through a whole day 12 mouse ovary stained using DRAQ 5™……..……155

Figure 5.6: Part of day 12 and day 42 mouse ovarian section stained for MVH and counterstained using haematoxylin…… 156

Figure 5.7: Four optical planes, a detail and a volume reconstruction of a day 12 whole juvenile mouse ovary…….....……...157

Figure 5.8: Background correction using thresholding on optical planes of a day 12 juvenile mouse ovary…….....……159

Figure 5.9: Imaging a day 8 whole mouse ovary using OPT……...161

Figure 5.10: Reference and look-up optical sections and details of day 12 whole mouse ovary…….....…….…..165

Figure 5.11: Reference and look-up optical sections overlayed……167

Figure 6.1: Light micrographs of mouse ovary tissue, stained using standard Haematoxylin and Eosin……..177

Figure 6.2: Brightfield and fluorescent mouse ovary sections showing MVH stained oocytes…….179

Figure 6.3: Two examples of input images of MVH stained mouse ovarian sections counterstained with haematoxylin……180

Figure 6.4: Block diagram of the proposed algorithm for oocyte segmentation and feature extraction…….180

Figure 6.5: ***a)*** *RGB* image, ***b)*** blue channel (*RGB*), ***c)*** *saturation* channel (*HSV*), ***d)*** *in-phase* channel (*YIQ)*.....181

Figure 6.6: Histogram of grayscale *in-phase* channel image of figure 6.5*b*…….182

Figure 6.7: Grayscale images of figure 6.3a, 6.3b, after pre-processing……..183

Figure 6.8: Images after the hysteresis thresholding……184

Figure 6.9: Thresholded images overlayed with the original…….……..184

Figure 6.10: Areas identified by the extended maxima operator, whose values are higher than their immediate background……..185

Figure 6.11: Colorized regions segmented using the watershed transform……186

Figure 6.12: Final segmented binary images……...187

Figure 6.13: Boundary classification by the MATLAB function *bwboundaries*...187

Figure 6.14: Least squares circular fit……189

Figure 6.15: Follicle recognition on ten ovarian sections used to test the proposed algorithm…….191-192

Figure 6.16: Automatic vs manual oocyte diamteter measurement……195
Figure 6.17: Proportion of growing follicles vs number of resting neighbours……..198

Figure 7.1: Cultured human KK1 cells, stained using the lipid dye BODIPY FL and nuclear stain Draq 5™……...205
Figure 7.2: Whole live ovary in culture; light scattering issue…….207
Figure 7.3: Two day 8 mouse ovaries cultured for 12h in BODIPY, fixed and stained for MVH…….208
Figure 7.4: Confocal images of a cultured ovary in BODIPY containing media……211
Figure 7.5: Parts of day 10 cultured mouse ovarian tissue, imaged for 12h, showing a follicle dying…….……..212
Figure 7.6: Time-lapse optical planes from a cultured day 9 mouse ovary, showing follicle shifting…….…….213
Figure 7.7: Image sequence showing an oocyte being expelled from a neonatal mouse ovary…….…….214
Figure 7.8: Schematic representation of the postulated oocyte extrusion process through the ovarian surface epithelium……217

Flowchart 9.1: Summary of the experimental processes of the thesis……232
Figure 9.1: Light micrographs of small human follicles……..235
Figure 9.2: Schematic diagram of a follicle sectioned through three different loci……...237
Figure 9.3: Screenshot of the image analysis software LUCIA……..…..238
Figure 9.4: Screenshot of the Graphclick application……..239
Figure 9.5: Whole adult human ovarian section, presented as a "collage" of stitched 2x magnification images……..240
Figure 9.6: 2x and 10x cluster of small human follicles…….…..241
Figure 9.7: Schematic representation of the images appearing in figure 9.6, as two individual coordinate systems…….…..242
Figure 9.8: Alexa 633 excitation and emission spectra……253

Abbreviations

AMH	Anti-Müllerian Hormone
BABB	Benzyl alcohol & benzyl benzoate (1:2)
BMP	Bone morphogenic protein
CT	Computed tomography (X-ray)
DAPI	4',6-diamidino-2-phenylindole (fluorescent nuclear dye)
DNA	Deoxyribonucleic acid
FSH	Follicle-stimulating hormone
FOXO3, FOXO3a	Forkhead box O3
GC(s)	Granulosa cell(s)
H&E	Haematoxylin and eosin
IGF	Insulin-like growth factor
IR	Infrared
KL	Kit Ligand (section 1.5)
LH	Lutenizing hormone
MCM-2	Mini-chromosomal maintenance-2 protein
MRI	Magnetic resonance imaging
MVH	Mouse vasa homologue protein
OPT	Optical projection tomography
PBS	Phoshpate buffered saline
PCOS	Polycystic ovary syndrome
PCR	Polymerase chain reaction
PGC(s)	Primordial germ cell
PSF	Point spread function
PI3K	Phosphatidylinositol 3-kinase (see section 1.5)
POF	Premature ovarian failure
pp	Post-partum
PSF	Point spread function
PTEN	Phosphatase enzyme (see section 1.5)
Qdots	Quantum dots
RNA	Ribonucleic acid
SEM	Standard error of the mean
UV	Ultraviolet

Chapter 1

Introduction

1.1 The ovary and its role

The *ovary* is an ovum-producing reproductive organ present in female organisms. It is commonly found in pairs as part of the vertebrate female reproductive system. Its main and most important function is to cache the organism's genetic material, and provide the means of passing it to the future generations. The ovaries also function as endocrine glands, secreting hormones necessary for reproduction. The basic unit of female reproductive biology is the ovarian *follicle*. These are spherical structures comprised by a single, centrally placed *oocyte*, also referred to as *egg*, which is surrounded by supporting somatic cells.

The survival of most species depends on sexual reproduction, which involves the formation of a zygote (embryo) from the fusion of an oocyte, which is produced by the female's ovaries, and a spermatozoon, produced by the male. This process is called fertilization. The zygote, which is the first cell of the offspring, carries all the genes that will be expressed to define the unique set of the organism's characteristics. Half of these genes are derived from the oocyte, and half from the spermatozoon.

1.2 Ovarian physiology and follicle formation

The ovaries are the elliptic shaped organs, located in the lower abdominal cavity in most mammals. In the human female, there is one ovary on each side of the pelvis, attached from one side to the pelvic bone by a fold of tissue carrying the blood vessels and nerves. On the other end, the ovaries are attached to the uterus by the ovarian ligament (Thatcher, 2000). Figure 1.1*a* presents a histological section of an adult human ovary, from an archive in our laboratory (Stubbs *et al*, 2007). The outer part of the ovary is called the *cortex*, and is mostly populated by small follicles (figure 1.1). The inner part, where large blood vessels and mature follicles are located, is called the *medulla*. The cortical area in the ovary can easily be located, as it is denser than the medulla (figure 1.1*b*). The bulk of the ovary consists of *stroma* cells (Sforza

and Forabosco, 2007). Interspersed in the stroma, and partly in the medulla, are follicles of various developmental stages (figure 1.1). Small follicles at the quiescent stage of development appearing in these sections (figure 1.1*b*), known as *primordial* follicles, have been dormant since fetal life. In humans, the pool of resting follicles is assembled around mid-gestation (Forabosco and Sforza, 2007). Primordial follicles are maintained in a quiescent state until triggered to grow; some of them are perpetuated in the ovaries for up to 50 years.

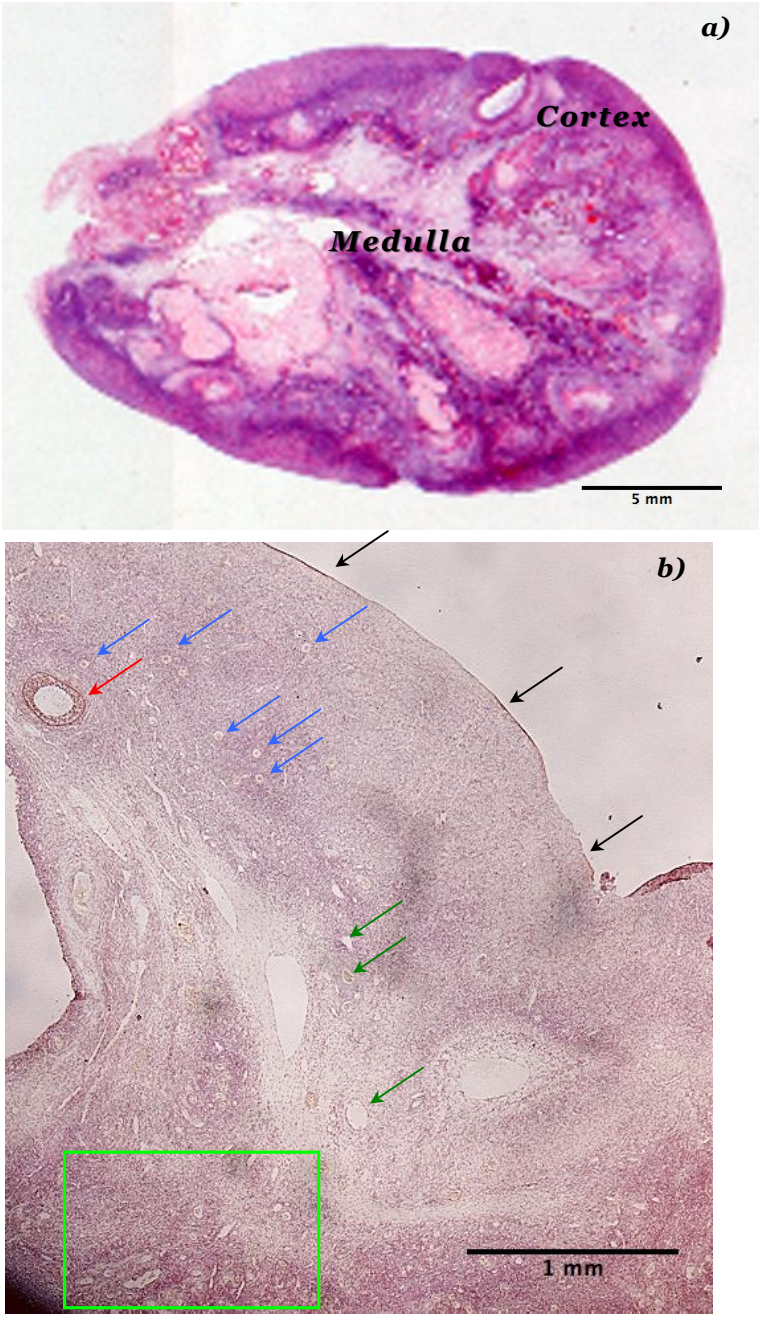


Figure 1.1: ***a)*** Adult human ovarian histological section, where the cortical and medullar areas are annotated. Fine structures such as small follicles and blood vessels are not distinguishable in such low magnification. ***b)*** Higher magnification micrograph of a part of an adult ovarian section. Various structures are shown in colour-coded arrows

In mammals, formation of oocytes is initiated in fetal life through a process known as *oogenesis* (Picton *et al*, 1998). Most of the molecular and biochemical processes, starting in embryonic life to create healthy and fully functional oocytes and follicles, are very similar in most mammalian species. Therefore in order to provide a more accurate and up-to-date review of the genesis of the follicle through fetal and neonatal life, the mouse is going to be used, as it is studied to a much greater extent than the human.

Overview of the primordial follicle formation

In the mouse, oogenesis starts with the formation of primordial germ cells (PGCs) in early gestational life (Picton *et al*, 1998). These cells respond to chemotaxic stimuli, enabling them to migrate from the yolk sac through the embryonic hindgut to the genital ridge (Picton *et al*, 1998, McLaughlin and McIver, 2009). On arrival, PGCs migrate inwards, forming primitive sex cords. In the female mice, PGCs in this phase lose their motility and become *oogonia* (Baker and Franchi 1967, Picton *et al*, 1998, Pepling, 2006). Oogonia divide by mitosis until approximately 14 days *post coitum* (mouse: Monk and McLaren, 1981, Pepling, 2006) and are developing in oogonial nests, which are also known as clusters and are connected by intercellular bridges (Pepling and Spradling, 2001, Pepling, 2006). Upon completion of mitosis, the oogonia enter the early stages of meiosis I, becoming oocytes (Monk and McLaren, 1981, Pepling, 2006). In the human, meiosis in the ovary starts at the end of the first trimester of pregnancy (Picton *et al*, 1998).

As birth approaches in the mouse, ovarian somatic cells (*pregranulosa cells*) invade the cortex from the medulla, surrounding the oogonial nests, causing them to break down. Naked oocytes lose their intercellular bridges and become surrounded by flattened pregranulosa cells (McLaughlin and McIver, 2009, Trombly *et al*, 2009). The somatic cell-surrounded oocytes arrest in meiotic prophase I, at the diplotene stage, becoming the *primordial follicles* (Baker and Franchi, 1967, Picton *et al*, 1998). In the mouse, this process completes within four days following birth (Pepling and Spradling, 2001, unpublished observations from our laboratory). In humans, primordial follicles are assembled around mid-gestation (Forabosco and Sforza, 2007).

In many mammalian species, large numbers of oocytes die early, before the formation of individual follicles (Baker, 1972). Cyst breakdown and oocyte loss in the mouse occurs within a small time frame, suggesting that these two events are developmentally regulated and closely correlated. Approximately only one third of the total oocytes in the nests survive to form primordial follicles (Pepling, 2006).

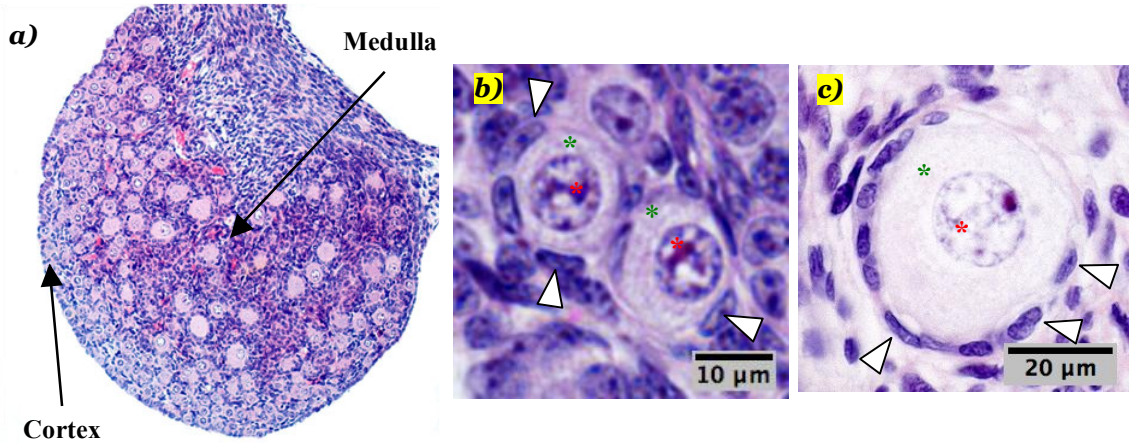


Figure 1.2: ***a)*** Day 4 mouse ovarian section after complete cysts breakdown and follicle formation. ***b)*** Light micrograph of fully formed mouse primordial follicles. ***c)*** Light micrograph of a human primordial follicle, obtained from an adult human ovarian section. White arrows point at squamous granulosa cells, green stars are oocytes and red stars are oocyte nuclei.

1.3 Follicle growth and development

The size and longevity of the pool of follicles at the primordial stage of development (primordial follicles) present within the ovaries is the primary determinant of the reproductive life-span in the female (Kezele *et al*, 2002, McLaughlin and McIver, 2009). During a female's life, primordial follicles remain quiescent in the ovary, until they are selected to grow. The mechanism of selection is still an unknown and perplexing process. The process of primordial follicle development is known as *initiation of follicle growth* (or *initial recruitment*, McGee and Hsueh, 2000). As soon as the primordial follicle stock is established, follicle recruitment begins and continues without halting (even during pregnancy) until the depletion of the quiescent pool; the follicle's fate is either ovulation of its oocyte for fertilization, or degeneration (Gougeon, 1996, Picton, 2001, McLaughlin and McIver, 2009). Once a follicle initiates growth (a process which will be discussed in section 1.3.1 and 1.5), it will usually develop until a stage where it is *gonadotrophin*

dependent (section 1.6). If at that point the organism has not reached sexual maturity, the follicle will die. Another way of follicular loss, described in the neonatal mouse, is oocyte extrusion to the peritoneal cavity, by merging its granulosa cells with the ovarian epithelium (Hiura and Fujita, 1977, Wordinger *et al,* 1990). However, this phenomenon ceases after approximately 12-14 days post-natal.

1.3.1 Initiation of follicle growth: Markers and order of events

Initiation of follicle growth (or primordial follicle activation) is characterised by several distinguishable morphological changes of the primordial follicle, which include (Picton, 2001, Kezele *et al*, 2002, Da Silva-Buttkus *et al*, 2008):

- change in shape of granulosa cells (from flattened to cuboidal)
- granulosa cell division
- oocyte growth

The aforementioned morphological criteria, categorized according to their order of event, are commonly used to distinguish between resting and growing follicles. The very first phase of development is characterized by the transformation of the flattened granulosa cells surrounding the primordial follicle oocyte to cuboidal (Picton, 2001). These flattened granulosa cells are entering the cell cycle after a long arrest at the G_0. There is however evidence of occasional flattened granulosa cell division, from studies presenting positive immunostaining for markers of proliferation in the neonatal mouse (e.g. Da Silva-Buttkus *et al*, 2008) and human (e.g. Stubbs *et al*, 2007), but is very rare.

As the number of granulosa cells surrounding the oocyte increases and the follicle progresses through the first stages of development, there is a fast increase in the size of the oocyte as well (Picton, 2001). This increase happens in mice almost at the same time as the granulosa cells start cuboidalizing and proliferating (Da Silva-Buttkus *et al*, 2008), whereas in the human, the oocyte starts growing when the follicle has approximately 15 cuboidal granulosa cells in the largest cross section (Gougeon and Chainy, 1987).

1.4 Follicle stages of growth

Ovarian follicles pass through numerous stages of morphological transformations and growth phases, from when they are quiescent and initiate growth until they ovulate (or become atretic). The growth stage of the follicle can be assessed based on morphological characteristics, such as the oocyte size, and/or the shape and the layers of the granulosa cells surrounding the oocyte.

As described in section 1.2, the smallest primordial follicles that constitute the ovarian quiescent pool contain a small oocyte arrested in diplotene of prophase I of meiosis, surrounded by a single layer of flattened granulosa (or pre-granulosa) cells (figure 1.2). The very first stage of follicle development is the *transitional* stage (figure 1.3*a*), where the flattened granulosa cells begin to cuboidalize; the oocyte has at least one flattened and at least one cuboidal granulosa cell around it. Once all granulosa cells around the oocyte are cuboidal, the follicle is then classified as *primary* (figure 1.3*b*) (classification of follicles in human ovaries: Lintern-Moore *et al*, 1974, Gougeon and Chainy, 1987, Stubbs *et al*, 2005, 2007; classification in mice: Pedersen and Peters, 1968, McGee and Hsueh, 2000, Picton, 2001).

As follicle maturation proceeds from the primary stage, granulosa cells become proliferative, forming many layers around the oocyte. Follicles that consist of two to four or five layers of cuboidal granulosa cells are classified as *secondary* (figure 1.4). A glycoprotein layer called the zona pellucida is readily visible between the oocyte and the granulosa cells (although it starts forming from the transitional stage onwards) (Gougeon, 1996). At the secondary stage, stroma cells near the basal lamina become aligned parallel to each other, forming the *theca cells*. In women a definite theca layer, comprising of the *theca externa* (same as the undifferentiated theca) and *theca interna* (also known as epithelioid cells), appears when the follicle has 3-6 layers of granulosa cells.

Secondary follicles of 80-100μm start being introduced to a supply of blood via one or two arterioles, directly exposing it to factors circulating in the blood. At this stage, a multilayered follicle is called a large *preantral* follicle, having generally more than five layers of granulosa cells and a well-defined theca layer. This period of follicle growth lasts at least 120 days in humans (Gougeon, 1996).

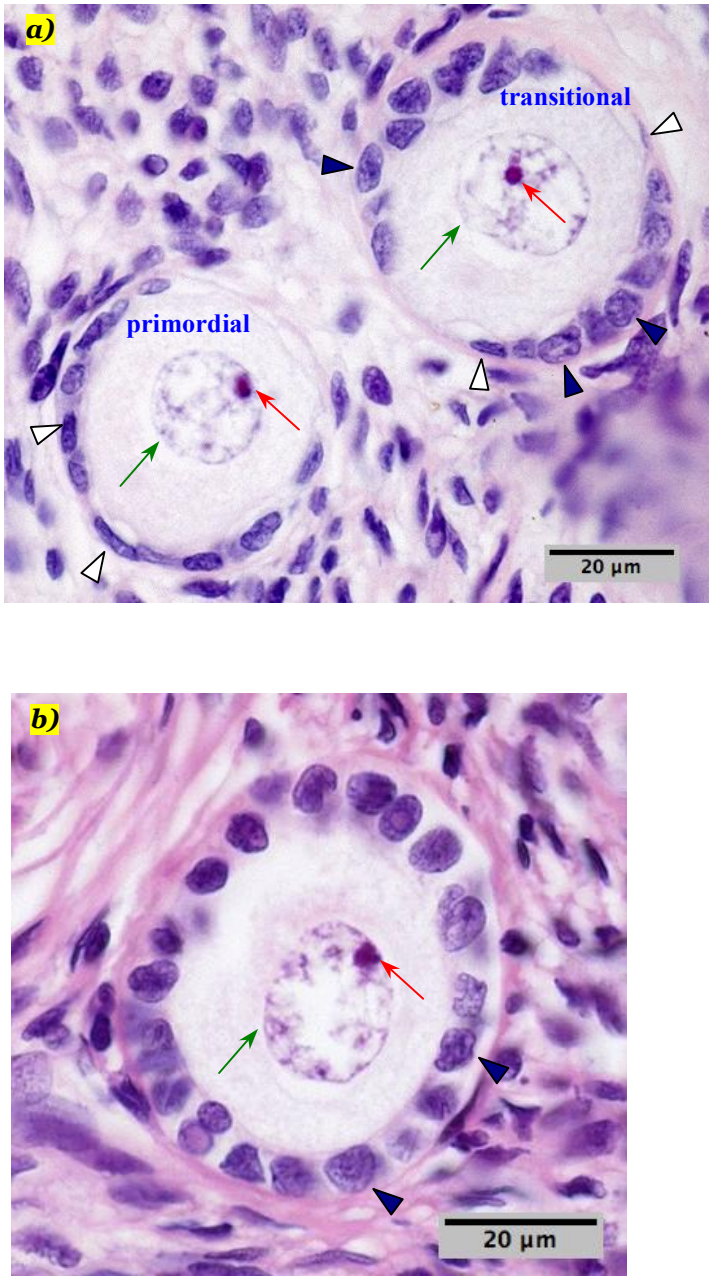


Figure 1.3: Micrographs of human ovarian follicles, obtained from adult ovarian sections stained with Haematoxylin (purple nuclei) and Eosin (pink cytoplasm) (H&E staining). ***a)*** A primordial and a transitional follicle. ***b)*** A primary follicle with a full layer of cuboidal granulosa cells. The oocyte nucleus and nucleolus are also shown. Green arrows point at the nuclei, red arrows point at the nucleoli, blue arrowheads point at cuboidal granulosa cells and white arrowheads point at flattened granulosa cells.

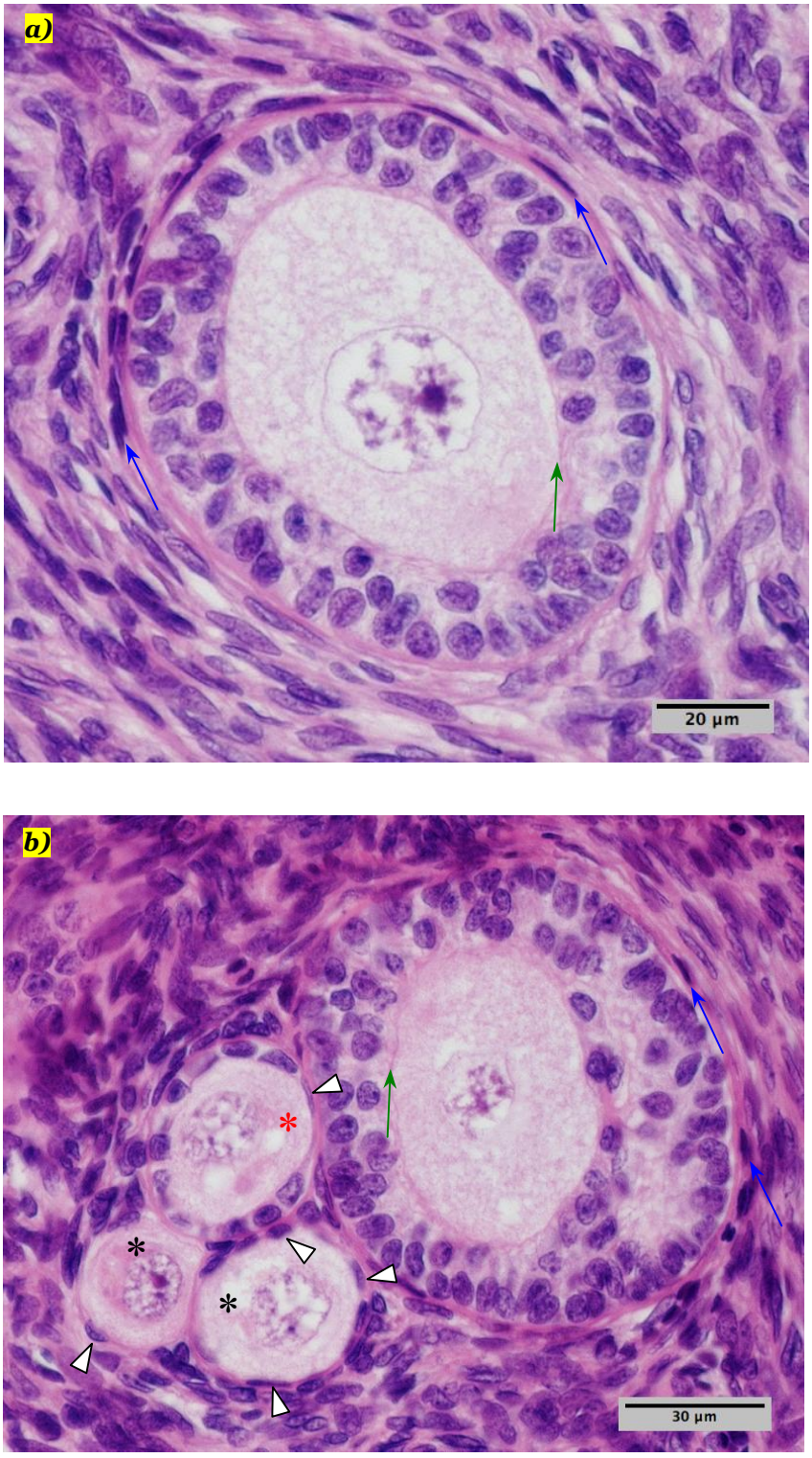


Figure 1.4: Micrographs of human follicles, obtained from adult ovarian sections stained with H&E. ***a)*** A secondary follicle, with two layers of cuboidal granulosa cells. The theca layer (blue arrows), as well as the zona pellucida (green arrow), are visible. ***b)*** An expanding secondary follicle, with the 4th layer of cuboidal granulosa cells just starting to form. Adjacent to it is one transitional follicle (red star) and two primordial follicles (black stars). White arrowheads point at flattened granulosa cells.

From a morphological point of view, after the preantral stage the granulosa cells split apart to form a fluid-filled space, called the *antrum*. The *antral* follicle (figure 1.5) increases greatly in size due to granulosa cell division and fluid accumulation in the antrum. Follicles before the secondary stage are hormone (gonadotrophin) responsive, but not hormone dependant. After the follicle has started forming an antrum, during the pre-antral stage, it also becomes dependant on hormonal activity, the absence of which leads to follicle degeneration and death. By the time of antrum formation, the oocyte has expanded its volume 150-fold in mice and 40-fold in human. The actual rate of granulosa cell division slows down in antral follicles, and under the control of follicle stimulating hormone (FSH; the hormones will be reviewed in section 1.6), the granulosa cells differentiate and become steroidogenic.

On average there are about five such follicles in healthy human females to reach the late antral stage, of which one will be selected to proceed, under hormonal regulation, to the *preovulatory* stage, where the follicle's diameter reaches 20mm. The preovulatory follicle consists of a layer of mural granulosa cells, surrounding the antrum, and layers of cumulus granulosa cells surrounding the oocyte. The final maturation stage lasts for about 14 days until ovulation of an oocyte occurs, discharged from the most dominant follicle.



Figure 1.5: Photomicrograph of a human antral follicle, obtained from an adult ovarian section stained with H&E. Various structures are colour-code annotated.

1.5 Activation of the primordial follicle

The initiation of follicle growth, which is essentially the activation of the primordial follicle to enter the growing pool of follicles, is defined by various follicular morphological changes, reviewed in section 1.3.1. Growth through the initial developmental stages, up to the secondary stage, is a long-lasting process (lasting more than 120 days in human (Gougeon, 1996) and more than 10 days in mice (Picton, 2001)), therefore making it difficult to study. Furthermore, these initial stages of development are hormone-independent, whereas from the late secondary stage and above, hormonal activity orchestrates the follicular development, and will be reviewed later. It is now well established that the follicle development at the very first stages of growth depends upon locally produced growth factors (Kezele *et al,* 2002, Skinner, 2005, Adhikari and Liu, 2009). However, the activation of the primordial follicle, and more specifically the mechanism(s) underlying the selection

of some primordial follicles to enter the growth phase whereas others remain quiescent, is up to date unknown. Numerous studies have proposed various theories regarding the activation of the primordial follicle. One of the earlier studies suggested that follicles whose oocytes entered the meiotic arrest first, are also the first to initiate growth. The theory is also known as the 'production line' hypothesis, proposed by Henderson and Edwards (1968). Studies have shown that there is higher recruitment of primordial follicles at birth (study done in rat), and gestational day of entry into meiotic arrest does influence the age of activation of the primordial follicles, but the effect is insignificant (Meredith and Doolin, 1997). Experiments have been performed to determine the effect of known growth factors on follicle initiation and growth. The most important of these growth factors are reviewed in the present section; these are compiled based on the following reviews: Kezele *et al*, 2002, Skinner, 2005, Adhikari and Liu, 2009, Mclaughlin and McIver, 2009.

Kit Ligand

Kit ligand (KL) (also termed as stem cell factor) is one of the first proteins that were shown to be important for triggering initiation of follicle growth (Huang *et al*, 1993). The kit system is comprised by the ligand (KL) and its receptor, a tyrosine kinase receptor (c-kit). The granulosa cells produce KL, encoded by the Steel Panda locus (Sl) (Huang *et al*, 1993), whereas c-kit is localized at the oocyte surface and theca interna, and is encoded by the white-spotting locus (W) (Chabot *et al*, 1988). Although six different transcripts of KL have been reported, tissue-specific patterns of expression were detected in only two mRNAs, encoding KL1 and KL2. The ratio of these mRNAs differs between tissues, between ovaries of mice of different age and between granulosa cells of preovulatory and ovulatory rat follicles (Thomas *et al*, 2008). Huang *et al* (1993) reported developmental arrest of follicles at the primary stage, on mice bearing spontaneous mutations at the SI allele (SI^{pan}/SI^{pan}). *In vitro* studies, where KL was added to isolated growing follicle culture showed an increase in oocyte growth; immunoblocking of c-kit receptor in fetal and neonatal mouse oocyte cultures arrested oocyte growth and disrupted follicle morphology (Packer *et al*, 1994). These experiments exhibit a strong relationship between oocyte and granulosa cells via the kit system (Skinner, 2005). Therefore KL induces primordial

to primary follicle transition, by acting on the oocyte, triggering its increase in size and initiation of its development (Parrott and Skinner, 1999).

Recent studies performed by Thomas *et al* (2008), suggested that KL2 isoform is associated with oocyte growth, by conducting *in vitro* studies using murine oocytes co-cultured with fibroblasts stably expressing either KL1 or KL2. In addition, KL2 was found to increase KIT receptor expression in the oocyte surface. Using Gleevec (Kit inhibitor) and ACK2 (anti-ckit neutralizing antibody), oocyte growth induced by KL2 producing fibroblasts, was shown to be suppressed (Thomas *et al*, 2008).

The Phosphatidylinositol 3-kinase pathway (PI3K)

Reddy *et al* (2005) reported recently that binding of KL produced by the granulosa cells to the oocyte c-KIT receptor regulates follicular development through the PI3K pathway. This signaling pathway is fundamental for regulating cell proliferation, migration, metabolism and survival, thus malfunctions of the PI3K pathway are implicated in diabetes and cancer (Cantley, 2002). The phosphatase and tensin homologue (PTEN) reverses the phosphorylation of the 3'-OH group on the inositol ring of inositol phoshpholipids that PI3K causes, therefore acting as a negative regulator of the PI3K pathway (Cantley, 2002). Another (synthetic) agent that specifically abolishes PI3K activity is LY294002 (Vlahos *et al,* 1994).

Reddy *et al* (2008) conducted an *in vivo* study by creating ovary-specific conditional PTEN knockout mice, as homozygous deletion of PTEN is embryonic lethal in mice. The study demonstrated that all primordial follicles initiated growth, leading to premature ovarian failure by adulthood. This established that the PI3K/PTEN pathway governs primordial follicle activation by controlling the initiation of oocyte growth. However, deletion of PTEN in oocytes of follicles of primary stage and above, the female mouse presented normal fertility, indicating that PTEN may not be essential for the further follicle development (Adhicari and Liu, 2009). John *et al* (2008) studied the mediation of the PI3K pathway through the forkhead transcription factor FOXO3, by creating transgenic mice with oocyte-specific deletions of the FOXO3 gene. FOXO3 transcription factor is suggested to enter the nucleus of the oocyte during primordial follicle assembly, and it is exported again when the follicle has initiated growth. FOXO3 null females present almost the

same phenotype as the PTEN negative, i.e. premature ovarian failure. Furthermore, John *et al* (2008) showed evidence that the only role of PTEN in the oocyte is to regulate FOXO3. In conclusion, the PI3K pathway is a major regulator of initiation of oocyte growth, essential for primordial follicle activation.

Basic Fibroblast Growth Factor (bFGF)

The basic fibroblast growth factor is expressed in oocytes of primordial and early developing follicles in ovaries of several species (Nilsson *et al,* 2001), but not in the human (Yamamoto *et al*, 1997). Nilsson *et al* (2001) conducted an *in vitro* study using floating organ cultures in neonatal rat ovaries; the bFGF treated group demonstrated an increase in the number of growing follicles, suggesting that bFGF promotes primordial follicle activation, in a similar way as the KL does. When a neutralizing antibody is used in the organ culture, the amount of spontaneous follicle development occurring in the organ culture was found to decrease. In summary, oocyte-produced bFGF influences primordial follicle development by acting on the nearby somatic cells (Skinner, 2005).

Leukemia Inhibitory Factor (LIF)

LIF and KL in combination have been shown to promote survival of primordial germ cells in mouse embryos, before primordial follicles are formed (Morita *et al*, 1999). Immunolocalization studies of LIF showed that it is produced by granulosa cells, and is acting on granulosa cells and oocyte (Nilsson *et al*, 2002). LIF is also produced by cultured human granulosa cells (Arici *et al*, 1997). In cultured neonatal rat ovaries, immunoblocking of LIF resulted in a slight decrease of spontaneous follicle development, whereas the presence of LIF is shown to increase primordial to primary transition (Nilsson *et al,* 2002).

Keratinocyte Growth Factor (KGF)

KGF is a fibroblast growth factor, localized in mesenchymal cells and stroma cells around primordial follicles in the rat ovary (Kezele *et al*, 2005). The unique receptor on which KGF binds to is the fibroblast growth factor receptor 2 (FGFR2)

(Bottaro *et al*, 1990). KGF is produced by the recruited theca cell precursors and acting on adjacent granulosa cells (Parrott *et al*, 1999). *In vitro* culture of rat ovaries in KGF rich environment showed a significant increase in primordial follicle transition; however, immunoneutralization of KGF in the culture was shown to attenuate KL stimulatory action on primordial follicles, suggesting that KL from squamous granulosa cells promotes the action or the production of KGF (Kezele *et al*, 2002).

Bone Morphogenic Proteins (BMP) & Growth Differentiation Factor-9 (GDF-9)

The BMP family of growth factors (which has around 20 members) is part of the wider transforming growth factor-ß (TGF-ß) superfamily. GDF-9 is also a member of the TGF-ß superfamily and is expressed only in the oocyte. Some of these BMPs that have a significant role in follicle development are reviewed in this section, namely BMP-4, BMP-7 and BMP-15, BMP-6 & GDF-9

BMP-4

BMP-4 protein is localized in theca cell precursors associated with primordial follicles, as well as in stroma cells and basement membranes of the follicles of neonatal rat ovaries. *In vitro* experiments of neonatal rat ovary cultures (whole organ) in which BMP-4 was added showed a higher number of growing follicles (Nilsson and Skinner, 2003). Immunoneutralization of BMP-4 in the cultured rat ovaries exhibited an effect on ovarian volume (smaller than control ovaries), as well as increased primordial follicle and oocyte loss, and an increase in cellular apoptosis, causing complete follicle depletion in 14 days (Nilsson and Skinner, 2003). This suggests that BMP-4 is a survival factor for the primordial follicles and oocytes (Skinner, 2005).

BMP-7

BMP-7 is present in the theca interna cells of the Graafian follicles, but is undetectable in any other cell type in the rat ovary (Shimasaki *et al*, 1999). *In vitro* culturing of neonatal mouse ovary in the presence of BMP-7 leads to reduced number

of primordial follicles and increased numbers of growing, from the primary up to the antral stage (Lee *et al*, 2004). Similar effects were observed when injecting BMP-7 in the ovarian bursa in rats (Lee *et al*, 2001). These findings suggest that BMP-7 facilitates activation of primordial follicles.

GDF-9, BMP-6 and BMP-15

Oocytes from early stage follicles, namely primary follicles in rodents and human were found to selectively express these three TGF-ß superfamily members, (McGrath *et al*, 1995, Elvin *et al*, 2000). GDF-9 is not expressed in primordial follicles of rodents, but it is expressed from the primary stage onwards, until ovulation. *In vivo* studies on mice lacking GDF-9 show follicle developmental arrest at the primary stage (Dong *et al*, 1996, Carabatsos *et al*, 1998). *In vitro* studies on rat ovaries cultured in the presence of GDF-9 do not show any effect on the primordial follicle development (Nilsson and Skinner, 2002), whereas in human cultured tissue, the presence of additional GDF-9 seems to facilitate activation of the primordial follicles (Hreinsson *et al*, 2002). Follicles reached up to secondary stage, and their viability was improved. Findings reported in the work published by Dong *et al* (1996) suggest that GDF-9 is implicated in sustaining the growth and differentiation of follicles after the primary follicle stage. These results show that GDF-9 may have a role in primary follicle progression, but does not affect primordial to primary follicle development (Nilsson and Skinner, 2002).

Null mutations in BMP-15 or BMP-6 gene have minimal effects on follicle development and fertility, in contrast to the infertile GDF-9 mutant animals. More specifically, BMP-6 null mice are found to be viable and fertile, and no defects are reported in tissues expressing BMP-6 (Solloway *et al*, 1998). BMP-15 null female mice are subfertile, with minimal ovarian histopathological abnormalities (Yan *et al*, 2001). Sheep with BMP-15 mutations have follicles arresting at the primary stage of development (McNatty *et al*, 2007); naturally occurring mutations in specific sheep families cause the heterozygotes to ovulate multiple eggs, whereas homozygotes to the mutation are infertile (Galloway *et al*, 2000). This suggests that concentration of BMP-15 is important and that phenotypes are observed in a dosage-specific scheme. Furthermore, double knockout of both BMP-15 and GDF-9 in mice show ovarian

phenotypes similar to the GDF-9 knockouts. Both BMP-15 and GDF-9 are important regarding the destiny of the follicle during follicle initiation and development, albeit the exact mechanisms through which GDF-9 and/or BMP-15 contribute to follicle development remain unknown (Yan *et al*, 2001).

Anti-Müllerian Hormone (AMH)

The anti-müllerian hormone, also known as müllerian inhibiting substance, is another member of the TGF-ß superfamily. In the ovary, it has been shown to regulate follicle development by inhibiting primordial to primary transition (Durlinger *et al*, 2002). In the ovaries of mouse and rat, AMH and its mRNA is not present at the primordial stage of development (Hirobe *et al*, 1992, Durlinger *et al*, 2002); once the follicle initiates growth, granulosa cells start to produce AMH, peaking at the small antral stage, where its production is stimulated by oestrogen (Durlinger *et al*, 2002). *In vivo* studies by Durlinger's group on AMH null mice revealed an elevated number of growing follicles, as well as a depleted primordial pool by the 13th month of age with reduced number of pre-antral and antral follicles in these mice (Durlinger *et al*, 1999). The findings were confirmed *in vitro* as well, on isolated mouse preantral follicles, where AMH was found to inhibit growth induced from FSH stimulation (Follicle Stimulating Hormone, section 1.6). Currently, this appears to be the only negative intra-ovarian regulator of primordial to primary follicle transition, but further studies are required to gain insight into the mechanism of AMH action, as the receptor for AMH is not expressed by primordial follicles (Adhikari and Liu, 2009).

Insulin

Insulin is produced by pancreatic ß-cells and is a hormone that has profound effects in metabolism. In the ovary, insulin receptors have been localized in stroma cells, as well as in granulosa and theca cells of developing follicles (Kezele *et al*, 2002). Insulin stimulates androgen production in cultured porcine theca cells (Barbieri *et al,* 1983), as well as oestrogen and progesterone production in cultured granulosa cells (Willis *et al*, 1996). Insulin has been shown to influence primordial to primary follicle transition in cultured hamster ovaries (Yu and Roy, 1999) and in rat ovaries, and it is suggested that insulin's site of action is the oocyte (Kezele *et al*, 2002(†)).

The effect of insulin on follicle development may be due to downstream signaling, resulting in inhibition of FOXO3 and allowing transcription of genes required for follicle activation (Jünger *et al*, 2003, McLaughlin and McIver, 2009).

Insulin-like Growth Factors (IGFs)

The IGF ligands and their receptors belong to the insulin super-family. There are two IGF ligands, IGF-I and IGF-II, and two receptors (the type-1 and type-2 IGF receptors: IGFR-1 and IGFR-2). Both of the ligands act mainly through the type 1 IGFR. Additionally, both IGF-I and insulin can stimulate each other's receptors, but with lower binding affinity (Jones and Clemmons, 1995). There is a family of six high-affinity IGF-binding proteins (IGFBP 1–6) that regulate transport and biological activity of IGFs, and associated IGFBP degrading enzymes (proteases).

IGFR-I receptors are expressed in the granulosa cells of both healthy and atretic follicles in the mouse, from primary to preovulatory developmental stage; IGF-I mRNA transcripts were found in the granulosa cells of growing healthy follicles, and their amounts are increasing as the follicle progresses through the various developmental stages (Wandji *et al*, 1998). IGF-II expression in mouse ovaries is very weak. In the human ovary, IGF-I were found in low levels in the theca cells of large follicles (3-5mm); high levels of IGF-II mRNA were detected in the granulosa cells of large antral follicles (Monget and Bondy, 2000).

IGFs may have a role in early follicle development, but are important in antral follicle growth and steroid production. *In vivo* studies in mice that were IGF-I null, follicle development was normal until the late preantral stage, where a developmental arrest was shown. The mutants however exhibited severe physiological deformations and infertility (Baker *et al*, 1996). Evidence has also been presented that activation of the IGFR-I stimulates the PI3K pathway in cultured bovine granulosa cells (Mani *et al*, 2010).

Synopsis of the set of local signals

The local signaling mechanisms described in the previous section that play key roles in regulating the activation of the primordial follicle are summarized in

figure 1.6. One can notice the complexity of the system of growth factors that coordinates the growth of the follicles, involving cellular communication between the different follicular compartments.

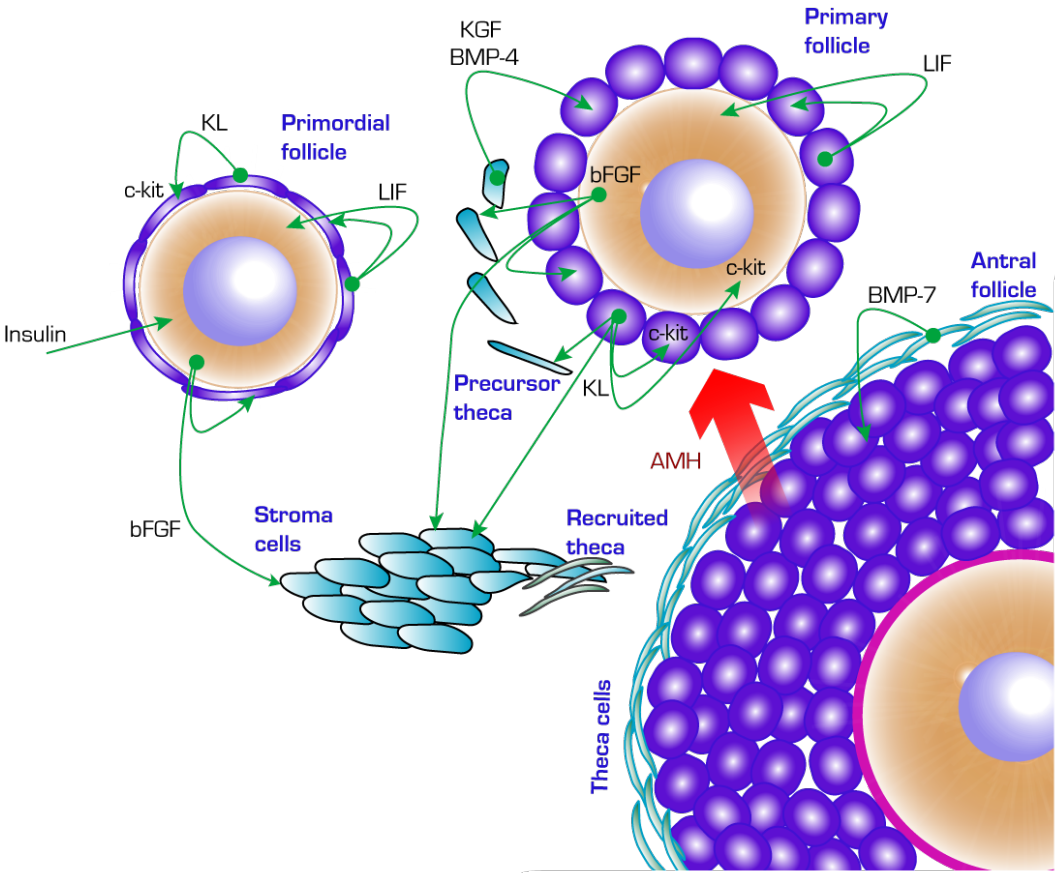


Figure 1.6: Diagram of ovarian growth factor signaling, reported in the present section. The green arrows denote promoters of follicle activation, whereas the red arrows denote inhibitors.

1.5.1 Molecular regulation of growth factors

The growth factors reviewed in the previous section can have an effect on primordial follicle regulation through a variety of molecular mechanisms; these effectively comprise many levels of regulation, which are part of a complex system for inter-cellular communication. These have been categorized in this section.

1. Extra-cellular: The signaling ligand is modified by a protein that binds to it, before it reaches the receptor on the cell surface. These can promote (agonise) or suppress (antagonise) protein binding to the receptor. Alternatively, the receptor may be occupied by another protein that binds to it, preventing the cognate ligands from activating the signaling pathway. Examples include IGF binding proteins (IGFBPs)

which can either inhibit or potentiate IGF action on target cells (Monget and Bondy, 2000), and BMPs, which have several high-affinity antagonist proteins including noggin, follistatin and chordin/SOG (Pangas *et al*, 2004).

2. Pseudoreceptors: A recently uncovered regulatory mechanism, where the protein receptor is lacking a kinase domain which is essential for intracellular signaling. These "inactive" receptors may be used to limit the signaling range of the ligands, by acting as morphogen sinks (see section 1.10, morphogen gradients). An example includes BAMBI (BMP and activin membrane-bound inhibitor) which is a type I TGF-ß superfamily pseudoreceptor (Onichtchouk *et al,* 1999). Additionally, the receptor TGFbr3 is not directly involved in TGF-ß signal transduction, rather acts as a "ligand reservoir" on the cell surface by trapping binding ligands, for other receptors to use (Andres *et al*, 1991). Another example of such a receptor is IGFR-II, which does not induce any specific cellular response when activated; however, knocking out the receptor in mice causes neonatal lethality (Dupont and Holzenberger, 2003).

3. Receptor expression: The receptor of a specific ligand can be differentially regulated within various tissues, by means of different isoforms or subtypes. Protein isoforms are different forms of the same protein, encoded from the same gene by means of alternative splicing. A subtype of a specific protein is an amino sequence that has similar function as the protein, but is encoded by a different gene. For example, TGF-ßs, have 12 receptor subtypes, 7 type I and 5 type II. Combinations of these are tissue and follicle specific (Derynck *et al*, 1988).

4. Intercellular signaling: Once the receptor is activated, the signal needs to be relayed rapidly inside the nucleus. The family of proteins that carry the signal to the nucleus specifically for TGF-ß signaling are the *Smads* (named after the ones that were first discovered, Sma in C. elegans and Mad in Drosophila). Smads are activated through a process called *phosphorylation*, and then are transported to the cell nucleus, where they become associated with other gene regulatory proteins, which activate or suppress the transcription of a certain gene. Inhibitory Smads can block Smad signaling by preventing phosphorylation (Alberts *et al*, 2008).

In summary, the presence of a ligand and a binding site (receptor) alone within a cell or a tissue does not guarantee signal transduction. A functional ligand-receptor-Smad pathway, regulated by the mechanisms described above, must be present in

order to successfully moderate a cellular process or response. Therefore in order to understand the underlying primordial follicle activation mechanisms, functional pathways within granulosa cells and oocytes need to be characterized.

1.6 Hormonal regulation of follicle growth

Initiation of follicle growth happens continuously during a woman's life from when the first follicles are formed until *menopause*, which is the stage when most follicles in the ovaries are depleted, with only a few small follicles left. Of all the follicles that will initiate growth during a female's life, only a very small portion of them will mature to the late antral stages, and fewer still will ovulate (Gougeon, 1996, Picton, 2001). Circulating gonadotrophins, follicle stimulating hormone (FSH) and lutenizing hormone (LH) are required to promote antral follicle development. During puberty there is a period of rapid growth and sexual maturation, during which the reproductive system becomes fully functional. Maturation of the hypothalamic–pituitary–gonadal axis in late puberty leads to cyclical gonadotrophin secretion and establishment of ovulation and the menstrual cycle.

Follicle initiation and growth, up to the point of hormonal dependence, takes approximately half a year in humans (Gougeon, 1996) and more than 4 weeks in rodents (McGee and Hsueh, 2000). The gonadotrophins and especially FSH are of critical importance for sustaining antral follicular growth, but early follicles, before the secondary stage, though not dependant on FSH, are FSH-responsive (Gougeon, 1996). Withdrawal of FSH triggers programmed cell death (Gougeon, 1996) in mature follicles, of secondary stage and above. Moreover, FSH promotes granulosa cell division through an indirect mechanism and triggers granulosa cells to become steroidogenic, causing them to secrete oestradiol (oestrogen). LH acts on theca interna cells (figure 1.7*a*), and with the action of *progesterone* (produced from circulating blood cholesterol), cause them to produce *androgens*. Androgens provide a substrate for *oestradiol* 17ß HSD-1 secretion by the granulosa cells; this reaction is catalyzed by aromatase, an FSH-dependent enzyme.

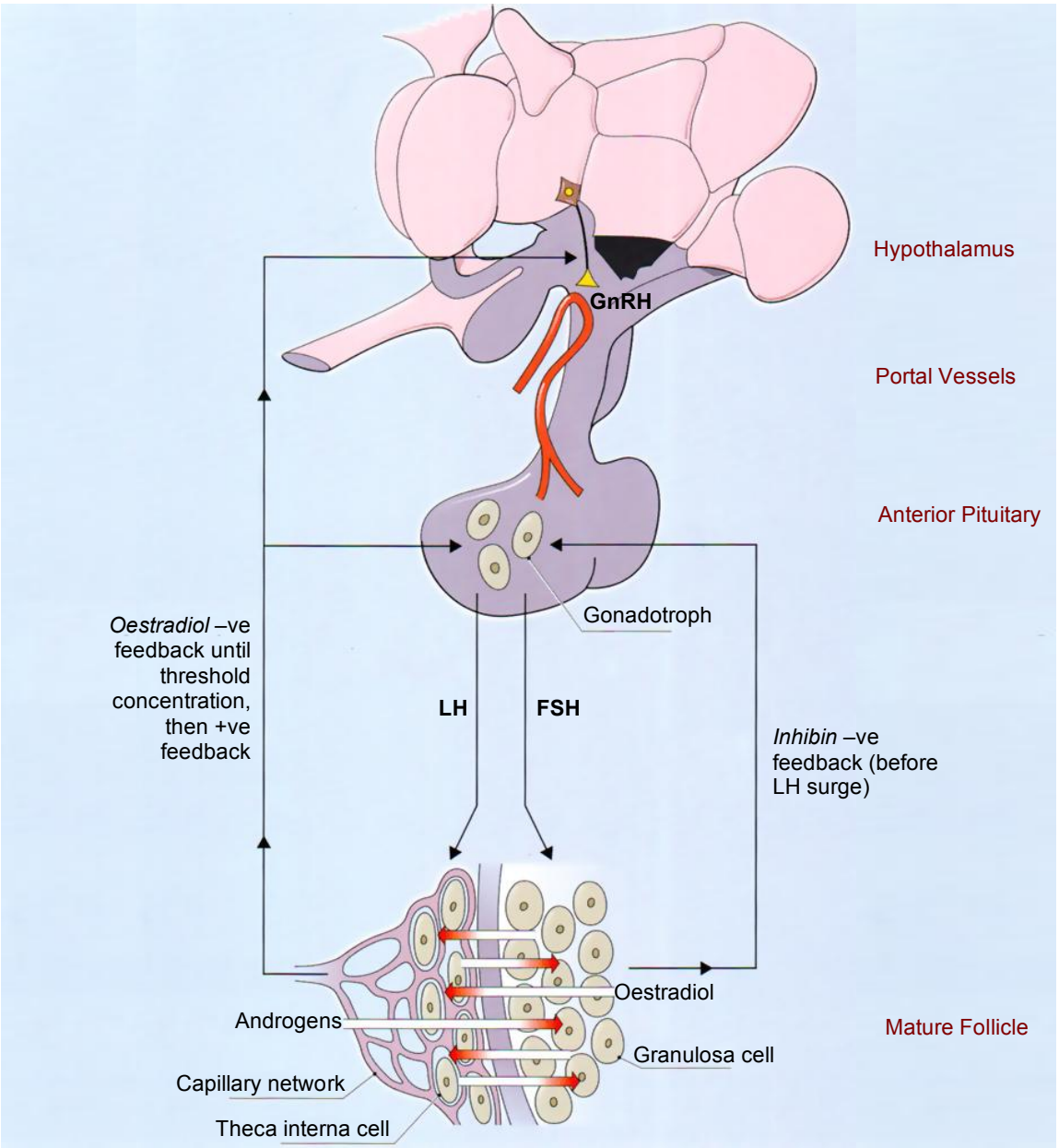


Figure 1.7: ***a)*** The negative feedback endocrine system, responsible for follicle maturation and ovulation. GnRH regulates FSH and LH prodution from the pituitary. LH acts on the theca interna cells, and with the action of progesterone they produce androgens, which are then converted to oestradiol by the granulosa cells, with the help of FSH (described in detail in image 1.7***b***). Oestradiol inhibits the production of LH and GnRH, until a critical concentration, above which oestrogen stimulates production of LH, leading to the LH surge of the menstrual cycle (figure 1.8). Images obtained and adapted from Johnson, 2007.

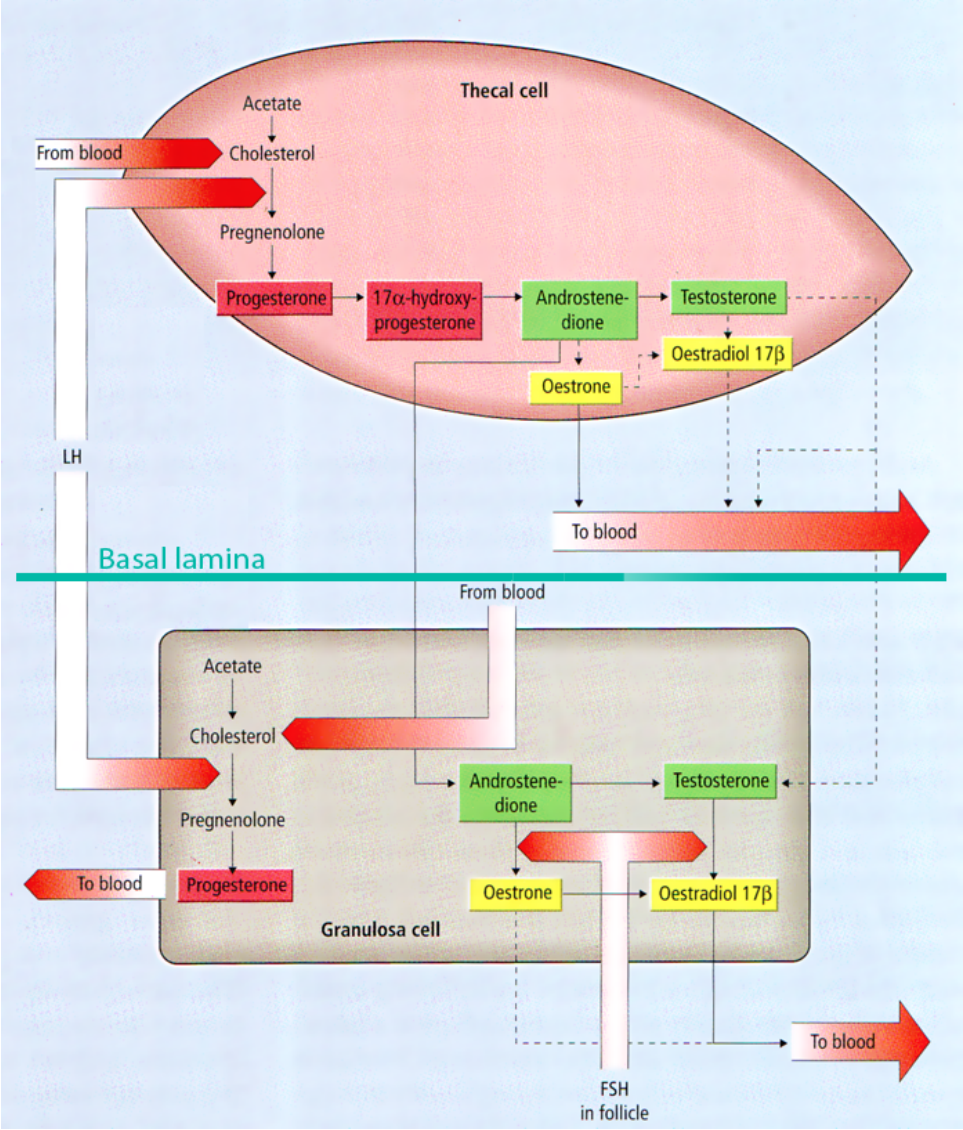


Figure 1.7: ***b)*** Detailed illustration of the theca – granulosa cell interaction in antral follicles, after these cells become part of the endocrine system, by secreting hormones. Cholesterol and LH from the blood supply transform into progesterone in the theca cells, which then acts on the granulosa cells, together with FSH to produce oestrogen. Image obtained and adapted from Johnson, 2007.

As follicular growth increases, granulosa cell numbers and secretion of oestradiol is also increasing, inhibiting FSH and LH production from the pituitary and GnRH release from the hypothalamus (figure 1.7*a*). In addition, i*nhibin B* produced by growing follicles also contributes to the negative feedback by selectively inhibiting FSH secretion. However, once oestradiol concentration in the blood crosses a specific threshold, LH secretion from the pituitary is stimulated (so called "positive feedback"), leading to the LH surge in mid cycle, which causes the follicle to rupture the ovarian surface and discharge its oocyte, in a process called *ovulation*. (figure 1.8). The described mechanism implies that the control of the menstrual cycle, as well

as the timing of ovulation is orchestrated by the ovary, not the hypothalamus or the pituitary.

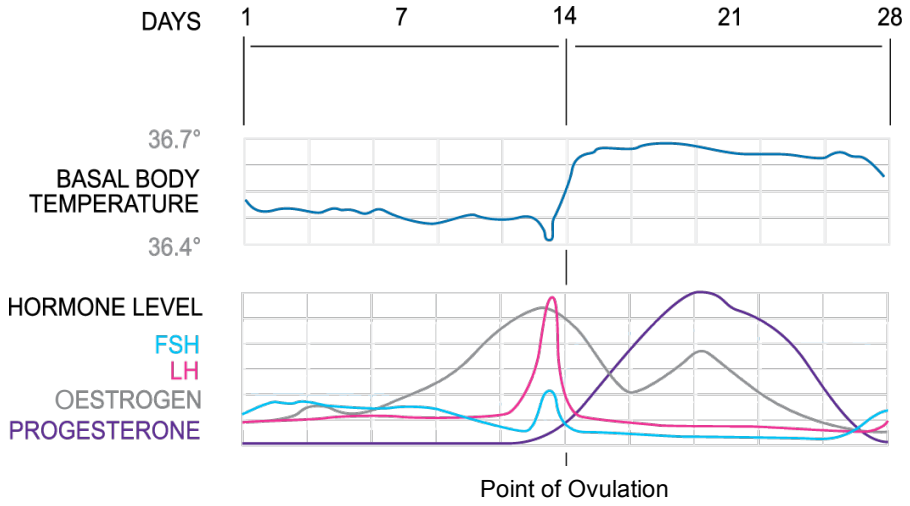


Figure 1.8: The human menstrual cycle. Follicles in the late antral stage, also termed "selectable", enter the menstrual cycle. Figure shows the fluctuation in concentration of the most important hormones, as well as of the body temperature. Image obtained and adapted from wikipedia, cross-checked with Johnson's textbook (2007) for consistency.

Follicles that fail to develop past the hormonal dependant stage, will degenerate and die through a hormonally controlled apoptotic process known as *atresia*. The remaining cohort of growing follicles continues to grow (though atresia still occurs among the more mature follicles), until they enter the menstrual cycle in the late antral stage, secreting large amounts of oestradiol. A dominant one will be selected and ovulated, 36 hours after the LH surge (figure 1.8). On average, the menstrual cycle extends among 28 days in human females, with one egg ovulated. In the mouse, the equivalent cycle lasts 4 or 5 days, yielding multiple eggs. Shortly before ovulation, the oocyte resumes meiosis, followed by the extrusion of the first and second polar bodies. The oocyte is now a haploid gamete, ready to be fertilized.

After ovulation, the ruptured follicle, under the influence of FSH and LH, forms a solid body in the ovary, known as *corpus luteum*. This structure produces significant amounts of hormones, particularly progesterone and oestrogens. The effect of progesterone is to render the endometrium receptive to implantation in the case of oocyte fertilization, as well as to increase body temperature. Unless the released egg is fertilized, the corpus luteum will slowly atrophy due to the low levels of LH. The

atrophy of the corpus luteum causes the levels of progesterone to reduce, eventually triggering menstruation. In case of fertilization however, the embryo produces human chorionic gonadotrophin (hCG), which maintains the corpus luteum to produce progesterone, providing an area rich in blood vessels in the endometrium, where the embryo can develop. Eventually, the placenta will take over progesterone production, and the corpus luteum will degenerate (Finlayson and Sanders, 2007).

1.7 Regulation of follicle growth

As follicles enter the growing phase from the primordial stage, the density of primordial follicles decreases steadily with time to maintain the growing pool (Marlies *et al*, 2006, Hansen *et al*, 2008). Figure 1.9 illustrates this decline in number of primordial follicles in humans, from birth until menopause.

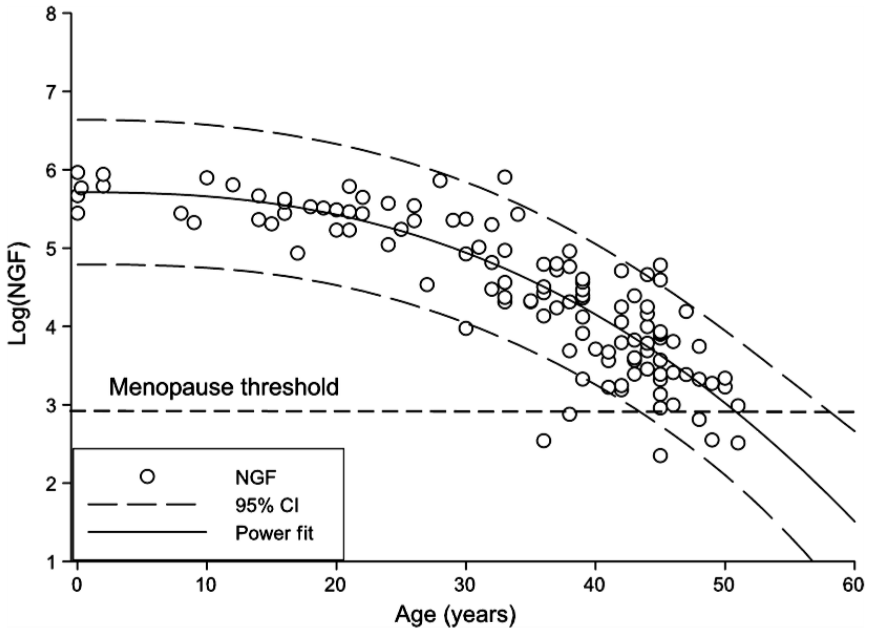


Figure 1.9: Power model of ovarian non-growing follicle (NGF) decay, in humans. The log of NGF is plotted versus age (years). The solid line indicates the fitted model (Hansen *et al*, 2008). Dashed lines are 95% confidence intervals. Graph obtained from Hansen *et al* (2008) work.

The maintenance of the growing pool necessarily depends on the rate of initiation of follicle growth and the rate of follicle loss either by ovulation or, much more commonly, by atresia. In the human ovary, the rate of depletion of the follicle

pool appears to increase in the late thirties (Faddy, 2000, Hansen *et al*, 2008) but it is not clear whether this is due to a reduced rate of recruitment, increased follicle loss or both.

The rate at which oocytes leave the quiescent pool must be tightly regulated to ensure a normal reproductive lifespan. However, research is only at the first steps of elucidating the cellular mechanisms that control the maintenance of the quiescent primordial follicle pool or the initiation of follicle growth. Recent findings have demonstrated that primordial follicle initiation of growth is controlled by means of a complex network of bidirectional signaling between the oocyte, granulosa cells and surrounding somatic cells, which involves cytokines and growth factors, as well as inter-follicular signaling (Skinner, 2005, McLaughlin and McIver, 2009, Adhikari and Liu, 2009). The role of inter-follicular signaling for primordial follicle regulation of initiation was verified by recent work carried out in our laboratory, modelling follicle spatial distributions (Da Silva-Buttkus *et al*, 2009). The intracellular signaling pathways that are activated in each cell category during follicle development are still largely uncharacterized (McLaughlin and Mclver, 2009), but are fundamental in understanding the underlying molecular mechanisms that ultimately lead to well-timed delivery of healthy oocytes for fertilization, throughout reproductive life.

Pathologies

Any malfunction to the delicately balanced process of initiation of follicle growth and follicle maturation can lead to a series of pathological states, such as premature depletion of oocytes, leading to an early menopause (also known as premature ovarian failure (POF)). This could be due to an acceleration of recruitment of follicles into the growing pool, or due to increased loss by apoptosis, or both. Another very important pathology, which may be attributed to malfunctions of this mechanism is polycystic ovary syndrome (PCOS) (Webber *et al*, 2003, Maciel *et al,* 2004, Franks *et al*, 2008), where women have multiple antral follicles in their ovaries, and a set of other hormonal disruptions associated with the ovarian malfunction (further reading about PCOS: Franks *et al*, 2008, Balen *et al*, 2009). The aetiology of PCOS is up to date unknown, although heritability studies suggest that there is genetic predisposition (Franks *et al*, 2008). There are two genes which have been recently

linked to PCOS, namely the fat mass and obesity associated gene (FTO) and Fibrillin-3. A UK based case control analysis by Barber *et al* (2008) revealed a significant link between PCOS and FTO genotype. Associations were most evident in obese subjects. Moreover, evidence was presented by Urbanek *et al* (2007) for the association of PCOS with the Fibrillin-3 gene, which is associated with metabolic features of the syndrome in post-pubertal women and their siblings.

The most intriguing question about a polycystic ovary is at which stage of follicular development follicles become abnormal. Webber *et al* (2003) presented a study reporting that PCOS ovaries have similar numbers of resting (primordial) follicles but significantly different numbers of primary follicles. Thus understanding follicle growth initiation mechanisms may lead to insight regarding the origin of both POF and PCOS.

1.7.1 Post natal oogenesis

Once the entire supply of oogonia is transformed to primordial follicles, the animal's stockpile of follicles is established and thereby declines without being renewed (Zuckerman, 1951, Baker 1963). This prevailing dogma of finite follicular reserve in the post-natal life was recently challenged, as a group of researchers presented data that were interpreted as evidence for oocyte renewal in the mouse (Johnson *et al*, 2004). The authors additionally used a study of follicle numbers (Kerr *et al*, 2006) to support their claim of the existence of a yet unknown renewal mechanism (Tilly and Johnson, 2007). In addition, Tingen *et al* (2009) present a "quorum sensing" model, which assumes a finite pool of follicles, that fits well with the experimental data, without the need for introducing unknown cells (stem cells according to Tilly and Johnson, 2007).

Regarding the origin of these stem cells, Johnson *et al* (2004) demonstrated the presence various large cells in the ovarian surface of young mice. These cells are more likely to be extruded oocytes from the ovary (Hiura and Fujita, 1977, Wordinger *et al*, 1990) as opposed to stem cells migrating inwards that was proposed (Johnson *et al*, 2004). The ovarian stem cell idea was recently bolstered up by the work of Zou *et al* (2009) claiming to have isolated female germline stem cells; these were taken from pre-pubertal and adult mice, using the mouse vasa homologue (MVH) protein which

is expressed in the oocytes. However, their technique has some obscurity, as to how a protein that is not expressed in the surface of a cell can be used to isolate these cells (Tingen *et al*, 2009). Furthermore, there is high likelihood that these isolated cells, as well as those described in an older study (Virant-Klun *et al*, 2008) are mitotic oogonia that have not entered meiosis yet, which exist in the neonatal ovary and will give rise to new oocytes (Bristol-Gould *et al*, 2006).

In this project, we will assume a finite follicle pool in the human and mouse, as well as in all mammalian ovaries, due to the lack of sound evidence for the existence of post-natal oogonia. Regarding the Tilly's group lines of argument, there seems to be misinterpretation of the nature of statistical inference in their work presented in (Johnson *et al*, 2004), according to the article published by Faddy and Gosden (2007). Therefore, it cannot be used to support their claim.

1.8 Ovarian cultures

Unveiling the functional details of the mechanism responsible for primordial follicle activation could have practical implications for contraception, alleviation of infertility, and regulation of the rate of follicle depletion (menopause). It would lead to new treatments for increasing the reproductive efficiency of women who suffer from specific reproductive pathologies, such POF and PCOS, and help women who can become infertile after gonadotoxic treatment (Sadeu *et al*, 2008).

Currently, in order to preserve the fertility of a woman, eggs can be cryopreserved by vitrification of mature oocytes, a process that can be effective but is not perfect (Cao *et al*, 2009). Understanding the mechanism responsible for the initiation of follicle growth would help develop techniques to grow oocytes from the much more abundant primordial stages in culture. Numerous techniques are established nowadays for ovarian cultures of different animal species, including rodent, cattle, primates and human (Fabbri *et al*, 2007, Sadeu *et al*, 2008). Most of these studies seek to produce competent oocytes *in vitro* (Obata *et al*, 2007). O'Brien *et al* reported a two-step culturing method (Eppig and O'Brien, 1996) that yielded very low success rates in the production of competent oocytes for meiotic maturation. The same group (O'Brien *et al*, 2003) reported in a later work a method for culturing neonatal ovaries using specific components in the culture media, enabling the

production of oocytes that have increased developmental potential. Despite this method providing proof that oocytes with full developmental potential can be produced *in vitro*, the production of high quality oocytes as those *in vivo* is still far from being achievable (further reading: O'Brien *et al*, 2003, Obata *et al*, 2007).

Research on primordial follicle activation and development is also dependent on ovarian cultures. For over 70 years (Martinovitch, 1938) researchers sought the mechanisms behind the initiation of the primordial follicle in the controlled environment of organ cultures. A wide variety of culturing methods and systems have been developed to grow tissue from various animal species. Tissue cultures include freshly dissected ovaries immediately placed into culture or ovaries that were maintained in a frozen state and thawed for culture, pieces of ovary, such as human cortical biopsies, and isolated follicles (for example, work from our laboratory on human isolated follicles and cortical biopsies in culture: Abir *et al*, 1997, Hovatta *et al*, 1999, Wright *et al*, 1999, Webber *et al*, 2007; and methods for mouse cultures reviewed in: Picton *et al*, 2008). Each of these culturing procedures offers a variety of advantages and are optimized using appropriate culture media (Fabbri *et al*, 2007).

Whole ovary cultures have the benefit of maintaining the whole organ, without causing any major structural changes (apart from the slight organ shrinkage). This is important as the 3D architecture of the follicles (theca-granulosa-oocyte complex) within the surrounding stroma is maintained, resulting in normal signaling between follicles, as opposed to isolated follicle cultures, where inter-follicular signaling is compromised. In addition, the follicles basal lamina (or extracellular matrix), which is extremely important in follicle development, remains intact in this type of culture (Rodgers *et al*, 2003, Da Silva-Buttkus *et al*, 2008). Therefore with whole organ culture systems, there is no deprivation of intra-ovarian produced growth factors or inter-follicular communication. However, this system is not ideal for specific monitoring of signaling among the small follicles, as there may be interference from the larger follicles, the lack of blood supply or from the numerous other structures in the ovary, in addition to some problems with low oxygenation and/or nutrient perfusion in the centre of the ovary. Such events can be avoided by culturing pieces of ovary, such as thin slices or cortical biopsies. In these pieces there are significantly fewer other structures that could be additional signaling sources, and

media permeability is improved; however the tissue may be damaged during the process, and this may affect development.

To address all these problems, as well as to conduct more targeted analyses, isolated follicle cultures have been developed (Eppig, 1977, Boland *et al*, 1993, Spears *et al*, 1994). These cultures are a versatile tool for studying specific follicle–follicle interactions through local signaling in various environments (Spears *et al*, 2002, Picton *et al*, 2008). The disadvantage of this system is the difficulty in isolating very small follicles, as it is a subtle procedure requiring dexterity; very low numbers of intact, usable follicles are yielded (Picton *et al*, 2008), and their survival *in vitro* is very poor (Abir *et al*, 1999). There are culture systems that are designed to maintain 3-dimensional follicle integrity once it is isolated from the ovary, so that its architecture is preserved in order to achieve further follicle growth. This has been achieved for isolated mouse follicles using collagen gels (e.g. primary mouse follicles: Torrance *et al*, 1989), or alginate hydrogels, which are encapsulating biomaterials that act as a supporting matrix for the follicles (Xu *et al*, 2006, West *et al*, 2007). The hydrogel's density can be adjusted to provide optimal bio-mechanical environment for follicle growth (West *et al*, 2007).

In general, depending on the question that needs to be answered by experimentation, the culture system is appropriately chosen and the culture conditions are tailored to support growth of the tissue. For example, isolated follicle cultures are usually optimal for studying growth of large preantral and antral follicles in rodents (Picton *et al*, 2008), whereas experiments examining the effect of a certain growth factor on small follicles are more efficiently conducted on whole ovaries (e.g. BMP-4 in rat ovaries: Nilsson and Skinner, 2003).

1.9 Assessing the number of follicles in the ovary

Studying the growth of organs such as the ovaries, liver and brain, either using fresh tissue or tissue from culturing experiments, is presented with a unique challenge; they are made up of very large numbers of individual functional units, that often need to be accurately counted in order to gain insight in their function or to compare these to pathological tissue. Example fields that require precise biological particle estimates include counting neurons (West *et al*, 1991), counting liver cells

(Santos *et al*, 2009) and in our case, counting ovarian follicles (for example in the rat: Meredith *et al*, 1999; in the mouse: Kerr *et al*, 2006; in human: Hansen *et al*, 2008). Specifically, in the ovary, the number of follicles of various developmental stages at a specific age of an individual can be indicative of fertility and/or pathological state. For example, an increased number of antral follicles in a sonogram may lead to further examinations for potential polycystic ovary syndrome, or very reduced numbers of resting follicles in a cortical biopsy may be indicative of approaching menopause. Quantitative histological analyses of follicle numbers within ovaries led to the ovarian stem cell line claims supported by the Tilly group (section 1.7.1) for renewal of follicles in the post natal mouse ovary in their initial study.

Numbers of small follicles in the ovary are particularly important. As extensively described in section 1.7, female gonads house a finite stockpile of primordial follicles that is irreversibly established in the females' early life. The number of quiescent follicles at a specific time reflects the reproductive potential of the female (McLaughlin and McIver, 2009), thus estimating follicle number as precisely as possible is desirable when conducting an experiment that may affect the animal's fertility. Typical examples where accurate estimates of ovarian follicles are required encompass studying the effect of gene knock-outs on model organisms (e.g in mice: Falender *et al*, 2005), assessing the effect of toxins to the reproductive system (*ovotoxicity*) (Hoyer *et al*, 2007), cancer chemotherapy (Perez *et al*, 1997) and studying quiescent follicle decline with ageing (for human ovaries: Block, 1952, Richardson *et al*, 1987, Gougeon *et al*, 1994, Charleston *et al*, 2007, Forabosco and Sforza, 2007, Hansen *et al*, 2008). Ovarian ageing in humans is particularly challenging to investigate from a quantitative and morphometric perspective, as rare whole ovarian specimens need to be acquired (Hansen and Soules, 2008), coming from organ donations. From these samples, the researchers need to obtain accurate and reproducible follicle counts, which is a challenging task, given the size of the human ovary (section 1.2, figure 1.1).

1.9.1 Approaches to estimating follicle numbers

Quantification of structures of interest is a common challenge for every scientist using specimen sections: use two-dimensional data (slices) to estimate the number of particles found in a volume (three dimensions). A specimen 'slab' endowed with particles of interest could be a kidney, a piece of brain or an ovary, for a biologist, or a lamina of rock, for a geologist. In both cases, investigators are interested in the internal microstructure of the 'slab', relying upon microscopy to quantify or estimate numbers of the structures of interest (Howard and Reed, 1998).

In the specific case of the ovary, estimates of the total number of ovarian follicles are obtained from histological sections. Given the complex follicle morphology, described in section 1.4, careful identification and staging of each of these diverse structures (when compared to single cells) is required, and is performed manually on each section by an experimentalist. Automatic recognition using appropriate computer software is not yet fully developed, so it is not currently employed as a standard practice. Thus a trained investigator is required to perform the very labour intensive and time-consuming task of examining, accurately counting and classifying the follicles in histological sections. In order to improve experimental efficiency in estimating follicle number, tissue sampling has to be employed, namely exhaustively serially sectioning the ovary and selecting sections for examining with a specific frequency (e.g. every 5^{th} section).

Upon dissection or termination of culture, ovarian tissue is prepared for examination using various fixation solutions (such as formalin or Bouin's solution), followed by sectioning on a microtome (typically 5μm thickness is used in our laboratory). Sections are mounted on a glass microscope slide and follicles, or any other structure of interest, are chemically stained on the tissue section. There are various methods for determining follicle number within an ovary from tissue sections. One of the most popular is to start from the first ovarian section and take every 5^{th} section. On these sections, every follicle that is presented with a clear nucleus or nucleolus is counted. This is done for every ovary available, both for the case and control, and then numbers are directly compared between the two groups. This method does not actually provide estimates of follicle numbers, as there is no

correction factor applied to the counts (e.g multiplication by the sampling frequency) however it is an accepted method in the literature for assessing follicle number variations (e.g. Hemadi *et al*, 2009). Additionally, this method requires less investigator training and less equipment for the counting.

Abercrombie's formula

Follicle number estimates can be obtained by counting all the follicles within a set number of sampled sections through the ovary; These raw counts can then be converted to an estimate of the true number of follicles, using an appropriately formulated equation which incorporates some properties of the follicles (or any object counted). Such an equation for obtaining estimates of object number from raw counts on sampled sections was proposed by Abercrombie in 1946:

$$\frac{n}{N} = 1 + \frac{H}{t} \tag{1.I}$$

where N is the estimate of the true number of particles in the volume, n is the raw counts on a section, t is the mean thickness of the sections used and H is the mean height of objects.

Abercrombie's equation is modified from Linderstrøm-Lang *et al* (1935) and converts the number of counted object segments n to an estimate of the true number N in the whole sample volume. Both H and t are measured in the Z axis, perpendicular to the XY section. Abercrombie's equation does not depend on the assumption that the objects considered are spheres, so in an ideal experiment, use of the formula (1.I) would give correct and accurate estimates, regardless of any object variation in shape, size or any other anisotropy (Abercrombie, 1946, Hedreen, 1998). Experimentally however, the major limitation of Abercrombie's correction is that the height of the objects (dimension vertical to the XY plane observed on the microscope) needs to be experimentally measured, using histological sections and the microscope micrometer, measured on the z direction. This measurement, especially when the height of the object is greater than the thickness of the section ($H>t$), is almost impossible to be accurate. Alternatively, the object height is calculated using its diameter on the

section, under the assumption that the objects (follicles in our case) are spherical. In general, inability to measure *H* and *t* from eq. 1.I with sufficient accuracy adds a source of error in the technique (Hedreen, 1998, Hedreen (†), 1998).

The unbiased stereologic technique

The modern, state-of-the-art number estimating technique, which is less commonly used in the ovary but is extremely popular in other fields such as neuron counting (West *et al*, 1991) is the *unbiased stereologic technique*, which was first put into context by the publication of the '*disector*' paper (Sterio, 1984). The disector method counts the objects directly and much more efficiently than other techniques. It consists of a pair of serial sections a known distance apart. The principle of the method is that if a transect of an object (e.g. a follicle) is seen in one section but not the next, then it is counted. There are two variations of the disector principle when it is applied to samples: the *optical* and the *physical* disector.

The **physical disector** consists of two thin sections; object transects visible in one of these, but not the other, are counted. Simple as it may sound, there is a very important practical caveat in the physical disector implementation, which is the perfect registration of the two images produced by the sections. It is found that upon application of the physical disector, most of the time during the whole procedure is spent on registering the sections (Howard and Reed, 1998). This issue has been addressed by using, for example, two projection microscopes so that the pair of sections could be viewed simultaneously (Pakkenberg and Gundersen, 1988), or by using a tandem projection microscope, where both sections could be mounted on a microscope and each could be *x,y* translated or rotated, so that they register and thereafter examined simultaneously, maintaining registration. In general, registration of two sections containing a large number of small objects, such as the neonatal mouse ovary, is very challenging.

The registration issues can be eliminated by application of the **optical disector**, where a single section at a time is considered. This section must be of large enough thickness that permits analyzing by optical sectioning on a microscope (using

high numerical aperture objectives). The microscope should also be equipped with an accurate micrometer for measuring *z*-direction distances. Two planes within the section, of set distance, are designated as the top and bottom, where the disector principle is applied (e.g. object transects visible in the bottom section, but not the top, are counted). It is very important that the depth traveled in the *z*-direction is accurately measured, usually by modern accurate opto-electronic microcators. The advantages of the optical disector over the physical is that it allows for "guard areas" above the top and below the bottom plane, that can be examined microscopically for small objects that are barely within or outside the focal plane (termed "lost caps", Hendreen, 1998†). These areas, in addition to the establishment of artificial top and bottom sections are free of the anisotropy on the section surface caused by physical sectioning of the tissue. The optical disector however cannot be applied to large samples, such as kidney glomeruli, or when the sample is opaque (Howard and Reed, 1998); in these cases, the physical disector is the only option.

The fractionator

The cornerstone of the unbiased counting methods is the ***random*** selection of samples (or sections) from the 'slab' (3D volume) that is endowed with particles of interest. Sampling is employed routinely in biology, not only because most of the times the specimen is opaque, making particles of interest invisible, but also because these are too many to count exactly. For this reason, the specimen is serially sectioned, and particle profiles are counted on selected sections (e.g. every 5^{th}); this is a simple sampling method. An unbiased sampling regimen similarly applied is termed *fractionator* and was put into context by Gundersen (1986).

The implementation of the fractionator principle (Gundersen, 1986) complements the application of the disector when applying the unbiased stereologic technique. The sampling principle underlying the fractionator is a very widespread approach of appreciable simplicity. Consider an object cut into 10 strips of arbitrary width. From this set, systematic samples of a given sampling fraction (or sampling frequency) are examined, for example 1/3. This means that every 3^{rd} section is considered, for example 2, 5, 8. An *unbiased estimate* of the total number of

structures in the object is the total number of every structure in this fraction (i.e. in sections 2, 5 and 8) multiplied by the inverse of the sampling frequency:

$$N = \frac{n}{f} \tag{1.II}$$

where N is the estimate, f is the sampling frequency and n is the raw counts. For example, if in the sections of our example there were $n=25$ structures counted, the estimate of the total number of structures in the whole object would be, according to eq. 1.II, $N=25x3=75$, for the sampling frequency selected (f =1/3). The most important caveats of the fractionator are that the fraction sampled should be explicitly known, and that it should have been selected with a random uniform probability (Howard and Reed, 1998). Practically, using the previous example, this means that for a sampling frequency of every 3 sections, a random starting point between 1 and 3 must be selected, with a uniform random probability. So the possible sampling combinations are the section sets (1, 4, 7, 10), (2, 5, 8) and (3, 6, 9).

1.9.2 Biological variability

The techniques described produce follicle numbers, either estimates on the whole ovary, such as the stereologic technique and the Abercrombie method, or 'relativistic' numbers for comparisons, by simple counting. There are two sources of error in an experiment that relies on follicle counting. The first one is the error on the estimate due to the sampling. This error must be random, i.e. by repeating the sampling it should either overestimate or underestimate the number. The technique then is referred to as *unbiased*. If, for example, follicle number is systematically overestimated, then there is a source of bias in the technique. The second source of error in estimating follicle number is *biological variability*, which is due to the intrinsic differences in follicle number within ovaries of the same species of the same strain and age (Faddy and Gosden, 2007). Biological variability for example in human ovaries can be seen in data presented when studying ovarian ageing, e.g. in Faddy's work (Faddy, 2000) and in Hansen's work (Hansen *et al*, 2008), where women of the same age, with no ovarian pathologies, can have even double the number of non-growing follicles in their ovaries (Hansen *et al*, 2008 dataset, two women of 14 years

of age have 229,357 and 462,206 follicles respectively). Remarkably, biological variability is not reflected by the age of menopause, which occurs at a more or less standard age in most species (51±8 years in humans).

In a group of animals of same species, strain and age, the follicle number within their ovaries varies around a mean value. When conducting an experiment where we have to compare different groups of animals, we wish to estimate this mean and its standard deviation, using one of the sampling techniques we mentioned before, which is also going to introduce an error (the technique's standard deviation). If the sample size is adequately large, then the error due to the technique is effectively eliminated.

Large sample sizes are very important when number of follicles is used as evidence for supporting hypothesis, such as the controversial work of Johnson *et al* (2004) which claims that the follicle stockpile is renewable. If experiment repetitions are not enough, then the results cannot and should not be conclusive, especially without appropriate statistical analysis that can confirm the result observed from the data (Faddy and Gosden, 2007).

1.10 Spatial distributions

Spatial relationships play an important role in development and regulation of biological functions in multi-cellular organisms. The presence of a developmental pattern of follicles within ovarian sections of most species has long been recognized, and is usually among the first observations to be recorded by experimentalists, which can be summarized as the small follicles (resting and early growing) being in the outer cortical area of the ovary, and the more mature ones being in the inner cortical area, towards the medulla. Patterns like those are usually linked to local regulatory processes, which act to target cells through diffusing ligands. This is a potential mechanism that may be involved to the initiation of follicle growth and development. In order to confidently deduce a conclusion as such in the ovary, follicular spatial patterns need to be extended from just qualitative assessment and be quantified. An example of an entirely qualitative assessment of the ovarian follicle pattern, and its linking with developmental processes is presented in the work of Byskov *et al* (1997).

The authors used cultured ovarian explants to assess whether rearrangement of the follicles would take place again, resulting a resting–growing follicle pattern, similar to that of the *in vivo* ovary. The assessment of the patterns is each case was done using visual comparison.

Principal examples of the pivotal importance of spatial properties of specific biological components are the morphogen gradients. A morphogen is a substance (or ligand) that spreads from a specific source in a reaction-diffusion pattern, forming a concentration pattern across the tissue (gradient); different concentrations of the morphogen generate distinct cell types during development (Turing, 1952). Spatial information is conveyed through a concentration gradient, causing distinct cell types to emerge by inducing or maintaining certain expression of genes at specific morphogen concentration thresholds. Examples include the formation of chick limbs (Summerbell, 1983) and the Hydra Vulgaris embryo formation (Turing, 1952, Soriano *et al*, 2009). Such a morphogen is the bicoid regulatory element, which is an RNA regulatory element, and is implicated in embryo differentiation, studied extensively in drosophila melanogaster (Gregor *et al*, 2007). Specifically in the ovary, there are reported morphogen gradients secreted from the oocyte that are responsible for the differentiation of the granulosa cells surrounding it into cumulus cells. A study performed by Gilchrist's group demonstrated that the oocyte actively prevents cumulus cell apoptosis by establishing a morphogen gradient of oocyte-secreted factors (GDF-9 and BMPs) (Hussein *et al*, 2005). However, the mechanisms behind the production of morphogen gradients, either in the ovary or during embryonic development, as well as the determination of spatial information, remain poorly understood.

As discussed previously, in most biological fields the analysis of spatial patterns and relationships is based on qualitative visual similarity, usually inferred from imaging data. There is a lot of material in the literature concerning descriptive quantification of spatial patterns. These techniques however are used in a diagnostic fashion; classifying sets of images to specific groups (e.g. healthy or diseased tissue), and in some cases also carry experimentalist bias (different operators may have different classification criteria). As an example for this, we can refer to research on patterns of hair follicle spacing and orientation (e.g. in Sick *et al*, 2006). The authors

use imaging data to visually compare hair follicle density between normal and transgenic mice, but without measuring any angular placements or distances between hair follicles. An alternative way to determine the density of follicles more accurately would be to extract their Cartesian coordinates and determine areas of different densities.

A good example where quantitative spatial arrangement was employed is the work by Roberts *et al* (2005); the authors examined the effect of FSH on spindle morphology and chromosome alignment. Using 3D confocal imaging, (see section 1.8), these investigators reconstruct the spindle and chromosomes, making it possible to measure the dimensions of the spindle and its spatial orientation, therefore specifically quantifying sizes and spatial *XYZ* distances of chromosomes. Chromosome separation can then be specifically studied (Roberts *et al*, 2005), whereas mere visual examination for the same investigation would severely weaken the results of the study. It is also worth mentioning other work presented by Solovei *et al* (2002) in which the authors study chromatin arrangement, where particle distances are quantified semi-automatically in three dimensions. Here the authors use image 3D reconstruction algorithms to extract numerical information about the chromatin topography within cell nuclei, and to track chromatin domain shifting in living cell nuclei, using *XYZ* coordinates of chromatin particles. Yet these data are not used to infer or model any cellular processes or mechanisms. In conclusion, unless spatial positions are explicitly quantified, it is impossible to carry out any statistical testing of significance, leading to inefficacy in strongly supporting any new biological mechanisms inferred from imaging data.

It must be stressed that this approach captures the known behaviour of the system and effectively predicts the existence of previously unknown signals and mechanisms, including their nature and range. Nevertheless, pure mathematical modeling cannot prove the correctness of the actual biological underlying mechanism, nor is able to explicitly identify the nature of the signals in questions. The method can merely provide experimental focus in a specified area, and with the use conventional laboratory techniques, which include immunohistochemistry, *in situ* hybridisation and Polymerase Chain Reaction (PCR; simple, quantitative or reverse transcription) specific proteins or highly expressed mRNAs can be identified.

1.11 Imaging

Light microscopy, in combination with proper histological sectioning and staining treatment, can provide a very clear view of biological structures of less than half a micrometer in size. There is a whole medical branch, histopathology, which relies on histological sections to accurately diagnose diseased and cancerous cases in tissue, based on expert's observations. Although the advantages of using histological specimens include important features such as very detailed structure, well-developed staining techniques and ease of handling and archiving, their biggest drawback is that the information carried within, cannot, in most cases, be extrapolated in three dimensions, without examining other sections. Given the thickness of a histological section (usually between 5μm and 15μm), examination of the three dimensional structure of even half a millimetre piece of tissue can be extremely laborious.

In the following sections, a brief overview of various techniques for tissue preparation and visualization is going to be presented, as well as a detailed description of the most popular light microscopy techniques currently used in biological research.

1.11.1 Tissue preparation

When doing *in vitro* studies of a specific organ or tissue, samples need to be prepared for microscopy, so that they can be maintained for a relatively long period of time, in parallel to significantly improve the contrast of the objects of interest. Histological sections are very thin slices of fixed tissue, which can be stained and prepared appropriately for examination under a microscope (light or electron). The process that is going to be described in this section is one of the most commonly used when examining tissue samples, although there are many alternative ones depending on the nature of the experiment that needs to be conducted. For further reading on tissue preparation techniques and stains, refer to (chapter 9, Alberts *et al*, 2008).

Fixing and sectioning

First of all, cells and cellular processes within the tissue need to be immobilized and preserved, through treatment with a fixative. The most commonly used fixatives are formaldehyde solutions (as referenced in most papers and protocols used in our laboratory). Formaldehyde forms covalent bonds with the amino group of proteins, cross-linking them so that they stabilize and lock into their position at the time. Following fixation, the tissue must be embedded in a supporting medium before sectioning, because it is soft and fragile. The supporting media permeate and surround the fixed tissue in liquid form, and then they get hardened either by lowering the temperature, if it is wax-based, or by polymerization, if it is resin-based, or by freezing, if using freezing compound media. The block containing the tissue can then be sectioned on a microtome, into a variety of thicknesses, ranging from 1μm to 15μm. The sections are then embedded on microscope slides (Alberts *et al*, 2008).

Staining

When studying the microscopic anatomy of tissue, it is usually necessary to stain the objects of interest, as biological tissue has little inherent contrast when examined under the light or electron microscope. Traditionally, sections prepared as described, are stained with organic dyes that bind to specific cellular components. For example, haematoxylin (Invitrogen, Mayer's Hematoxylin) and DAPI (Invitrogen, DAPI Nucleic Acid Stain) both bind to nucleic acids in the cells (DNA and RNA), and are used as nuclear dyes. Their difference is that haematoxylin is visible using an optical microscope, while DAPI is a *fluorescent* dye, i.e. in order to become visible it needs to be excited by light of specific wavelength, in the visible or ultra-violet (UV) spectrum.

Immunohistochemistry

A very popular staining method that enables biologists to stain theoretically any protein within a cell is immunohistochemistry, which makes use of antibodies.

First, an antibody that targets the protein of interest (or *antigen*) is introduced to the cells or tissue (after mounting on the slide as we explained). This antibody, called primary, has been established in a different organism, by injecting the antigen into it and then collecting the antibodies. Once all primary antibodies are bound to the antigen of interest, a secondary antibody is introduced, which targets the primary. This secondary antibody is attached to a marker molecule, which makes it detectable, by means of light microscopy. Note that this method applies only for using light microscopy. In the case of electron microscopy, the sample must be differently prepared (chapter 9, Alberts *et al*, 2008).

Quantum Dots (Qdots)

Qdots are polymer-encapsulated semiconductor (cadmium selenite) particles that can fluoresce at a variety of visible-spectrum wavelengths. Their coating is hydrophilic, in order for them to be water-soluble. These can be bioconjugated to protein probes, such as antibodies, and can then be introduced to cells or tissue and bind to the protein of interest. The fluorescent light wavelength emitted from the quantum dots is dependant on the size of the semiconductor crystal; the big Qdots emit red light, whereas smaller ones emit blue light, however they are all excited by the same near-UV light. Unlike most fluorescent organic dyes, Qdots have improved photobleaching resistance and can sustain their functionality under harsh conditions such as strong corrosive environments and varied salt conditions (Alberts, 2008, Kherlopian *et al*, 2008).

Autofluorescence

Cells contain molecules that can naturally fluoresce light upon excitation by light of suitable wavelength (UV or visible radiation). This is an intrinsic property of the cells, termed *autofluorescence*; this is opposed to fluorescence induced by the addition of fluorescent markers by the experimentalist (Alberts *et al*, 2008). The most important endogenous fluorescent molecules are pyridinic (class of aromatic

heterocyclic compounds containing a ring of five carbon atoms and an nitrogen atom, such as NAPDH) and flavin coenzymes. When imaging tissues, the extracellular matrices usually contribute more to autofluorescence emission than the internal cellular components, due to collagen and elastin that also fluoresce. These have a higher quantum yield, i.e. higher emitted to absorbed photons ratio (Monici, 2005). Autofluorescence is usually an unwanted property of tissue, especially when it is fixed and stained for a specific structure, as it contributes to background fluorescence. There are however cases where autofluorescenece can be invaluable, such as when performing *in vivo* imaging of tissue that cannot be stained; pathological or metabolic changes in live cells can have a direct effect on the amount and distribution of autofluorescence (e.g. dermatological imaging exploiting collagen structural transitions; Tsai *et al*, 2009). Moreover, imaging using autofluorescence eliminates the preparation time, as no special treatment or staining is required (Monici, 2005).

1.11.2 Imaging approaches

There is a multitude of tools and approaches available to fit practically any experimentalist's needs for stained specimen examination. The "challenging" part is to identify the optimal method for the case of study, considering the parameters of the various systems. The most important of these parameters are the *optical resolution* that can be achieved by the instrument, (Figure 1.10), the preparation required for the sample (fixing, staining, culturing etc.), how *invasive* the technique is and of course the cost and availability of the required devices to run the experiment. The term "invasive" refers to the technique destroying elements that are directly or indirectly linked to the structure of interest. Examples include laser phototoxicity in live cells (Trigo *et al*, 2009), excessive heating of fixed or cultured tissue from infrared laser photon absorption (Koester *et al*, 1999) and gamma-ray nucleic acid mutations.

In human subjects, internal structures and organs, including ovaries, can be examined *in vivo* using ultrasound-based diagnostic imaging techniques, termed diagnostic sonography or ultrasonography. Ovarian ultrasonography is used mainly in a diagnostic manner (Dewailly *et al*, 2010), as big follicles (>2mm in diameter) can be visualized and, for example, can help identify cases of polycystic ovarian

syndrome. This imaging method is considered extremely safe; it is non-invasive, but its drawback is that the resolution is very poor. The reason being that ovaries are quite deep inside the human body, so the ultrasound has to be tuned to lower frequencies that allow deeper penetrations but at a cost of reduced axial and lateral resolution.

Resolution plays an important role in our project, to enable accurate follicle examination of all stages, especially the early developmental stages in the range of primordial to secondary (Figure 1.10). Thus ultrasound is not appropriate for studying ovarian function at primordial follicle level. Instead, histological sections of fixed ovaries (both human and mice) are used. The Transmission Electron Microscope can provide resolutions of a few nanometers, with the best of them able to visualize silicon atoms, a resolution of 0.78Å (0.078 nanometers) (High-Resolution Electron Microscopes - O'Keefe *et al*, 2001).

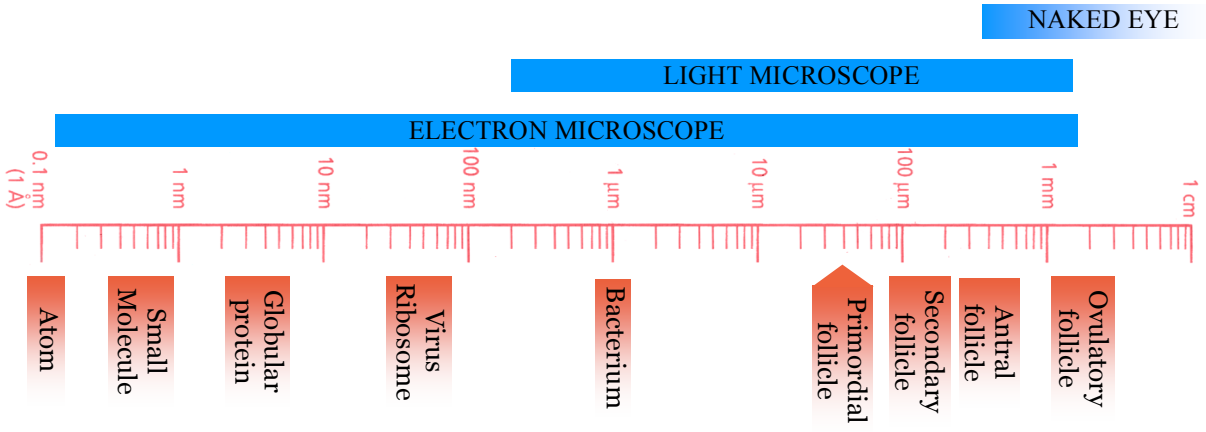


Figure 1.10: Resolutions of various detection systems, and the range of cells and their components that can be detected, drawn on a logarithmic scale. Follicle sizes reported are approximate and refer to human. Obtained and adapted from Alberts *et al* (2008).

However, the resolution provided by the electron microscope is neither necessary nor practical for the studies of follicle dynamics, unless details of the follicle ultrastructure are required. The instruments of choice for ovarian biologists are optical and confocal microscopes, which provide adequate resolution (up to a few micro-metres), and can be versatile in that they can visualize samples prepared with a variety of techniques. These include fixed and stained histological sections, which can be observed using either optical or confocal microscopes, as well as whole tissue

imaging (3D acquisition) of fixed tissue or even live time lapse imaging of cultured tissue, observed using the confocal microscope.

1.11.3 Optical instruments for fluorescent microscopy

Fluorescent or widefield microscope

The most common method used to examine fluorescently labeled samples is through a fluorescent microscope (*widefield* microscopy). The instrument is used to directly detect emitted fluorescent light from the stained structure. The sample thickness ranges between 2-5μm, up to 15μm. Figure 1.11 presents the principle of operation of a conventional fluorescent microscope. The basic concept is that the sample is illuminated by a light source, which is within a specific wavelength band in order to appropriately excite each fluorophore. The light emitted then passes through a dichroic mirror and an emission filter (so that any reflected excitation light can be eliminated) and is detected either by eye through the eyepiece or by a digital camera (further reading: Pawley, 2006).

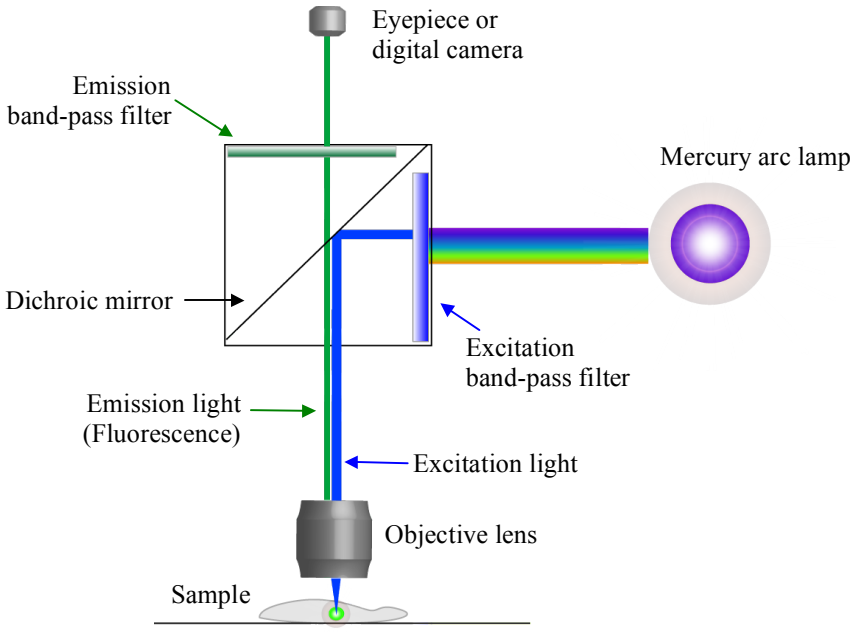


Figure 1.11: Illustration of the basic parts comprising a conventional (or widefield) fluorescent microscope. An example of light path is also shown, to demonstrate the interaction with the various microscope components.

The confocal microscope

The fluorescent microscope only provides a sharp image of one plane of focus, which is where the sample can be observed at maximum clarity. Any images obtained above and below the focal point will be blurred, as they contain light coming from the entire volume of the specimen that is illuminated (figure 1.11). This is one of the most important limitations of this microscopy technique. A solution to this problem comes from the relatively recently developed confocal microscope (compared to the optical, which dates back to the 16th century) by Marvin Minsky in 1957 (Masters, 2006). The confocal microscope can be considered as a variant of a conventional fluorescent microscope, because the samples that are examined need to be stained using fluorescent dyes. The basic idea behind the confocal microscope design is that in order to improve image quality, each point on the focal plane of the sample must be free of out of focus light contribution (Masters, 2006). This is implemented by illuminating each point on the sample separately, instead of bathing in light the entire sample, and by adding a pinhole to the system, to exclude as much out-of-focus light as possible. This design, which is the basis of the confocal microscope, is presented in figure 1.12. The discovery of the laser facilitated the development of the confocal microscope enormously, as it can provide monochromatic light for fluorescent excitation, while the beam can be focused on an extremely small and intense point on the focal plane. The point diameter is comparable to the wavelength of the excitation light, usually ~500nm. The sample is scanned in a raster pattern by the focused laser beam, and the emitted light of each focal point is collected in a photo-multiplier tube. The image is constructed on the computer screen.

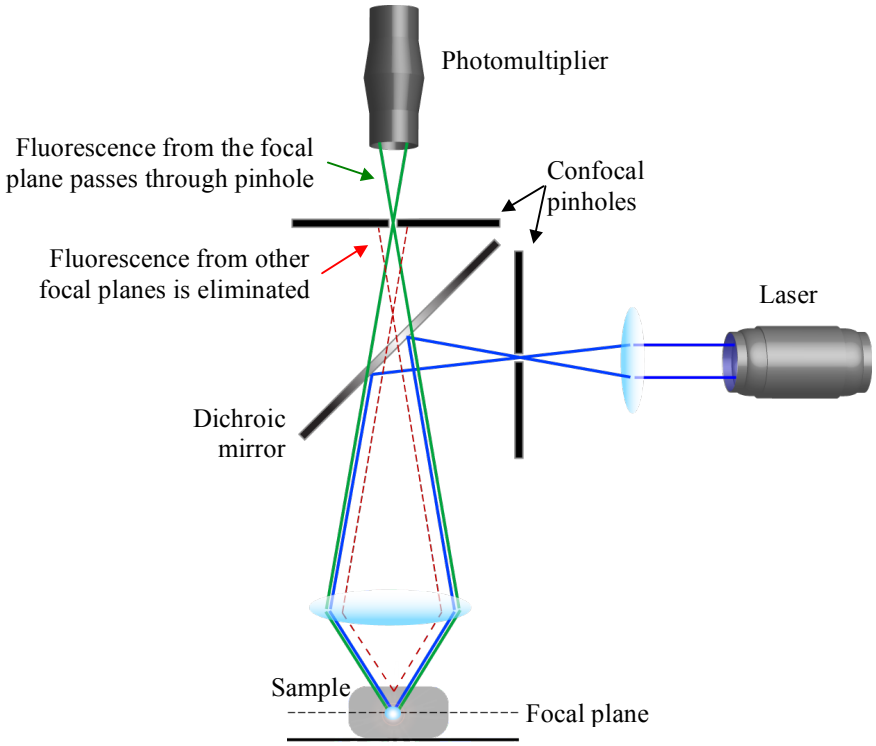


Figure 1.12: Schematic diagram of the basic parts of a confocal microscope. An example of light path is outlined. Note that the out-of-focus light is outlined in red. Additionally, a small amount of out-of-focus light passes through the pinhole opening, which can be reduced by reducing the diameter of the pinhole.

Confocal microscopy is ideal for use with specimens that cannot be sectioned (e.g. for live tissue imaging) or with thick samples (Zucker, 2006), as it dramatically reduces out-of-focus fluorescence. However, regions of the specimen above and below the focal point are exposed to the intense light converging and diverging from the illuminated spot. This is one of the fundamental limitations of the system, i.e. the "infinitely" small focused point actually covers a non-negligible excitation area, which can be problematic when the specimen is very thick, because overlapping of certain structures, as well as slight blurring, may occur. Of course, this is not comparable to the extreme blurring happening at the out-of-focus planes on the widefield microscope, but it can still be problematic.

Deconvolution

The out-of-focus light in images produced either from the widefield or the confocal microscope can be digitally removed by means of image processing, based on the optical properties of the imaging system, as explained below. Figure 1.13 presents schematically the way the out-of-focus light is introduced in the image from a fluorescent micro bead.

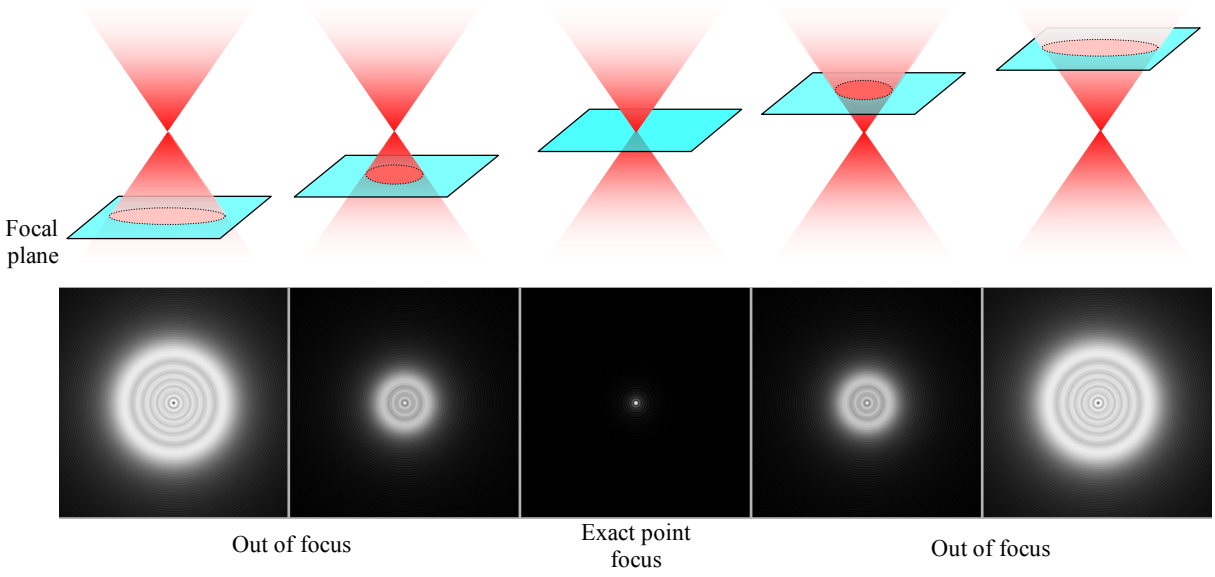


Figure 1.13: Various focal planes of a point source (e.g. excited fluorescent micro bead) as imaged by a system without any optical aberrations. The system response, when imaging a point source, describes its Point Spread Function (PSF). (Bottom set of pictures obtained from wikipedia.org).

Light that is emitted by a single point source, excited in a fluorescent microscope, is captured by the objective lens at various focal points (figure 1.13). This can also happen in the confocal microscope, as a very small amount of out-of-focus light passes through the pinhole (figure 1.12). A set of diffraction fringes is obtained from the out-of-focus light, known as the *Point Spread Function* (PSF) (see Pawley, 2006, textbook). The PSF is characteristic of every optical system and differs depending on the various components of the instrument (objectives, dichroic mirrors, prisms etc.). Any image captured on a particular system, *I(x,y,z)* is the result of the *convolution* of the function describing the real light distribution at the specific focal

plane in the sample, *R(x,y,z)*, with the instrument PSF, *p(x,y,z)*. This process is illustrated in mathematical form in eq. 1.III, and is depicted in figure 1.14.

$$I(x,y,z) = R(x,y,z) * p(x,y,z) \qquad (1.III)$$

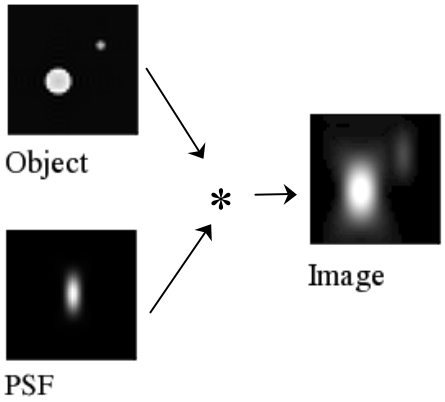


Figure 1.14: *XZ* view of a reconstructed image of a widefield microscope. The 3D distribution in the final image results from the convolution of the actual light emitted from the object with the systems *PSF*. (Images are for illustrative purposes and are obtained from wikipedia.org, released into the public domain).

Therefore, the inverse mathematical operation on an acquired image, termed *deconvolution*, reverses this process and results in an image that reveals the true light distribution in a given optical plane (further reading on deconvolution: Pawley, 2006).

The main advantages of using light microscopy in combination with deconvolution are that the image acquisition using a conventional widefield microscope is extremely fast, and the processing is software-based, which reduces cost significantly. The limitations are that the actual deconvolution process is too computationally intensive, even for modern desktop computers (with up to 8-core processors) that are normally used; currently, immediate, real-time results cannot be produced. In addition, changes in the optics (refractive index of sample, instrument misalignment) prevent good deconvolution. Overall, the technique when applied correctly on a widefield microscope produces significantly improved results, comparable to those obtained by confocal microscopes (Pawley, 2006, Alberts, 2008).

Multi-photon excitation microscopy

Non-linear optics can provide solutions for two other fundamental limitations imposed when imaging large sample volumes using the aforementioned techniques; the depth of imaging and the out-of-focus collected light. Imaging is performed on a system like the one described in figure 1.12, but the laser source is a pulsed laser. Two or three ultra-short (10^{-15} sec apart) light pulses are used to excite the fluorescent dye. The underlying principle was originally proposed in 1931 by Maria Göppert-Mayer, but effectively applied after the invention of the first ruby laser in 1960 by Theodor Maiman (Masters, 2006). Maria Göppert-Mayer discovered that there is possibility for an electron to absorb two photons which arrive within a very short difference of time (10^{-12} sec or less), in order to reach an excited state (figure 1.15). Based on this, and with the development of the Titanium:Sapphire mode-locked pulse laser in 1990 (further reading on mode-locking pulsed lasers: Cundiff and Ye, 2003, Masters, 2006 "Part 3, non linear microscopy"), multi-photon microscopy was introduced in the same year by Denk, Strickler and Webb (Potter, 1996).

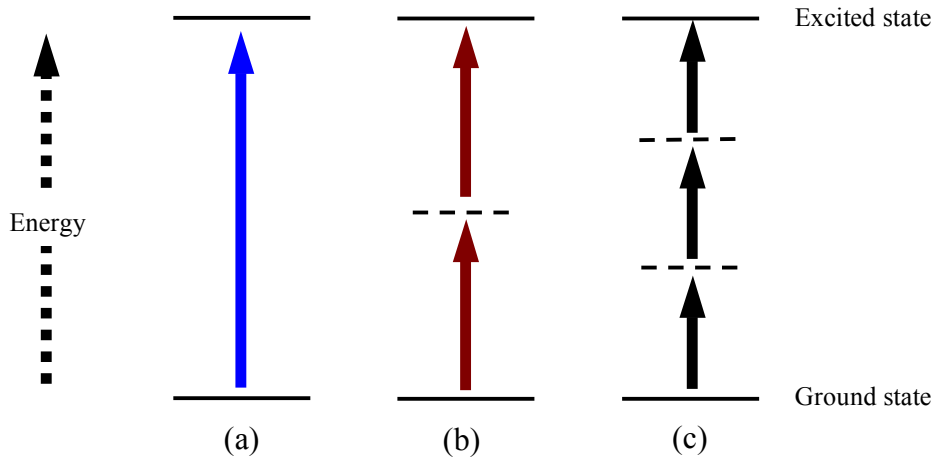


Figure 1.15: Schematic diagram showing the electronic transitions to the excited state by (a) one photon absorption, (b) two photon absorption, (c) three photon absorption. Dashed lines represent virtual states. Adapted from (Masters, 2006).

In the case of two-photon excited fluorescence, two near-infrared photons in the spectral range of 700–1200 nm (the spectral range corresponds with the wavelength range of tunable Titanium:sapphire lasers) are absorbed simultaneously (Schenke-Layland, 2008). Each photon provides half of the energy, which is normally

required to excite the fluorophore into a higher electronic state. Therefore, the blue, green, yellow and red emission of fluorophores can be induced with low-energy, near-infrared photons (figure 1.15). Multiphoton processes require a high concentration of photons in space and time, therefore excitation only happens at the focal point, where photon density is maximal; the need for a pinhole is eliminated, because all emitted fluorescence comes from the actual focal plane. Additionally, infrared photons can penetrate deeper in the tissue, and do not cause phototoxic effects to the cells, rendering the method suitable for live tissue imaging. Moreover, there is no photobleaching of the fluorophore, as individual low energy infrared photons passing through the specimen do not excite the fluorescent molecules (Masters, 2006).

Limitations of this method include laser output power, which is relatively high for the phenomenon to happen, compared to single photon microscopy, thus if the tissue or medium absorbs near infrared light, it can be overheated and destroyed (Chia and Levene, 2009). In addition, because of the nature of the phenomenon, the emitted light is in most cases much less than the one detected in normal confocal, decreasing the signal-to-noise ratio, especially if the fluorophore is not suitable for multi-photon microscopy. This results in images with poor staining visualization and increased snow-like noise in the stained areas (Masters, 2006).

Optical Projection Tomography

Confocal and multiphoton microscopy is often limited by the size of the sample. In our case, if we would like to study the ovary from bovine species instead of mouse, the size of our specimens would be significantly larger than the ones we have now, thus we would not be able to capture their entire three–dimensional structure using confocal microscopy. Instead, a newly developed technique can be used, which is equivalent to the X-ray computed tomography, termed *Optical Projection Tomography* (OPT) (Sharpe, 2004).

Contrary to the confocal and widefield microscopy, where the sample is placed on a stage and *XY* images are acquired in the *Z* direction, the OPT uses a cylindrical holder for the sample, usually made from agarose, so that it can be symmetrically rotated (figure 1.16). A series of transverse projections *XZ* are acquired at a number of different projection angles. These are then used to reconstruct the

projection images to a stack of *XY* slices, using the same mathematical principles of CT, applied directly (Sharpe, 2003, Sharpe, 2004, McGinty *et al*, 2008).

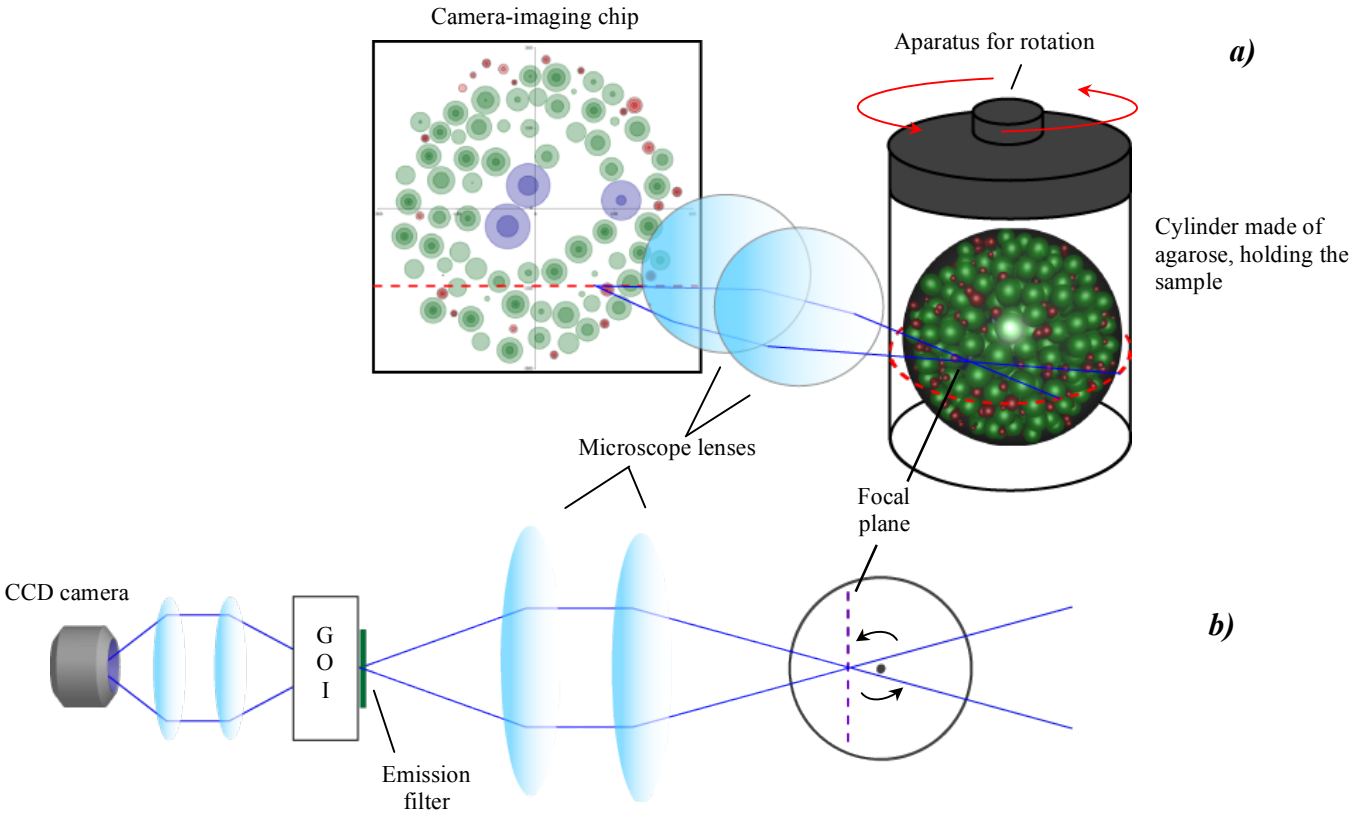


Figure 1.16: Optical Projection Tomography. ***a)*** The specimen is rotated within a cylinder of agarose, which is bathed in a chemical for optical clearing. The light emitted from an *XY* plane, perpendicular to the axis of rotation, is focused on a single row of pixels on the camera-imaging chip (red ellipse). Blue lines show the light path through the sample, which creates a single pixel. ***b)*** The image projected on the CCD is an *XZ* projection of the specimen at the focal point. The fluorescence is imaged on the photocathode of a gated optical intensifier (GOI) and a CCD camera records the resulting time-gated intensified fluorescence signals. Image ***a)*** adjusted from (Sharpe, 2003), and ***b)*** adjusted from (McGinty *et al*, 2008)

OPT, just like confocal microscopy, requires the sample to be bathed in some clearing agent, so that it can become transparent, scattering the light as little as possible, to obtain high quality reconstructions. The need for deep penetration within the tissue is partly eliminated, but the projections need to be acquired at an adequate depth, so that a full 360º rotation will cover the whole volume of the specimen (figure 1.16). Infrared excitation wavelengths can be used as well, which have the ability to transverse up to approximately 500µm (Chia and Levene, 2009) in living tissue, but

the high scattering (especially where chemical clearing is impossible) means that only low-resolution reconstructions are feasible (Chen *et al*, 2000).

In general, microscopic imaging and appropriate staining techniques are essential in order to conduct experiments such as follicle counting, spatial distributions quantification, or even for histological examination of diseased tissue. A fundamental part of biological research is tissue examination, which is followed by experimental measurements and/or qualitative assessments. Imaging plays an important role in modern biology, as any regions of interest within a specimen can be digitally stored within one or more images for future examination and processing. Most tissue examination equipment comes with embedded technology to export any observations into digital images (e.g. optical and fluorescence microscopes, x-ray machines, etc.), while others depend entirely on digital image processing and storage techniques to enable the user to visualize the specimen (e.g. confocal and electron microscopes, ultrasound devices, Magnetic Resonance Imaging, Computed Tomography, OPT, etc).

1.12 Object recognition

As discussed in the previous section, the discovery and development of new imaging technologies such as ultrasound, X-Ray CT scan and MRI have contributed to the tremendous progress in medicine, in both diagnosis and treatment (Sharpe, 2004). However, it was the parallel progress of computer science that allowed efficient use of these technologies. For without computational processing of the images acquired, the medical and biological community would be unable to probe into the structure, function and pathology of tissue, or plan treatments and surgery, most of which are currently performed in real time, non-invasively. At other times, information needs to be interpreted in a timely and accurate manner, to benefit health care. There are numerous medical fields where computational image analysis can provide insight into treatment of various diseases, such as cancer, by revealing information otherwise invisible to the physician. As an example, we can refer to a clinical method for detecting cervical cancer, using imaging spectral analysis (Soutter *et al*, 2009). This system relies on accurate image registration in real time in order to avoid false positives when detecting cancerous lesions. Therefore it would be

impossible to make the most of this imaging technology if it were not for computational analysis.

Modern computers can perform complex mathematical tasks much faster, more efficiently and more precisely than humans. However, in many other problems, such as tasks involving recognising an image, a three-year-old can outperform the most sophisticated algorithms available today (see figure 1.17). This comes as a result of the lack of intelligence, which encapsulates the ability to learn, adapt and extrapolate; this is the basis of computer vision, which belongs to the broader scientific area of machine learning.

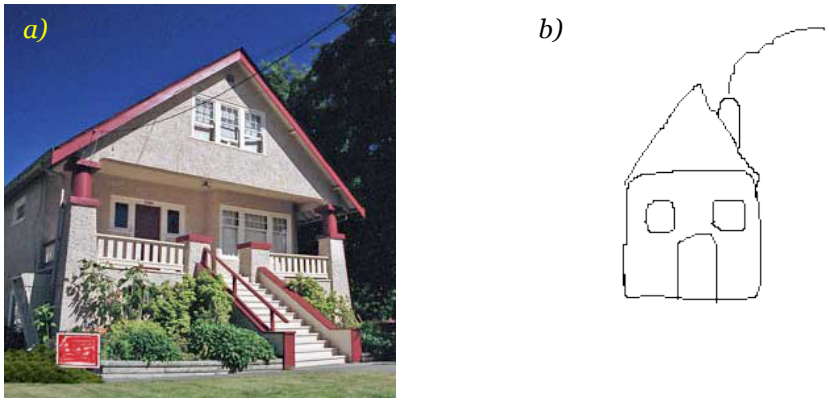


Figure 1.17: It is easy for a human to understand within milliseconds that both images depict a house. The computer however would require different algorithms to recognize the house in image ***a)***, which is a photograph with a lot of background (trees, garden etc), and relate it to the simple diagram house in image ***b)***. Tasks that seem trivial for the human brain often require extremely complex algorithms to be reproduced by the computer.

Artificial Intelligence may not as yet be developed to an extent where the computer could be trained to recognise objects in a robust way, as the human brain does; but the increase of inexpensive desktop computer power and the development of supercomputers with thousands of processing cores (currently, the fastest computer is the "Cray Jaguar" with 224,256 processing cores, able to perform 1750.10^{15} calculations per second: http://www.nccs.gov/computing-resources/jaguar/#XT5-6-Core-Upgrade) has enabled researchers to implement increasingly complex algorithms to perform image analysis and facilitate or automate object recognition to as a broad extend as possible. There are six fundamental classes of algorithms used in modern medical and biological image processing (Bankman, 2009):

- Image Enhancement (preprocessing)
- Segmentation
- Quantification
- Registration
- Visualization
- Compression, Storage, Communication

The most important and challenging algorithm classes are the first three, as they are the core of object detection and are continuously being improved to increase their efficiency. Segmentation in particular is the essence of object recognition, where structures of interest need to be discriminated from the image background.

Preprocessing

Image enhancement, or preprocessing, is the stage where the image is prepared for the object recognition. This encompasses noise removal from the image, and increase of the contrast of the structures of interest. Comparison between images of normal and pathological tissue in biology could become difficult if noise levels are high; therefore enhancing those could significantly improve structure recognition and analysis (Bankman, 2009). The challenging part, either in scientific imaging or medical imaging, is to ensure that any noise removal or contrast enhancement does not alter the information conveyed, i.e. does not falsify results in biological imaging by stressing or removing weak staining, or does not conceal or enhance areas in medical images that could lead to a different diagnosis. Figure 1.18 shows two examples of digital image enhancement on blots, one improving image quality and one where enhancement is inappropriately used.

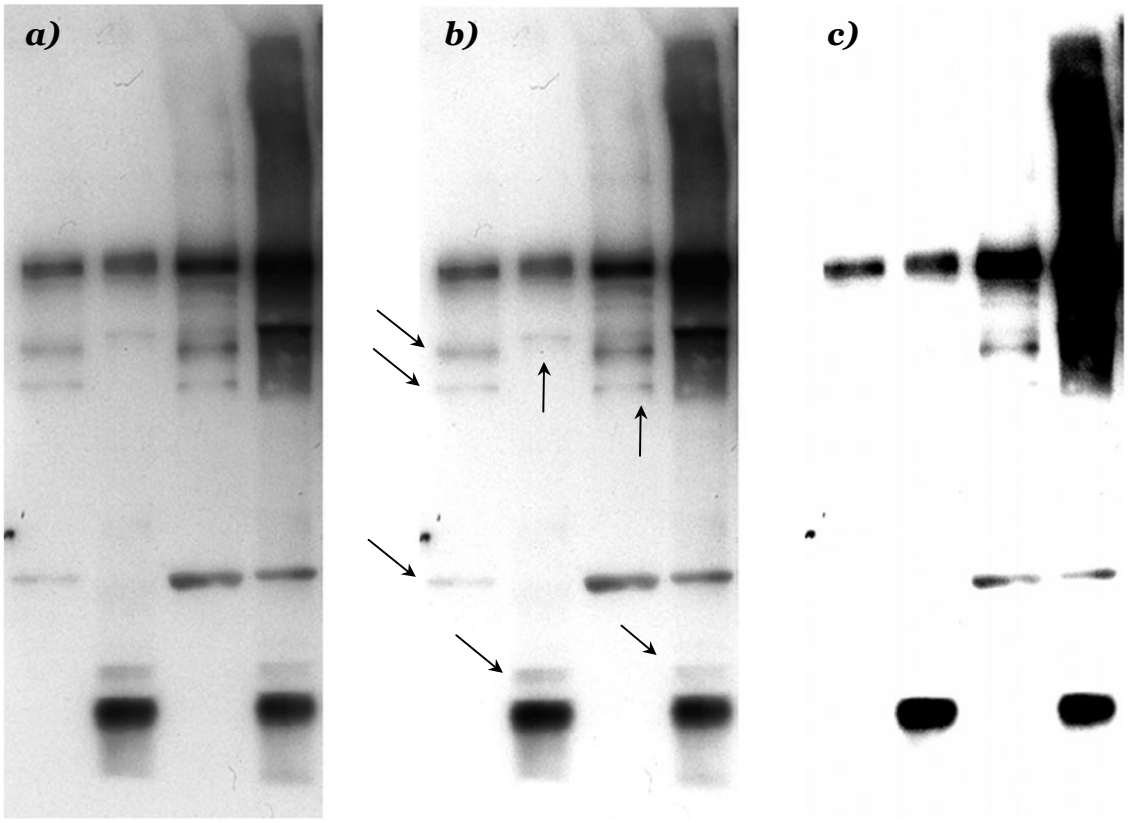


Figure 1.18: ***a)*** Original image of a blot. ***b)*** Acceptable contrast adjustment which reduces background noise uniformly, so that all the bands are still visible. Arrows point at weak bands, which have been preserved. ***c)*** Coarse contrast adjustment, completely removing the background along with weak bands (arrows in image ***b)***. This type of processing is considered as scientific misconduct. Images obtained and adapted from (Rossner and Yamada, 2004).

Segmentation

In computer vision, segmentation is the algorithmic process of partitioning a digital image into multiple segments, represented as sets of pixels, effectively discriminating areas or objects of interest (*foreground*) from the rest of the structures on the image (*background*) (Pratt, 2007). The goal of segmentation is to simplify and/or change the representation of an image into something that is more meaningful and easier to analyze (Shapiro and Stockman, 2001). More precisely, image segmentation is the process of assigning a label to every pixel in an image such that pixels with the same label share certain visual characteristics.

The result of image segmentation is a set of segments that collectively cover the entire image, or a set of contours extracted from the image. Each of the pixels in a region is similar with respect to some characteristic or computed property, such as *colour*, *intensity*, or *texture*. Adjacent regions are significantly different with respect

to the same characteristic(s) (Shapiro and Stockman, 2001). Figure 1.19 shows an image segmented using an intensity-based segmentation method (watershed segmentation, Russ, 2007).

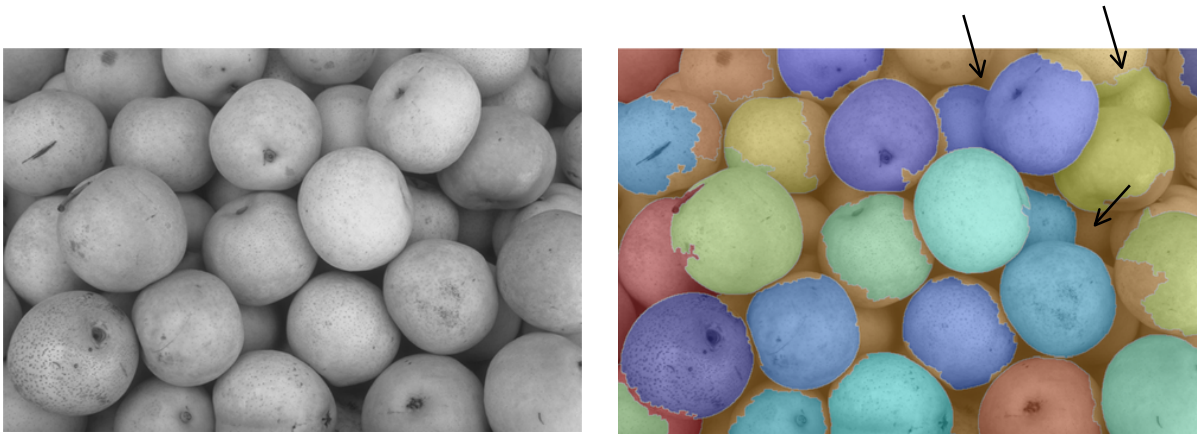


Figure 1.19: An image of pears, which is segmented by the "watershed" transformation, an intensity-based segmentation technique (see also chapter 6). The segmented areas by the algorithm on the right image were pseudo-coloured for contrast. The human vision system can immediately recognize the pears, whereas to the computer, the image is just a set of pixels of different intensities; errors are easy to occur. Erroneous segmentation is shown on the right image with the arrows. Images obtained from a MATLAB R2007a demo (Mathworks).

Computer algorithms are constructed to operate on image properties (intensity, colour, texture) using techniques that include thresholding, region growing, deformable templates and pattern recognition techniques, such as neural networks and fuzzy logic (Bankman, 2009). Separation of structures of interest may be effortless and swift for the human visual system, but it is often a considerable challenge for the computer to perform. As mentioned before, segmentation dictates the outcome of the whole analysis, since all measurements and analyses are performed on segmented regions.

Quantification

Structures or areas segmented can be computationally measured, using quantification algorithms, to extract various metric properties such as shape, size, texture, angle and even motion vectors if an image sequence is analyzed (Bankman, 2009). Object measurements are usually computed either from the grayscale intensity distribution within its boundaries, or from the binary representation of the segmented object, which is the result of some thresholding process, which classifies the pixels as

black (0) or white (1) according to specific criteria. Measurements can then be based on size, shape or the intensity values within the segmented object. Such measurements can be the area, length, perimeter and the centre of mass. The histogram can capture the statistics of an object's gray levels, whereas gray levels structure and spatial distribution is captured by texture measures. These are among the simplest examples for quantification of recognized objects (Wu *et al*, 2008).

These properties can be used to assist diagnosis or to quantify numbers, protein expression or cell motility in biology. However, because of the variety of measurements and tissue used, as well as the dimensions of the data where analysis is applied (2D: image only; 3D: image stack or reconstructed volume; 4D: time-lapse volume information), numerous techniques that address specific applications have been developed.

1.13 Overview, aims and hypotheses

The current dogma of reproductive biology supports the hypothesis that the ovarian follicle reserve is fixed before birth; it is non-renewable and declines steadily with time. The regulation of follicle growth in the beginning of a female's life, when the levels of gonadotrophins are low (not affecting follicle development), is an important process hidden behind a complex local inhibition mechanism, not as yet fully understood. Primordial follicles in particular, as well as follicles of early developmental stages must have a pivotal role in this mechanism. Figure 1.20 presents a diagrammatic summary of a follicle's cycle; the main focus of this thesis will be at the primordial and early growing stage of follicle development.

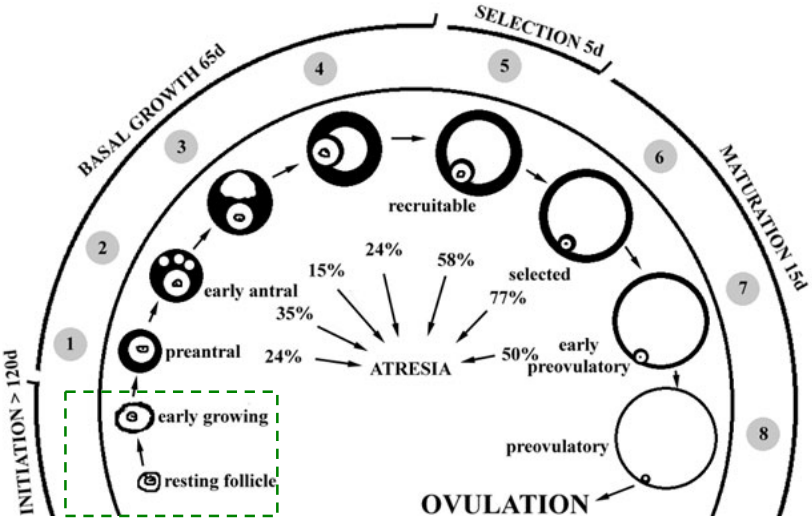


Figure 1.20: Diagrammatic illustration of follicle developmental stages in human, and the time each transition requires. In our project, we are going to focus on the Initiation phase (green square). Image adapted from (Gougeon, 1996).

What triggers some of the primordial follicles to grow, while the rest of them are kept in a quiescent state, is an as yet unanswered fundamental subject of ovarian ageing. This project addresses this subject; **the central hypothesis is that initiation of follicle growth is locally regulated, through a complex system of inhibitors and activators of primordial follicle growth.**

This project's general aim is to develop and apply new techniques, beyond the conventional biological approaches, in order to contribute towards expanding our understanding of the initiation of follicle growth and ovarian ageing. The following hypotheses are going to be addressed individually in each of the chapters:

1. Spatial distributions

A new approach to study ovarian signaling has been developed in our laboratory, and implemented on neonatal mouse ovarian sections (Da Silva-Buttkus *et al*, 2009). This technique explicitly quantifies ovarian follicle patterns, by mapping their *XY* coordinates on individual ovarian sections and relating follicle developmental stage to its distance from potential sources of growth regulatory signals. The analysis performed yielded strong evidence for the existence of a local inhibitor which diffuses in the ovarian stroma within a certain annulus, which is part of a proposed local inhibition mechanism.

The spatial relationship analysis will be expanded and implemented on adult human ovarian sections, in order to test whether the new mechanisms proposed for the neonatal mouse also apply to adult human ovaries, and if so, given the different size of the adult human ovary (100 times bigger than the neonatal mouse ovary), at what range the inhibitor acts.

Additionally, spatial distributions of follicles were quantified in neonatal mouse ovaries that were cultured for several days, to compare with non-cultured ovaries. Ovaries devoid of blood supply should have different follicle arrangement from the freshly dissected, if growth factors are circulated in the blood stream. This will answer whether the proposed inhibition mechanism is truly local.

2. Assessing the error on estimating follicle number in the ovary

Determining the number of small follicles in the ovary is of vital importance in experiments comparing normal and pathological tissue as well as in ovarian ageing. These estimates must be as precise as possible; however there are two sources of error

in the process: The sampling error, and biological variability. When tissue samples are adequate, the error due to the technique is overshadowed by biological variability. This error is going to be investigated using a novel mathematical tool developed, the Simulated Ovary. These ovaries are computationally modeled and reconstructed neonatal mouse ovaries; being modeled, follicle number and spatial properties are explicitly known. Simulated ovaries effectively provide an endless source of material to conduct *in silico* experiments.

3. Whole tissue imaging

Follicle spatial relationships need to be extended in three dimensions, in order to investigate spatial signaling in the *XYZ* plane. Using existing staining and imaging methods, a new protocol has been compiled that permits scanning through whole samples, obtaining clear optical sections. This is applied to the ovary, using the non-growing oocyte-specific mouse vasa homologue antibody, which reveals the spatial position of the oocyte. In addition, a new method will be presented, demonstrating how to rapidly estimate follicle numbers by applying the stereologic technique, whole mount immunohistochemistry and laser scanning confocal microscopy. The process can be parallelized and executed for many ovaries at a fraction of time that would be required if conventional sections were used, so that high-throughput results can be obtained when large sample-sizes are required.

4. Automating follicle counting

Qualitative analyses, such as determining follicle stages, bring variations to the measurements due to experimentalist bias. In addition, estimating the number of structures in large sample sizes, is extremely laborious even when modern stereologic techniques are employed. Therefore new automated methods that eliminate subjectivity and processing time need to be developed. An implementation of image processing algorithms in a custom-made computer programme will be presented,

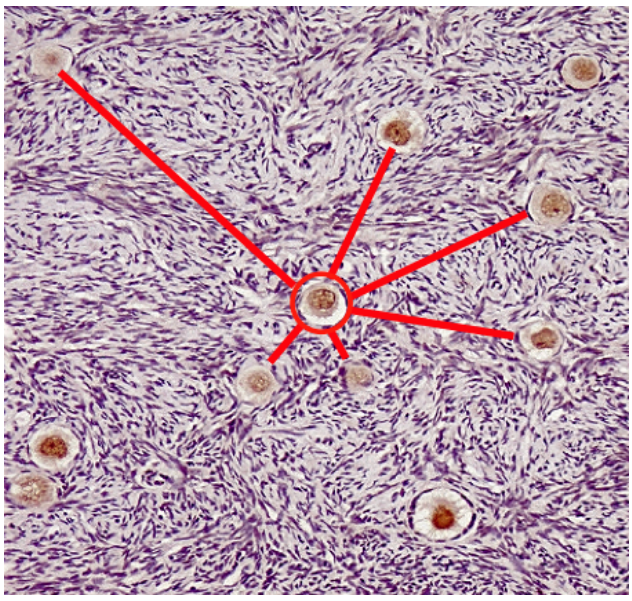
which is capable of counting follicles, estimating the developmental stage and mapping their *XY* coordinates on specially prepared ovarian sections.

5. Time-lapse whole organ culture

Most studies on ovarian ageing are conducted on data obtained from fixed tissue of certain age, i.e. a static capturing of the system at a specific time. In fact, a key assumption in that the spatial analyses that will be presented is that follicles remain static in the ovarian cortex. Introducing the time factor in the studies, by monitoring the organ while still functional, could provide new insight into the dynamics of follicles. A culture system has been set up for time-lapse imaging using single photon confocal microscopy. Basic follicle motility is going to be investigated in neonatal mouse ovaries, cultured for up to one day. The phenomenon of follicle loss by extrusion from the ovarian surface epithelium will also be examined and discussed.

Chapter 2

Prediction of local mechanisms regulating initiation of follicle development in the human ovary by application of spatial analysis



2.1 Introduction to ovarian local signaling

Follicle maturation takes approximately half a year in humans (Gougeon, 1996). The initial follicle transition, leaving the resting pool by transforming from primordial to transitional and primary, is defined as initiation of follicle growth. This phenomenon is also known as folliculogenesis (Gougeon, 1986), and the most widely accepted theory is that it is coordinated by local regulatory mechanisms (Kezele *et al*, 2002). This is in contrast to the later stages of follicle development, where hormones orchestrate development, the most important of which being LH and FSH (section 1.6). However the way this mechanism functions, triggering some primordial follicles to grow while others stay in the quiescent state, is still unclear (Picton, 2001).

2.1.2 Control of initiation of follicle growth and hypotheses

It is unclear whether the signals that trigger the initiation of follicle development originate from neighbouring follicles, the oocyte, the surrounding granulosa cells, or from stroma cells. Identifying this signal, which is responsible for appropriate regulation of initiation, therefore maintaining some primordial follicles in the resting state for a prolonged period of time (over a year in the mouse, up to 50 years in the human) is a major subject of research. We are going to attempt to identify the source of this signal using a different approach, which is based on the distribution of follicles within the ovary. By qualitative assessment of neonatal mouse ovarian sections, we can deduce some hypothetical modes of function of this mechanism, which we can assume operates via a diffusible ligand, produced by a source (neighbouring follicles) which targets resting (primordial) follicles.

One possibility is that growing follicles produce an inhibitor that keeps the primordial follicles in the quiescent stage (Durlinger *et al*, 1999, Durlinger *et al*, 2002, Marlies *et al*, 2006, Da Silva-Buttkus *et al*, 2008). However in this case, in neonatal mouse ovaries where no growing follicles are present, all the primordial follicles should start growing at once, something that doesn't happen. This leads us to infer that there must be another inhibitory mechanism in place.

An alternative possibility is that primordial follicles themselves produce an inhibitory signal, which prevents them from initiating growth. Primordial follicles on the cortex-medulla boundary, which have fewer surrounding primordial follicles, may be receiving a weaker signal and start growing. On the other hand, follicles that are closely packed together in clusters in the cortical region would be receiving a much stronger signal, maintaining them in their resting state.

There is also the possibility that the ovarian surface epithelium may produce an inhibitory signal that weakens as the distance to the surface increases, so the follicles that are closer to the ovarian surface epithelium are much more likely to stay in a resting stage.

In order to test these three hypotheses, previous studies in our laboratory quantified the spatial distribution of resting and growing follicles in the early postnatal mouse ovary (Da Silva-Buttkus *et al*, 2009). A novel quantification method was developed which involved capturing an image of an entire histological section of

mouse ovary and measuring the size and *XY* coordinates of each and every follicle on the section. The spatial distribution of the follicles in the ovary was then obtained by calculating the relative Euclidian distances between all follicles, and between all follicles and the ovarian surface epithelium.

The most important finding of this study was that the majority of primordial follicles had one or more neighbouring primordial follicles within 10 μm. Follicles which had started to grow were more likely to have no primordial follicles close by. This strongly suggested that the primordial follicles were producing an inhibitory factor that was maintaining neighbouring primordial follicles in a resting state, and that isolated follicles were more likely to initiate growth due to lower levels of the inhibitory signal. This provides a realistic explanation of why all primordial follicles do not start growing at once in the neonatal mouse ovary.

Aim of this study

In this project this method is extended, by application to human ovarian sections, to assess whether the spatial pattern observed in the neonatal mouse (and by extension the inhibition model) also applies to humans. The analysis was conducted on histological sections of five normal and on nine polycystic ovaries from adult women of various ages. The challenge in this case is that human ovarian sections are substantially larger compared to the neonatal mouse ovarian sections, their size being around 200-fold greater. Thus new methods and computational tools had to be developed, described extensively in the Materials and Methods (9.2 – 9.6).

Two of these normal ovaries and one of the polycystic ovaries were examined as part of my MSc project (Bioinformatics MSc, Imperial College London). A first approach for the analysis was developed, including the computational tools (coded in MATLAB). This study has been extended for this project, adding another three normal and eight polycystic ovaries for examination. It should be stressed that for the neonatal mouse analysis, the granulosa cell shape is used as a criterion for initiation of follicle growth (Introduction, section 1.3.1). The same initiation identifier will be used in this project, however the consistency of the results was verified additionally in the case where granulosa cell proliferation is used as an initiation marker.

2.2 Approach

Archived human tissue and histology

Ovaries were obtained from women who have undergone oophorectomy for non-malignant gynaecological disorders (9.1). Ovaries were classified according to patient history either as *normal* or *polycystic* (9.1). After surgical removal from the subjects, ovaries were fixed, serially sectioned and prepared for immuno-histochemistry to identify the mini-chromosomal maintenance-2 protein (MCM-2), a marker of cells being in the cell cycle. Initial studies used the classic proliferation marker Ki67, but very few granulosa cells were labelled, as early development in the human is slow. MCM-2 was therefore chosen as an alternative marker (Stubbs *et al*, 2007). All procedures up to this point were carried out by Dr S. Stubbs (Stubbs *et al*, 2005 and 2007).

Experimental plan

Briefly, the main procedures followed to accomplish the project objectives, considering the background information from the previous introduction, were to:

- Select ovarian tissue samples
- Capture images of follicle clusters (9.2)
- Categorise follicles according to developmental stage (9.2)
- Measure follicle diameters (9.3)
- Determine the coordinates of follicles (9.4)
- Create a computer programme for calculating inter-follicle distances (9.5)

A significant part of the work involved experimental data collection, extracted from images of ovarian sections captured using a light microscope and a digital camera attached to it.

Imaging data collection

Five sections from normal ovaries and nine from (ovulatory) polycystic ovaries were selected. The clinical information about these ovaries appears in table

9.1. All follicles visible on the ovarian sections, examined under the light microscope had their developmental stage assessed and their diameter measured (9.3). Given the size of the human ovarian sections, photographs were captured of cortical areas rich in follicles (clusters) at low magnification (x10), ensuring that all follicles on the section were included in the images (9.4). In contrast to the neonatal mouse ovary, more than 50 (x10) images would be required to cover the entire surface of a human ovarian section.

XY coordinates, follicle distances and proportions

The captured images were used to obtain the *XY* coordinates of the centre of each follicle using GraphClick (Arizona software) (9.4). One of the challenges of the project was that the follicles appear on several images for each section. Therefore a computer programme was developed in MATLAB to transform all *XY* coordinates to a common origin for each ovarian section (9.4.1). When the coordinates of every follicle referring to a common origin became available, the inter-follicular Euclidian distances were computed by another computer programme, also coded in MATLAB (9.5). The resulting distances were then used by the same programme to calculate the number of neighbours of each developmental stage within set distances of the surface of each follicle. The follicle proportions reported in the graphs in the results section were calculated by logistic regression analysis on Stata 8 software (9.6).

2.3 Results

Summarising the procedure described in the Materials and Methods, follicles in human ovarian sections have been counted, had their diameters measured and their developmental stage assessed. Each follicle was assigned *XY* coordinates relatively to the histological section. This enables us to determine inter-follicular distances. A map of the follicles on an ovarian section appears in figure 2.4. At first glance of figure 2.4, the most important observation was that transitional follicles were greater in number than the primordial follicles. Primary follicles were outnumbered compared to the other two follicle types, and this was the case in all the ovarian sections that have been examined.

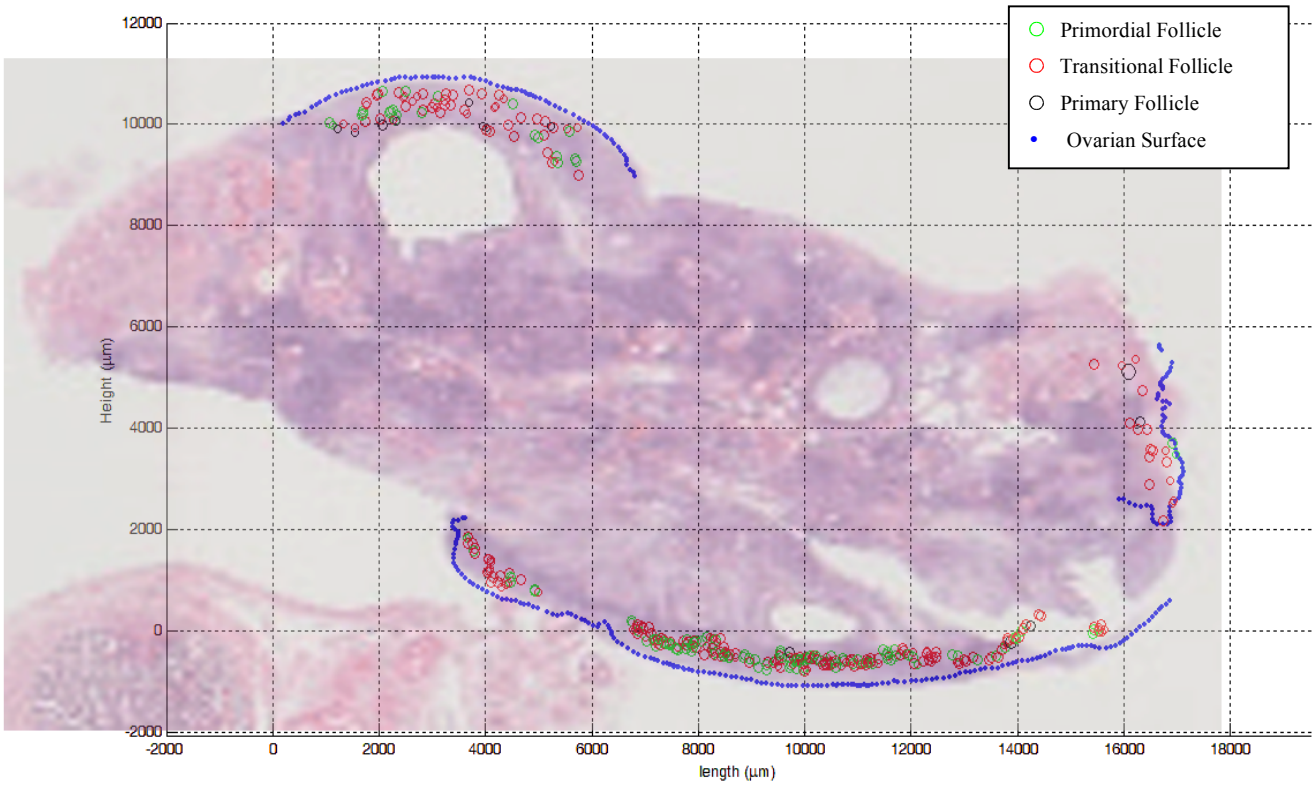


Figure 2.1: Photomicrograph (1x magnification) of a human ovarian section, overlapped with a plotted map of the follicles and the ovarian wall. Note that overlapping is not perfect because the image of the ovarian section is not the same slide as the one used for data acquisition, because a low power photograph was not available. Such low power photographs are impossible to take on conventional light microscopes and this was taken on a specialized histopathology microscope loaned by Nikon. This section is 50μm away from the one used.

In order to analyze the follicle spatial distribution, we needed to study for each follicle the distribution of its neighbouring follicles. This can provide information about potential signaling sources. We considered any follicle as the *target* of a potential signal. The neighbouring follicles within a given radius were considered as the *sources* of this signal, as we are interested in local inhibition mechanisms (figure 2.2). For each follicle within each section, we calculated the number of neighbouring follicles within specific radii from that follicle's surface (figure 2.2*b*).

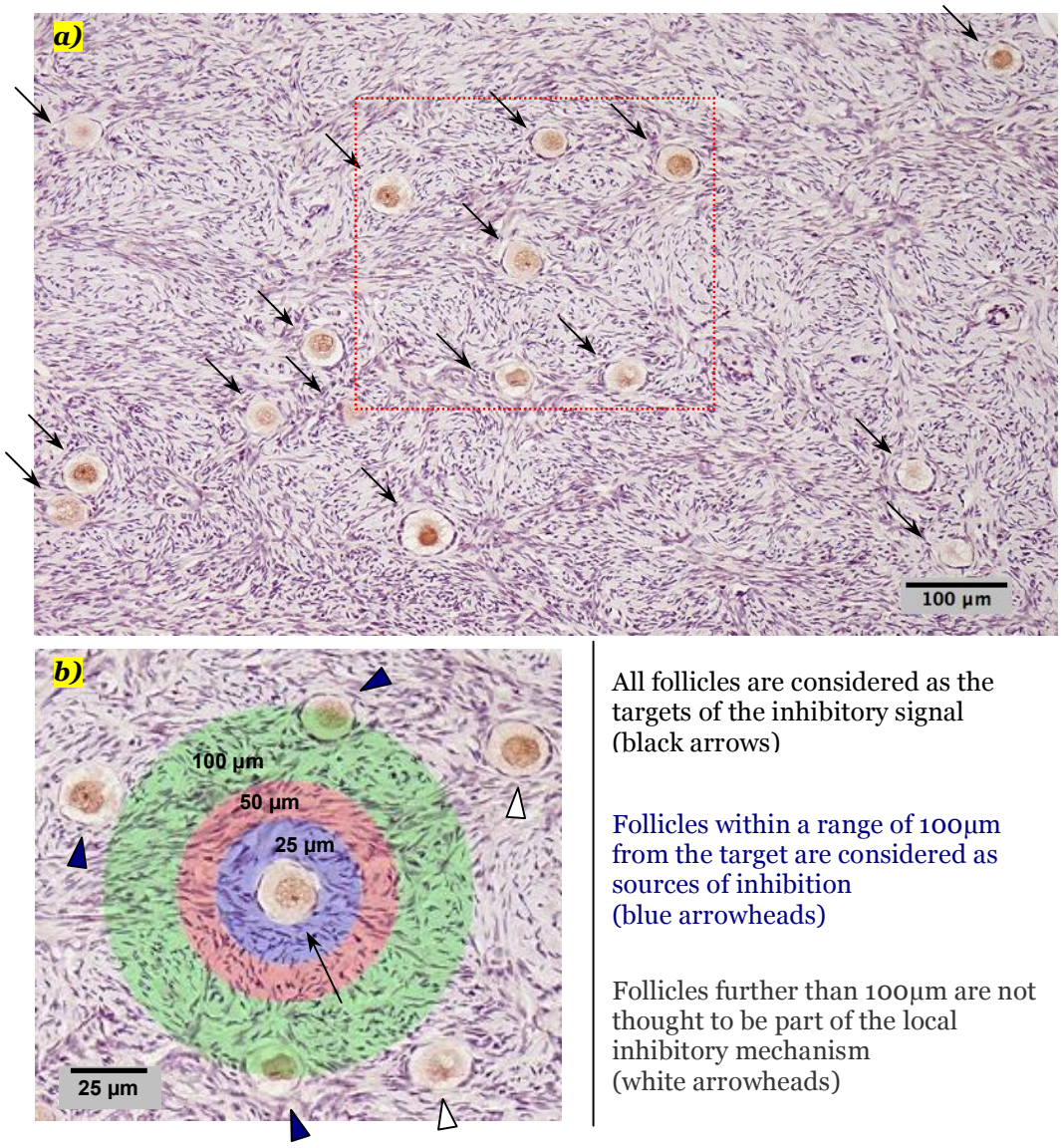


Figure 2.2: ***a)*** Photomicrograph of part of a human ovarian section, stained using haematoxylin and MCM-2 (see 9.1). Every follicle on the entire ovarian section was considered as the target of a local inhibitory signal, with its neighbours being the sources of the signal. ***b)*** The local signaling mechanism is examined for various set distances from the target follicle. In this example, the zoomed area of photograph ***a)*** (red dotted box) shows realistically the three distances we use. No follicles are within 25µm (blue ring) or 50µm (red ring) from its surface, whereas there are three within 100µm (blue ring).

In table 2.1, a summary of the number of follicles analysed is presented. The very first observation one can make is that there is a higher number of transitional follicles compared to the growing ones, on the sections. The numbers of atretic follicles (dense nuclei and deformed oocyte) were high as well, but this could be due to the strict selection criteria, by which a follicle is considered for the analysis only if it was flawlessly presented on the section. However, atretic follicles were also

analysed (had their diameters and *XY* coordinates measured), in case they are required for future studies.

Table 2.1: Number of follicles analysed on human histological sections from normal and polycystic ovaries. Follicle diameters reported are obtained only from follicles that were presented with a clear nucleus (see also section 9.2 & figure 9.2). The difference in follicle diameters between normal and PCO is not statistically significant ($p > 0.05$).

	Normal Ovaries (n=5)		***Polycystic Ovaries (n=9)***	
	Total	***Average diameter ± SEM (µm)***	***Total***	***Average diameter ± SEM (µm)***
Primordial	157	42.14 ± 0.48	205	40.32 ± 0.41
Transitional	264	42.03 ± 0.46	393	41.81 ± 0.4
Primary	18	56.93 ± 6.88	76	58.44 ± 4.26
Secondary & above	3	–	8	–
Atretic	75	–		–

Our initial hypothesis was that the primordial follicles produce a diffusible inhibitory signal that keeps the other primordial follicles in a resting state. In terms of spatial arrangement, we assumed set distances (radii) of 25µm, 50µm and 100µm from the surface of a follicle (figure 2.2*b*), and we examined, for each target follicle, the number of neighbouring follicles included within each distance, of specific developmental stages. For every ovarian section, and for the various distances that we set, representing the signal range, follicles were assigned into groups, according to how many **neighbouring primordial** follicles there were within these radii (0 neighbours, 1, 2, etc, up to seven groups in total). Then the proportion of the follicles in those groups that were *growing*, (*ie* of any developmental stage except primordial) were calculated and presented in the graph shown in figure 2.3. Proportions were computed by employing logistic regression analysis, using Stata 8 (Stata corporation) (section 9.6). Robust standard errors, clustered by ovary were used to determine the 95% confidence intervals in all cases where the observed proportions are not 0 or 1, and are presented in all the graph figures in this chapter, unless specified otherwise in the figure legend.

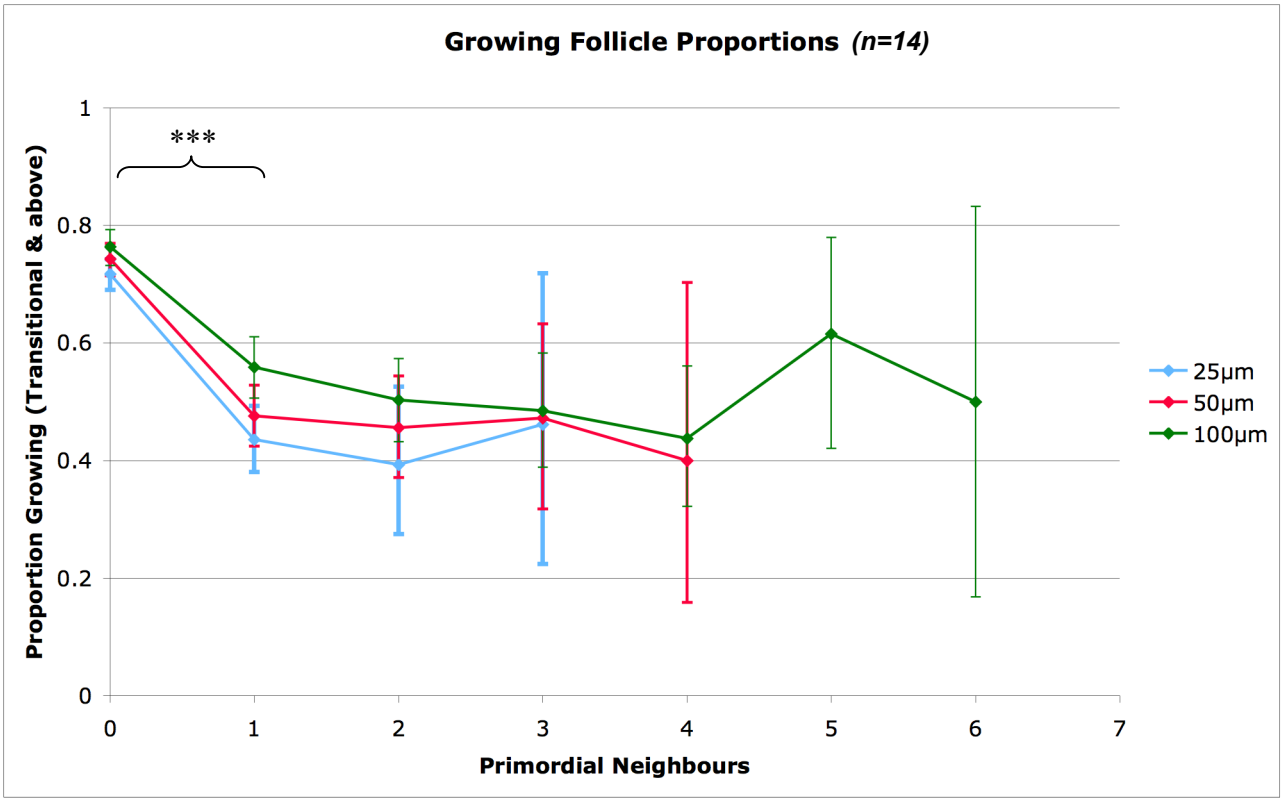


Figure 2.3: Plot of the proportion of the follicles that are growing (transitional, primary or secondary) in each group of follicles that have 0,1,2, ..., 6 primordial follicle neighbours, for different threshold circular distance of the target follicle (different colour line). Error bars reported are 95% confidence intervals. Stars indicate highly significant difference (p<0.01).

In addition, the data from all ovarian sections were amalgamated together in figure 2.3, because deducing conclusions for each ovarian section separately does not provide statistically meaningful results. This included binned data from both normal and polycystic ovarian sections. It was found that the spatial distribution of small follicles (primordial to primary) in the polycystic ovaries was the same as in the normal ovaries (concluded from a similar analysis of proportions, data not shown).

Figure 2.3 shows that there was a decrease in the probability of a follicle being growing (i.e. not a primordial) as the number of neighbouring primordial follicles increased. The decrease was significant (p-value < 0.01) only when going from zero to one neighbour, for all the three signal range radii. As the number of nearby neighbours increased, the further drop in the proportion illustrated was not significant. In addition, the graph illustrates that the probability of a follicle to be growing, when having a set number of primordial neighbours, was bigger as the distance of the assumed signal range increased. Nevertheless, this effect was not statistically

significant. The message this graph conveys is that the closer non-growing neighbours were to the target, the lower the probability that the target was growing itself. The trend agrees with the proposed hypothesis of primordial follicle inhibition, but the inhibitory effect was much weaker compared with the effect observed in the neonatal mice ovarian sections (Da Silva-Buttkus *et al*, 2009), when investigating the same case.

The distance of the closest primordial follicle to any follicle was also calculated, in a similar procedure as the one described above. The follicles were classified into groups according to the distance of their closest primordial follicle neighbour, namely follicles that had the closest primordial neighbour within the range of 0μm to 10μm were the first group, the next one was within the range of 11μm to 25μm etc. The proportion of follicles in every group that were *growing* was calculated, and is presented in figure 2.4. The regression analysis and the binning of PCO and normal data were done as described for the previous case.

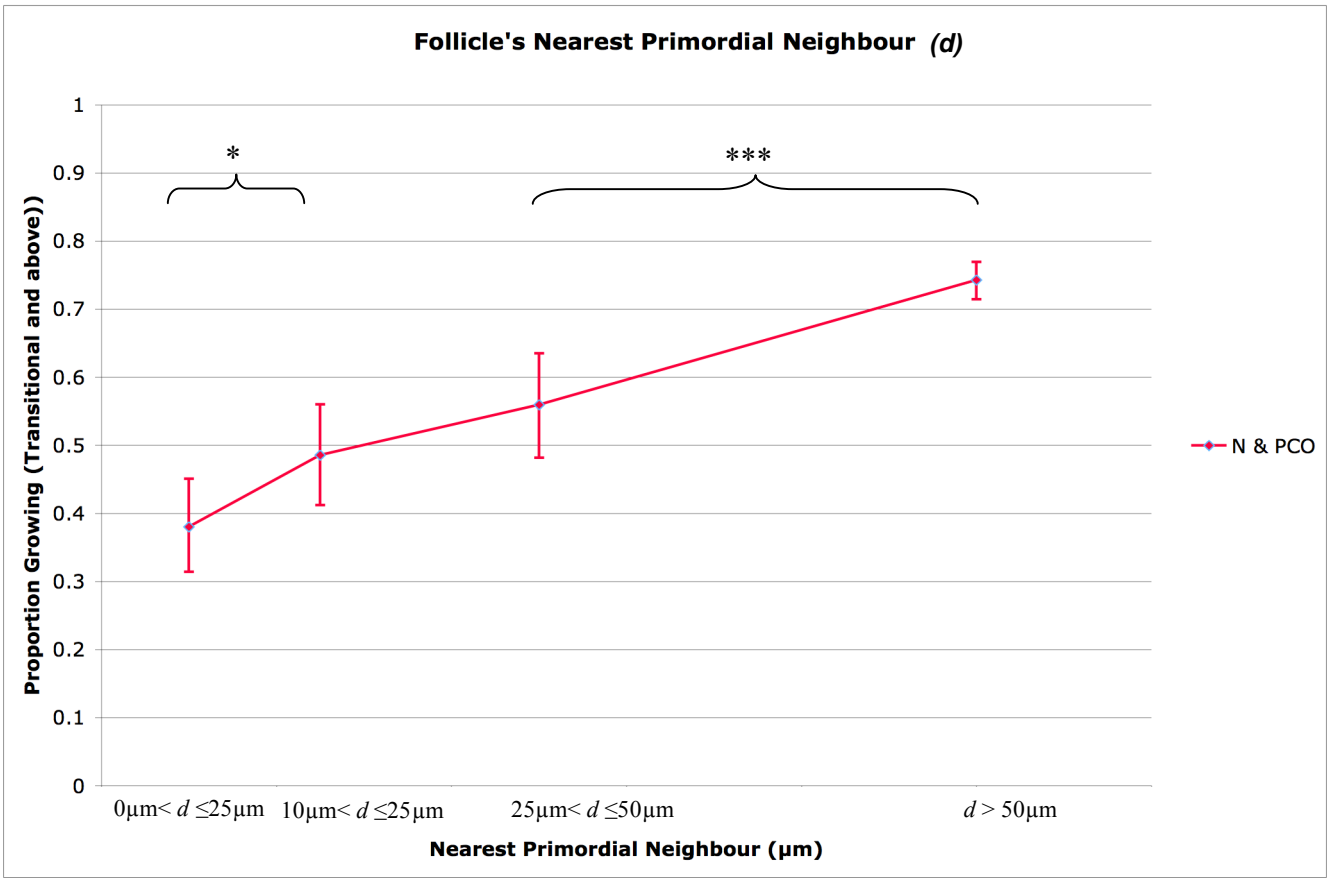


Figure 2.4: Proportion of follicles that are growing (transitional, primary or secondary), within the closest primordial range groups 0μm-10μm, 10μm-25μm, 25μm-50μm and 50μm-100μm. Error bars are 95% confidence intervals. Stars indicate levels of significance, one star for $p \leq 0.05$, three stars for $p \leq 0.01$. Normal and PCO data were amalgamated ($n=14$), as previously explained.

Figure 2.4 shows an increase in the probability of a follicle being a growing follicle as the distance to the closest non-growing neighbour increased. If the closest primordial neighbour to a follicle was located up to 10μm from its surface, then the probability of this follicle being growing was around 40%. As the distance between the closest primordial neighbour and a target follicle increased to between 20 and 25μm, the probability of the target follicle being a growing follicle increased significantly ($p<0.05$). The majority of the follicles that were growing (approximately 75%) had their closest primordial neighbour more than 50μm away; in the specific case of primary follicles, more than 80% of them did not have any primordial neighbours within 100μm. The increase in the probability of a follicle being a growing was highly significant ($p<0.01$) when looking at primordial neighbours more than 50μm away from them. The trend depicted also supports the hypothesis of inhibition by primordial neighbours.

Therefore, the results reported in figures 2.3 and 2.4 concur with the hypothesis of a local inhibitory signal, originating from primordial follicles and targeting nearby primordial follicles. The effect of the signal was much weaker in our case, compared to the *XY* study conducted in mice. Namely, one primordial follicle within 25μm radius could potentially inhibit growth in the human, but increasing the number of nearby primordial follicles would not significantly affect the growth inhibition, whereas in the mouse this increase would have a much more significant effect (Da Silva-Buttkus *et al*, 2009).

Granulosa cell proliferation as a marker for initiation

In order to further investigate our hypothesis, we have examined an alternative marker of initiation of follicle growth, namely granulosa cell proliferation. Positive immunolabelling of cells for the cell cycle protein MCM-2 indicates granulosa cells that are in the cell cycle, hence identifies follicles where granulosa cells will divide at some point. In this case we assumed that the follicles with granulosa cells that are positive for the MCM-2 marker were the ones that were growing. This was regardless of the shape of the surrounding granulosa cells, i.e. an oocyte surrounded by a layer of squamous granulosa cells, with some of those positive for MCM-2, was classified as growing for the analysis.

Furthermore, it was found that MCM-2 positive staining in the granulosa cells increased as the developmental stage of the follicle progressed (Stubbs *et al*, 2007). Therefore, there was high likelihood that the ones that had no MCM-2 positive granulosa cell staining were primordial by cell shape classification as well. Follicles were grouped according to the number of neighbouring primordials within a given radius, and then the proportion of the follicles in each group that were MCM-2 positive was calculated, using logistic regression. The results are reported in figure 2.5.

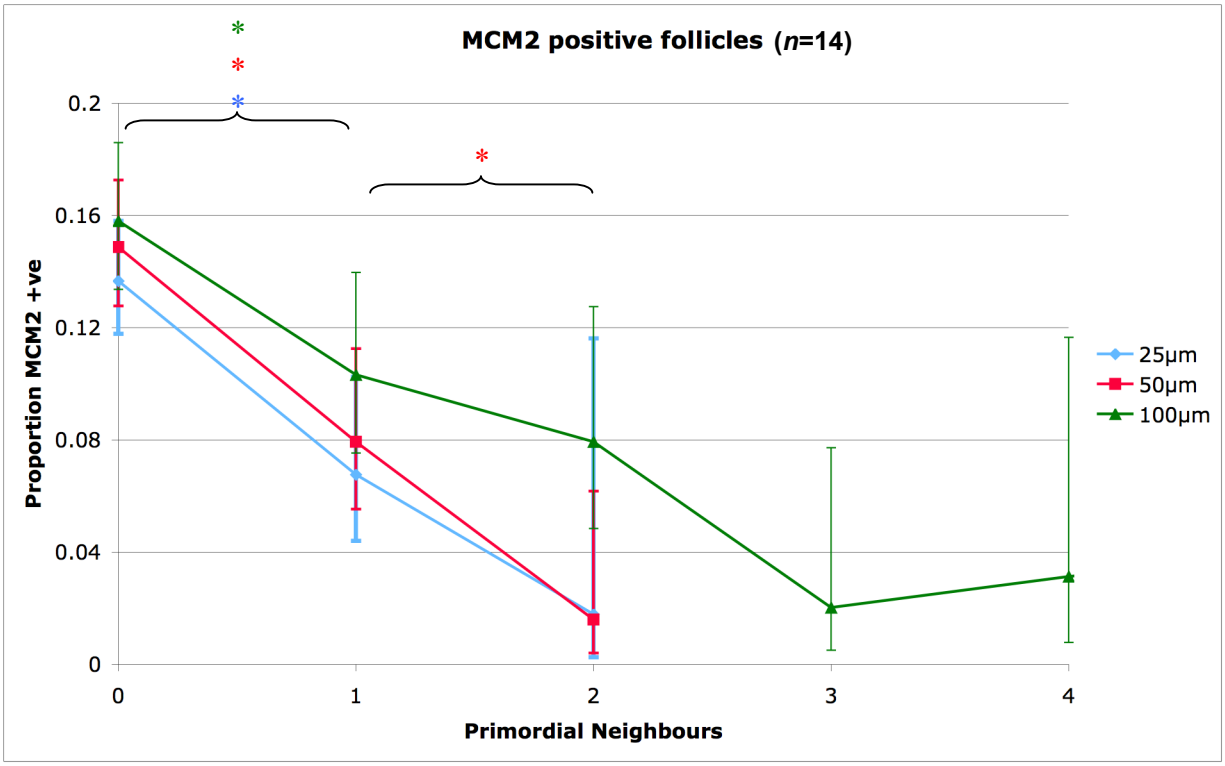


Figure 2.5: Proportion of follicles positive to the MCM-2 marker, which are considered as growing, vs the number of primordial (resting) neighbours within three specific radii (represented in different colours). Error bars are 95% confidence intervals. Stars denote statistical significance and their colour represent the corresponding line (one star: $p< 0.05$).

The trend showed in figure 2.5 illustrates a decrease in the probability of a follicle being a growing one as the number of its nearby primordial neighbours increase. The decrease was highly significant ($p<0.01$) only when neighbouring primordial follicles increased from zero to one, though in the case of 100µm radius the decrease was not as significant ($p<0.05$). Thus the inhibition hypothesis is partially verified in the case where growing follicles were identified by MCM-2

positive immunostaining. Furthermore, because the proportion numbers were so small compared to the ones we obtained from the previous analyses (figures 2.3, 2.4), we can conclude that classifying a follicle as growing based on the proliferation of its granulosa cells may not be as efficient and accurate as assessing granulosa cell morphology.

2.4 Discussion

Normal vs. Polycystic ovaries

Franks *et al* (2008) report in their review that there are more small pre-antral follicles in the polycystic ovary (also reported in Maciel *et al,* 2004, referring specifically to primary follicles). Although no absolute counting was employed, an increase in number and proportions of primary follicles in polycystic ovaries was also observed in our sections, as shown in table 2.1. Primary follicles that were considered in the PCO ovaries were much higher in number. In addition, from the same table we can see that there were no substantial differences in the diameters of the small follicles between the normal and polycystic ovaries, on the sections used for the analysis.

The quantification of spatial distribution of follicles did not yield significantly different results between normal and PCO histological sections. Namely, one neighbouring follicle inhibited growth as depicted in figure 2.3, in both cases. However, when considering more neighbouring primordial follicles, there was much more variability in the data (higher 95% confidence interval error bars). It was decided that since the data from normal ovaries and PCO showed similar patterns (see table 2.1), they should be considered all together in the analysis, as this would reduce the statistical error. It should be highlighted that most of the adult ovarian sections (both normal and PCO) had very few follicles, and there was generally much dispersion in the follicle positions, as opposed to the neonatal mouse. In conclusion, the additional number of primary follicles and the greater overall size of the polycystic ovaries (Stubbs *et al*, 2005) did not seem to affect the local neighbour distribution of small follicles.

Strength of the signal and ageing

In the human, the effect of the primordial follicle inhibition on neighbouring primordials was found to be weaker than the one observed in the mouse. This can be corroborated by comparing the slope of the graphs depicting the effect of primordial neighbours for the neonatal mouse (Da Silva-Buttkus *et al*, 2009) and the adult human (figure 2.3). In the neonatal mouse, if a follicle had one primordial neighbour within 10µm, the probability of that follicle to have initiated growth decreased from 85% to 45% (40% drop), and if more than 4 primordial neighbours were near, the probability of the target follicle to have been growing was almost zero. In the human however, if a follicle had one primordial neighbour within 25µm (see also figure 2.2*b*), the probability of having been growing reduced by 30%, and stayed at approximately that level regardless of any additional primordial neighbours in close proximity.

A plausible explanation for this effect is the difference in follicle densities between the two types of tissue, the neonatal mouse ovary and the adult human ovary. The juvenile mouse ovary was endowed with a very high density of follicles, whereas in the human tissue the follicles were much more dispersed, with significant areas of the ovarian section being devoid of follicles. Small follicles were generally found in clusters on the adult human sections (figure 2.4), though even among clusters there was a lot of dispersion, in contrast to the neonatal mouse where most follicles practically touched each other and were more closely packed. These observations, combined with the weaker effect of the predicted inhibitory signal, suggest that the proposed mechanism is crucial during development and in early life, when the number and density of follicles in the ovary are high, to maintain the resting pool until a certain number of later growing follicles appear. These growing follicles may then be more important in providing inhibitory signals (eg AMH) to the primordial pool. From that point onwards, though the mechanism involving signaling between primordial follicles may still be functional, it has a secondary role in the regulation of follicle growth. Such a mechanism, functioning in the way described, has been hypothesized by Gougeon's group (Gougeon *et al*, 1992, Gougeon 1996), though in our work we present specific quantitative evidence of its existence.

Transitional follicles

Another interesting observation from our data (table 2.1) was the fact that the number (and proportion) of transitional follicles was greater than primordial follicles, in both normal and polycystic ovaries, which was not the case in the neonatal mouse. Various groups studying follicle dynamics regard transitional follicles (or intermediary) as resting, belonging to the pool of *non-growing follicles* (NGF) (e.g. Gougeon *et al*, 1994, Gougeon, 1996, Hansen *et al*, 2008), whereas others consider them as growing (e.g. Faddy and Gosden, 1995, Picton, 2001, Da Silva-Buttukus *et al,* 2009). In this study, we considered that a follicle that had at least one cuboidal cell had entered the growth phase (Picton, 2001), therefore was regarded as growing. However, if the case was that all the transitional follicles were to enter the growth cycle immediately, these would be lost within a year, meaning that the ovary would be depleted within the next 2 to 3 years. Gougeon (1996) reports that the time follicles up to the primary stage require to reach the preantral stage is not known.

It is thus plausible that primordial follicles do enter the growth phase by the initiation of granulosa cell cuboidalization, but progression to the next stages of developments is extremely slow. This can also be reflected by the follicle diameter data presented in table 2.1, showing that primordial and transitional follicles are the same size (also reported by Gougeon and Chainy, 1987). In addition, this further extends the possibility of the predicted mechanism to be of secondary importance in the adult human ovary, as follicles that have initiated growth can be kept in a quiescent state by some other inhibitory process, possibly by the AMH hormone, secreted by large preantral and antral follicles, which are dominant structures in the adult ovary.

The nature of the inhibitory signal

The most important drawback of our method is its inability to explicitly identify the predicted signal. This needs to be identified by means of biological experimental investigations. There is a wide variety of experiments (such as *in situ* hybridization, quantitative PCR) that can be performed in search of potential inhibitors of initiation of growth, including growth factor antagonists (Adhikari and Liu, 2009) (see Introduction, 1.5). Primordial follicles could be isolated, for example,

and expression of specific mRNAs can be measured using reverse-transcription polymerase chain reaction (rt-PCR), or specific proteins can be detected by means of protein immunoblots (known as western blots).

So far, the dynamics of the primordial follicle pool is not as yet known, but it involves reciprocation of activation, atresia or continuation of resting state. A variety of growth factors are known to be important in regulating follicle growth. Members of the transforming growth factor (TGF-ß) superfamily are known to be important in initiation of follicle growth (Trombly *et al*, 2009). Experimental research could therefore focus on identifying any antagonist proteins produced from primordial follicles, which target bone morphogenic proteins (BMPs) (Da Silva-Buttkuss *et al*, 2009).

Recently, much attention has been drawn to the PI3 kinase pathway in the oocyte, by extensively studying its role in follicular activation (Tingen *et al*, 2009), (Introduction, 1.5). There is in particular the work done by Reddy *et al*, 2008, showing that oocyte specific deletion of the PI3K antagonist, PTEN, causes the entire pool of primordial follicles to initiate, leading to premature ovarian failure. This suggests that there needs to be sustained inhibition of the pathway to maintain the quiescent state. This could potentially reveal the inhibitor that was predicted from our study.

Conclusions

In our work, we have extended the new computational approach developed to quantify the spatial distribution of resting and growing follicles in histological sections of mouse ovary, so that they can be applied to sections of adult human ovary. We confirmed a new way of predicting the existence, nature and range of unknown regulatory signals, which can be easily applied to a variety of similar biological problems.

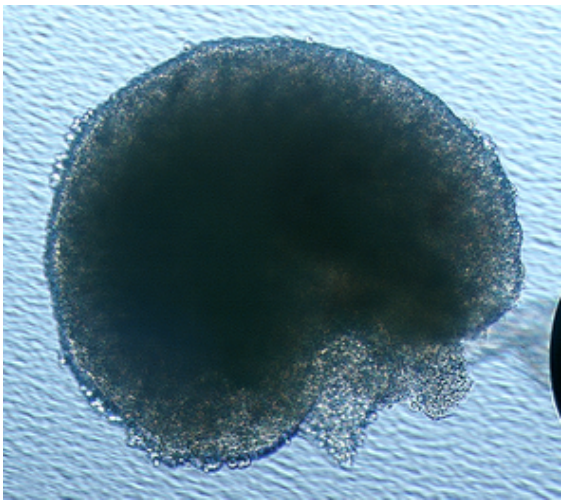
Using a simple, easy to apply method, we demonstrated that the proportion of growing follicles that have neighbouring primordial follicles within set distances from their surfaces decreased as the number of primordial neighbours increased and as the distance to the closest primordial decreased. Therefore, primordial follicles must be producing an inhibitory signal (in the form of diffusing ligands), which acts locally

and weakens with distance. These results provide evidence for the existence of a new inhibitory signal that has been suggested. More specifically, the hypothesis that primordial follicles play a regulatory role in follicle initiation, examined in the mouse model as well (Da Silva-Buttkus *et al*, 2009), is supported by our results in the human.

The proposed approach is, however, limited by the fact that it is only applied in two-dimentional ovarian transects. There was no accounting for the follicles that may be present above or below the section examined. In order for this to be efficiently investigated, new three-dimensional imaging techniques need to be employed; such a method is presented and discussed in chapter 5.

Chapter 3

Spatial analysis of juvenile cultured mouse ovaries



3.1 Introduction

The exact mechanism that controls the initiation of follicle growth and progression through the earliest stages of follicle development remains unknown. It is observed from qualitative studies (e.g. Sforza *et al*, 2003) that follicles in the cortex-medulla boundary of the ovary start growing first. As discussed in chapter 2 (section 2.1.1), this is either due to *a)* inhibitory effects from the ovarian surface or *b)* local inhibition effects from adjacent follicles (see also figure 3.1); in addition, growth of follicles close to the medulla may be due to *c)* stimulatory factors from the circulation or *d)* they were among the first to be formed in the ovary (production line hypothesis, section 1.5). The ovarian cortex is relatively devoid of blood vessels, whereas the medulla is rich in blood supply. Thus there may be a connection between the blood supply and initiation of follicle growth, which can be investigated *ex-vivo*, using ovaries cultured for several days.

The culture conditions play a key part for the development of the follicles in the cultured ovary. Previous experiments in our laboratory, carried out by Dr Sharron Stubbs and Catherine Wright (Wright *et al*, 1999), showed that factors such as FSH, insulin and IGF-I promote follicle development in human tissue slice culture. This is confirmed by the results obtained by the groups of Louhio *et al* (2000), as well as by the results on frozen human tissue, performed by Fabbri *et al* (2007). Absence of the various growth factors in the culture system results in follicle developmental arrest to the transitional stage, with extremely few progressing to primary follicles. Consequently, setting up a culture system without any growth factors, followed by interventional studies where specific growth factors are added, is a useful way of investigating the initiation of follicle growth.

We have shown that in the mouse (Da Silva-Buttkus *et al*, 2009) and in human ovaries (chapter 2) a local signaling mechanism is implicated in the regulation of follicle growth. The existence of this mechanism was inferred by conducting spatial analysis on images of ovarian sections. These spatial studies have shown that the number of neighbouring follicles within a small radius around a follicle is important, and that autocrine–paracrine signaling of primordial follicles maintains them in a relatively quiescent state. The mode of operation of the mechanism is thought to work as illustrated in figure 3.1, which describes the simulated concentration heat-map of an inhibitory factor produced by the follicles and diffusing within the ovary. The figure shows that follicles with more neighbours and close to the ovary surface experience more inhibition

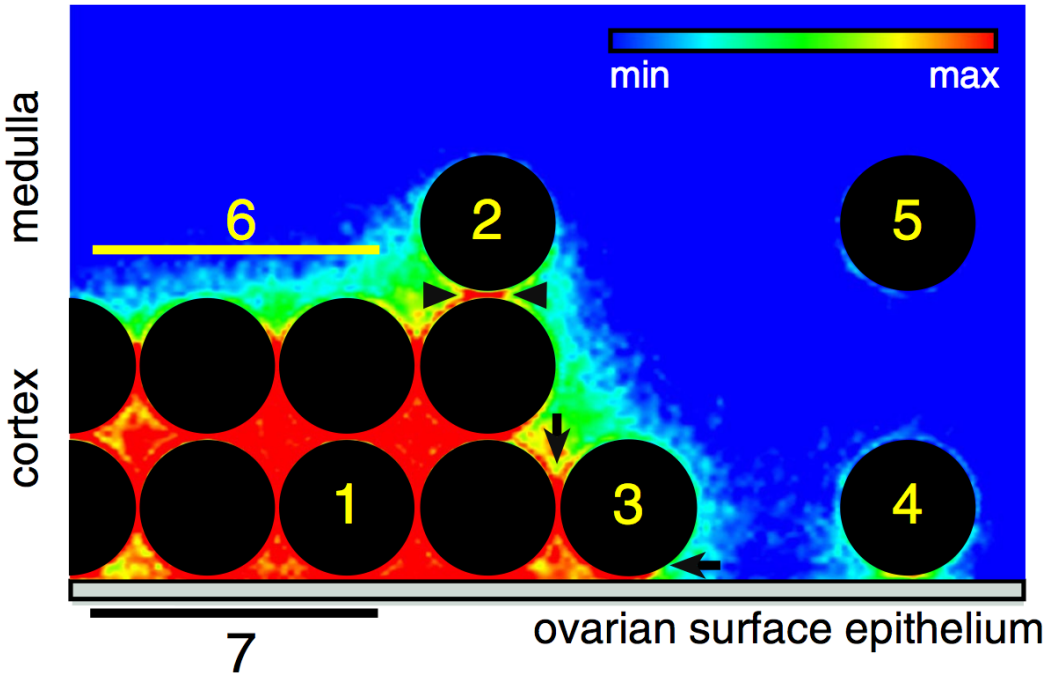


Figure 3.1: Simulated concentration map of a putative inhibitory factor which is produced and consumed by primordial follicles (black circles): red colour represents high concentration and blue low concentration. The higher the concentration of the inhibitor the less is the possibility of the follicle to initiate growth. Follicle 1, surrounded by other follicles and close to the ovarian epithelium (gray line), is exposed to high levels of inhibitor, and therefore is very unlikely that it will initiate growth. Follicles 2 and 3 are partially exposed to high concentrations of the inhibitor (arrows and arrowheads), thus they are more likely to start growing. Follicles 4 and 5 are completely isolated, exposed to minimal inhibition, and are very likely to initiate growth. Areas 6 and 7 are the cortex edge and outer ovarian space respectively, where there is no inhibitor present. This model presents a plausible explanation for why the follicles in the inner cortical area start growing first. Image obtained from Da Silva-Buttkus *et al*, 2009.

The concentration gradient presented in figure 3.1 relies on a very fundamental condition: the impermeability of the ovarian surface epithelium. This layer of epithelial cells, connected via tight junction proteins such as ZO-1 (see Ecker & Fleming, 2008), occludin and claudin-1 (Aravindakshan *et al*, 2006), do not allow ligand exchange with the extra-ovarian environment (tight junctions: Niessen *et al*, 2007; no specific work is published for the neonatal ovary yet). We therefore assume that there is no "leaking out" of intra-ovarian growth factors from the ovarian wall, which acts as a reflective surface. In the opposite case, that is if the surface was absorbent or transparent to various ligands, there would be no high concentration of growth factors; therefore the observed gradient could not be sustained.

In order to be able to identify the nature of this signal (or signaling network), biological research is essential. Mathematical approaches alone cannot provide insight into which of the many growth factors involved in follicle development (Adhikari and Liu, 2009) are responsible for regulating initiation of follicle growth. However, our

mathematical spatial analysis can be used to further investigate potential signaling sources.

Hypothesis and aims

One of the questions that need to be answered is whether the inhibitory process we predicted is truly local. More specifically, we would like to examine if local inhibition happens the same way in ovaries lacking systemic input (blood supply). This question can be answered by analyzing the spatial arrangement of follicles in neonatal mouse ovaries grown in culture, where the tissue is sustained without any blood supply. A culture system has been developed in our laboratory as part of a different experiment, which is aimed at investigating the effects of culture on the development of follicles in the neonatal mouse ovary. In the following section we will present an overview of the methods and techniques used to culture the neonatal mouse ovaries, and to obtain and analyze digital images used to conduct the spatial analysis.

3.2 Approach

Tissue examination and data collection

Ovaries from 4 day old mice (9.7) were either fixed immediately or cultured for 8 and 12 days as described in 9.8. Figure 3.2 presents the various culture experiments conducted on the neonatal mouse ovaries. The spatial analysis was conducted on nine ovarian sections in total – 1 section per ovary; three ovaries were dissected and immediately fixed in formalin from three mice of 12 days of age (ovaries referred to as '*in vivo*'), and another six ovaries were dissected from three mice of 4 days of age, cultured for an additional 8 days, as described in 9.8 and then fixed in Formalin (ovaries referred to as '*in vitro*').

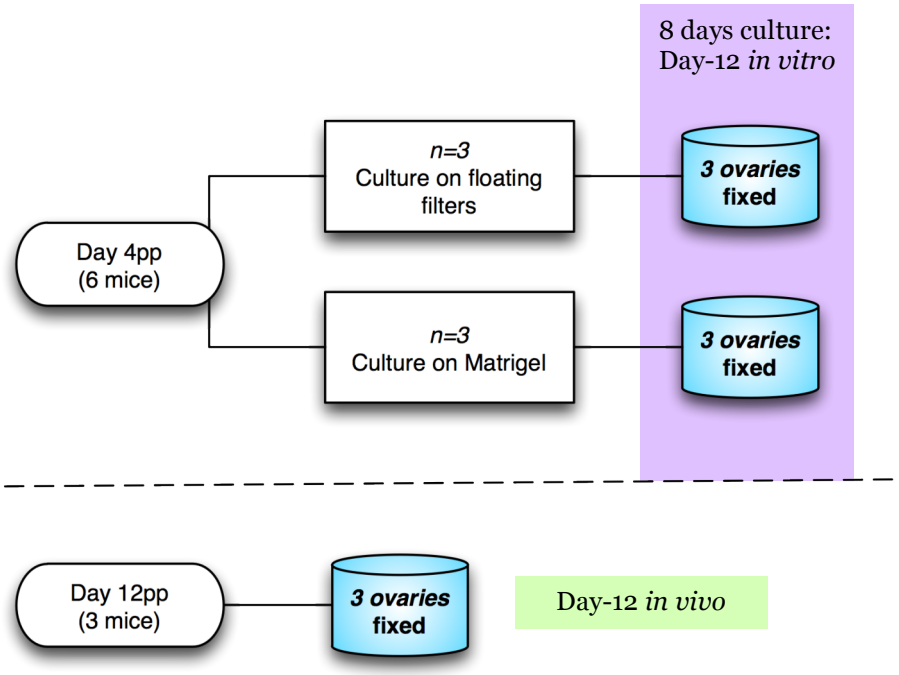


Figure 3.2: Juvenile mouse ovaries allocated for the culturing experiments. One section per ovary (cyan marked boxes) was used for the spatial analysis, namely 3 day-12 *in vivo* (uncultured) and 6 day-12 *in vitro* (day-4 ovaries cultured for 8 days).

Fixed tissue was paraffin embedded, serially sectioned and stained with Haematoxylin and Eosin (9.9). Ovarian sections from each specimen were examined by light microscopy and images of entire sections were captured using the camera attached to the microscope (9.10). Follicles had their developmental stage assessed, their diameters recorded and their *XY* coordinates mapped on the section (9.4). In addition, the *XY* coordinates of several points on the ovarian surface were also obtained. All tissue processing and data collection procedures up to this point were carried out by Dr Sharron Stubbs.

Follicle distances and statistical analysis

With the *XY* coordinates available, the inter-follicular Euclidian distances were calculated as described in (9.5.1), using a computer programme coded in Fortran 77. The programme then calculates the number of each developmental stage around a 10µm radius from any follicle in the sections. Furthermore, every follicle's minimum

Euclidian distance to the ovarian surface is calculated by the programme (9.5.2). Follicle proportions are computed by conducting logistic regression analysis using the Stata 8 software (9.6).

At this point it should be stressed that the ovaries used for the spatial analysis were cultured with or without Matrigel (9.8). There were no significant differences ($p<0.05$) in oocyte diameters, follicle diameters and follicle health found between the two culture conditions (Dr S. Stubbs personal communication). The data from the two experiments were thus amalgamated.

3.3 Results

The morphology of control and cultured ovaries were first assessed by examination of histological sections. Figure 3.3 presents the largest cross section of a non-cultured (a) and a cultured ovary (b). The distribution of follicles in both sections is visually similar, though follicular atresia in the cultured ovary appeared more obvious (assessed visually by pyknotic nuclei; see yellow arrows in figure 3.3).

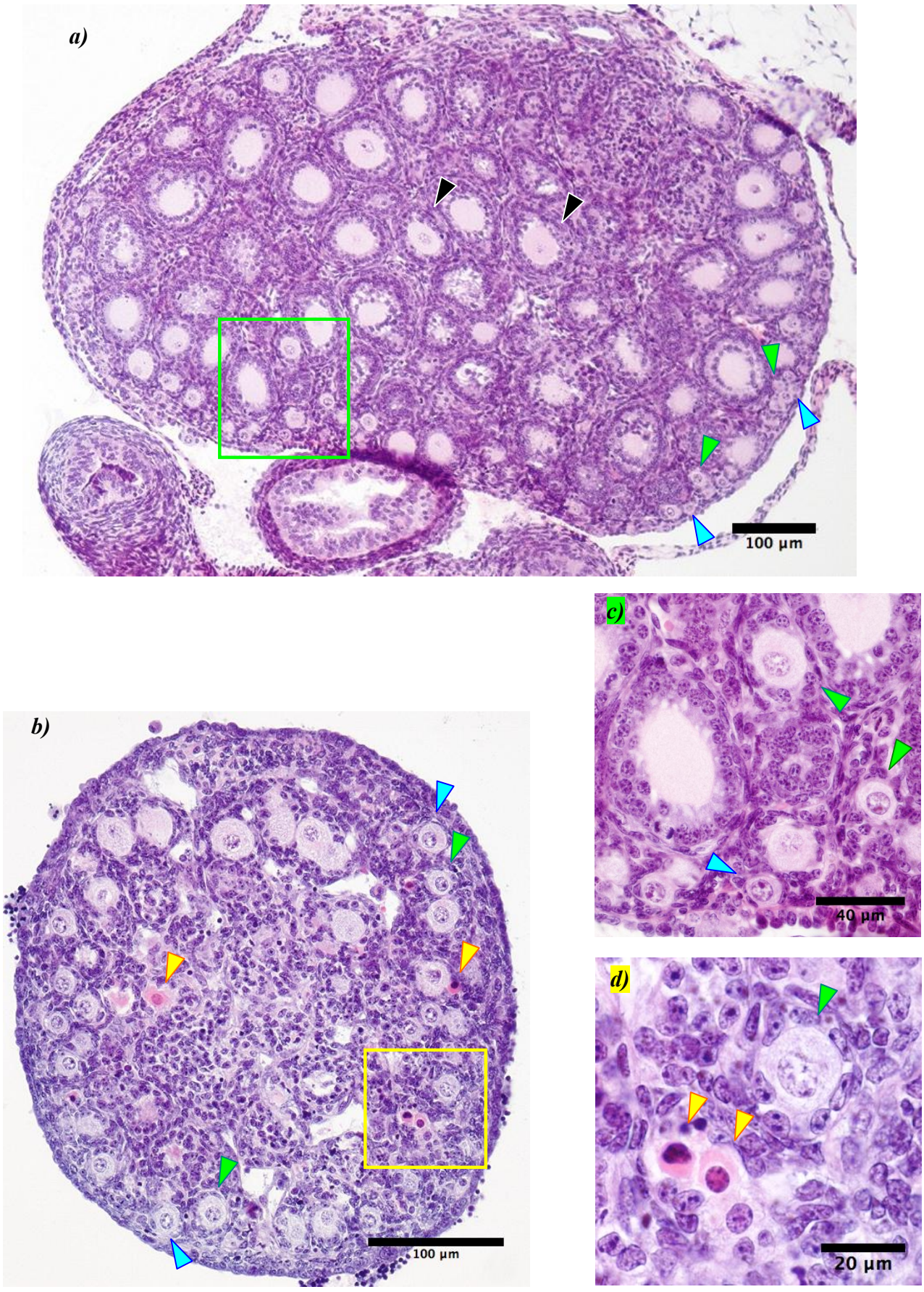


Figure 3.3: Largest cross sections of ***a)*** a day-12 mouse ovary, ***b)*** a day-4 mouse ovary, cultured for 8 days (equivalent to day-12). Sections have been stained with haematoxylin and eosin. Image ***c)*** represents a high power image of section a), enclosed in the green square, to depict follicle morphology. Image ***d)*** is a detail of section ***b)***, enclosed in a yellow square. Blue arrows point at primordial follicles, green at transitional, black at primary plus and yellow at atretic follicles.

However, it should be emphasized that these observations are purely qualitative. Quantitative comparison of the patterns in the two cases can result from the analysis of the follicle distances to the ovarian surface, which is part of the novel spatial distribution analysis proposed in chapter 2 and in (Da Silva-Buttkus *et al*, 2009). In section 9.5 the distance calculation for each follicle to the ovarian surface is reported. The minimum distance calculated was then selected. Follicles are then grouped into specific bins, according to their distance from the surface. The proportion of growing (transitional or above) follicles in each bin was calculated by logistic regression analysis (section 9.6), performed on Stata 8 (Stata corporation), and plotted in figure 3.4 versus the ovarian surface distance. Error bars are 95% confidence intervals, determined from the regression analysis errors clustered by ovary. Atretic follicles were excluded from this analysis.

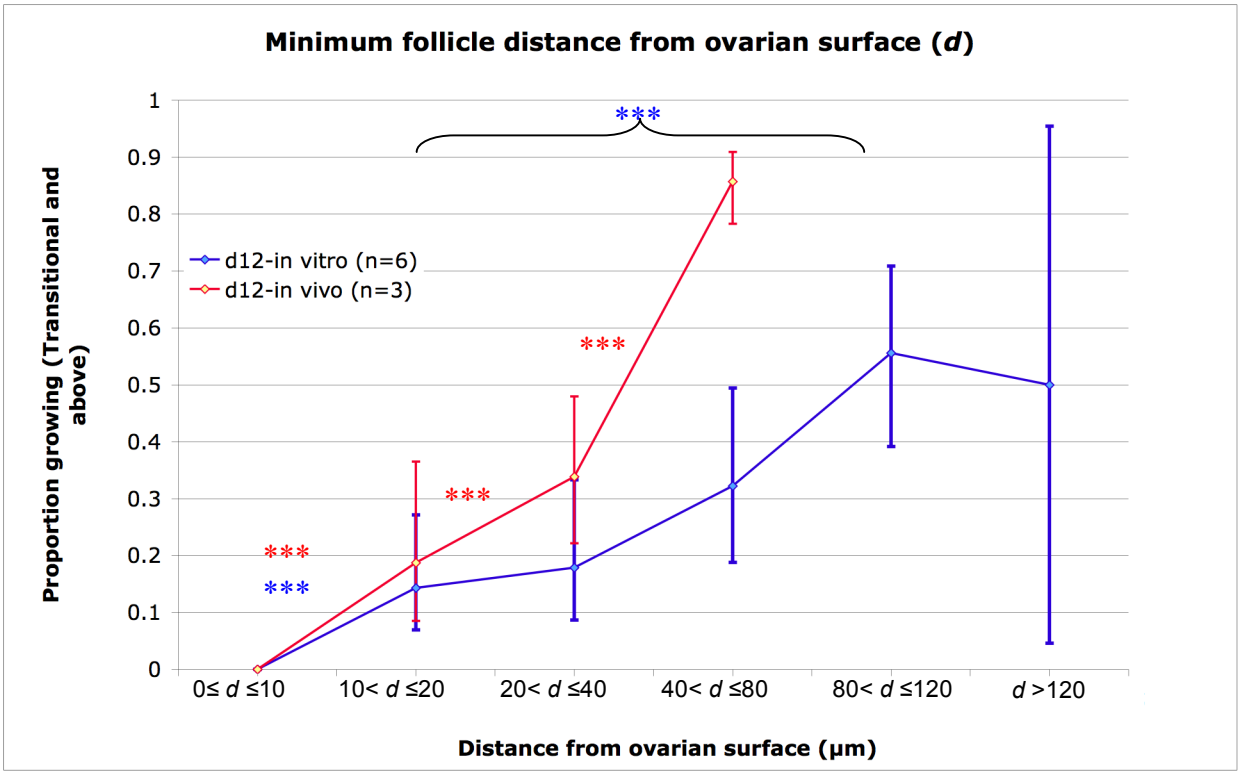


Figure 3.4: Proportion of follicles initiating growth as the distance from the ovarian surface increases. Error bars are 95% confidence intervals. Blue lines and stars on the graph refer to the *in vitro* ovaries; red refer to the *in vivo*. Three stars between two points indicate high statistical significance ($p<0.01$) in the difference of the values. Nb only healthy follicles are included to the analysis.

The graph in figure 3.4 shows that the further a follicle is located from the ovarian surface increases, the higher is the probability that this follicle is growing. In the case of *in vivo* ovaries (red line), all differences within the distance groups are highly significant ($p<0.01$), whereas for the *in vitro* ovaries the difference is statistically highly significant ($p<0.01$) only when the distance from the ovarian surface increases from around 20µm to around 100µm. The message conveyed from this graph is that both types of ovaries show a gradient of growth, from the ovarian surface to the medulla; primordial follicles are located close to the ovarian surface, and growing located further inside. This is present regardless of the absence of blood supply. Notably, although the qualitative assessment of the images from ovarian sections shows that there are no differences in the arrangement pattern of the follicles between the *in vitro* and *in vivo* ovaries, the graph in figure 3.4 depicts a slightly different pattern for the *in vitro* ovaries. The slope of the *in vitro* (blue line) is reduced, most probably because the overall proportion of growing follicles is much lower, when compared to the *in vivo* ovaries (shown in table 3.1).

Follicles in the cultured ovaries rarely progress beyond the transitional stage. Although the oocytes increase in size, surrounding granulosa cells do not change their shape. In the *in vitro* sections, the granulosa cell height is much less when compared to *in vivo*, meaning there is little evidence of cuboidalization in culture (Dr S. Stubbs personal communication). This could be due to the lack of growth factors (or FSH) in the culture medium. Alternatively, the failure of granulosa cells to change shape fully could be due to mechanical constraints. Cultured ovaries shrink in culture; this could be introducing mechanical forces capable of preventing cells from cuboidalizing. In order to highlight the differences between the two types of ovaries, the numbers of follicles that were counted in the ovarian sections are reported in Table 3.1. The effect of the culture on the number of follicles, counted on the largest cross section, can be seen in figure 3.5. The figure reports the proportion of follicles in each developmental stage, as a percentage of the total number of follicles counted.

Table 3.1: Follicles counted on the largest ovarian cross-section (one per ovary), considered for the spatial analysis. Both *in vivo* and *in vitro* ovaries are day-12. Standard errors of the mean are reported where applicable.

	In vivo (n = 3)		*In vitro (n =6)*	
	Total	**Average per section (± *SEM*)**	**Total**	**Average per section (± *SEM*)**
Primordial	126	42 ± 7.23	282	47 ± 9.44
Transitional	45	15 ± 1.15	97	16.2 ± 1.92
Primary	21	7 ± 1.53	3	0.5
Primary Plus	46	15.3 ± 2.96	0	0
Secondary	8	2.67 ± 1.67	0	0
Atretic	1	0.3	98	16.33 ± 2.53
Total analysed	247	82.3	480	80

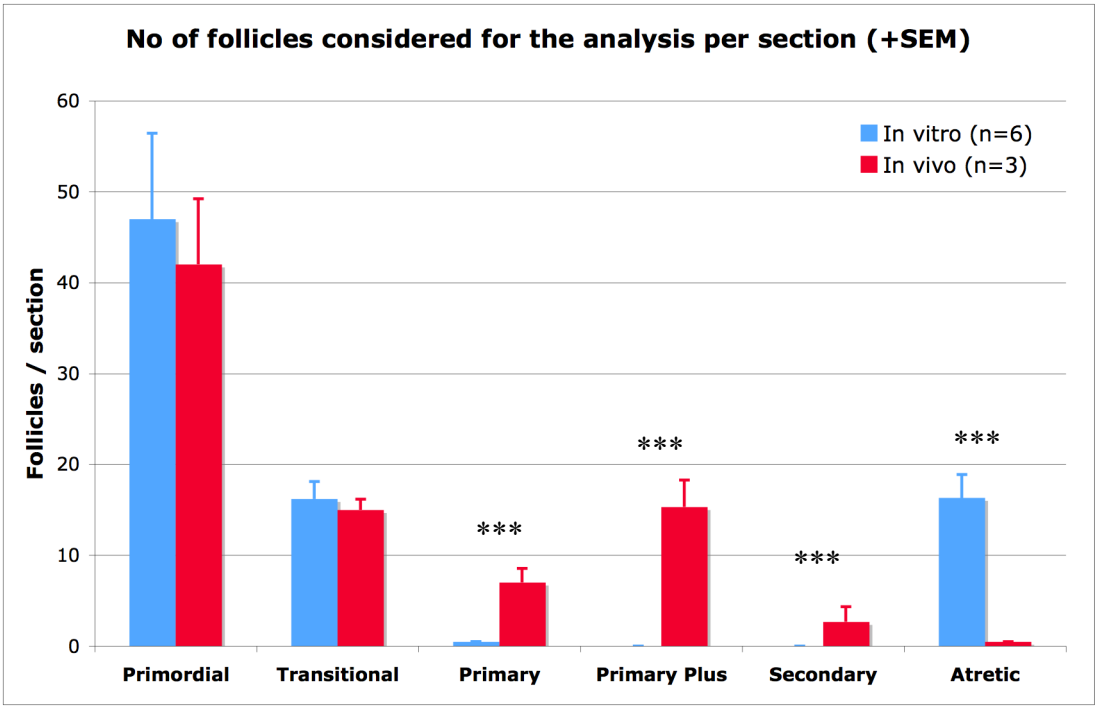


Figure 3.5: Follicles counted (+SEM) of each developmental stage for *in vitro* and *in vivo* ovarian sections, considered for the spatial analysis. Stars denote significant statistical differences between groups ($p<0.01$). The numbers used appear in table 3.1.

Interestingly, primordial and transitional follicle numbers are very similar for both cultured and uncultured ovaries (figure 3.5). Emphasis should be given to the lack of almost any follicles beyond the transitional stage, and high proportion of atretic follicles in the *in vitro* ovaries. Given that no growth factors were used in the culture media, in order for follicles to develop beyond the primary stage, either blood supply must be present to support growing follicles with various nutrients and FSH (Saha *et al*, 2000), or the culture conditions should be further improved to allow further growth (as in Sadeu *et al*, 2008, although from personal communication with Dr Stubbs, replicating Sadeu's culture conditions did not yield the follicle growth reported in their work). Furthermore, judging from the similarity in proportions of primordial and transitional follicles in both cases, the proposed local inhibitory mechanism seems to be active also in the cultured ovary, maintaining a balance between the resting and growing follicles. This can be further corroborated by our spatial analysis technique, which looks into the number of primordial and growing neighbours for each follicle.

The analysis of the spatial arrangement of follicles was performed as described in section 2.3 for the adult human and in the work of Da Silva-Buttkus *et al* (2009) for the neonatal mouse. Namely, follicles were categorized into groups according to the number of primordial follicle neighbours each follicle has within a distance of 10μm from its surface; the proportion of growing follicles within each group was then calculated. The distance of 10μm was selected based on the results published in the work of Da Silva-Buttkus *et al*, 2009, where the authors demonstrated that the effect of the signal is weak beyond the distance of 10μm in the neonatal mouse (hence the hypothesis that the mechanism is local). We considered any follicle that is of transitional stage and above to have initiated growth, based on the morphological criteria reported in sections 1.3.1 and 9.2. In addition, any primordial follicle with an oocyte diameter greater than 20μm was classified as transitional for this analysis. This is because oocytes showed increased size despite the absence of significant cuboidalization of granulosa cells. The results of the spatial analysis are presented in figure 3.6. Proportions were calculated using logistic regression analysis, using Stata 8 (Stata corporation).

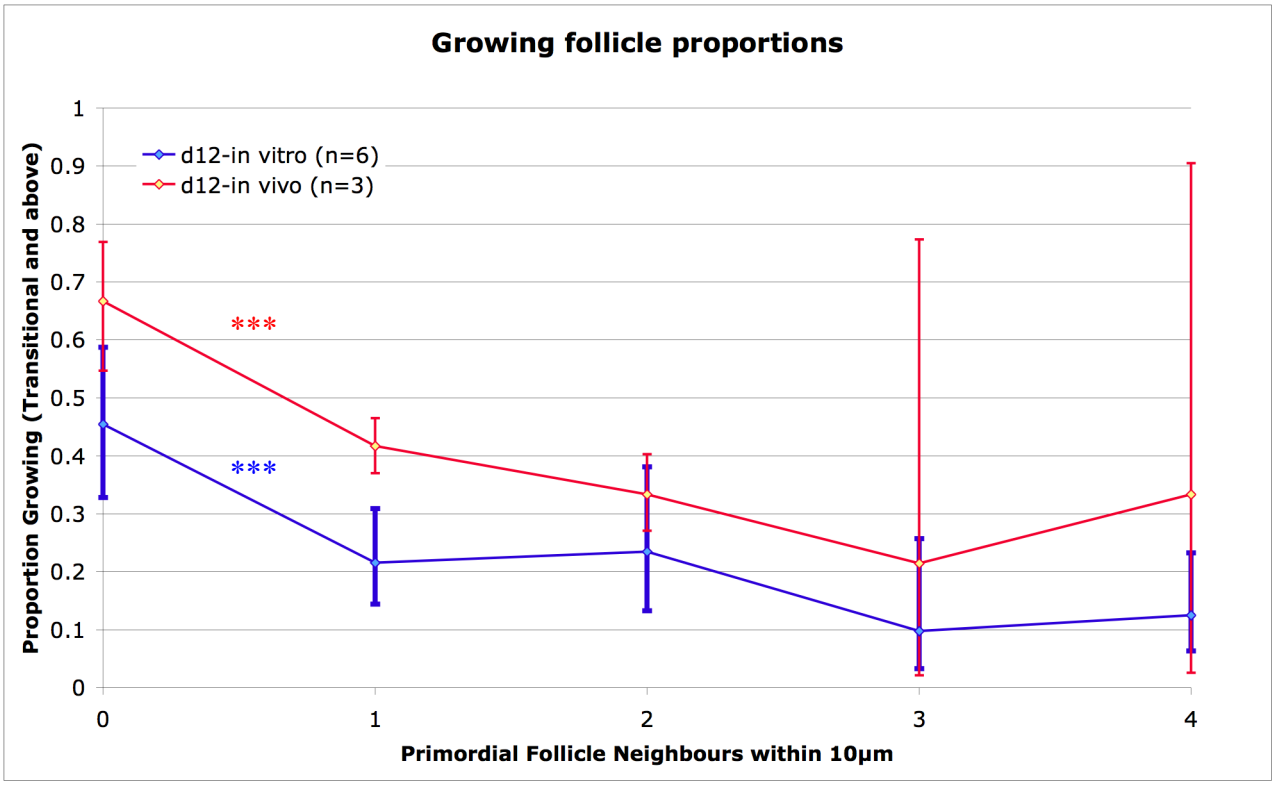


Figure 3.6: Proportion of follicles in each group (groups are assigned according to the number of neighbours the follicle has within 10µm from its surface) that have initiated growth. The blue line and stars correspond to the d12 *in vitro* ovaries and the red to the d12 *in vivo*. Error bars are 95% confidence intervals. Three stars between points 0 and 1 indicate high statistical significance (p<0.01) between the two values.

The results presented in figure 3.6 show that there is a decrease in the probability of a follicle to be a growing one as the number of primordial follicles within 10µm increases. More specifically, in a day-12 *in-vivo* mouse ovary (red line in figure 3.6), if a follicle had no primordial neighbours in close proximity (within 10µm), then there was a probability of ~68% that this follicle was growing. This probability reduced to ~42% (highly significant, p<0.01) when there was a single primordial follicle in its neighbourhood. There is a further reduction in the probability of the follicle to be growing as the number of primordial follicles increases. Therefore the inhibitory relationship between nearby primordial follicles and initiation of follicle growth that we observed in the adult human, and also shown in the neonatal mouse (Da Silva-Buttkus *et al*, 2009), is verified by our results.

The same trend is observed in the case of day-12 *in vitro* ovaries (blue line in figure 3.6). Specifically, if a follicle had no primordial neighbours within 10µm from its surface, there was ~45% probability that it was a growing follicle. This probability

was reduced to ~22% if one primordial follicle was nearby, which is highly significant ($p<0.01$). As the number of nearby follicles increased, the probability of the follicle being a growing follicle reduced (not significantly), in a similar pattern as for the non-cultured ovary. It is important to stress that in figure 3.6, the slopes of the first segment of the lines define the strength of the mechanism, showing that the probability of a follicle to be growing, if one primordial follicle is within 10μm from its surface, is halved in both *in vitro* and *in vivo* ovaries. Hence, the local inhibition mechanism that we hypothesized to be responsible for keeping the primordial follicles in a resting state, is also present in the cultured ovary. The blue line (*in vitro* ovaries) in figure 3.6 is shifted downwards, because of the overall lack of growing follicles, compared to the *in vivo* ovary (see also table 3.1).

The level of atresia in the *in vitro* ovaries is remarkably high as shown in figure 3.4. Visual observations show that there are many more atretic follicles in the middle of the cultured ovary. In order to quantify atresia and its distribution within the ovarian sections, the positions of atretic follicles in the *in vitro* ovarian sections were analyzed, so that their distance from the ovarian surface could be mapped. Figure 3.7 reports the proportion of follicles that are atretic within groups defined according to the minimum follicle distances from the ovarian surface. Proportions were computed by doing logistic regression analysis, using Stata 8 (section 9.6).

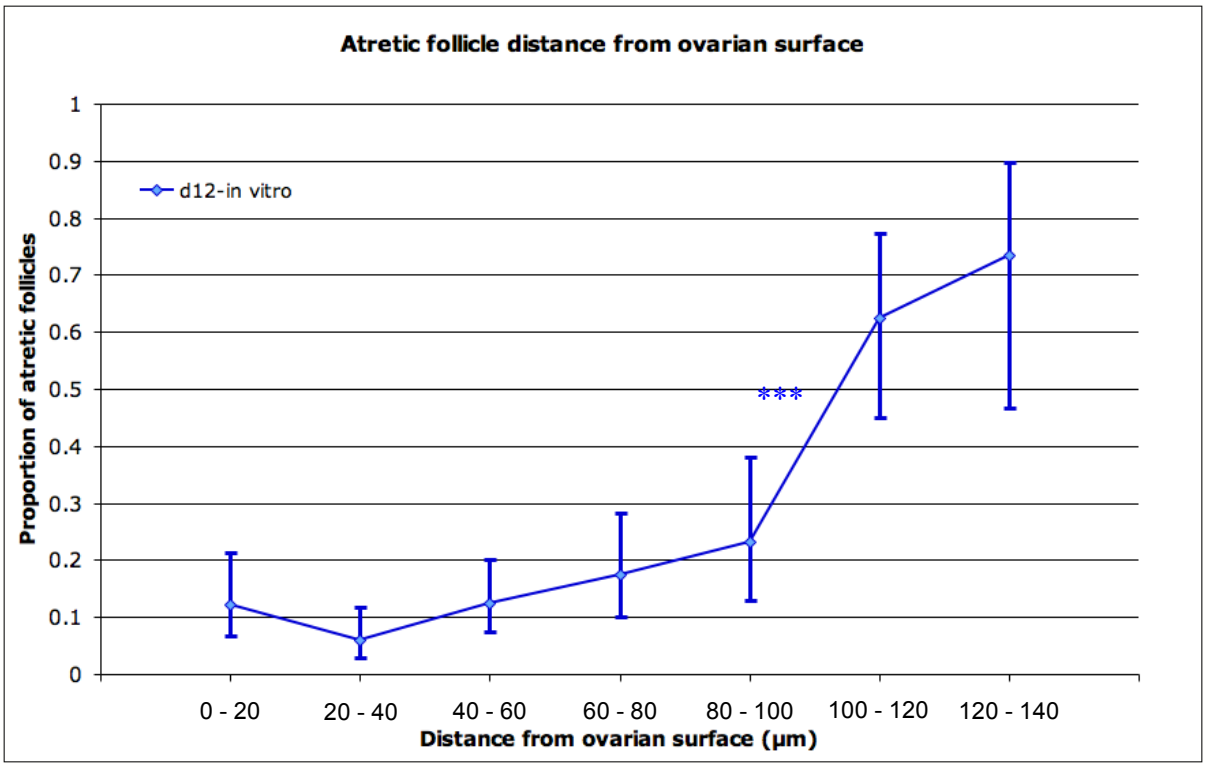


Figure 3.7: Proportion of atretic follicles vs distance from the ovarian surface, for cultured ovaries. Error bars are 95% confidence intervals. Three stars indicate high statistical significance ($p<0.01$). *In vivo* ovaries were not considered, as there is only one atretic follicle observe in the sections examined.

Figure 3.7 shows a non-significant change in the proportion of atretic follicles in the cultured ovaries that are up to 100µm away from the ovarian surface. When past this distance, the increase in the proportion of atretic follicles is highly significant ($p<0.01$), meaning that as we move from the outer cortical area to the medulla area of the ovary, significantly more follicles have died. In contrast, atresia levels in the *in vivo* ovaries were almost zero, with only one atretic follicle observed in the sections examined. The overall results indicate that systemic input or appropriate optimization of culture conditions (not yet achieved for mouse in any hitherto published work) is necessary for proper follicle development through developmental stages that are not hormone dependent.

3.4 Discussion

When qualitatively assessing the spatial organization of primordial and growing follicles in ovarian sections of cultured juvenile mouse ovaries, one can see that follicle development follows similar arrangement as in the uncultured ones

(Eppig *et al*, 1996). Using our follicle spatial distribution analysis, this was also quantitatively verified; namely, it was shown that immature follicles of early developmental stages are located in the cortex of the ovary, close to the ovarian surface, whereas the more mature ones are situated in the inner cortical area (figure 3.4). It was therefore hypothesized that the same local inhibitory mechanism should be active in the cultured ovary as well, characterized by absence of blood supply. Quantification of the spatial arrangement of the follicles relatively to their distance from the ovarian wall (figure 3.4) revealed that the ostensibly similar developmental gradient *in vitro* and *in vivo* in fact is different in that growing follicles did not increase significantly as one moves away from the ovarian surface, while atretic follicle numbers increased (figure 3.7). This is yet another example of the usefulness of our method for quantification of follicle spatial properties, utilized to detect subtle follicular pattern differences between the two systems, which are not detectable by simple visual comparison.

Concerning the blood supply, our results suggest that nutrients, growth factors and hormones dispensed to the ovary are crucial for appropriate follicle development past the transitional stage. Insulin-like growth factors (IGFs) and follicle stimulating hormone (FSH) that are circulated by the blood, for instance, are key components for follicle growth and steroidogenesis (Fabbri *et al*, 2007, Kwintkiewicz and Giudice, 2009), though these affect mostly large multilayered and antral follicles. In our culture system, there were no follicles past the primary stage. Similar behaviour was observed in knockout animal studies, which involved mice with BMP-15 and GDF-9 deficiency; follicles arrested development at the primary stage (Yan *et al*, 2000). This is thoroughly discussed in the work of Sadeu *et al*, 2008, where molecular studies were also performed to assess this similarity in abnormal follicle development. The authors postulate that there is low expression of GDF-9 and/or BMP-15 *in vitro*, affecting follicle transition beyond primary stages, though there is no evidence supporting this hypothesis. This may well be the case in our culture system as well, and can be further investigated experimentally by adjusting the culture conditions, adding GDF-9 and/or BMP-15. Alternatively, the lack of FSH may lead to certain growth factor pathways not sufficiently being augmented (see Introduction, 1.6). FSH receptor is not expressed in primordial follicles; however, it is experimentally shown that the presence of FSH in culture exhibits a “positive effect” on survival and

development of follicles from the primordial stage up to early secondary, a phenomenon for which there is no convincing explanation as yet (Adhikari nad Liu, 2009).

Furthermore, our results show that the proposed inhibition mechanism is indeed present in the cultured ovaries, with the strength of the signal being the same as to that of the non-cultured ovaries. This is observed in figure 3.7 where the two lines, red for *in vivo* and blue for *in vitro*, have almost identical slopes for each segment. The downward shift in the case of *in vitro* ovaries is due to the lack of growing follicles, as opposed to *in vivo*, where the full range of developmental stages are present, from primordial to secondary (the ovary is too young for follicles to develop further in the early antral stage).

The numbers of primordial and transitional follicles, which were counted on each section in order to conduct the spatial analysis, appear in table 3.1. Although absolute follicle numbers in each ovary were not determined, the average number of primordial and transitional follicles per section is similar in both *in vitro* and *in vivo* ovaries (figure 3.4). This also verifies that the mechanism is present, as the resting pool is being kept at a stable level (similar number of primordial follicles in both cases) with a steady number of follicles initiating growth (similar number of transitional follicles). Similar observations, based entirely on follicle numbers, are reported in the work of Sadeu *et al,* 2008. The authors state that despite the lack of anti-müllerian hormone (AMH), which is a known inhibitor of primordial follicle growth, there is no resting follicle decrease in culture (however the authors consider transitional follicles as resting). AMH is expressed in the granulosa cells of growing follicles of early primary through to the antral stage, and it has been demonstrated that AMH knockout mice exhibit early depletion of the primordial pool (Durlinger *et al*, 1999). In the cultured ovary though, there are not as many growing follicles as in the *in vivo* ovaries, hence the AMH inhibition may be significantly reduced. These observations, combined with the results drawn from the adult human could lead us to infer that the proposed primordial follicle inhibition mechanism is crucial for regulation of follicle growth when the ovary is still young. This mechanism may still be active in adult life, but according to our results from chapter 2, the strength of the inhibitory signal exerted by primordial follicles is much weaker, and most probably the mechanism is already obsolete. This can be postulated from the fact that follicles

are very dispersed and isolated, in contrast to the neonatal mouse where follicles occupy almost the entire volume of the ovary. The most probable scenario is that the mechanism is not acting alone, rather in combination with other regulatory mechanisms, such as the AMH inhibition from growing follicles, to ensure that the follicle pool is properly maintained. As the animal reaches puberty, a change in the hormonal environment may supplement or even override the local inter-follicle inhibition process existing early in development.

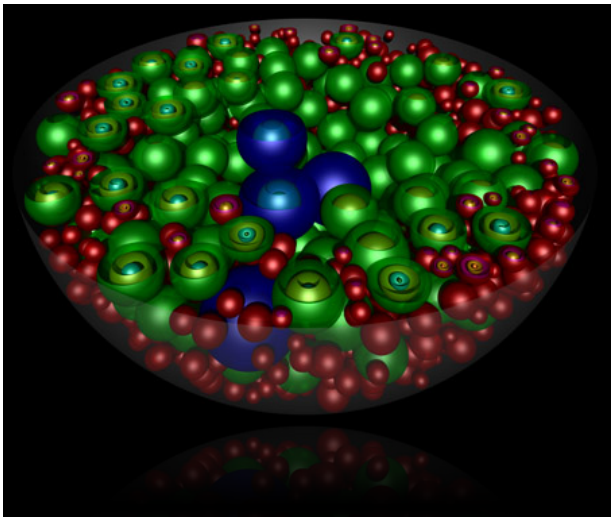
Conclusions

The mechanism we proposed for regulation of primordial follicle initiation and growth is hypothesized to function via paracrine-autocrine signaling, which locally inhibits primordial follicle growth. The spatial arrangement of the follicles is therefore important, and if the mechanism is truly local, spatial patterns in both live and cultured ovaries should be similar. Follicle arrangement patterns have been reported to be similar in cultured and uncultured ovaries, from qualitative observations on the ovarian sections (Eppig *et al,* 1996). Visually, this seems to apply in our case as well (figure 3.3). Namely, follicles follow a geographically determined pattern (Sforza *et al*, 2003), with small immature follicles located in the cortical area near the ovarian surface and the more mature ones in the inner cortex, close to the medulla.

In this chapter, the aforementioned follicle pattern was quantified, using the method of spatial analysis presented in chapter 2. Additional evidence for the existence of a local inhibitory mechanism was presented, which is responsible for primordial follicle regulation of initiation of growth, showing that is also present in the juvenile mouse even when the blood supply is absent. This prediction is entirely based on mathematical analysis of spatial information, extracted from imaging data. As discussed in chapter 2, though this approach can direct the focus of biological experiments, it cannot provide explicit information on the nature of the signals.

Chapter 4

Computer-generated ovaries for assessing the effect of biological variability on number of follicles in the juvenile mouse ovary



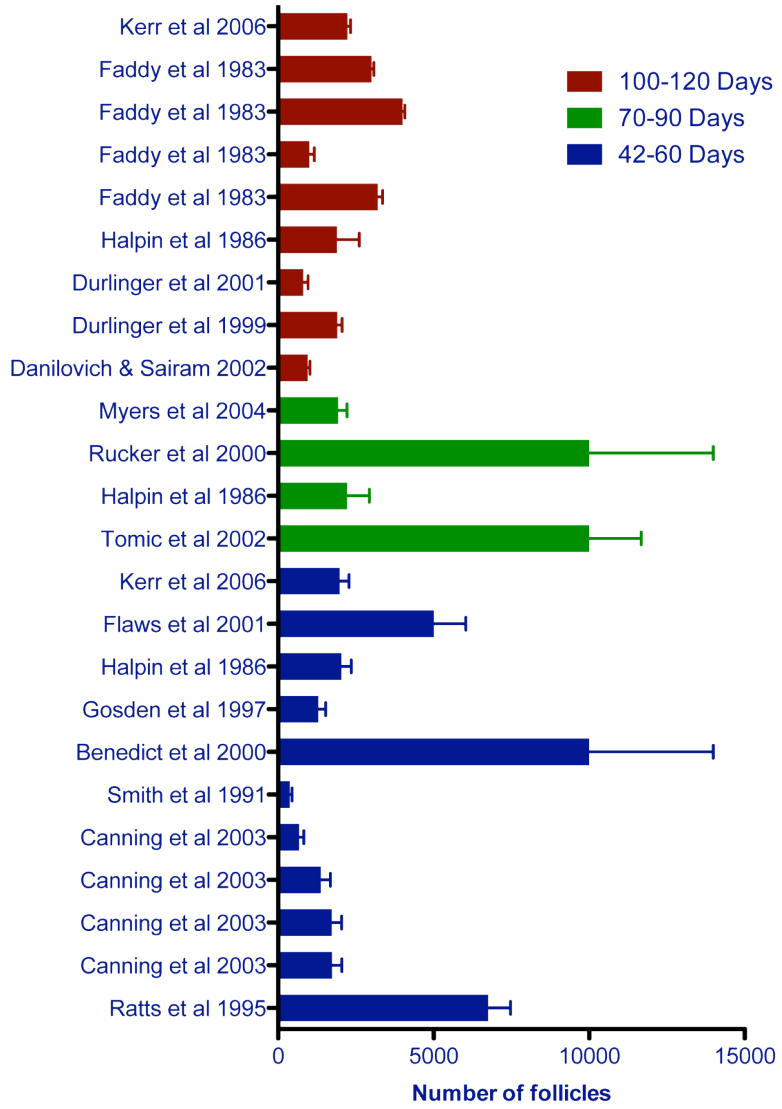
4.1 Introduction

Progress in the field of ovarian biology relies heavily on the ability to count follicles accurately. Accurate follicle counts are important for the comparison of follicle number distribution between normal and mutant mice (Falender *et al*, 2005), as well as determination of the adverse effects of environmental toxins (Hoyer *et al*, 2007) and cancer chemotherapeutics (Perez *et al*, 1997). Furthermore, precise follicle counts can increase our understanding of follicle initiation and development, from birth until the menopause. Ovarian ageing specifically is a field of research that is highly dependent on accurate estimation of follicle number, as the process is dominated by decrease in follicle quantity and quality (Broekmans *et al*, 2009), and requires exhaustive counting studies, such as in the work performed by Hansen *et al* (2008) on 122 human ovaries of various ages.

The follicle number within ovaries of the same species can be considered as a statistical variable that follows a certain distribution, with the quantity of interest being the mean and standard deviation of this distribution. We assumed a normal (Gaussian) distribution, in the interest of simplicity, as there is no published work reporting what distribution the number of follicles within an animal of specific strain and age follows. In order to accurately test hypotheses relating to follicle numbers, an accurate estimate of the mean number for the ovarian population has to be established. The error associated with the estimate is also very important (Faddy *et al*, 2007). Generally, the wider the distribution, the more the distribution needs to be sampled, *i.e.* more ovaries need to be counted. Average follicle numbers in mice (which are widely used as model organisms) are known to vary considerably between animals (Myers *et al*, 2004) and also strains (Canning *et al,* 2003). It is on this basis that Faddy (2007) emphasizes that much larger datasets than the ones currently used are required to properly assess the follicle numbers within ovaries of specific species, strain and age. An example of this variability is reported in Table 4.1; different groups report different follicle numbers for similar aged mice of various strains. Remarkable is the variability presented specifically in the C57Bl/6 mouse strain, in same age groups, which is noticeable in Table 4.1

The sampling technique used is another factor that affects the accuracy of the estimation of the actual mean follicle number, and the variation that is induced is reflected by a range of sampling techniques reported in the literature (see Table 4.1; Myers *et al*, 2004). Nevertheless, regardless of the sampling technique, it is evident that the more ovaries (of the same age and strain) are sampled, the less is the error associated with the estimate. However, it is essential for experimentalists, in order to achieve maximum laboratory efficiency combined with minimal use of animals, to obtain the most accurate measurements possible with the minimum expenditure of tissue and labour.

Table 4.1: ***Primordial*** follicle numbers estimated in mouse ovaries of various strains and age, from different groups using different estimating methods. The graph reports the average primordial follicle number (+SEM) from each published work, aligned with the mouse strain and technique used. Redrawn and adapted from Myers *et al*, 2004.



Average number of follicles	Strain	Estimating method
2227	C57Bl/6	Optical disector / Fractionator
3000	RIII	As reported in Jones and Krohn, 1961
4000	A/CBA	As reported in Jones and Krohn, 1961
1000	CBA	As reported in Jones and Krohn, 1961
3200	Strain A	As reported in Jones and Krohn, 1961
1890	C3H/HEH+101H	--
800	C57Bl/6	--
1900	C57Bl/6	--
950	129/Sv	Fraction of sections
1930	J129/C57B6	Physical disector / Fractionator
10000	129/SvJ	--
2220	C3H/HEH+101H	--
10000	--	Fraction of sections & Thickness
1976	C57Bl/6	Optical disector / Fractionator
5000	Fvb/N	Fraction of sections & Thickness
2030	C3H/HEH+101H	--
1290	C57Bl/6	As reported in Faddy *et al*, 1987
10000	129/Sv	Fraction of sections & Thickness
371	C57Bl/6	Serial section count
671	Fvb	Fraction of sections
1366	C57Bl/6	Fraction of sections
1721	Dba/2	Fraction of sections
1729	129/Sv	Fraction of sections
6750	C57Bl/6	Fraction/nucleator

One frequently used approach for estimating follicle numbers within an ovary consists of serially sectioning the tissue and counting all follicles with a definable oocyte nucleus within those sections that have been sampled, eg every 5th section. By sectioning the ovary, follicles of various sizes are not cut with equal probability; transects of follicles appear on the section proportionally to their size, or more specifically their height, perpendicular to the section. Bigger secondary and antral follicles with bigger oocytes and bigger nuclei have higher probability of being sectioned than small primordial follicles, therefore the chances of double counting these are bigger. In the project described here, the *unbiased stereologic technique* (Gundersen and Jensen, 1985, Howard and Reed 1998) is employed to rectify this sampling problem. The technique utilizes either the *optical* or the *physical disector* principle (see Approaches, 4.2.2) to estimate the number of particles (follicles) of any shape within an object (ovary) of any shape, using a simple principle: considering a pair of sections of known distance apart, if a particle's transect appears on one section, but not the next one, then it is counted. The disector effectively replaces all particles by infinitely small points, by identifying a geometric point on each particle (follicle). This way, each follicle has equal probability of being sampled as any other within the ovary, rendering the method unbiased (see also Introduction, 1.9.1).

4.1.1 Aim of our study

Our interest lies in assessing how biological diversity affects counting experiments, and what the optimal number of animals required is, to avoid drawing invalid conclusions from underpowered studies, and obtaining inaccurate follicle estimates. We have developed computer algorithms to computationally generate neonatal mouse ovaries, based on characteristics derived from measurements performed on actual ovarian sections. We can therefore conduct all the necessary experiments *in silico*, having an infinite source of material to use. These experiments have two purposes:

1. To quantify the deviation of the follicle number estimates from their actual mean, using different numbers of ovaries, as the sampling frequency (number of sections on which follicles are counted) changes.

2. To determine the minimum number of ovaries to be analysed in order to robustly compare different follicle number distributions in, for example, normal and mutant mice; i.e. how many ovaries do we need to count to detect the difference between two groups of mice with a specific statistical significance.

Overall, we want to quantify two effects (number of animals vs number of sections) and determine which one is more important.

4.2 Approach

4.2.1 Generating the simulated ovaries

Simulated ovaries have been computationally generated to conduct stereological analysis. Follicle sizes and positions in these ovaries resemble a realistic follicle distribution in neonatal mouse ovaries, and are obtained from the spatial distribution analysis performed on ovarian sections.

It must be stressed that these simulated ovaries were generated on the basis of real biological data. Follicle diameter distributions, as well as follicle spatial distributions inside the simulated ovaries were based on analyses performed on neonatal mouse ovarian sections in our laboratory by Dr Gianluca Marcelli and Patricia Da Silva-Buttkus (Da Silva-Buttkus *et al*, 2009). Follicle numbers were obtained from the data published by Kerr *et al* (2006). Simulated ovaries, as well as follicles, oocytes, nuclei and nucleoli are assumed to be spherical.

At this point, it should be noted that Kerr *et al* (2006) report follicle numbers for 7 day old mice, whereas we have the follicle spatial properties (diameter, distance to the ovarian surface, etc) for mice of 8 days of age. Both stereologic counting of follicle numbers within 6 mouse ovaries, and spatial distribution analysis on 2 ovarian sections are processes that are extremely laborious and time-consuming. It was therefore decided that repeating one of the two procedures was not time and laboratory efficient, especially since changes within 24 hours in the structure of the ovaries or the morphology of the follicles do not change in an extent that could influence this particular work.

All data tables and the complete method for producing a simulated ovary are described in detail in Materials and Methods (9.17). We developed a computer

programme, coded in Fortran 77, which generates these ovaries. The algorithm can be summarized in the following steps:

1. Randomly select the number of primordial, primary and secondary follicles to populate the spherical ovary, from the appropriate distributions (Table 9.6)

2. Assign a random radius to every follicle, from the corresponding distribution, according to the follicle type (Table 9.3); then, calculate and assign the radii of oocyte, nucleus and nucleolus, from the data reported in Table 9.4.

3. For each follicle, pick a random point on the spherical surface (random direction) and a random distance to the ovarian surface, according to the follicle stage (Table 9.5), and place the follicle to that position. If the position is occupied, keep the same distance and pick a new random direction. Repeat (*t=10,000* iterations), or restart the process, until an empty space is found.

4. After the whole ovary is populated, take the equatorial section and calculate the proportion of the section that is occupied by follicles (density, the area follicle section occupy divided by the total area of the ovarian section) (Eq. 9.XII). If it is within 10% of the values reported in Table 9.7 then the ovary is accepted. Otherwise a new ovary is generated.

The procedure described above ensures that the ovaries generated have a realistic follicle spatial and diameter distribution. The algorithm is also schematically illustrated in figure 4.1. Examples of a day 7 and a day 12 simulated ovary are reported in figure 4.2. The equatorial cross sections of these ovaries are illustrated in figure 4.3. Note that all the profiles are displayed, with their associated diameters. Observing the three dimensional simulated ovaries gives an idea of the extremely small amount of primordial follicles included in a single cross section, in comparison to the ones actually distributed in the inner surface of the sphere.

Figure 4.1 (next page): Schematic representation of the steps for producing a simulated ovary. Details can be found in Materials and Methods, 9.17.

Generation of a Simulated Ovary

1. Assigning the number of follicles within each ovary: Randomly pick number of follicles of each type (Primordial, Primary or Secondary) for a given ovary from appropriate Gaussian distributions. Distributions obtained from Kerr *et al* (2006) data.

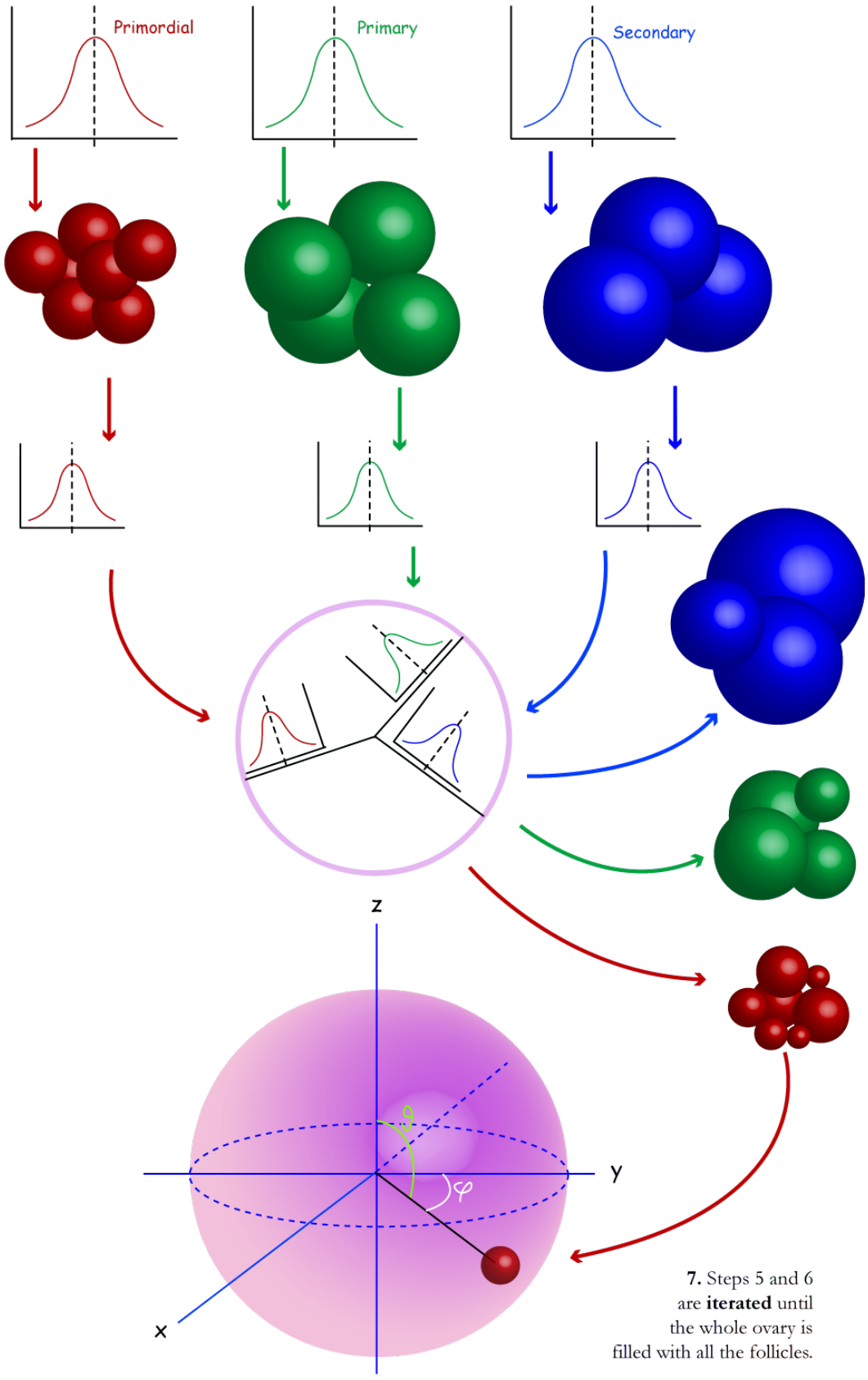
2. Assigning Follicle Diameters: Randomly pick diameters **for each** follicle, from Gaussian distributions. The distributions were obtained from our mouse follicle measurements data.

3. The ovary is envisaged as a sphere.

4. Placing the follicles in the ovary For each follicle, assign a random distance to the ovarian wall, chosen randomly from Gaussian distributions. Those distributions were again generated from our mouse section spatial analysis.

5. For each follicle, a random direction is chosen (ϑ,φ), keeping the distance to the ovarian surface constant (as assigned in step 4).

6. If space is occupied by another follicle, a new random direction is chosen, until a place is found.



7. Steps 5 and 6 are **iterated** until the whole ovary is filled with all the follicles.

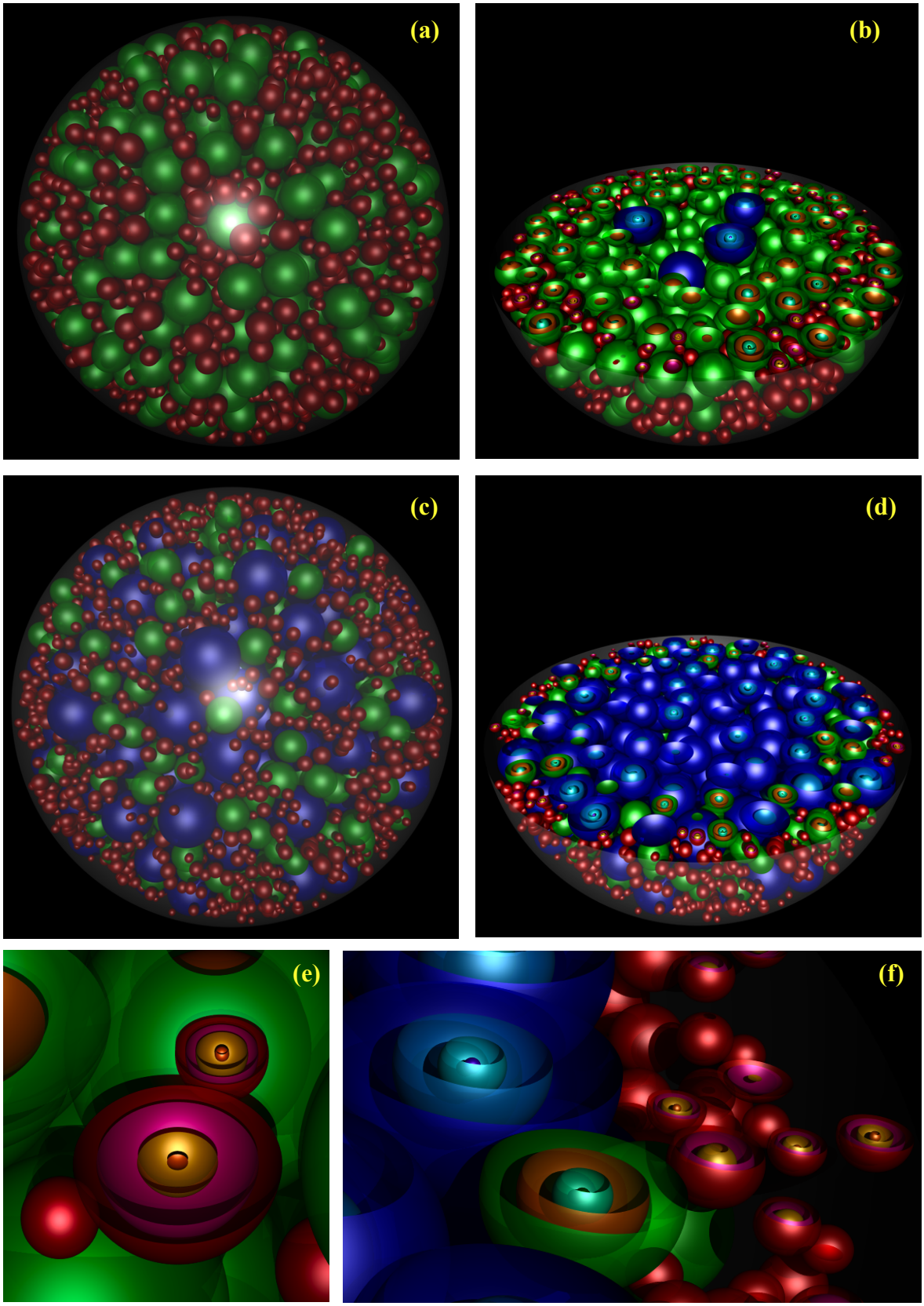


Figure 4.2: 3-D renderings of a day 7 (***a,b***) and day 12 (***c,d***) simulated ovaries, created using POV-Ray (www.povray.org). The programme generates the spherical objects at the coordinates specified, by ray tracing light. Red spheres are *primordial* follicles, green are *primary* and blue are *secondary* follicles. Each follicle has a unique diameter (e,f), selected from a specific distribution, as well as an oocyte, nucleus and nucleolus, as seen in (***e,f***). Images ***a)*** and ***c)*** present the whole spherical volume; when cut in half, images ***b)*** and ***d)*** are obtained respectively.

Follicle numbers for Day 7 simulated ovary (***a,b***): 2058 Primordial, 768 Primary, 5 Secondary

Follicle numbers for Day 12 simulated ovary (***c,d***): 2245 Primordial, 428 Primary, 389 Secondary

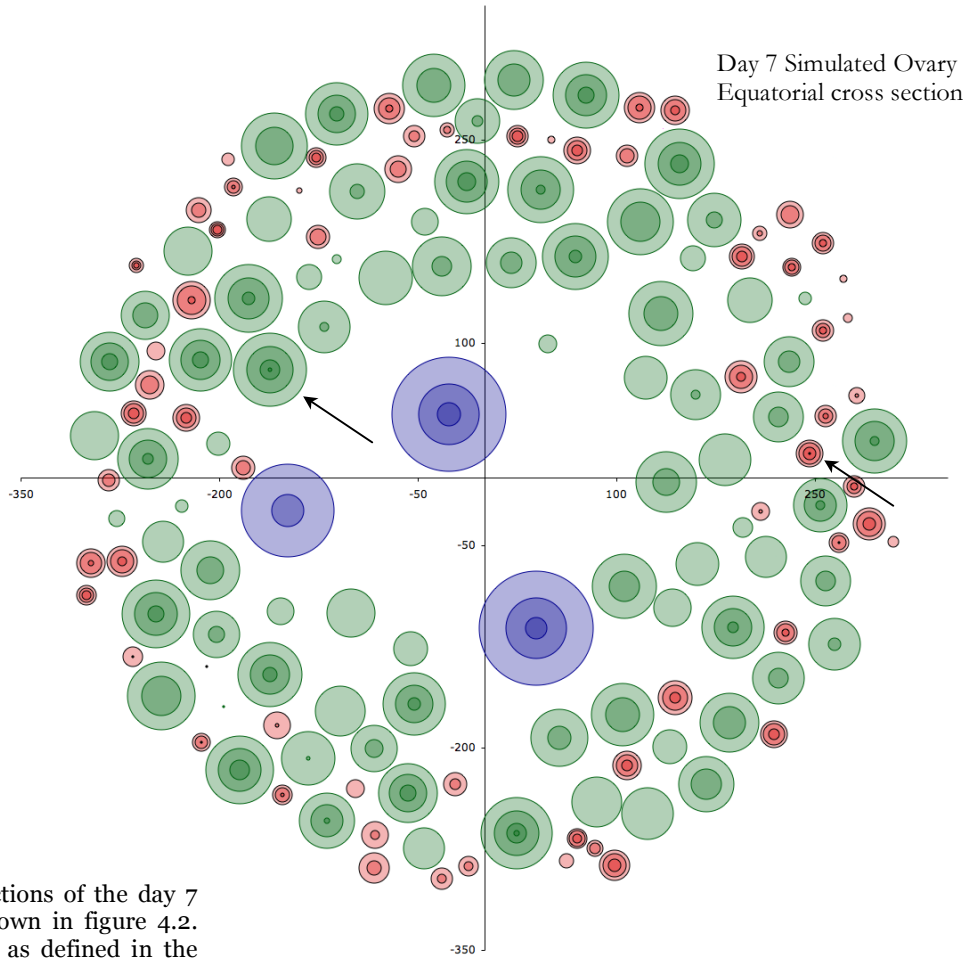
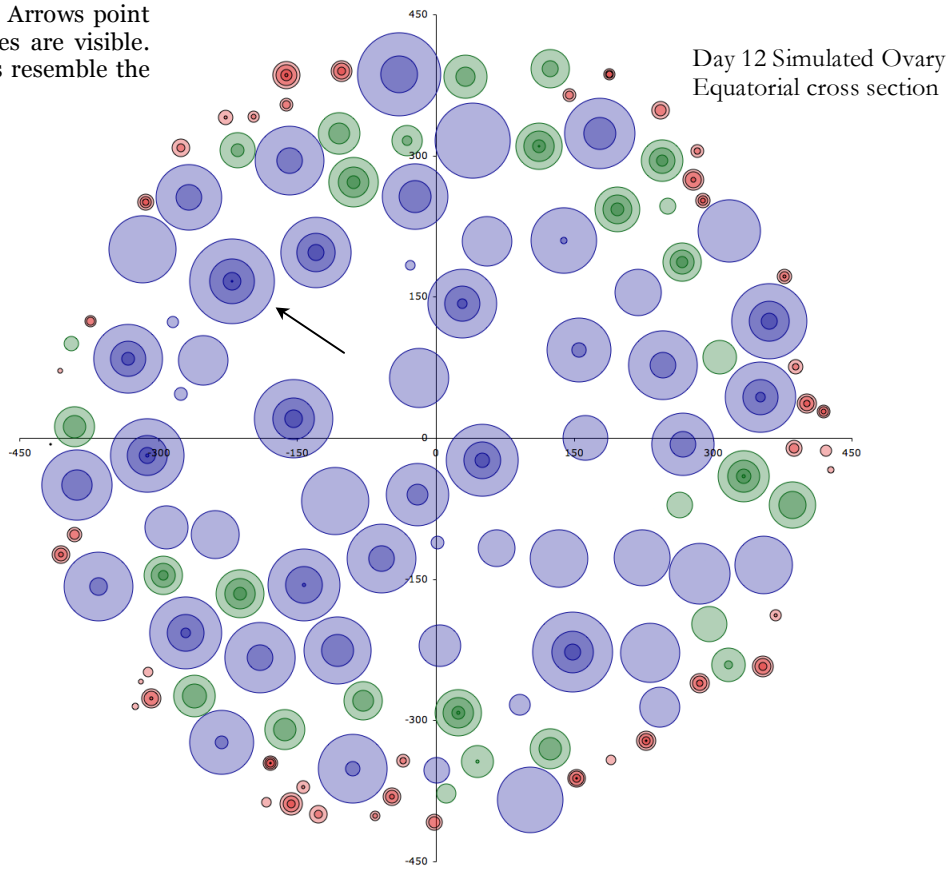


Figure 4.3: Equatorial cross sections of the day 7 and day 12 simulated ovaries shown in figure 4.2. Colours of follicles are the same as defined in the previous figures. Visualization is done in MS excel, and the distances are reported in µm. Arrows point at follicles where all the above profiles are visible. Follicle distributions on these sections resemble the real mouse ovary sections.



The simulated ovaries

The computer programme that generates the simulated ovaries takes a considerable time to complete, especially when there is a large number of secondary follicles which occupy most of the spherical space in the simulated ovary; the programme then searches for an available position for a follicle, (see sections 2.2.1 and 9.17) for a considerably longer time. For day 7 ovaries, the programme can take up to six hours to generate one ovary, whereas in the case of day 12 ovaries it could take up to one day. These times are measured on an Intel dual core processor, clocked at 2.16GHz, and can be improved by using a faster processor computer. Moreover, the programme is compiled to run on one processor core, so by increasing the number of cores or processors (or both), many ovaries can be generated in parallel, however, several days are required to generate a considerable number of simulated ovaries. The programme was executed on the computer mentioned, generating two ovaries in parallel, as well as on another remote personal computer which had two quad core Intel Xeon processors, clocked at 3.0GHz, generating eight ovaries in parallel. Optimization of the algorithm could significantly improve execution times, but optimization techniques are beyond the scope of our research.

It is of pivotal importance to generate an adequate number of simulated ovaries so that their distribution, assumed to be Gaussian, is accurately sampled. It was computationally verified that 300 simulated ovaries of each category (day 7 and day 12) had primordial and primary follicle numbers whose mean and standard deviation matched almost exactly the actual mean and standard deviation of the original distribution (more than 99.9% accuracy to the numbers reported in table 9.6, data not shown). It was therefore decided that generating 350 ovaries would be statistically sufficient to represent the biological variability in each category. The same number was used for simulated ovaries of knockout animals (section 4.2.4)

4.2.2 Application of the unbiased stereological technique

In this work we want to assess the accuracy of a simple unbiased stereological technique (Gundersen and Jensen, 1985), which combines the fractionator scheme and disector method (Howard and Reed, 1998) in counting follicle within the mouse ovary. The basic principle of the fractionator of counting particles within an object is

very straightforward. A simple example consists in cutting the object (ovary) in sections. A sampling frequency (*f*) and a random starting point are chosen, which provide a sample of sections of the whole ovary. Every particle (follicle) in the sampled sections is counted (raw count), and then an unbiased estimate of the total number of the particles in the object is obtained by multiplying the raw count by the inverse of the frequency (1/*f*). In order to properly count the particles within a sampled section (called the *reference*) the disector method needs to be applied. In this method the adjacent section (called *look-up*) to the reference one is considered. A particle is counted only if the particle's profile (cross-section) is present only in the reference section and not in the look-up section. A simple example of the disector method is illustrated and explained in figure 4.4. Further details and applications of the unbiased techniques can be found in Howard and Reed, 1998.

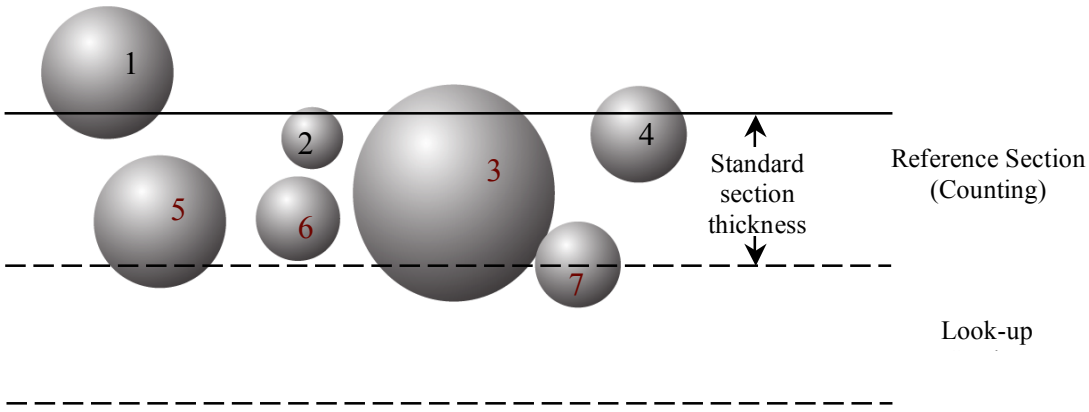


Figure 4.4: Two sections of an object containing spherical particles. The particles that would be counted are those cut only by the reference section and not by the look-up section. In the present example, spheres 1, 2 and 4 would be counted. Spheres 3, 5, 6 and 7 would not be counted.

Fortran code has been developed to apply this stereological technique to the simulated ovaries we generated. The algorithm virtually cuts through the ovary, producing sections of given thickness. The ovarian sections' thickness considered for this work was 5µm since this value is routinely used in our lab for standard immunohistochemistry procedures. The frequency of the counting can also be chosen. The disector counting technique is then applied to the sampled sections, starting from a random section. For example, let's assume that the user selects a thickness of 5µm and a counting frequency of every 10 sections, for a 500µm diameter ovary (100 sections in total). The algorithm will start from a random section between the 1st and

10th, e.g. the 7th. Then the sections considered will be the 7th, 17th, 27th, … and 97th. For each sampled section, the programme will count the profiles (follicles, oocytes, nuclei or nucleoli) appearing on top of this (reference) section but not appearing on the top of the adjacent section (look-up section). In this way, a raw count of the follicles (different for each developmental stage) is produced. To produce an *estimate* of the actual number of follicles in the whole ovary, the raw count is multiplied by the inverse of the sampling frequency. In the case of the example, the raw count is multiplied by 10. This method provides an *unbiased estimate* of the total number of follicles in the ovary.

4.2.3 Follicle estimates and the associated error

The simulated ovaries are sectioned *in silico* and the number of follicles of each stage of development in each selected pair of sections is counted using the disector principle to produce estimates of the total number of follicles in each simulated ovary. This allows us to assess the dependence of the estimate error on the sampling frequency and on the number of ovaries used. Sampling frequencies of one pair every 5, every 20 and every 50 sections were used, and the procedure was repeated for up to 20 ovaries; sampling was performed using the unbiased stereologic technique (Gundersen and Jensen, 1985, Howard and Reed, 1998), as described in 4.2.2.

The numbers of follicles were estimated for all 350 simulated ovaries. The advantage of simulated ovaries is that the actual number of follicles within them is also known. Therefore each ovary is characterized by an estimate of follicle number, and by their actual number, which can be used to assess the accuracy of the estimating technique. Figure 4.5 illustrates the basic steps of the implementation of a simple statistical analysis by applying the bootstrapping approach to assess this accuracy (Press *et al*, 2007 – Numerical Recipes, chapter 15, p. 810). Bootstrapping is a statistical method to improve the approximating probability distribution of a statistical variable (in our case the number of follicles within a population of ovaries) by drawing with replacement from an original finite sample of that population

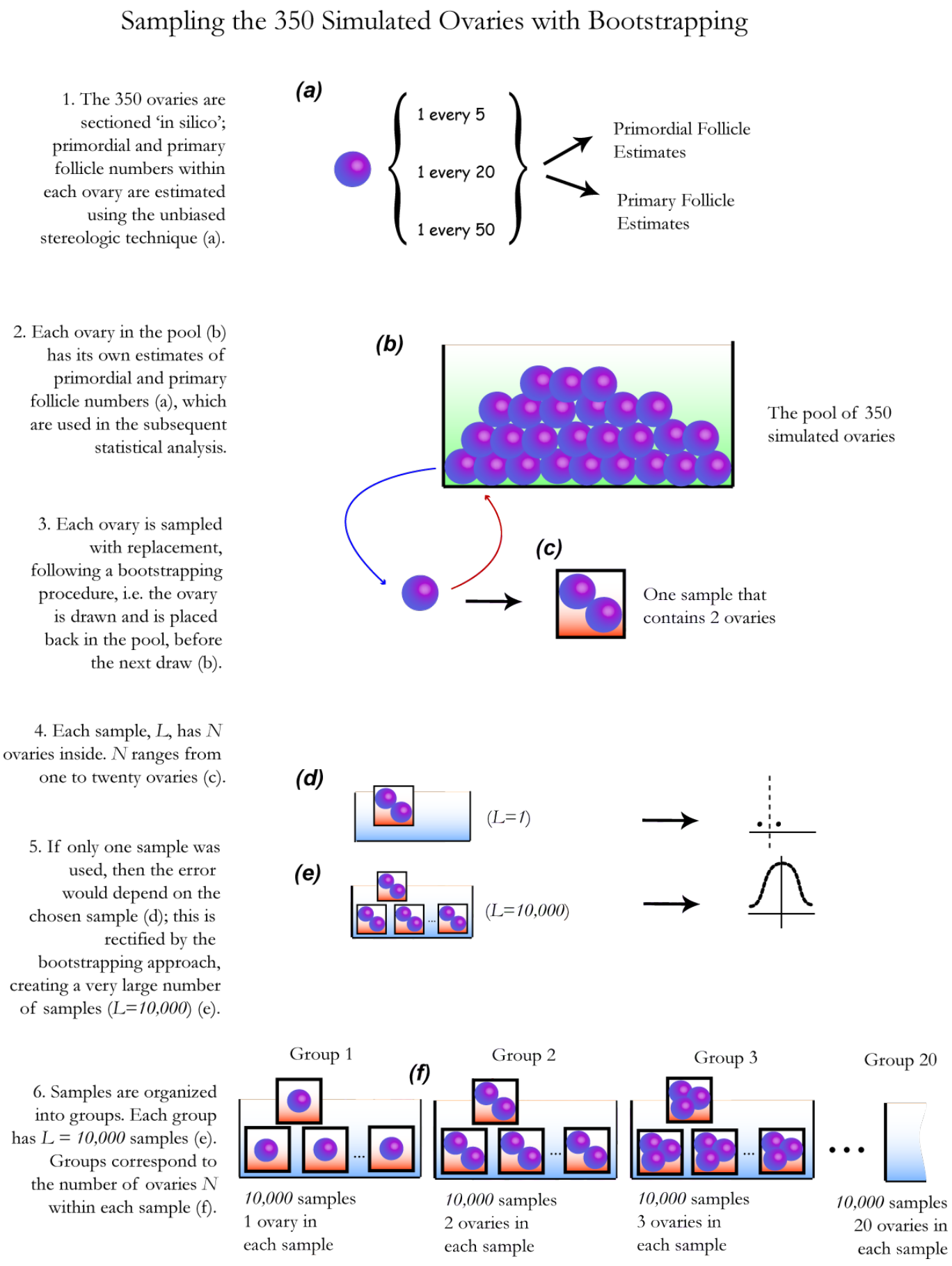


Figure 4.5: Schematic representation of the bootstrapping approach to sample the 350 ovaries

The counting technique described previously, produces estimates of follicle number, primordial or primary, for different sample sizes, *N*, and sampling frequencies (we used every 5, every 20 and every 50 sections). These estimates can be considered as the values of a random variable following a probability distribution that characterizes the whole population. Each time an ovary is chosen from the population, a different value for the number of follicles is obtained. We recall that we generated simulated ovaries according to a distribution of known mean, μ, and standard deviation σ.

In this work we want to provide an estimate of the *standard error of the mean,* $SEM^{N,f}$, for the number of follicles, when using a sample of *N* ovaries and a sampling frequency *f*. This $SEM^{N,f}$ is effectively an estimation of the error an experimentalist would have when counting follicles with *N* ovaries

In order to estimate the $SEM^{N,f}$ with sufficient statistical power, we generate *L* samples, of *N* ovaries each. Each sample provides a different sample mean, $m_i^{N,f}$ (the arithmetic average of the *N* estimates of the follicle number). The $m_i^{N,f}$ themselves are values of a statistical variable following its own distribution and standard deviation $\sigma_m^{N,f}$. This $\sigma_m^{N,f}$ is exactly what we want to estimate. Note that it is impossible to calculate exactly $\sigma_m^{N,f}$, which would require the entire population in the distribution to be considered, therefore, it needs to be estimated. An estimate, $s^{N,f}$, of $\sigma_m^{N,f}$ is provided by the following formula:

$$\sigma_m^{N,f} \cong s^{N,f} = \sqrt{\sum_{i=1}^{L} \frac{\left(m_i^{N,f} - \mu\right)^2}{L}} \qquad (4.I)$$

In equation 4.I, μ is the mean originally used to generate Gaussian distribution of the follicle numbers in the simulated ovaries, which can be found in table 9.6. Since the true mean of the distribution is known, the division in the standard deviation equation is by *L*, and not by *L-1*, as would be appropriate if the true population was

not known, which happens in most cases in statistics. Furthermore, if we were to use only one sample of N ovaries, the $SEM^{N,f}$ would depend on the sample chosen; to eliminate this problem, we used L samples, and applying eq. 4.I. Finally, we have chosen as an estimate of the error of the mean eq. 4.I: $SEM^{N,f} \cong s^{N,f}$.

4.2.4 Comparing follicle numbers for control and knockout mice

We use the simulated ovaries to reproduce a common experiment of comparing the mean number of follicles in ovaries of control mice and in ovaries of (hypothetical in our case) mice lacking a gene implicated in follicle development and number – "knockout" mice. Day 7 and day 12 knockout ovaries were computationally generated following the same procedure used for the normal ones. The number of primordial follicles in these new "knockout" ovaries follows a Gaussian distribution with a standard deviation identical to the control case but with a mean which is 50% lower (mean = 1000). Differences of 50%, and lower, between control and knockout mice have been reported in the literature (Falender *et al*, 2005). We also assume that primary and secondary follicles follow exactly the same distribution as in the control case.

Two sets of *L=1,000* samples, containing N ovaries each, are selected from the control and knockout pools of 350 ovaries each. The unbiased stereological technique is applied for a given sampling frequency, to derive the estimates of the mean follicle number in each sample. The sampling procedure is similar to the one described in the previous section, also illustrated in figure 4.5.

Note that in this case, *L=1,000* samples are utilized, instead of *10,000* used before (see 4.2.3), as they are sufficient in order to conduct the assessment of the level of statistical significance in distinguishing the two distributions. More precisely, the *t*-student statistical test for unpaired variables is performed, which compares the two sample means, having equal variances, producing two-tail *p*-values. Fortran code has been developed to perform this test.

4.3 Results

4.3.1 Calculations of Standard Error of the Mean (*SEM*)

The unbiased stereological approach of estimating numbers of follicles is applied to computationally generated ovaries (Approach, 4.2.2). *L=10,000* samples, each containing *N* ovaries, were picked using the bootstrap sampling method and the number of follicles was estimated according to a given sampling frequency, *f*. The standard error of the mean was estimated as described in the Approach section, 4.2.3, for different sample sizes (namely *N* = 1, 2, 3, 4, … and 20 ovaries), for different counting frequencies (every 5, every 20 and every 50 sections) and different ages and follicle stages. The results presented in this section include graphs reporting only the errors (*SEM*). We only report the error of the mean because that is what we want to assess: the accuracy by which the number of follicles is estimated. The mean occurring from the at least *10,000* estimates in each group is the same as the distribution mean, in all cases, therefore there is no point in reporting these averages.

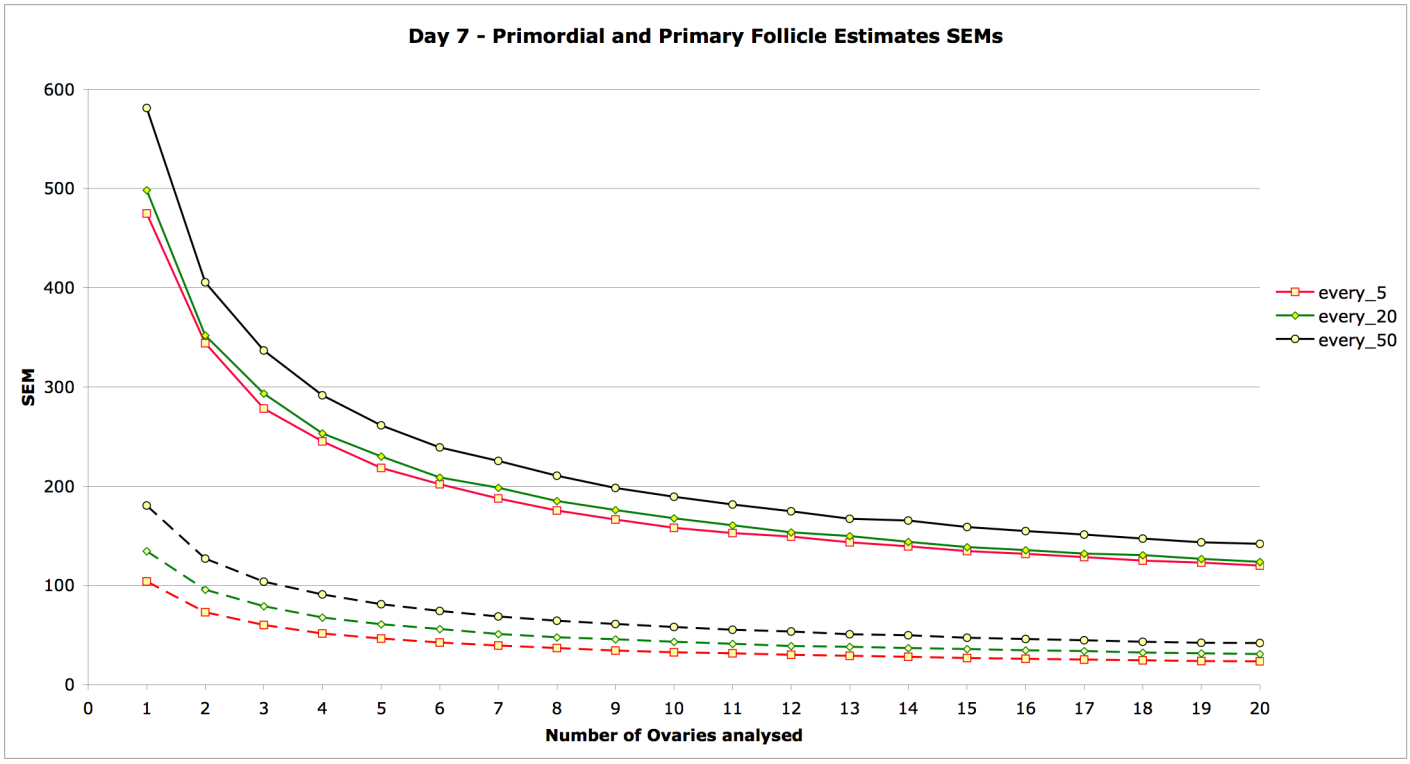


Figure 4.6: *SEM* of 10,000 samples in each group of ovaries (1,2,...,20 ovaries), for primordial (straight lines) and primary (dashed lines) follicle numbers, for different sample sizes and sampling frequencies, for day 7 ovaries. The distribution means used are: Primordial: **2000**, Primary: **570**. Ovaries were sampled using the bootstrapping approach (figure 4.5).

Figure 4.6 reports the *SEM*s of day 7 mouse ovaries for primordial and primary follicles. This figure shows a clear trend displaying a decrease in the *SEM* as the number of ovaries used increases. For instance, the graph shows that in the case where two ovaries are used (with a counting frequency of every 5 sections) the relative deviation of the primordial follicle numbers from the mean (2000 primordial) is 17.2%, whereas for 10 ovaries, the deviation drops to around 8.3%. It is also interesting to notice how the sampling frequency affects the *SEM*s. In the case that two ovaries are used, the relative deviation of the primordial follicle number from the mean (2000 primordial) for a counting frequency of every 20 sections is 18.2%, while for a counting frequency of every 50 sections the deviation increases to 21.4%, which corresponds to around a 100 follicles difference between the two cases.

Similar behaviours are obtained when counting **primary** follicles in day 7 ovaries, as shown in figure 4.6 (dashed lines). In this case, while the *SEM*s are lower, the relative deviation from the mean does not change significantly (around 13% for every 5 – every 20 sampling frequency, and 6% for higher sample sizes). The discrepancy between different sampling frequencies is similar compared to the primordial follicles case.

The *SEM*s for day 12 ovaries are reported in figure 4.7, which show a similar trend to that of day 7 case, since the two sets of ovaries do not differ significantly in the number of primordial and primary follicles.

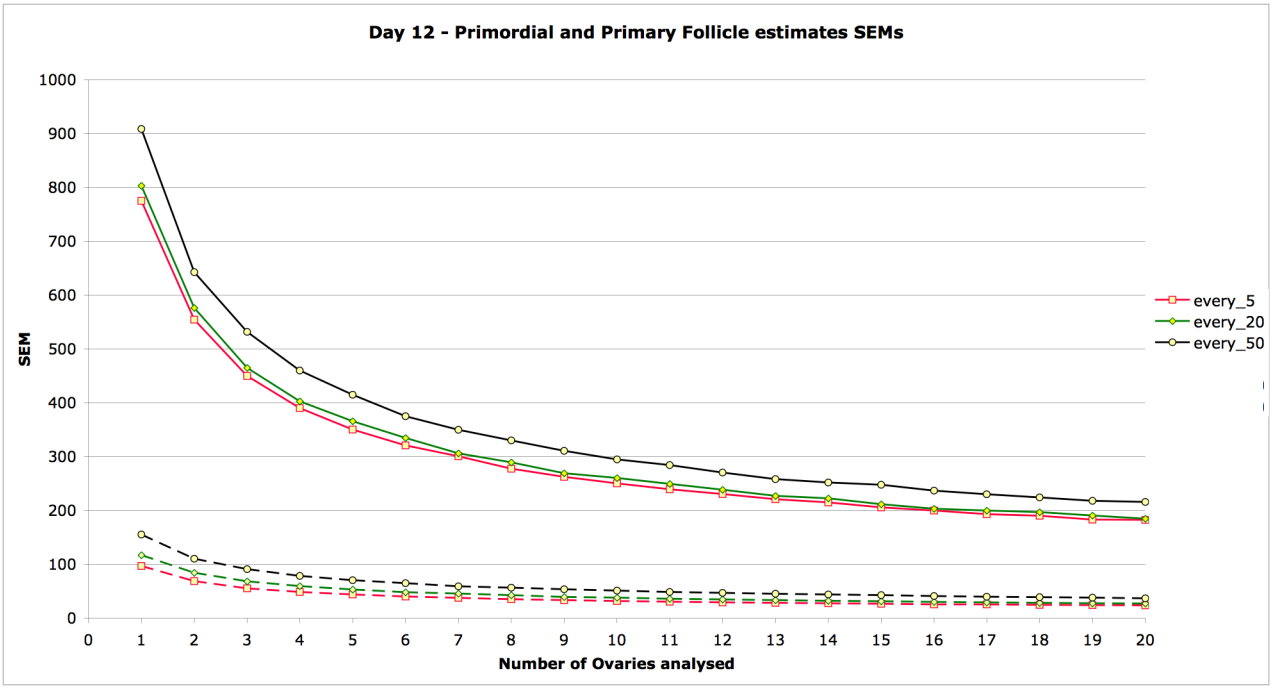


Figure 4.7: *SEM*s of primordial (straight lines) and primary (dashed lines) follicle numbers, for different sample sizes and sampling frequencies, for day 12 ovaries. The distribution means used are: Primordial: **2300**, Primary: **360**. The number of samples picked for every number *N* of ovaries is 10^4, using the bootstrapping method.

Observing the results presented above, the general conclusion is that the sampling frequency plays an important role only for low ovary numbers. Most important is that in order to obtain estimates closer to the actual number of follicles, a large number of ovaries needs to be analysed, rather than analysing few ovaries with higher sampling frequency.

4.3.2 Normal – mutant comparison

We generated an additional 350 simulated mutant ovaries with 50% the number of primordial follicles found in the wildtype ovaries, using the same techniques described earlier. In figure 4.8 the *SEM* of the mutant ovaries is plotted. Only primordial follicle estimates are shown, as primary follicles follow the same trend.

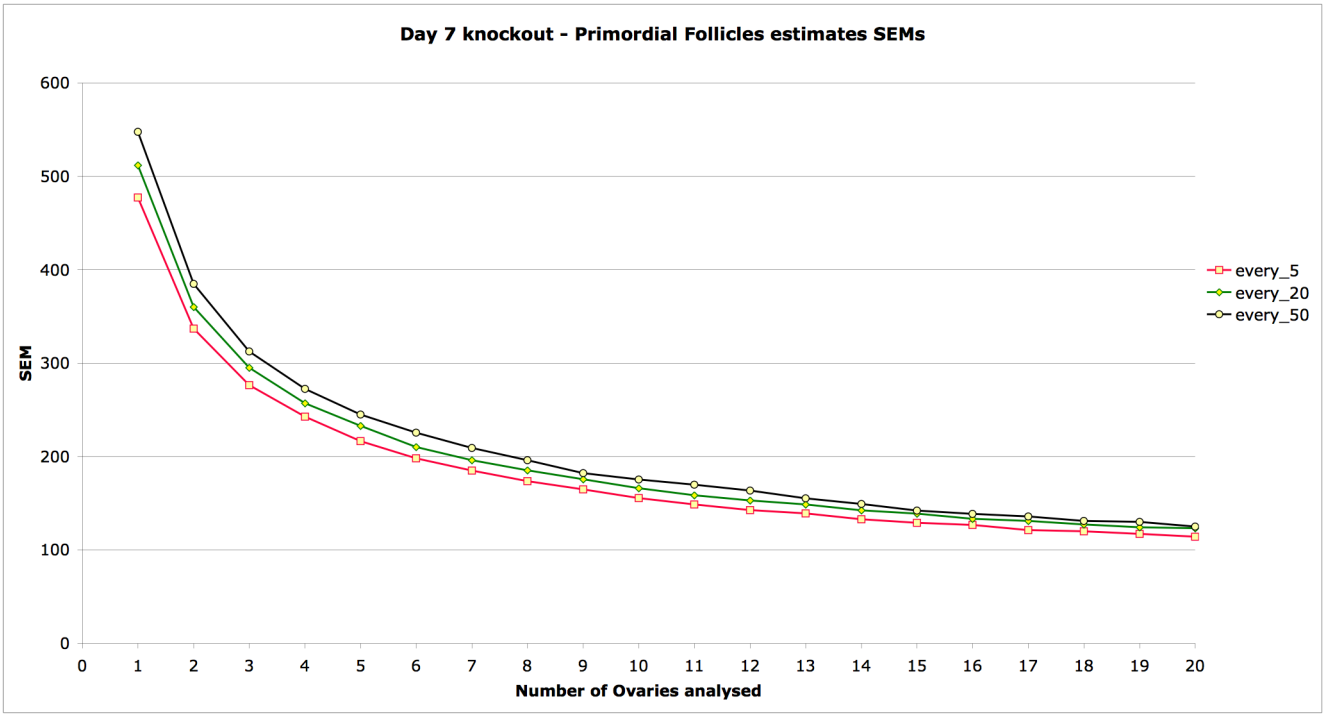


Figure 4.8: *SEM*s of primordial follicle number, for different sample sizes and sampling frequencies, for day 7 knockout ovaries. The distribution means used are: Primordial: **1000**, Primary: **570**. The number of samples picked for every number N of ovaries is 10^4, using the bootstrapping method.

In order to assess the level of statistical significance of distinguishing between the control and knockout distributions, two samples are selected from the two distributions. The unbiased stereological technique and the *t*-student statistical test are performed to compare the two sample means, producing two-tail *p*-values. The question we want to answer with these tests is how often the unbiased stereological technique is going to show the difference in the two distributions. To assess that, we choose a *p*-value threshold. In the case at hand, three representative significance level thresholds have been selected, namely $p = 0.05$, $p = 0.01$ and $p = 0.005$. The bootstrapping method is applied to generate two sets of 1,000 samples each, from the normal and knockout distributions, and the corresponding 1,000 *p*-values are calculated. The proportion of these tests that give a *p*-value lower than the selected threshold is calculated. This proportion is plotted on the following graphs for different sample sizes, N, and different sampling frequencies, f.

Note that for significance testing using student's *t*-test, the degrees of freedom for this test are $2N$-2, where N is the elements (ovaries) in each group. Thus the testing was performed for groups containing from 2 to 20 ovaries.

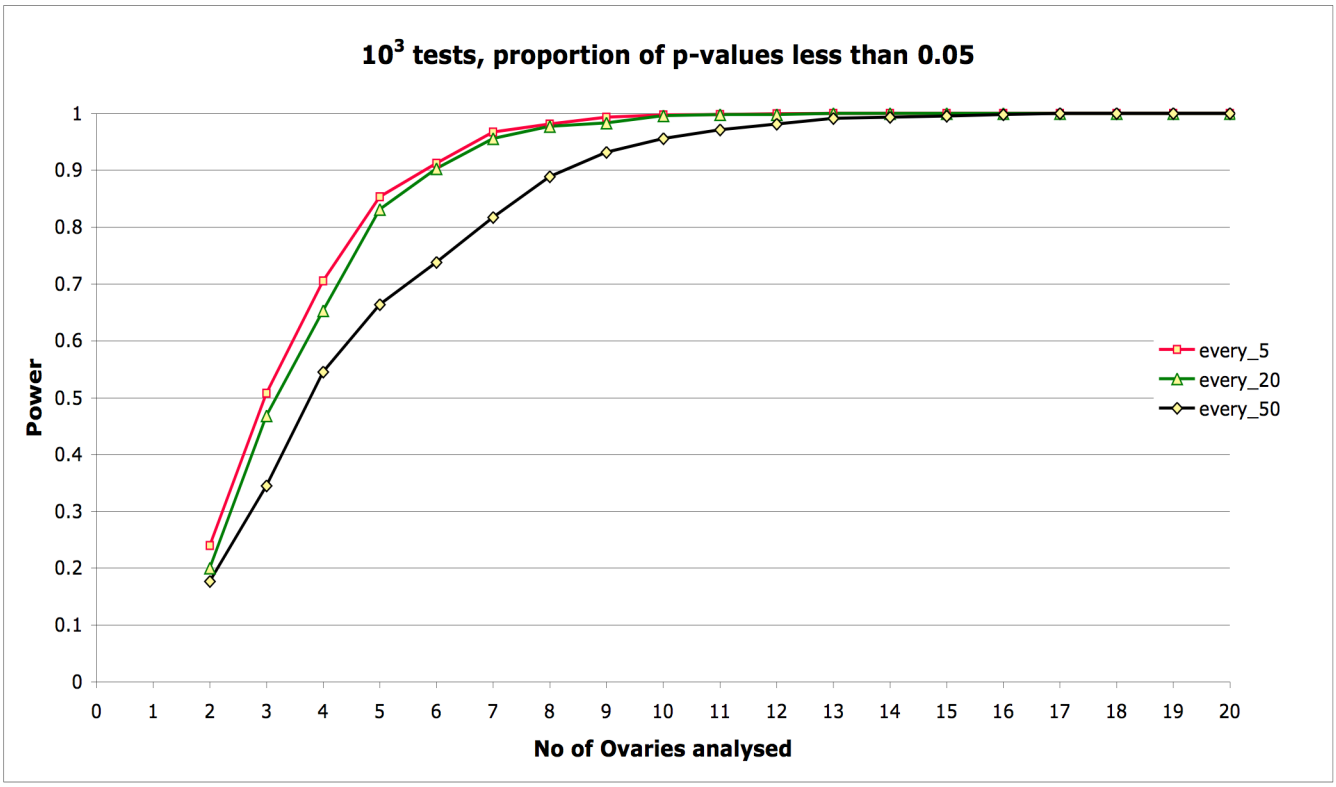


Figure 4.9: Proportion of the 10^3 *t*-student tests with a *p-value* ≤ 0.05.

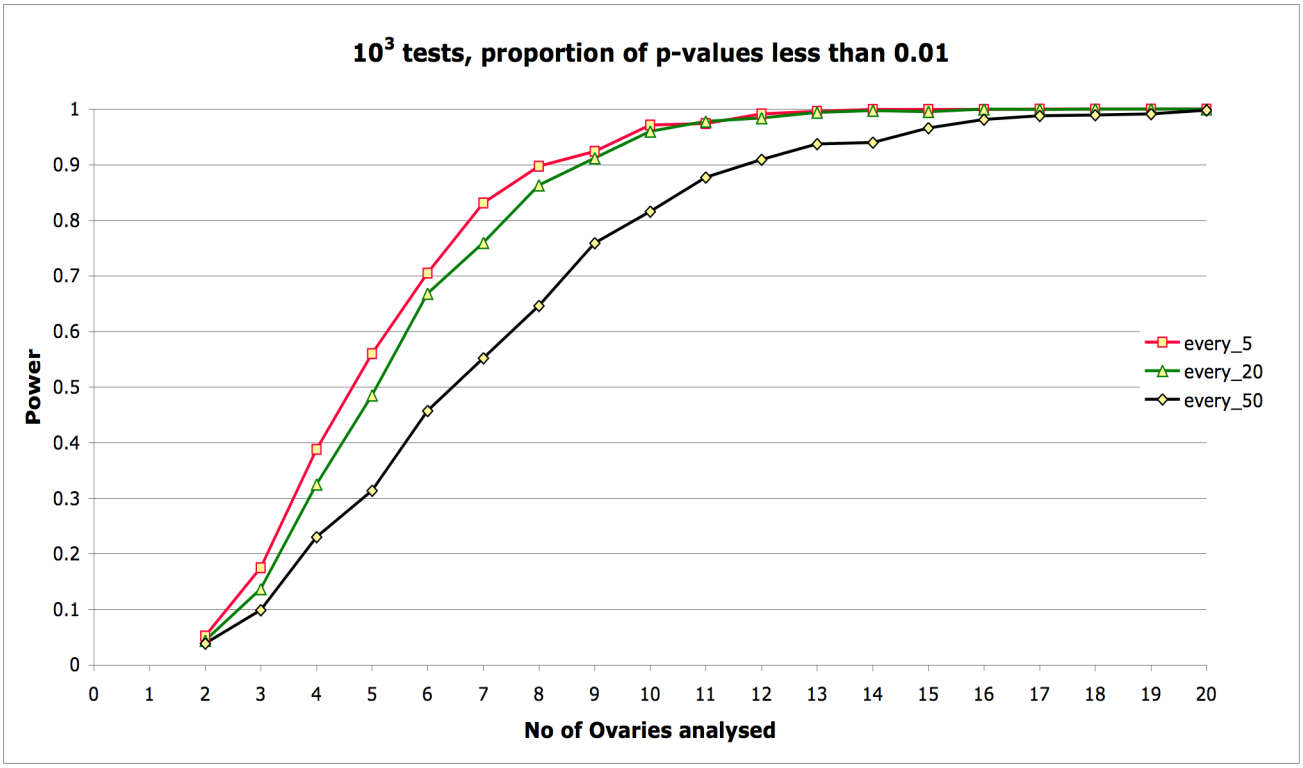


Figure 4.10: Proportion of the 10^3 *t*-student tests with a *p-value* ≤ 0.01.

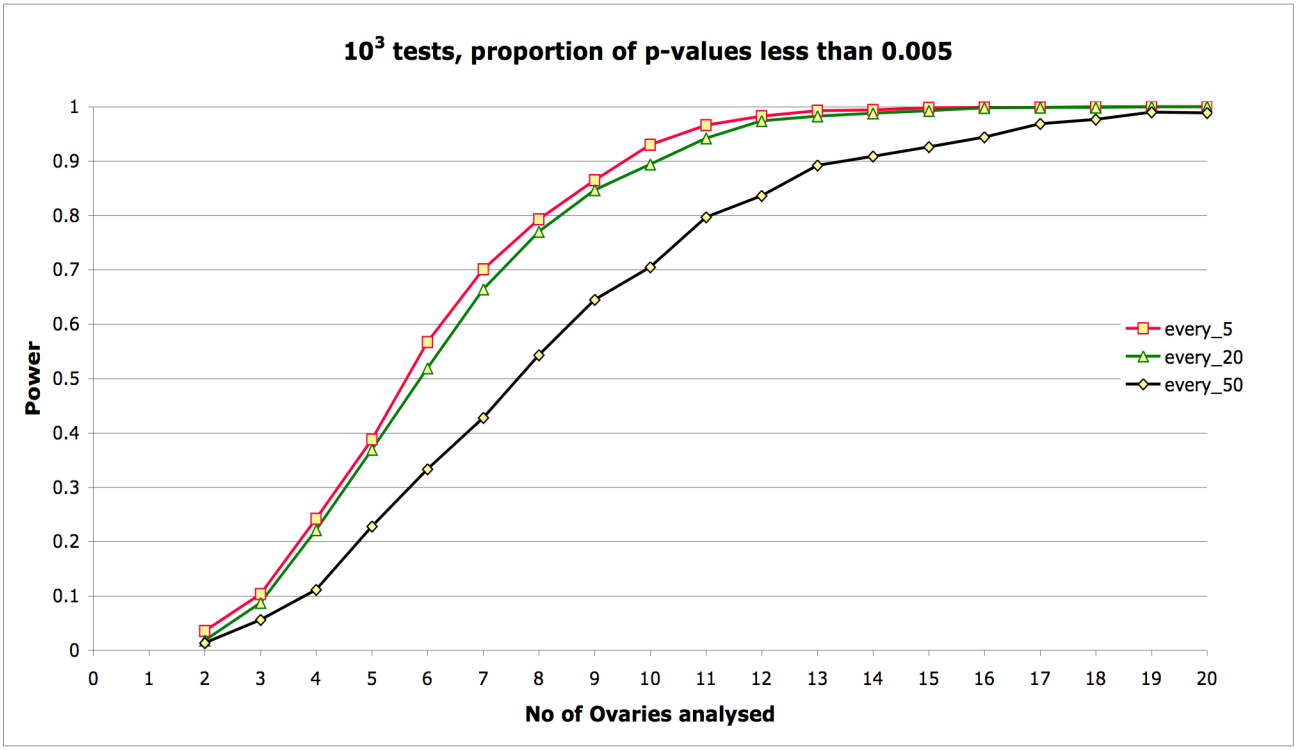


Figure 4.11: Proportion of the 10^3 *t*-student tests with a *p-value* ≤ 0.005.

As expected, using smaller sample sizes (fewer ovaries) produced more often high *p*-values. For example, using a sample of 5 ovaries, has a chance of around 50% of producing a *p*-value higher than 0.01. Using, instead, more than 10 ovaries, provides most of the time (more than 70% at least) *p*-values lower than 0.005. It is also interesting to notice the effect of the sampling frequency. While a 1/50 frequency reduces significantly the occurrence of low *p*-values, the 1/5 and 1/20 appear similar.

4.3.3 Planning experiments to detect differences in follicle number distributions

Based on the results we obtained from comparing the normal with the mutant mice, we created a series of different mutant ovaries, sampling them as explained before and comparing them to the normal mice. The results of the analysis are presented in graphs that illustrate the number of ovaries required in order to detect each of the differences, using various sampling frequencies and different levels of

statistical significance. These can be used as a guide when experiments are planned, in order to use the appropriate number of ovaries.

We computationally generated a total of 10 groups of mutant ovaries, each consisting of 350 ovaries. The distribution means are 400, 600, 1000, 1600, 1800, 2200, 2400, 3000, 3400 and 4000 primordial follicles, with the same standard deviation as the normal. Primary and secondary follicles are not considered in this case. The same procedure as described in 4.3.2 is repeated to obtain the *p*-values for different number of ovaries and sampling frequencies, in *10,000* experiment simulations each time. The proportion of these *10,000* experiments that give a *p*-values which is lower than two thresholds (0.05 and 0.01) is calculated and presented in figures 4.12 and 4.13. The *x* axis represent the percentage difference from the mean of 2000 follicles, which is what we consider as normal number of follicles. The *y* axis represents the proportion of the *10,000* cases where a difference is detected with a certain confidence (*p*-value ≤ 0.05 for 4.12 and *p*-value ≤ 0.01 for 4.13).

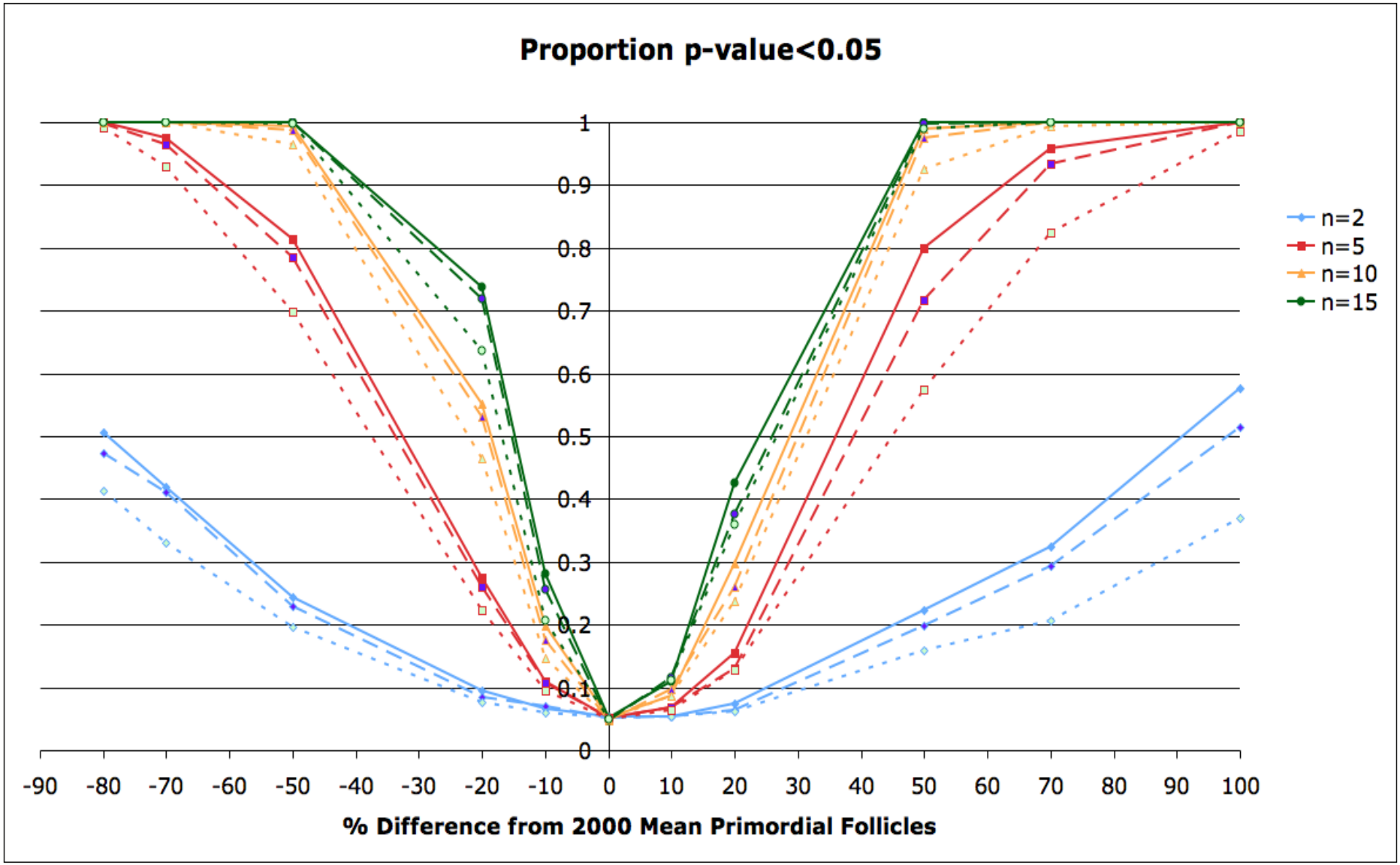


Figure 4.12: Proportion of the 10^4 *t*-tests that detect the difference in each group with significance of 0.05, for various sampling frequencies. Straight lines represent sampling **every 5** sections, dashed lines are **every 20** and dotted lines are **every 50**. This is performed for different groups of ovaries, namely 2, 5, 10 and 15; each group has been assigned a different colour in the graph.

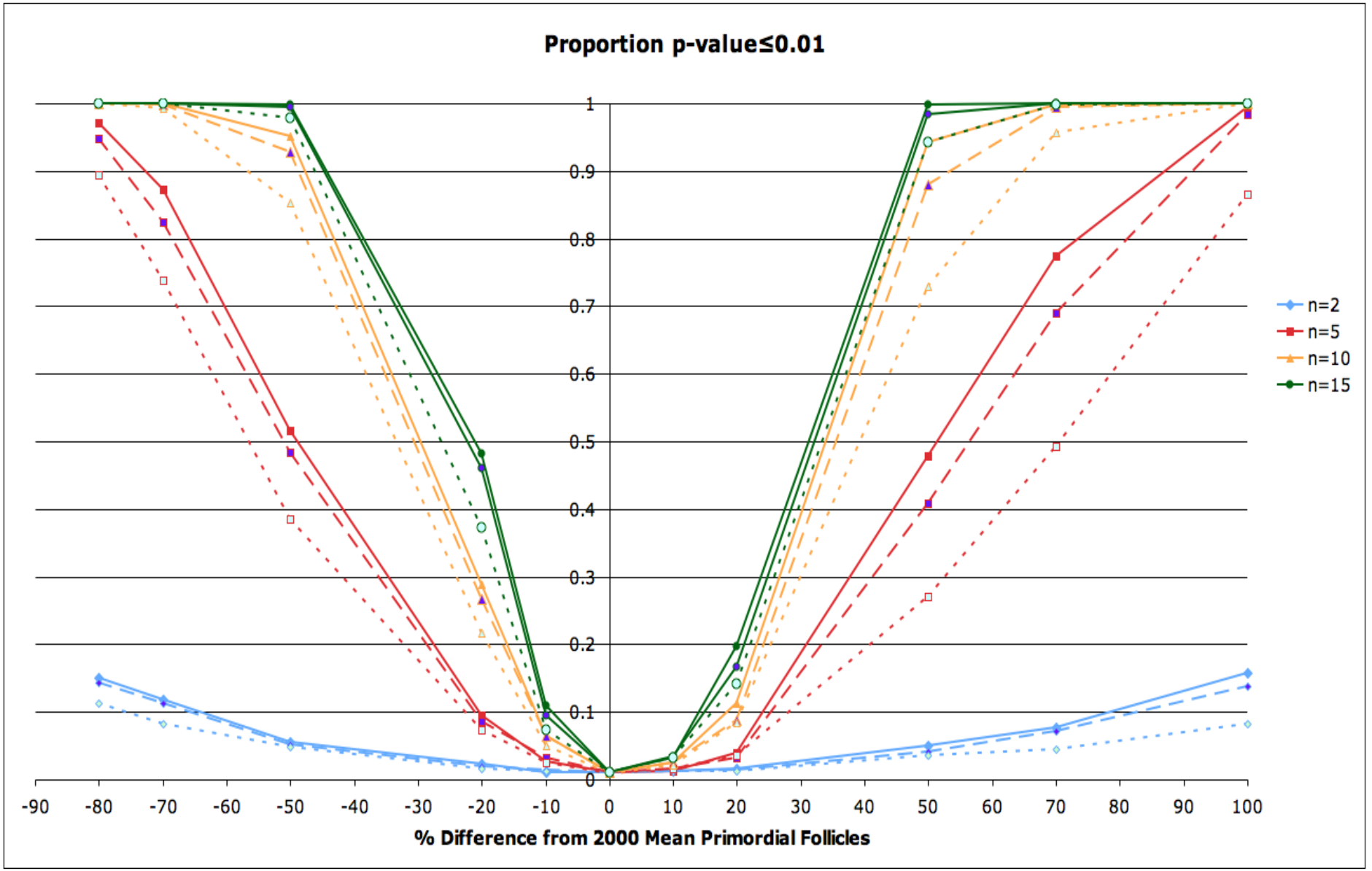


Figure 4.13: Proportion of the 10^4 *t*-tests that detect the difference in each group with significance of 0.01, for various sampling frequencies. Straight lines represent sampling **every 5** sections, dashed lines are **every 20** and dotted lines are **every 50**. This is performed for different groups of ovaries, namely 2, 5, 10 and 15; each group has been assigned a different colour in the graph.

These graphs confirm the conclusion that the more ovaries are available, the bigger the probability is that a difference may be detected, especially in cases where the difference in follicle numbers in a mutant group of mice is subtle. Additionally, the sampling frequency appears to be less important, as previously concluded. In figures 4.12 and 4.13 we can see that a more accurate estimate is obtained using 5 ovaries and sampling every 50 sections than using 2 ovaries and sampling every 5. This conclusion is very important and should be taken into consideration when doing real experiments.

Considering an example where mutant mice were produced, which have the PTEN gene deleted causing activation of the entire primordial follicle pool (see Introduction, 1.5), an experimentalist may want to assess the number of primordial follicles in the ovary at a certain age, in comparison to a same strain control mouse. For simplicity, we assume that the ovaries from all animals have a 500μm diameter. Sectioning these at a thickness of 5μm would produce 100 histological sections. Counting with a frequency of every 5 would require sampling a maximum of 20 sections, counting every 20 would require 5 sections and counting every 50 would require 2 sections. Using the graphs 4.12 and 4.13, the experimentalist can realize that in order to detect for example a 50% or greater difference with high statistical confidence, at least 10 ovaries, per treatment, from each animal are required. Sampling 10 ovaries every 50 sections (a total of 20 sections!) has higher likelihood of detecting this difference than using 5 ovaries and sampling every 5 (a total of 100 sections). The graphs show in addition that using only two ovaries, regardless of the accuracy of the sampling, the probability of detecting even extreme differences is reduced. In the case where 10 ovaries do not show difference between the two animals, the experimentalist can either conduct additional experiments using more ovaries, or conclude that at the particular age, the mutation does not have a profound effect on the number of follicles at the particular age.

Generally, by examining these graphs, one can see that when a difference of around 50% in the follicle number of two mice groups (case and control) is expected, 10 or more ovaries are required from each group, so that the difference can be seen with confidence. The sampling frequency can be moderated to reduce workload and increase efficiency. Generally, the more subtle the difference, the more ovaries are

required to detect it. Of course there are factors that may affect the result in different experiments, such as varying standard deviation of the distributions because of different mice strains or divergent effects of the experiment on the mouse. Nevertheless the two graphs presented in figures 4.12 and 4.13 can be used as a guide to plan counting experiments so that the resulting conclusions are robust.

4.4 Discussion

The determination of accurate estimates of the mean follicle number in mammalian ovaries is crucial for the progress in the field of reproductive biology, but it is still a challenging task (Charleston *et al*, 2007). The accuracy in estimating follicle numbers is affected by two factors: the biological variation within a given species, and the counting technique used (Myers *et al*, 2004). The present work quantified the effects of these two factors, using computer-generated ovaries, created from real experimental data in order to reproduce a realistic biological variation. These ovaries were *in silico* sectioned and had their follicles counted for different counting frequencies using the unbiased stereological technique combining the disector and fractionator.

We have presented in detail how the error of estimating the mean follicle number decreases by increasing the number of ovaries and increasing the counting frequency (figures 4.5 and 4.6). The use of these curves allows for better experiment planning. For instance, while on one hand a higher number of ovaries may be required to reduce the error to a given threshold, on the other hand this allows reducing the number of sections analysed, which may result in a less labour-intensive experiment. As an example, if an accuracy of 10% is required, 10 ovaries must be used (figure 4.5), but the sampling frequency can be reduced to 1 section out of 20 and even less.

In the second type of *in silico* experiment we assessed how the number of ovaries and counting frequency affect the level of significance of telling apart two different follicle number distributions, for example in normal and mutant mouse. Similarly to the previous case, the curves we produced aim at assisting in better planning those experiments used to compare two sets of ovaries (figures 4.8, 4.9 and 4.10). For example, if two types of mice with a 50% difference in follicle number are considered, using 10 ovaries from each animal and counting every 5 sections would

provide a 95% possibility of producing a *p*-value = 0.005 or less. The same results can be achieved if the investigator chooses to use 15 ovaries and count every 50 sections. The difference in the two options lies in the total number of sections counted in each case. Assume that the average ovary diameter is 600μm with an average of 2000 follicles, and that each section's thickness is 5μm. Each ovary would be sectioned in around 120 sections. Thus in the first case (10 ovaries and every 5 sections) the experimentalist would count approximately 240 sections in total, or around 4000 follicles, while in the second case (15 ovaries and every 50 sections) would count approximately 36 sections in total, or 600 follicles!

On the other hand, in a hypothetical experiment where the differences between the distributions are unknown and have to be determined, our results can help work out the differences (figures 4.11, 4.12). The experimentalist wants to have a threshold *p*-value that occurs with a 95% probability. At first, 10 ovaries can be used for counting, as this would detect differences of around 50% or more with a very high probability. If the desired significance level is not achieved, then more ovaries have to be utilized, suggesting also that the difference in the two distributions is less than 50%, as this is the threshold set in the study that is being conducted. Generally, the results of this study can provide guidance in cases like the one described, as they provide the best-case scenario on the errors that can be reported in an experiment, in optimal conditions.

A very important factor that affects the overall precision of the counting in this case is the human factor. Follicles can be miscounted, or even over-counted, as the ovarian sections contain structures other than follicles, so for example, a blood vessel in a cross section could be mistaken for a follicle; or a follicle can be missed when mixed with other ovarian components.

In practical terms, our results show that the use of simulated ovaries can be used to help the experimentalist to plan and optimize experiments. When smaller sampling frequencies are used (e.g. every 20), then more sections can be available for further experimentation, staining them for immunohistochemical markers, or preparing them for *in situ* hybridization, in order to examine other aspects of their pathological state. This by extension means that more animals are spared from sacrificing, as best use is made of the mice required to produce statistically acceptable results.

One of the caveats of the requirement for a large number of ovaries is it challenging to produce them, as mice need to be bred, which can be expensive and time-consuming, so that a few homozygote null mice can be produced. Furthermore, if the mutation affects fertility or the health of the mouse, as well as the follicle numbers, it may not be possible to produce sufficient ovaries. In this case, the sampling frequency can be increased, although according to our results, it may not be possible to achieve statistically robust results when comparing with the control, unless more ovaries become available. This particularly applies to experiments performed using human ovaries, which are extremely rare and hard to obtain (e.g. the data set in Hansen *et al*, 2008). Therefore careful experimentation planning and best use of tissue, as described previously, is of pivotal importance to ensure that follicle number is estimated with high precision and that there is spare tissue to conduct other types of experiments.

There are numerous hypotheses in the ovarian biology field, which in order to be confirmed, require high precision in estimation of ovarian follicle number. The general conclusion of this study is that to strengthen the answer to any hypotheses as such, the most crucial step is to gather a sufficient pool of ovaries to be sampled, in order to effectively tackle the problem of species biological diversity. We proved that in this case the number of sections that need to be sampled can be significantly reduced, often resulting in less laborious experiments. This can sometimes require large datasets, but it is the only way forward for any accurate scientifically equitable research.

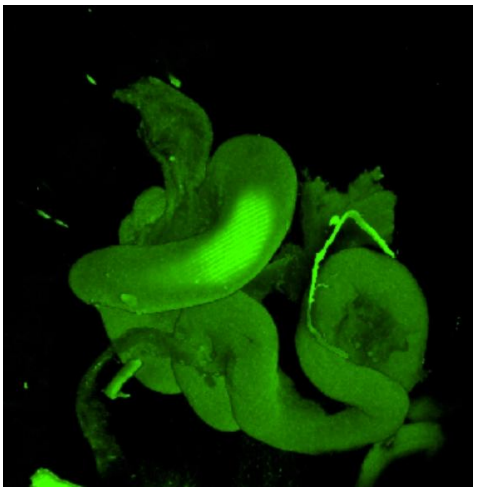
Conclusions

In summary, a robust technique has been presented in this chapter, which modeled the number and distribution of follicle number in the ovaries of an animal of specific age and strain, using computer-generated ovaries. This model can be applied for ovaries of any animal, provided that follicle numbers and spatial distributions (i.e. sets of follicle coordinates and distances to the ovarian surface) are available; these can be experimentally obtained. Modelling can help the experimentalist to be more efficient when counting follicles, both in terms of use of tissue and laboratory time.

The need for larger datasets opens a whole new door in the studying of ovarian biology. Although our model shows that sampling using much lower sampling frequencies can provide accurate estimates of follicle numbers, this task still requires a significant amount of time which is consumed for tissue fixation, sectioning, staining and registration (for the disector). New methods should therefore be explored that can reduce the required time for counting follicles, without compromising the quality of the results obtained. Such a technique is presented in the following chapter, demonstrating the fact that many of the old-fashioned ways (e.g. serial sectioning and counting, performed since the beginning of the study of ovarian ageing) need to be modernized to increase their efficiency.

Chapter 5

Imaging of whole tissue: New methods for 3D-morphology investigation and rapid follicle number estimation



5.1 Introduction

When studying the anatomy of a biological component or organ, the three-dimensional structure is invaluable in understanding tissue development and functionality. There is an increasing appreciation that single isolated tissue sections, or even monolayer cultured cells, very rarely provide accurate information regarding the structure and spatial localization of key components within the tissue (Sharpe, 2003). Conversely, technologies used to perform whole organ imaging do not as yet provide the resolution required for cell-level analyses (Alanentalo *et al,* 2008). However, obtaining the full three-dimensional (3D) complexity of a structure of interest helps us to comprehend its functionality, its relationship with nearby structures and also its developmental progress.

Until recent years, the only technique available for mapping the 3D structure of an organ required the construction of actual physical models of them. This way the model's structure could be studied by the naked eye, or using stereo microscopes if it

was too small. The model construction principles are still used in Scanning Electron Microscopy (SEM) (Alberts *et al*, 2008). Briefly, this method involves coating the sample with substances (conductive material in case of SEM such as gold, platinum, chromium etc), which mould to the shape of the organ and remain solid, while the actual tissue is dissolved using chemicals (Alberts *et al*, 2008). The anatomy of the tissue can then be examined. Obviously, this technique only reveals information about the shape of the sample, or if the sample is cut, it may also reveal some skeletal properties (Mackay *et al,* 1992). It cannot be used to visualize the entire internal volume, and cannot be combined with staining of any kind.

Visualization of the specimen three-dimensional structure, both internal and external, is made possible through the advancing of computer graphics technology, and more specifically by the development of algorithms for volume reconstruction and surface rendering (Sharpe, 2003). These shapes can be rotated, zoomed and manipulated in general, producing astonishing results without the need to build physical models. Data for such reconstructions can come from a variety of sources, which include technologies like X-ray Computed Tomography (CT scan) and Magnetic Resonance Imaging (MRI) (for biological applications reviewed in Kherlopian *et al*, 2008). Both these technologies are non-invasive, in the sense that the specimen doesn't need to be sacrificed or dissected, in contrast to sets of photographic images of thin serial specimen sections, which can also be reconstructed into a volume. These sets of section images, when used to reconstruct the specimen, produce 3D volume rendering with very fine detail and resolution (Sharpe, 2004). The approach however is extremely labour and time intensive (especially if the samples are prepared for electron microscopy). The section samples need to be prepared and stained all together to avoid any experimental deviations, before being photographed. The digital images obtained must then be registered, i.e. each section must have the same orientation as the previous and the next, and must be at the same position on the image. Therefore the ease and speed of non-destructive imaging technologies is desirable when designing an experiment, provided that the resolution is adequate.

X-ray CT scanning and MRI, while both being excellent techniques for imaging completely opaque specimens, as they are routinely used in hospitals for diagnostic purposes, have drawbacks, the most important of which being that they require expensive equipment and poor imaging resolution at cell level (Kherlopian *et*

al, 2008). In addition, these techniques cannot be used to image the distribution of histological staining; therefore for biological experimentation, optical microscopy techniques are most suitable (Sharpe, 2003). Currently, there are three ways of obtaining three-dimensional information from a sample, using visible light microscopy without serially sectioning the specimen, a process that requires a significant amount of laboratory work. All three methods are based on *epi-fluorescence* imaging (section 1.11).

Maintaining the original 3D architecture of the sample by avoiding the sectioning procedure is presented with several advantages, the most important being the removal of the time-demanding paraffin or resin mounting of the tissue. Additionally, destruction of microstructures or tissue slight deformation due to temperature (in the case of paraffin embedding) is avoided, as well as the occasional freeze fracture of ultrastructural particles when frozen sections are used. These contribute towards obtaining a clearer and more accurate image of the tissue morphology and function.

The usefulness of the 3D volume versus the 2D section can be best illustrated in the case of brain neurons. It is virtually impossible to track the neuron transects in even adjacent sections, not only due to their small size, but also due to the branched projections of these cells (dendrite part of the neuron) (Howard and Reed, 1998). Similarly, in the case of the ovary, though it may be possible to follow follicle transects in adjacent sections, the numerous smaller follicles render such a task extremely laborious and error-prone. The 3D distribution of structures is very important when local signaling is studied. As depicted in figure 5.1, when a single ovarian section is used to assess follicle spatial patterns, an incomplete depiction of the local neighbourhood is obtained. Namely image 5.1*b* shows that there are only two primordial follicles (red circles 2 and 5) in close proximity to follicle 4, which is also primordial, whereas by examining image 5.1*a*, one can see that there are at least 5 additional primordial follicles in close proximity underneath the section (solid red spheres in 5.1*a*, yellow arrows), as well as more in the missing part above the section.

The same principle applies for studies on cell monolayers in culture; intercellular signaling is confined in 2D, resulting in different signaling patterns than the ones that would be present if the original 3D cell architecture was maintained. Of course, this does not imply that such cultures are problematic, but that need to be

adapted if paracrine-autocrine cell signaling is studied. In conclusion, obtaining and visualizing the full 3D structure of the sample is presented with numerous advantages over the classic approaches of sectioning and studying the 2D sections, such as better understanding tissue morphology, eliminating the need for section registration and is crucial for investigating spatial patterns and signaling of structures of interest.

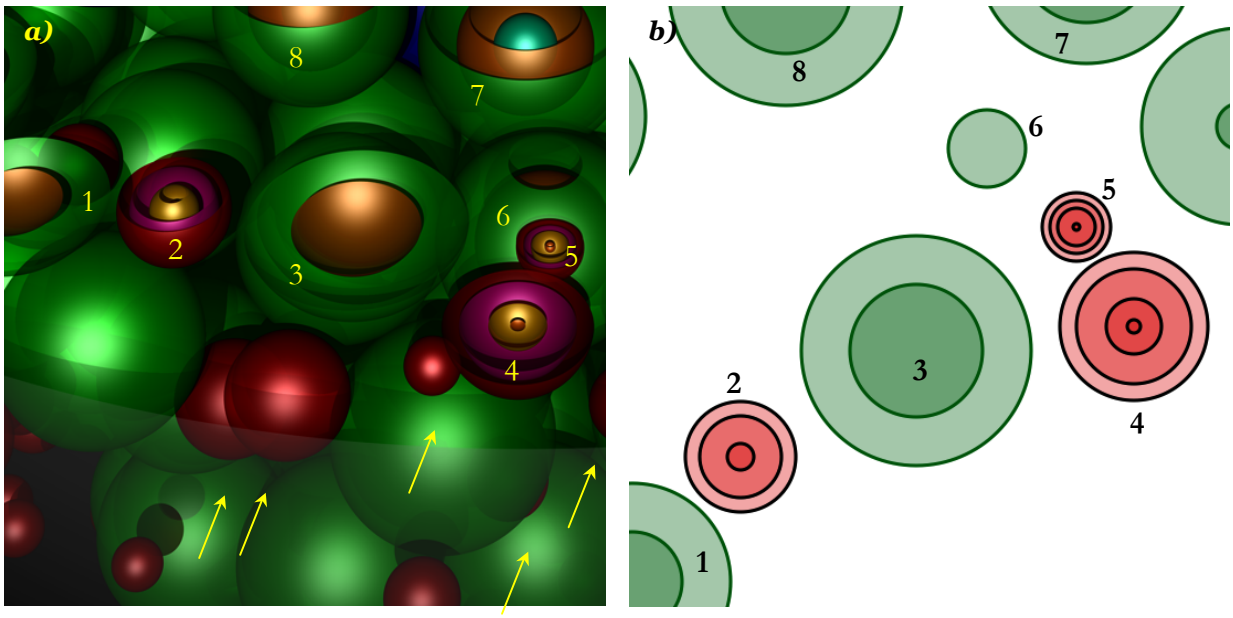


Figure 5.1: ***a)*** Part of a Simulated Ovary, cut in half with the top part removed in order to show the distribution of the follicles in three dimensions. ***b)*** Follicle transects that appear in two dimensions in a single section, corresponding to the part depicted in ***a)***. Numbers correspond to sectioned follicles, and are the same in both images. The follicles above and below (appearing in ***a)*** as solid spheres) the sectioned follicles are completely invisible to the investigator, when examining 2D sections. Red spheres are primordial follicles; green spheres are primary follicles Yellow arrows point at primordial follicles that are in close proximity to follicle 4, but are not visible in the 2D section ***b)***. Images were computationally generated, and follicle positions are the same in both images; visual dissimilarity is due to the added perspective in image ***a)*** to create the depth effect.

5.1.1 Aims

Our interest is to gain insight in the physiology of the juvenile mouse ovary, to investigate three-dimensional follicle spatial distributions, effectively extending the work presented in chapters 2 and 3 in three dimensions, and to quantify objects of interest (follicles). A chemical clearing and imaging protocol has been compiled, in order to achieve optical slicing through the whole volume of the juvenile mouse ovary, without any physical sectioning, using laser scanning confocal microscopy or

optical projection tomography. Obtaining the three dimensional arrangement of the follicles in the ovary can help quantify their numbers, and study their three-dimensional distribution. Our specific aims of this work are as follows:

1. To gain insight into the 3D morphology and arrangement of the follicles in the juvenile mouse ovary, in fine detail.
2. To compare the morphology obtained from the confocal microscope and the one from the newly developed optical projection tomography (OPT) system.
3. To extend *XY* spatial analysis performed in 2D on ovarian sections to *XYZ*. This will provide with a more accurate analysis of interfollicular signaling.
4. To use the resulting optical planes to develop a fast method for follicle number quantification.

To achieve our aims, 3D morphology was obtained using both single photon and multi-photon confocal microscopy as well as OPT. Visualization was performed on tissues using:

- Autofluorescence
- Draq 5™ nuclear stain
- Immunohistochemistry for Mouse Vasa Homologue (expressed specifically in the oocytes of small follicles)

The procedures were performed in a variety of juvenile mouse tissue, in order to optimize the methods; a few characteristic examples will be presented in the results section, along with the caveats and challenges of the technique. Before this, a short description of the experimental procedures will be presented in the following section.

5.2 Materials and the proposed experimental approach

Imaging through thick tissue samples (typically ≥ 30μm thick) requires the use of Laser Scanning Confocal Microscopy in order to obtain very thin optical sections, which are typically less than 2μm thick (Zucker *et al*, 2000). Conventional microscopy fails to image thick slabs, thus, as explained in section 5.1, deconvolution techniques are used to retrieve clear images. However, normal single photon light microscopy allows for less than 50μm imaging into the z direction, as light scattering

both from the light source (visible laser) and from the signal (fluorescent emission) is extreme, resulting in very weak image reconstruction. The most popular ways of reducing optical radiation scattering within the sample is to use either multi-photon confocal microscopy (Masters, 2006), or tissue chemical clearing (Zucker and Jeffay, 2006), or both. Multi-photon microscopy utilizes mode-locked pulse lasers emitting infrared photons in ultrashort pulses (typically one pulse every 10^{-15} seconds) that penetrate deeper into the sample volume (section 1.11.3). Chemical clearing of the sample is performed by submerging the tissue in a clearing solution for a short period, such as Murray's clearing agent (Zucker, 2006), to ensure rectilinear photon propagation. Both techniques were tested, as well as a combination of both, and the best results in our case were obtained using single photon confocal microscopy and tissue chemical clearing.

For the project at hand, an appropriate marker that distinctively stains each follicle (and especially those of early developmental stage) needs to be selected so that accurate follicle recognition in the mouse ovary can be achieved. Such a marker was recently identified by Noce's group (Toyooka *et al*, 2000); the mouse vasa homologue (MVH) protein, an ATP-dependant helicase encoded by the *vasa* gene, was found to be specifically localized in the cytoplasm of oocytes of primordial follicles. Its expression was found to decrease as the follicle progresses through the developmental stages, but is clearly detectable up to primary plus stage (Toyooka *et al*, 2000). The antibody we used that targets MVH was kindly offered to our lab by this group. It should be noted at this point that since this staining was used merely for follicle detection purposes, and not for quantifying the expression of MVH in oocytes, no negative controls were produces, as this would be a waste of tissue.

The chemical and imaging procedures performed to obtain optical slices of whole ovaries are described in detail in chapter 9, sections 9.12 – 9.15. The methods were described specifically for the ovary, but exactly the same technique is followed for any other piece of tissue. Mice were collected and sacrificed as described in section 9.12, and had their ovaries (or other tissue, such as oviduct) removed and fine dissected. Ovaries were fixed and then immediately processed for immuno-histochemical staining, as described in 9.13. This process takes 3 days to complete, albeit it can be performed simultaneously for many pieces of tissue (with up to 10 ovaries in parallel) in well plates. When autofluorescence is used for visualization

(Introduction, 1.11.1 & in chapter 9, 9.15), the processing time is significantly reduced, as tissue can be mounted on the agarose block immediately after fixation. Stained tissue was then mounted on a block of agarose, which was then cleared in BABB overnight (section 9.14). Cleared tissue in the agarose block was then placed in a slide chamber and imaging was performed on an inverted confocal microscope (described in section 9.15). Resulting optical planes were then computationally reconstructed to a 3D volume render (or "volume reconstruction") using computer software Volocity (Improvision Volocity) (9.15).

5.3 Results

5.3.1 Optical slices, volume renderings, clarity of technique

Confocal laser scanning microscopy was employed to obtain images through the entire tissue volume, comparable to histological sections. In order to achieve imaging in an adequate depth without compromising clarity due to light attenuation inside the tissue, specimens were chemically cleared using a mixture of Benzyl Alcohol and Benzyl Benzoate 1:2. We first used a variety of unwanted tissue from mice sacrificed for other experiments in our group to test the imaging clarity and depth after mounting the tissue in an agarose block and clearing it. As a first step, no staining was performed on the tissue, instead natural fluorescence was used to visualize structures (sections 1.11.1 & 9.15 – autofluorescence). In figure 5.2 we present three optical slices of a juvenile mouse oviduct, in various depths, and a volume render performed using Improvision Volocity (9.15); the final two images shown are details from images 5.2*b* and 5.2*c* respectively. The full list of optical slices, as well as an animated volume rendering of the tissue is presented in supplementary material.

Using the x10 magnification objective, we were able to image through approximately 70μm of tissue without loss of signal. Structural details of the oviduct, such as the different types of cell layers forming the oviduct can be distinguished, as depicted in images 5.2*e* and 5.2*f* of figure 5.2. Image 5.2*e* was digitally zoomed from images 5.2*b*, and false colouring (or pseudo-colour) was employed to better visualize the various areas of the oviduct. Comparing image 5.2*e* to the high-detail image 5.2*f*, the individual groups of cells can be discriminated, despite the lack of fine structures.

Pseudo-colouring is an accepted method for enhancing the contrast of biological structures; however, the contrast and sharpness of the image offered by the current magnification is not enough for cell-level analyses, as opposed to the contrast offered by sections, which can be imaged using high numerical aperture lenses and higher magnifications.

If more detail is required when doing whole mount imaging, the x20 objective can be used, in combination with the zooming function of the confocal microscope, until the desired magnification is achieved. It is not possible to use any oil immersion objective or a dry objective of greater magnification, as these do not have the working distance to image in adequate depth. If the experimentalist decides that still more magnification is required, then the conventional method of sectioning needs to be employed, so that it can be imaged with high magnification oil immersion objectives (e.g image 5.2*f*). Using the 3D reconstruction one can examine the entire tissue volume. Supplementary material reports animations showing an even more complete visualization of the whole tissue, reconstructed from the optical section.

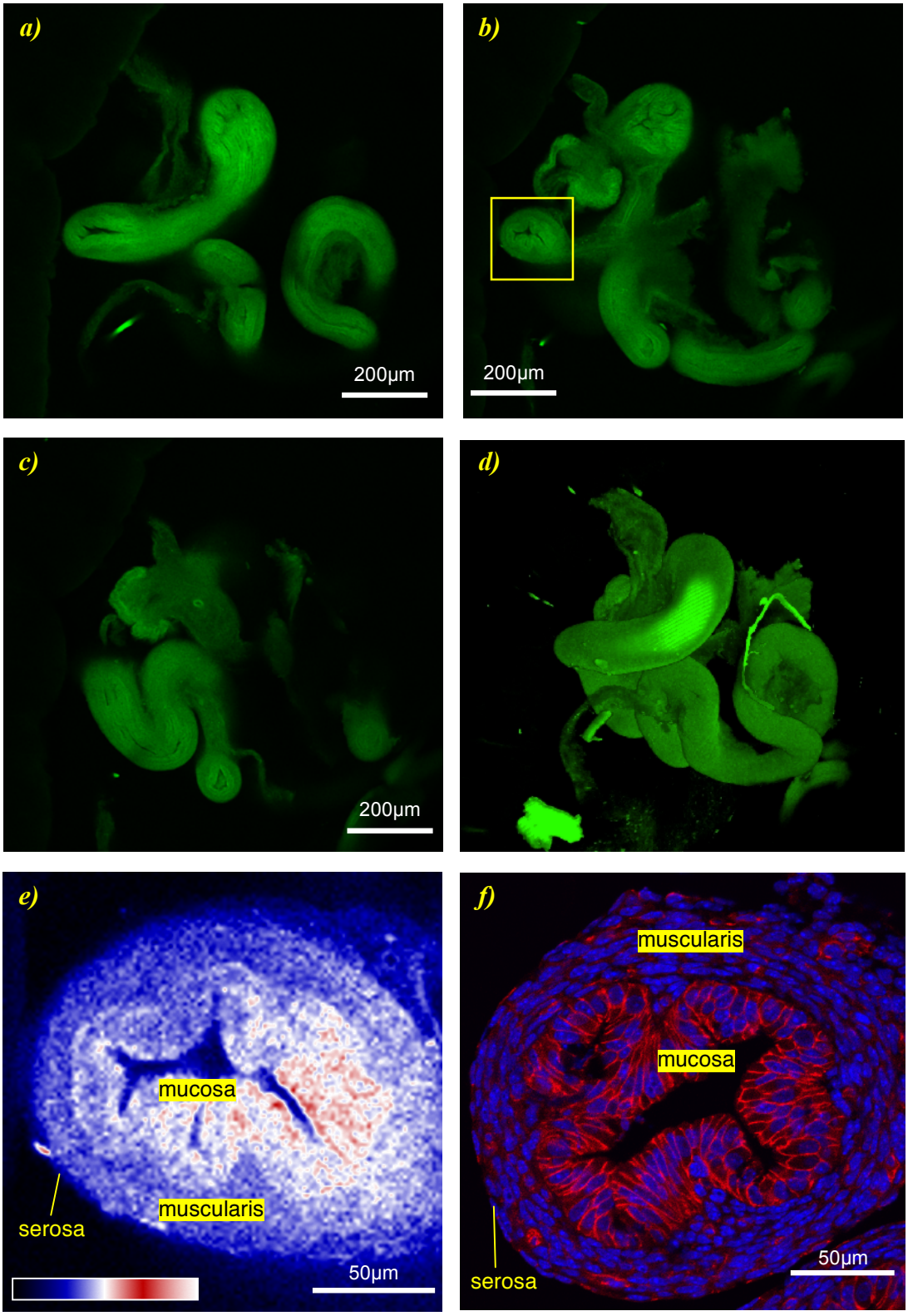


Figure 5.2: Three optical slices of a juvenile mouse oviduct ***a)-c)*** and a reconstructed volume render ***d)***. Image ***e)*** is a detail marked by a square in images ***b)***; image ***f)*** is oviduct from juvenile mouse on a section, imaged with a high numerical aperture objective, depicting very fine cell detail (blue cells – DAPI stained) and structural detail (red ß-catenin, cell adhesion), added for comparison. Image ***e)*** has been pseudo-coloured, so that the various groups of cells (the serosa, muscularis and mucosa) are more distinguishable. The areas match closely those appearing on the stained image ***f)***. Whole tissue was fixed, mounted on agarose block, cleared and imaged. No stain was added; images were obtained using autofluorescence. Exciatation laser is 488nm, autofluorescence emission is in the range of 495nm-550nm. Complete set of images and animations in supplementary material. Figure continues to next page

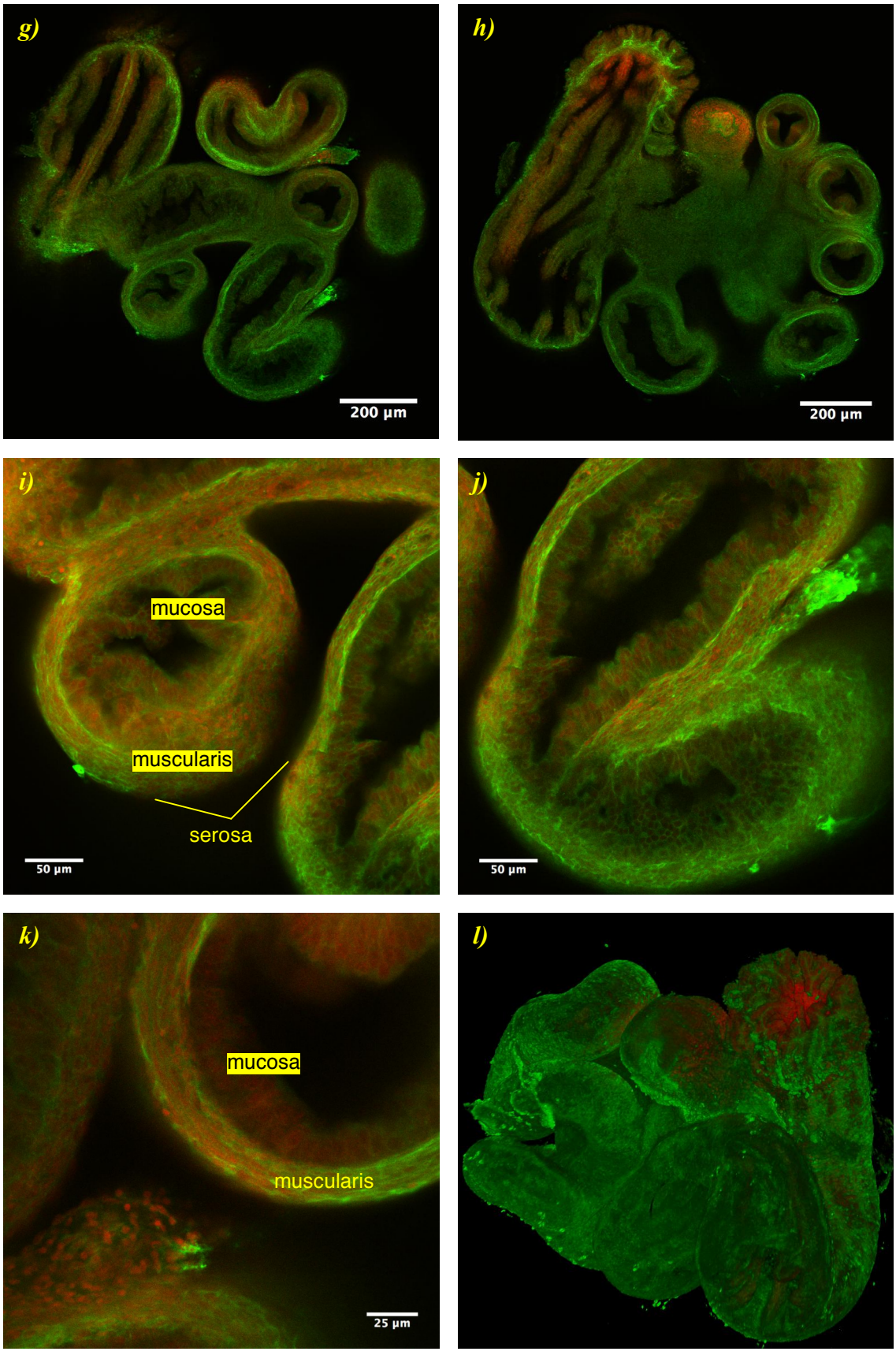


Figure 5.2 \ cont'd: Optical slices (***g-k***) and volume reconstruction (***l***) of a whole oviduct that has been stained with the nuclear stain DRAQ 5™ (red cells). Green channel is autofluorescence. Images ***g)*** and ***h)*** show a good structural morphology; images ***i) – k)*** were obtained using higher magnification and numerical aperture objectives (not the ususal x10), resulting in greater detail as individual cells are more clearly visible, but due to their limited working distance cannot capture images beyond a certain depth in the volume. Structures appear slightly blurred due to light scattering in the tissue volume, as opposed to image 5.2*f*, which from a physical section. Some of the cell groups of the oviduct are added to images ***i)*** and ***k)***.

As a next step, we examined large pieces of kidney and gut from the juvenile mouse, using the same technique. Three optical slices of juvenile mouse gut and kidney are presented in figures 5.3 and 5.4 respectively, as well as their volume renderings. Both are unstained, visualized using autofluorescence. The complete sets of optical sections, volume renderings and animations can be found in supplementary material.

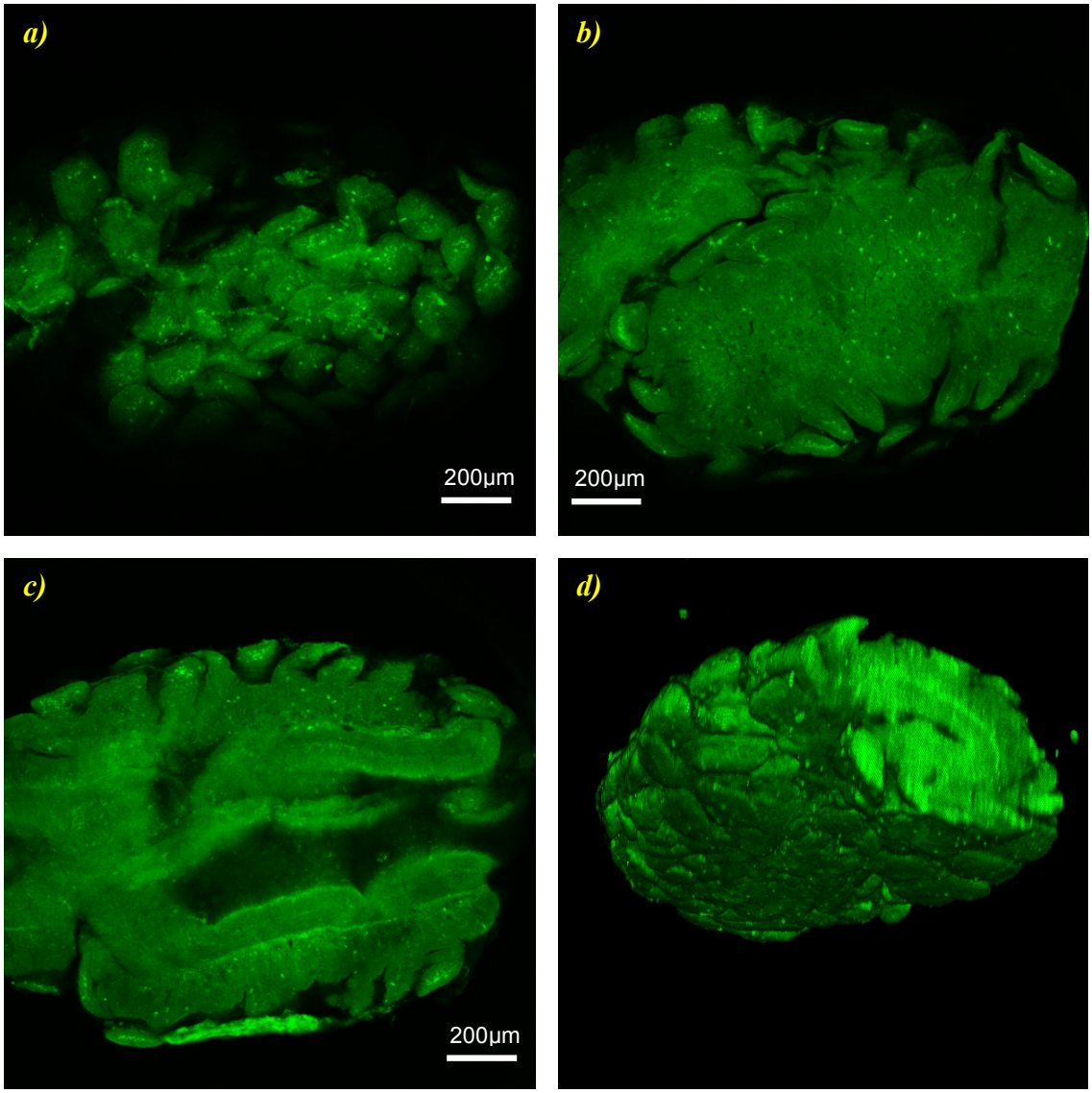


Figure 5.3: Three optical slices of a juvenile mouse gut slab ***a)-c)*** and a reconstructed volume render ***d)***. Images are unstained; images obtained using tissue natural fluorescence (1.11.1 & 9.15). Complete set of images and animations in supplementary material.

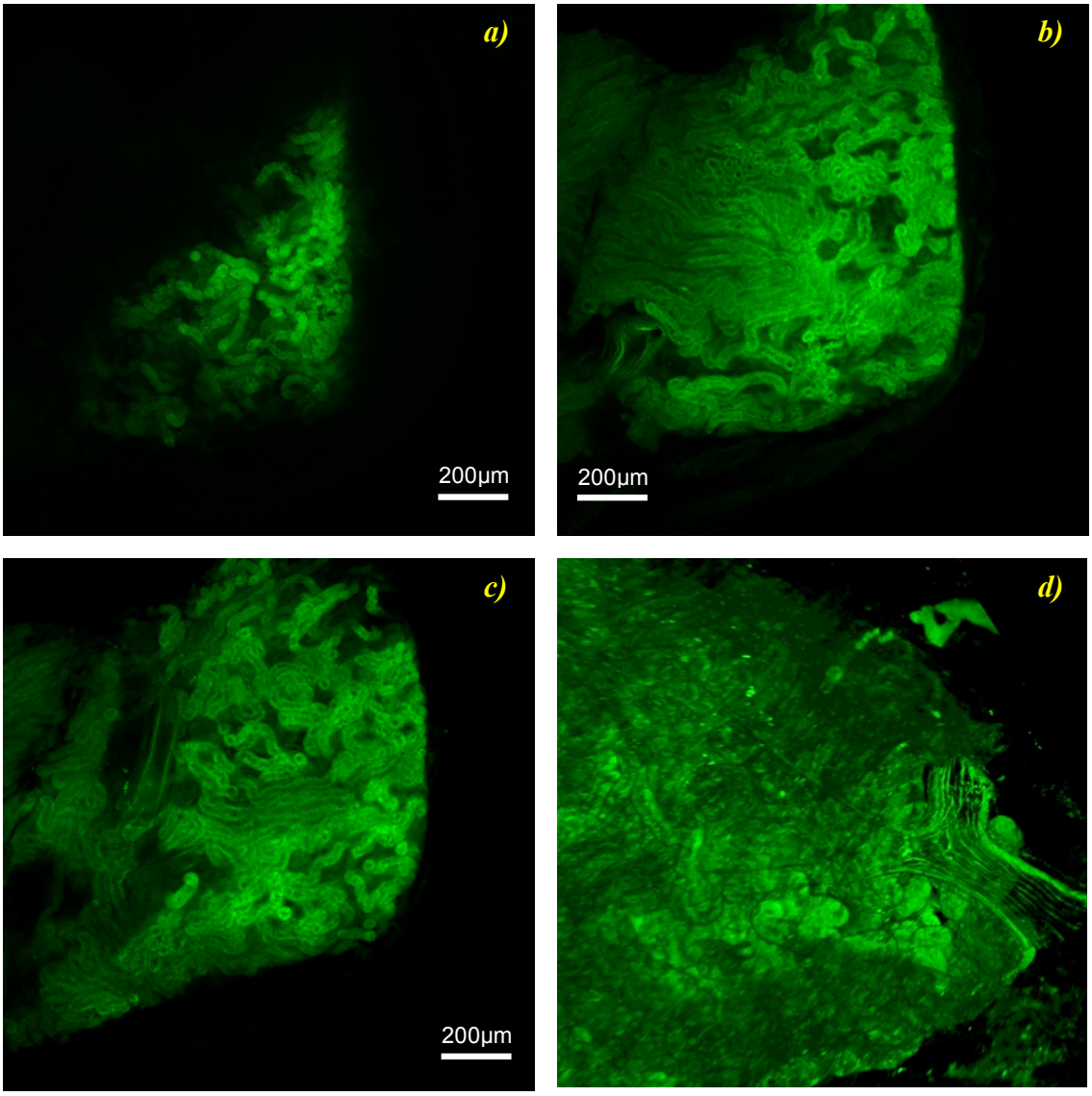


Figure 5.4: Three optical slices of a juvenile mouse kidney ***a)-c)*** and a reconstructed volume render ***d)***. Images are unstained; images obtained using tissue natural fluorescence. Complete set of images and animations in supplementary material.

These samples were imaged deeper, up to 450µm for gut and 500µm for the kidney. Using the chemical clearing method, light penetrates the tissue deep enough to cover the entire slabs or organs of the juvenile mouse that we trialed. There was only a slight attenuation of the fluorescent signal when imaging the final optical slices of the kidney. However, images are clear enough so that structures can be visible.

Using these samples we were able to optimize the imaging and staining techniques, before applying it to ovarian tissue. The maximum depth that was reached with the x10 objective is 500µm (figure 5.4), which is adequate for imaging the entire

juvenile ovary. The ovaries were examined at first using autofluorescence, but the follicles that are the structures of interest in our project are poorly distinguishable from the background. As a first attempt to rectify the poor resolution, the ovary was stained using a nuclear dye, DRAQ 5™ (Biostatus ltd). Although there are reports in the literature that this dye is inappropriate for staining and imaging big tissue volumes (e.g. Miller *et al,* 2005), we did not encounter such problems. The benefit of using this dye compared to other common nuclear dyes such as DAPI or Hoescht (both can be obtained from Invitrogen) is that it does not photobleach, i.e. fluorescence intensity is not attenuated over laser excitation for prolonged periods. Furthermore, this dye is excited in the red area of the spectrum, emitting in the far red (dye is excited using a 633 laser, collecting emission in the range of 650nm-750nm), meaning there is space for additional fluorescent stains without emission overlapping. In addition, the red laser light, as well as the emitted light (longer wavelenght), is less likely to scatter inside the tissue compared to the UV or blue light necessary for other dyes, hence increasing the maximum imaging depth. Optical planes from the stained tissue are reported in figure 5.5. The imaging depth is approximately 360µm.

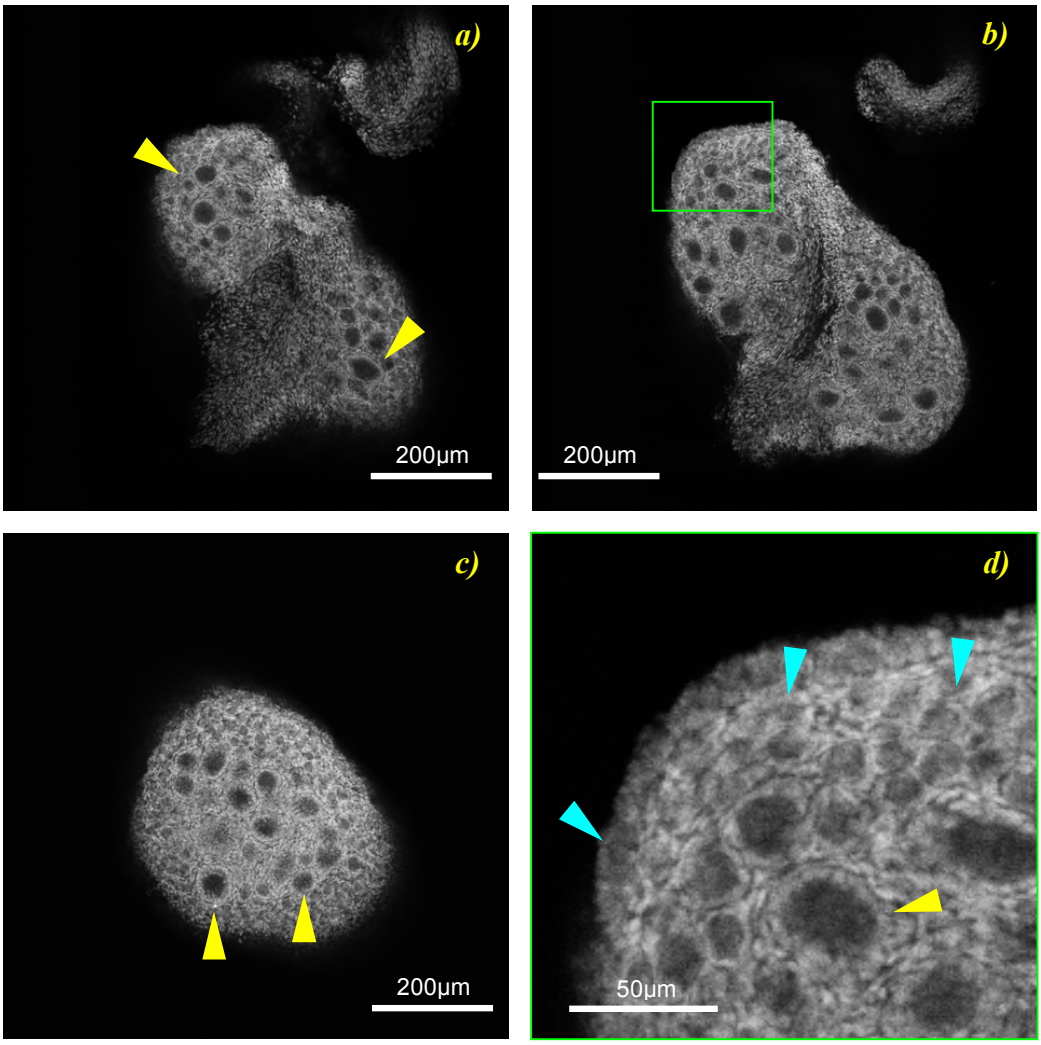


Figure 5.5: Optical planes ***a)-c)*** through the entire volume of a day 12 mouse ovary. Image ***d)*** presents a magnified part of image ***b)***, marked by the green square. Ovary is stained with the nuclear stain DRAQ 5™. Mature follicles are visible (yellow arrows), but smaller follicles are very difficult to recognize (cyan arrows), as every cell nucleus is stained.

Images obtained from the ovaries stained with DRAQ 5™ are sufficiently clear, but small follicles are not easy to recognize using nuclear stains only. The magnification is adequate to see follicles from the primary stage onwards (yellow arrows), when the oocyte is sufficiently large to create a black area on the optical section. Primordial and transitional follicles (cyan arrows on image 5.5*d*) are very difficult to distinguish, as the oocyte is very small (~ 20μm) and their stained nucleus is difficult to be discriminated among the stained granulosa cells. To rectify these problems and be able to visualize the follicles clearly, whole mount immunohistochemistry was performed on the ovaries to stain for the Mouse Vasa

Homologue (MVH) protein† (Toyooka *et al*, 2000, Pepling and Spradling, 2001), which is localized in the cytoplasm of oocytes of small healthy follicles (figure 5.6).

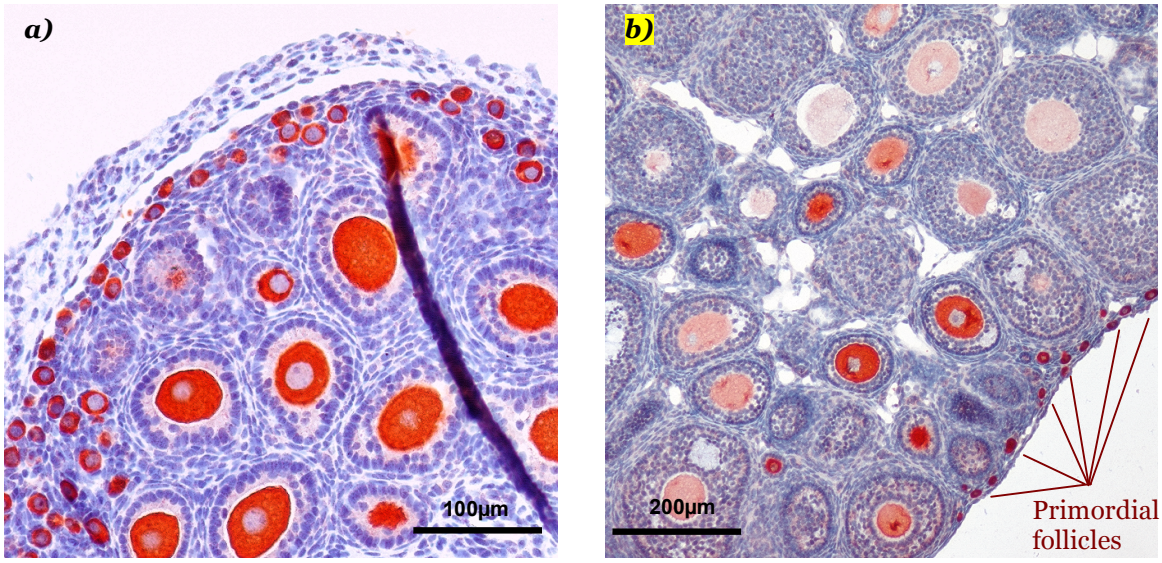


Figure 5.6: Part of ***a)*** day 12 and ***b)*** day 42 mouse ovarian section. They are immunohistochemically stained for MVH, localized in the oocytes (bright red dye), and counterstained for haematoxylin (blue cell nuclei). MVH is localized in the cytoplasm of oocytes of up to early secondary stage, which are abundant at day 12 (***a***). After this stage, MVH production is downregulated (Toyooka *et al*, 2000). Follicles with weaker stain in image ***b)*** are late preantral. Images were kindly provided by Dr Mark Fenwick.

When MVH immunostaining is applied to the whole ovary, without any counterstaining, the only visible structures are the oocytes, appearing as circles around a dark area (unstained nucleus); granulosa cells are not visible. Imaging is performed as described in 9.15, using a x10.0 objective and 1.2 zoom factor, so that every optical section is visible on all focal planes. The imaging depth for this ovary is 468 μm, and there was no loss of image clarity. Results of the imaging appear in figure 5.7; all optical planes are available at the supplementary materials. Follicle oocytes are visible as round rings, which can be observed in detail on image 5.7*e*. The small rings, brightly stained, are primordial follicles, or early transitional, where the oocyte has not started growing yet. Clusters of resting follicles are visible in all four images (*a-d*) in figure 5.7, marked by cyan arrowheads.

† We would like to acknowledge at this point Dr T Noce of the Mitsubishi Kagaku Institute of Life Sciences, Tokyo, Japan, for providing us with the MVH antibody.

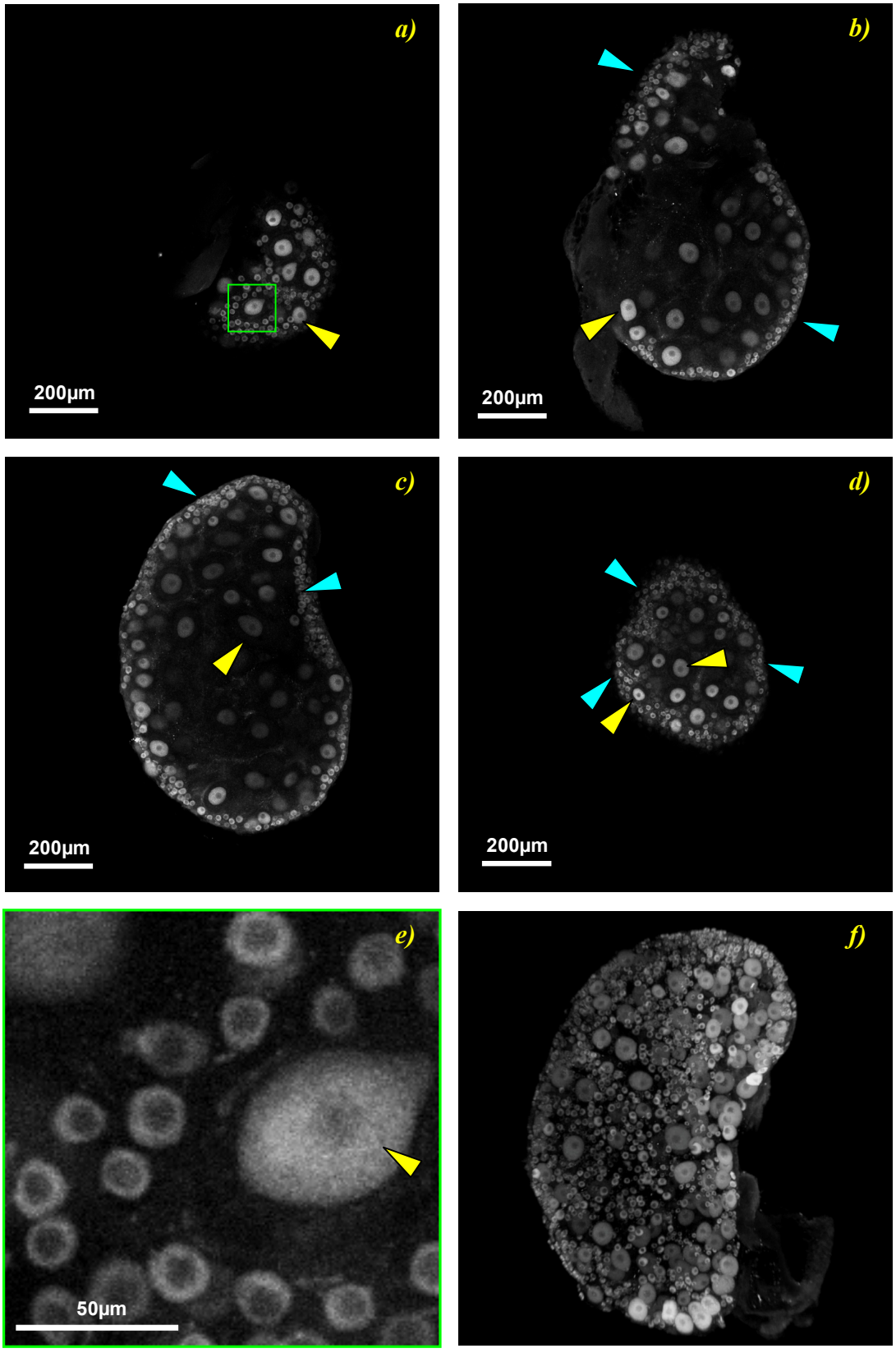


Figure 5.7: ***a)*** **–** ***d)*** Optical slices in various depths through an unsectioned day 12 juvenile mouse ovary, immunofluorescently stained for MVH (localized in the oocyte cytoplasm of the follicles). Oocytes appear as white rings with an unstained nucleus in the middle. ***e)*** Detail of image ***a)*** (square), showing a cluster of resting follicles and one growing follicle. The developmental stage of the follicle can be assessed by the size of the oocyte; cyan arrows in images point at clusters of resting follicles; yellow arrows point at growing follicles. Image ***f)*** shows a volume rendering, made using Volocity software. All planes and animations of the 3D volume of the ovary are available in supplementary material.

Growing follicles have noticeably larger oocytes, and are occasionally less bright. They are marked on the images of figure 5.7 with yellow arrowheads. There are cases when follicles are very faint, like the one marked with a yellow arrowhead on image ***c)*** of figure 5.7. This is not due to poor antibody penetration in the tissue, rather it happens because the follicle is at an advanced stage of maturity, usually greater than secondary, therefore the oocyte MVH production ceases slowly, resulting in weaker staining (Toyooka *et al*, 2000; see also figure 5.6*b*).

Results obtained using our proposed technique are very promising; oocyte staining appears very clearly in all optical sections and the imaging depth is sufficient to cover the whole ovary. Up to date, there is no published work in the literature that includes imaging of the whole mouse ovary. In the particular experiment, images are captured at a resolution of 2048x2048, which is the double along each dimension of what we used for the images presented in the previous chapters, capturing structures with increased detail. However, this quadruples the image size, making processing more computationally demanding. The additional information conveyed by the extra details visualized in the high resolution is not useful for our experiment, therefore in the remainder of this chapter images will be reverted to the original resolution.

5.3.2 Limitations of the technique

At this point, some issues need to be highlighted regarding the quality and properties of the optical planes obtained by our proposed imaging approach. One of the drawbacks when doing whole mount immunohistochemistry is non-specific antibody binding, which generates weak background fluorescence. This is shown in figure 5.8*a* and in more detail in figure 5.8*c*, where one can notice a dark gray dust-like formation of the background fluorescence around and inside the ovary. Setting to zero all the pixels within the image that have a grayscale value of below a specific threshold can mitigate this problem. The grayscale intensity of a pixel can range between 0 (black) and 255 (white) in the 8-bit images we acquire, namely 2^8 gray levels. If a pixel belongs to an oocyte, it will be brighter, so its value will be close to 255. If a pixel belongs to the background, it should have a lower value. By setting to 0 all the pixels that have a grayscale value up to 20 the dark gray background can be

reduced. Figure 5.8*b* reports the new image after thresholding, while figure 5.8*d* reports further details, where the background reduction can be observed more clearly. The objects of interest, i.e. the stained oocytes, are not affected by thresholding the image background, which merely enhanced the contrast of their boundaries. The thresholding is performed on the Leica Application Suite that is included with the Leica SP5 inverted microscope.

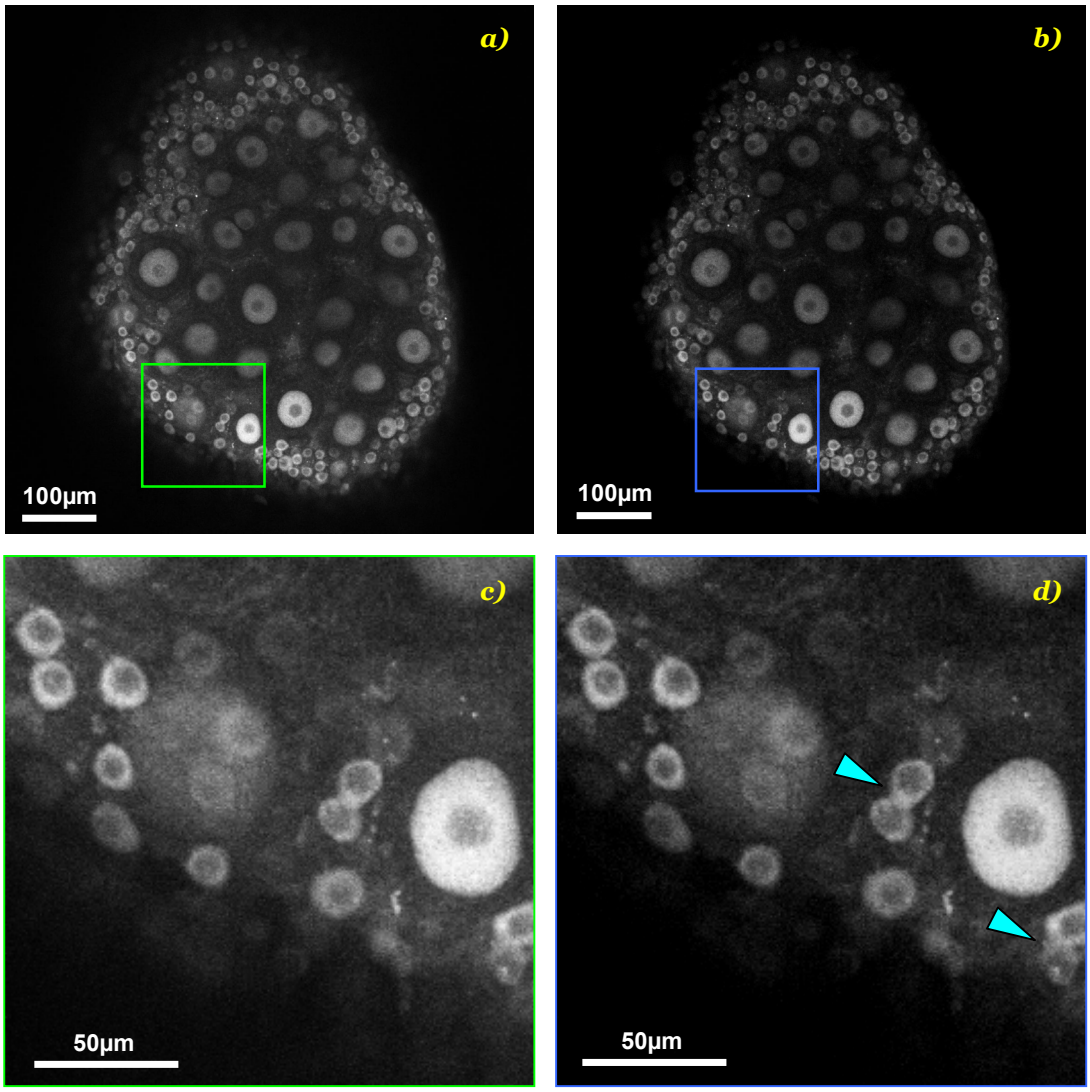


Figure 5.8: Optical planes from the day 12 ovary presented in figure 5.12. Image ***a)*** is the optical plane obtained at 420µm inside the ovary, and a detail of this appears in image ***c)***. Images ***b)*** and ***d)*** are created after thresholding of the image on the Leica Application Suite software, using a factor of 20. Cyan arrowheads show two sites where two primordial follicles overlap, a problem that is common in our optical planes.

Due to the imaging technique used, individual optical planes show an overlap of small follicles (cyan arrowheads in figure 5.8*d*), even after the thresholding. This is because the focal plane is not infinitely thin, but instead it has a specific thickness; excitation happens in a volume around the focal point of the laser inside the specimen, distributed above and below the optical plane. A way to reduce this problem would be to decrease the pinhole radius from 1AU (airy units) to 0.5AU, which is the apparatus minimum. It must be stressed that there is a tradeoff between the amount of light collected and the thickness of the optical section. Despite the pinhole reduction, the problem is not rectified, as overlapping still occurs, even at the minimum setting of the pinhole. This problem occurs also in the images reported in the following sections.

5.3.3 Comparison with Optical Projection Tomography images

Our images obtained using single photon laser scanning confocal microscopy were compared with images produced using an optical projection tomography system (section 1.8.2 – OPT). Tomography imaging was performed in the optics and photonics laboratory of Professor Paul French, at the Physics Department of Imperial College London, by Dr James McGinty. The system they developed was successfully used to image whole mouse embryos, using fluorescence lifetime imaging (Sharpe, 2004, McGinty *et al,* 2008). Given that optical projection tomography is a very promising technique for imaging big tissue volumes, the goal of this part of the project was to assess its performance on the juvenile mouse ovaries.

Ovaries used were immuno-stained for MVH. The tissue processing and clearing was done in the same way as described in section 5.2.1, but instead of mounting the sample on an agarose block, it was positioned at the central axis of an agarose cylinder. The imaging was then done by placing the sample on a rotating apparatus, submerged in BABB (see section 1.11.3, figure 1.16), and obtaining 400 images at different rotation angles (further reading: Sharpe, 2004, McGinty *et al*, 2008) The final results, after reconstruction from the rotation planes, are shown in figure 5.9.

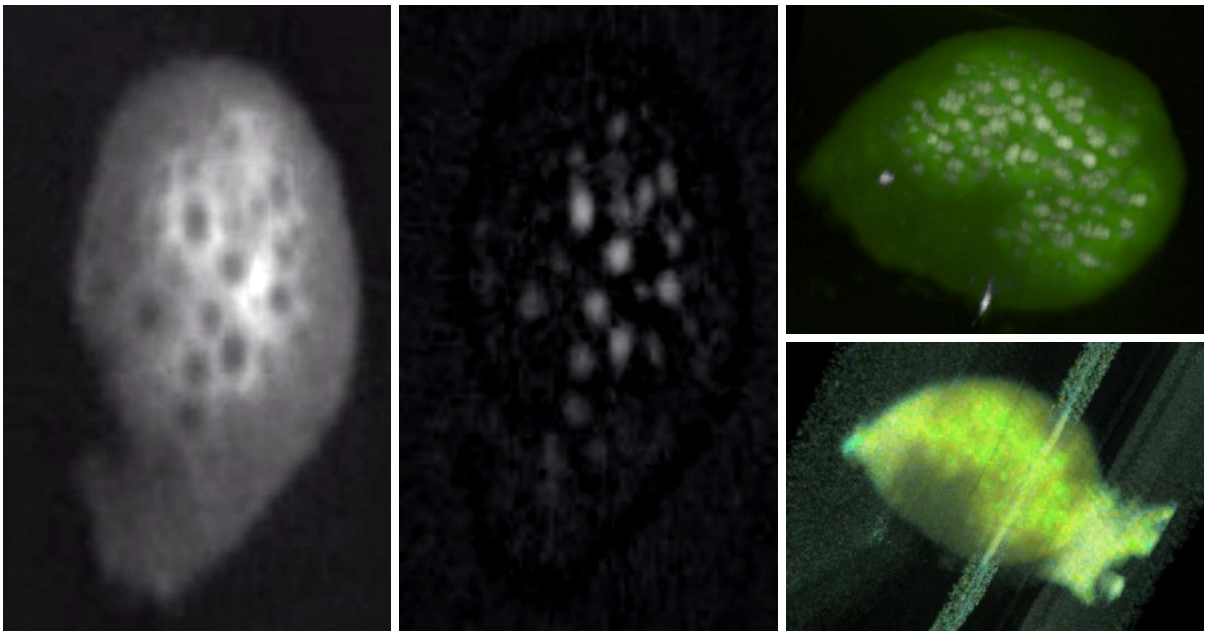


Figure 5.9: Results from imaging a whole day 8 mouse ovary, stained for MVH, using optical projection tomography. The first two images are reconstructed planes of autofluorescence and MVH channel, respectively (at around 4x magnification). The final two images are the volume reconstructions of the ovary, using fluorescence intensity and fluorescent lifetime (FLIM) (McGinty *et al,* 2008).

The images acquired from the optical projection tomography are not very informative for our project, as their resolution is not adequate for visualizing small follicles. This is because the objective lens used for imaging is a x4, as a working distance of a few centimeters is required for the experimental apparatus. There is no possibility of using much higher magnification objectives in order to achieve higher resolution, unless the experimental design is modified in the future. For example, the x10 previously used, which may have given better results, has a maximum working distance of only 1.1cm, and would not be appropriate to use with the experimental setup described here. Given the poor resolution of the images, we concluded the tomography imaging technique is not suitable to visualize the whole mouse ovary. OPT may be useful for large follicle counting in adult mouse, using appropriate immuno-histochemical markers such as GDF-9 (expressed in oocytes of larger follicles, see Introduction, section 1.5), or with ovaries from larger domestic species, whose size would not permit performing our proposed 3D imaging approach.

5.3.4 Trials using two-photon laser scanning confocal microscopy

All the results presented in this chapter were obtained by single-photon laser scanning confocal microscopy, i.e. confocal microscopy using conventional lasers operating in continuous wave mode, emitting light continuously (Masters, 2006). Multi-photon laser scanning microscopy, where pulsed infrared lasers are utilized (as described in section 1.11.3), is a very promising technique for imaging through deep sample volumes (Masters, 2006), therefore could prove extremely helpful in our case, should necessity arise to image much bigger ovaries, such as those of adult mice. In addition, the fact that fluorescence excitation is only happening exactly at the focal plane could possibly rectify the problem with overlapping objects on adjacent planes we highlighted in section 5.3.2, and it could reduce the overall photobleaching of the fluorescent dye. Consequently, we tested this technique to determine whether its performance suits our needs.

We used the Leica SP5 system described in materials and methods 9.15, with a Ti:Sapphire pulsed infrared laser attached to it. The two-photon excitation mode was used on ovarian tissue stained with the Alexa 488 dye for the MVH protein. The staining protocol was exactly the same as the one used before, with the only difference being the use of another fluorophore. Alexa 488 has optimal excitation at 500nm, therefore the laser's output photon frequency was set to 1000nm, which is close to the maximum output potential of the laser, meaning that more photons are emitted at each pulse, and hence the excitation is higher. The pinhole of the confocal was set to maximum opening, making sure that there were no other light sources close to the microscope that could interfere with the detected signal.

The imaging was repeated three times using sections of juvenile mouse ovaries, prepared by Dr M. Fenwick, stained for MVH using the Alexa 488 dye. The images (not reported) we acquired were not as clear as the ones obtained with the conventional confocal microscope. Images had remarkably noisy background, with the signal being extremely weak. For these reasons, it was decided not to pursue with this technique and to continue using single-photon lasers on the Leica SP5 inverted microscope hereafter.

5.4 Follicle counting and stereology

5.4.1 Estimating total number of follicles

Once the staining and imaging protocol have been optimized, more juvenile mouse ovaries stained for MVH were imaged. The goal of these experiments is to estimate the number of follicles in the juvenile mouse ovary. Theoretically, it is possible to obtain the exact number of small follicles in an ovary, since the optical planes cover the whole volume of the ovary. However, according to the concepts introduced in chapter 4, even if the number of follicles within each available ovary was exactly recorded, the uncertainty due to biological variability would not eliminated. The mean number of follicles for a specific age group may in fact be very similar to the mean resulting from a finite number of ovaries, only if an adequately large pool of ovaries is sampled.

It should be stressed at this point that although the follicles were all captured in the 3D rendering, it was not possible to count them exactly using automated object recognition. This was mainly due to the fact that such complex algorithms were not available in Volocity (software used for object reconstruction), and making them from scratch would require significant amount of time. In addition, due to the optical plane overlap that was reported in 5.3.2, the shape of a primordial follicle in 3D, if examined in detail was cylindrical rather than spherical or ellipsoid, and overlaps occurred between these. This adds another level of complexity for the object recognition algorithm. Manual determination of number of the number of follicles was also ruled out. Counting follicles is feasible on sections, where numbers do not exceed a few hundred and follicles are spaced out so that they can be clearly identified, but in the 3D volume, where follicle number is more than 2000 (see chapter 4), manual counting would be extremely time consuming and error prone.

The stereologic technique however, using the optical disector and fractionator principles (see section 4.2.2), could be conveniently applied in our samples, as the optical planes are already available, and no image registration was required. This was the most straightforward way to obtain fast and accurate results from our acquired images.

Two day-12 mouse ovaries are used to estimate their number of follicles. A random start-section was selected, and two adjacent sections were picked, at a given

frequency. Due to the problem of overlapping follicles reported in section 5.3.2, if two adjacent planes were used which were too close to each other, the chances are that no follicles would be counted, because all follicles/oocytes would appear in both sections. Therefore, when selecting pairs of sections for the disector, we considered the randomly selected one as reference, the immediately next was skipped and the one after was considered as the look-up. For example, if section 40 is selected, we use sections 40 and 42. This ensured that the distance between the chosen two sections was bigger than the average oocyte diameter. The sections are 6μm apart in our case; this distance is dependant on the z-interval selected on the confocal microscope for image acquisition, and should be considered when calculating the distances in different focal planes.

We sampled the ovaries first at a frequency of every twenty and then every fifty sections. Presented in figure 5.10 are two adjacent optical planes from a day 12 mouse ovary. Image 5.10*a* is the reference section of the disector, and image 5.10*b* is the look-up section. We used the nucleus (black area surrounded by the stained oocyte) as the identifier. Therefore any oocytes with a visible nucleus in the reference section and no nucleus in the look-up section, were counted, otherwise they were ignored. A dot on top of each oocyte, green for the reference section and red for the look-up was added if its nucleus was visible, to facilitate counting. These appear in figure 5.10. Images 5.10*c* and 5.10*d* are magnified areas of the images reported above them, in order to demonstrate how the captured detail can be used to better examine these images.

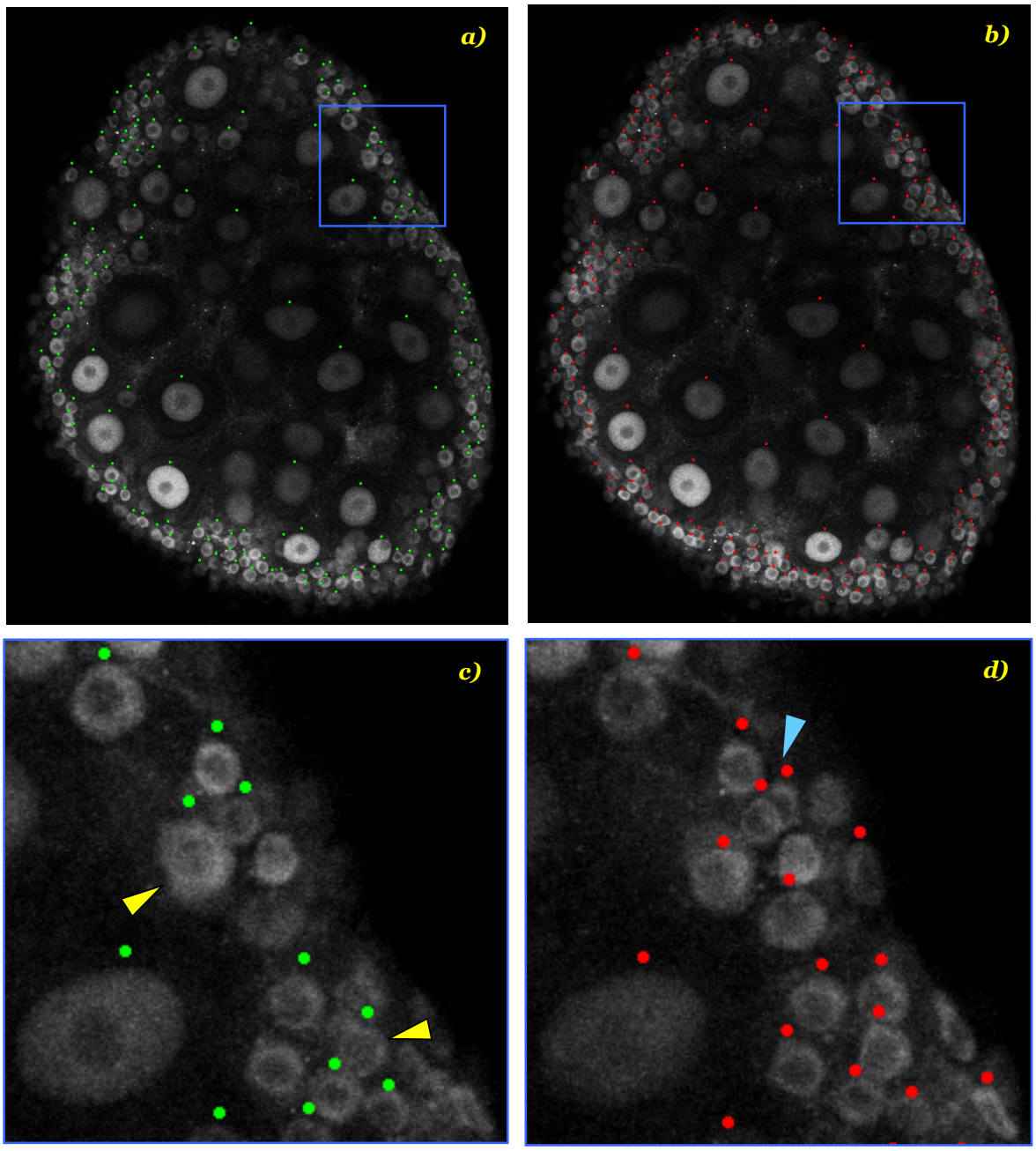


Figure 5.10: Two optical sections of a whole day 12 ovary. Used as reference is image ***a)*** (image ***c)*** is the magnification of the blue area) and look-up is image ***b)*** (and corresponding magnification, image ***d)***). Sections like these were considered when applying the stereologic technique. Optical plane ***a)*** is at 441µm depth in the tissue; plane ***b)*** is at 447µm. Dots denote oocytes that have a visible nucleus, and therefore considered for the counting. Green dots were used for the reference section and red for the look-up section. When the oocyte nucleus is fuzzy (yellow arrowheads) the follicle is still considered for the counting. Oocyte overlapping does not affect the implementation of the stereologic technique (cyan arrowhead), therefore is ignored. Scale bars were not added, in interests of simplicity; images are from the same ovary as reported in figures 5.7and 5.8, thus scales can be obtained from there.

In order to facilitate the recognition of the oocytes to be counted, the two planes were assigned different colour schemes, by using lookup tables in the ImageJ image-analysis program (rsbweb.nih.gov/ij/). In Image Processing, a lookup table is

used to transform input data into a more desirable output format (Russ, 2007), which in our case translates to transforming the grayscale into a scale of red or green. We used green colour for the reference section (figure 5.10*a* and 5.10*c*) and red for the look-up (figure 5.10*b* and 5.10*d*). All the oocytes that had a visible nucleus regardless of its fuzzyness were marked with a dot on top of them respective to the colour of the image (green for reference and red for look-up). The two images were then overlaid in Adobe Photoshop, resulting in an image as the one presented in figure 5.11. Oocytes that had their nucleus visible on the reference section, but not on the look-up section had only a green dot on top of them, and were very easy to distinguish in the overlaid image by colour; the oocyte appeared in a dark teal colour (yellow arrowheads in figure 5.11*b* and 5.11*c*).

As an additional measure of safety to ensure that no false counts were performed, the three images (the reference, the look-up and the overlaid) were displayed on the computer monitor at the same time, so that every oocyte was properly checked on all three sections simultaneously. An example of a false negative is depicted in image 5.11*b*, marked by a purple arrowhead. This oocyte was falsely marked as having a visible nucleus on the look-up section (marked with a red dot). The error was detected once all three images were compared simultaneously on the computer screen. Similarly, a false positive is marked on image 5.11*a* by a cyan arrowhead, where the operator failed to notice the fuzzy but visible nucleus on the look-up section (no red dot is present). This procedure was done for every set of images selected in each ovary, producing follicle estimates rapidly and reliably.

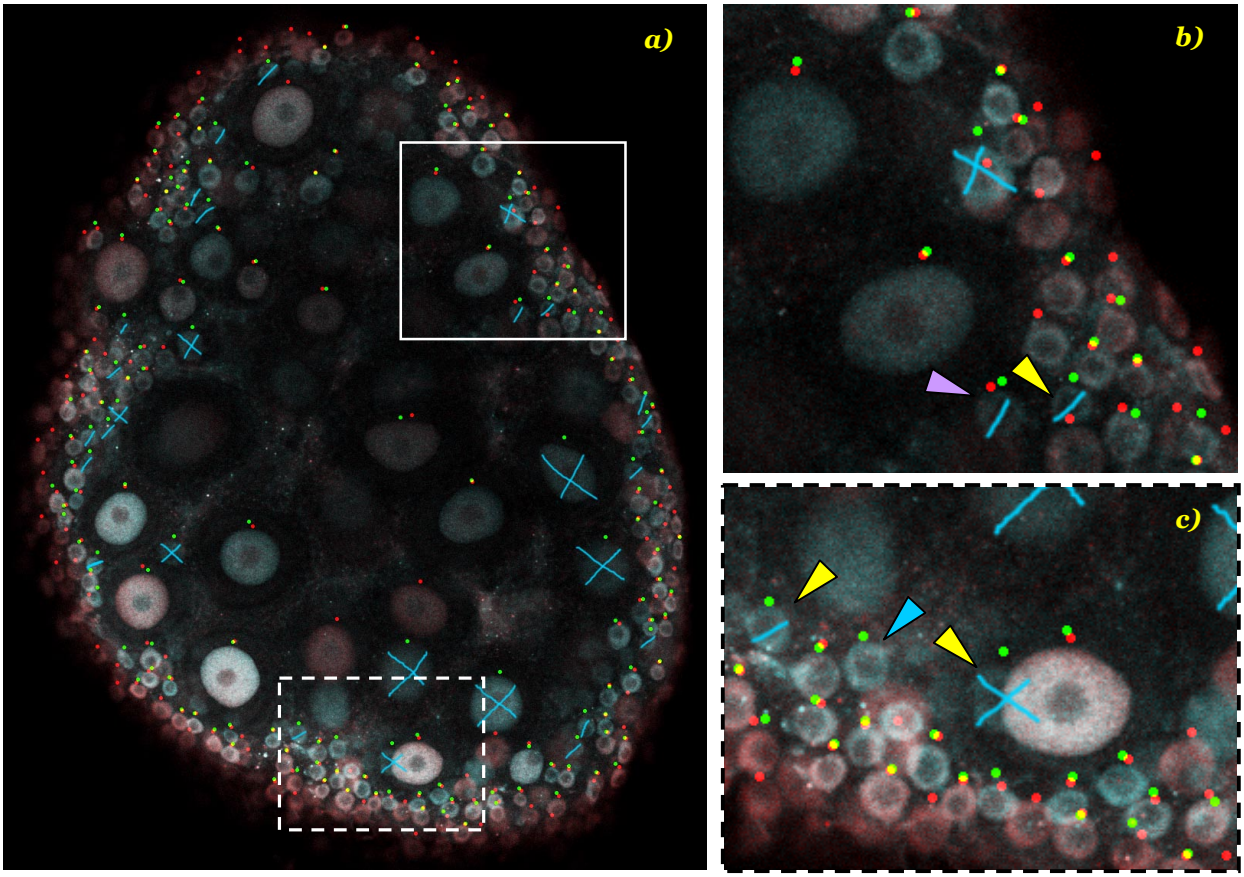


Figure 5.11: Reference (green) and look-up (red) sections are overlaid in Adobe Photoshop, resulting in image ***a)***. Image ***b)*** is the area in the white square. Image ***c)*** is a magnified area of ***a)*** enclosed in the dashed white square. Growing follicles are marked with a cyan 'X'; resting follicles are marked with cyan '/'. Yellow arrowheads point at oocytes with a visible nucleus only on the reference (green) section, which have a dark teal colour. The purple arrowhead points at a false negative and the cyan points at a false positive. Again, in the interest of simplicity, scale bars were omitted; scale can be obtained from figures 5.7 and 5.8

The developmental stage of the follicles was assessed qualitatively, by estimating the size of the oocyte. We used in this case only two follicle categories, *Resting* and *Growing*. Growing follicles had an easily distinguishable larger oocyte diameter compared to the resting follicles (arrows in figure 5.11). Ideally, in order to assess the follicle developmental stage more precisely, the ovaries could additionally be stained using a nuclear dye. However, given the limitations described in 5.3.2, determining the shape of the granulosa cells around the small follicles could be problematic mainly due to optical plane overlapping and small magnification. Nevertheless, the numbers finally obtained with our qualitative staging criterion were realistic. Reported in table 5.1 are the raw oocyte counts for each ovary, and the estimate of the total number, when counting every 20 and every 50 sections.

Table 5.1: Oocyte number estimates of two day 12 ovaries, using the stereologic technique. Each ovary has been sampled using two sampling frequencies, every 20 sections and every 50 sections. Estimates of the total number are the product of raw counts times the inverse of the sampling frequency (see also section 4.2.2).

	Ovary 1		**Ovary 2**	
	Every 20	*Every 50*	*Every 20*	*Every 50*
Pairs of sections sampled	8	3	8	3
Total ***resting*** follicles raw counts	159	59	141	55
Total ***growing*** follicles raw counts	37	14	37	18
Resting follicle No. estimate	3180	2950	2820	2750
Growing follicle No. estimate	740	700	740	900

Kerr *et al* (2006) reported follicle numbers of juvenile mice (the group used the same strain as the one we used; the C57BL/6) at day 12 equal to approximately 2300 for resting follicles (with a standard deviation of 720), and 690 for growing follicles (with a standard deviation of 127). These estimates compared well with our counting reported in table 5.1. Therefore, our oocyte number estimates fall in the range of the day 12 distributions, which can safely be considered realistic, as they are within the standard deviations reported by Kerr *et al* (2006).

5.4.2 Use of Simulated Ovaries to corroborate experimental follicle counts

In the present section we used the Simulated Ovaries presented in Chapter 4 to corroborate the experimental estimates of the follicle numbers reported in section 5.4.1. In particular, we generated two simulated ovaries each with a number of resting and growing follicles equal to the estimates obtained experimentally with a frequency of every 20 sections (reported in table 5.1). In doing so we assumed that the estimates from a 20-section frequency are the closest to the actual follicle numbers; we then used the simulated ovary to check in which statistical range the experimental estimates from 50-section frequency fall in. In order to do that, the two simulated

ovaries were sampled as explained in chapter 4, using sampling frequencies of every 50 sections. Follicle numbers were calculated *10,000* times, each time randomly rotating the simulated ovary and selecting a new starting point. We are interested in evaluating the standard deviation of these *10,000* counts. Table 5.2 reports the standard deviations for each set of simulations, corresponding to a given simulated ovary, as well as the experimental counts obtained with a 50-section frequency from each imaged ovary.

Table 5.2: Standard deviations of the *10,000* simulated follicle-number estimations and experimental estimates for both resting and growing follicles. Sampling frequency used equals to every 50 sections.

	Resting follicles			**Growing follicles**		
	Actual number in Simulated ovary	Standard deviations from Simulated ovary	Experimental follicle count	*Actual number in Simulated ovary*	Standard deviations from Simulated ovary	Experimental follicle count
Ovary 1	*3180*	514.28	2950	*740*	187.00	700
Ovary 2	*2820*	460.75	2750	*740*	182.13	900

Table 5.2 shows that the experimental estimates differ from the actual values by less than the standard deviations. We can therefore infer that the experimental technique we propose produces estimates of the follicle numbers at least within the 68% range from the mean. Thus sampling an ovary to estimate the total follicle number even at a low frequency, such as every 50, produces estimates within reasonable error intervals.

5.5 Discussion

The confocal microscope, ideally, can acquire optical sections through a sample without the need for physically sectioning it, allowing for computed-assisted volume reconstruction. The problems associated with shrinking and compression resulting from tissue section processing were eliminated by whole mount imaging. In addition, optical planes of the sample were already registered and aligned; therefore computational volume reconstruction can be performed without any prior processing.

Emphasis was given to the time required for the results to be obtained, which is significantly less than the time required to get the same results from histological sections. This will be more extensively discussed, when more specific comments will be made on the technique proposed in this chapter.

It should be stressed here that a significant amount of time during this project was dedicated to method optimizations, in order to compile the set of methods presented in 9.13 – 9.15. Specifically, optimal concentration of staining antibodies had to be achieved, a task that was experimentally realised (not reported here; in the Methods chapter, only the optimal protocols are included). In addition, designing a chamber which could hold the clearing agent (BABB) for more than two hours was challenging, as most adhesives are dissolved by the BABB. Nunc slide chambers (square volume of approximately 1ml) were found to be efficient for this application.

Imaging techniques

The confocal microscope like every other instrument has limitations due to the optics of the individual lenses and the properties of light. The resolution of the images we presented is affected by a number of factors, both from preparation and from imaging. It is very important that all the steps taken to ensure sample refractive index matching, using a clearing agent, are carefully carried out. This was the most crucial part of the preparation; our imaging protocol can be applied to any tissue up to 1mm thick that can be cleared.

During imaging, the resolution was mostly affected by the objective lens used and the light scattering effects at the depth of imaging (Pawley, 2006). Higher numerical aperture objective lenses, as well as oil immersion objectives (with refractive index similar to the clearing agent's refractive index) produce much greater detail on the images obtained, something that can be directly observed in tissue histological sections. However, these objectives have very small working distances to use with whole tissues, and therefore only dry objectives could be used in our case. Furthermore, as the magnification of the objective used increased, the required laser light intensity increased as well, and for single photon microscopy, this resulted in the dye photobleaching (Miller *et al*, 2005).

The optical projection tomography is a very promising and widely used technique for imaging whole organs and small embryos (Alanentalo *et al*, 2008, McGinty *et al*, 2008, Sharpe, 2004, Sharpe, 2003), yielding extremely good results. However, in our case where greater resolution was required, the imaging system needed improvement in order to produce images of higher magnification and resolution, to enable observations to be made at a cellular level. When this is achieved, the method will be invaluable for observing large tissues, eliminating light attenuation through the big sample volume.

Exploring tissue morphology

Our proposed whole mount tissue imaging approach is excellent for exploring tissue morphology at an almost cellular level, using a sufficiently high magnification objective (up to x20 in our case). Tissue clarity in the optical planes obtained from ovaries and other juvenile mouse tissue was comparable to the crispness of histological sections, providing very good morphological detail (Zucker, 2006, Zucker and Jaffay, 2006). Tissue natural fluorescence, as can be seen in images of figures 5.2 – 5.4, can be very informative when examining tissue anatomy. For example, it would be very difficult to examine the spatial folding of the oviduct (image 5.2*d*) or the arrangement of the small tubes in the kidneys (image 5.4*d*) just from looking at histological sections. Autofluorescence is usually an unwanted property of tissue when performing imaging; however, we have shown in this work that it can also be informative, divulging spatial and structural properties (figures 5.2 – 5.4). It can also be very useful when staining is not possible; for example in the work of Zhinov *et al* (2009), natural fluorescence is used for imaging of the corneal surface and epithelium on human subjects.

In juvenile mouse ovaries, autofluorescence was not informative for examining follicle morphology or for counting, although it revealed very clear structural information, as it has been demonstrated on the other tissue. Thus whole mount immunohistochemistry was performed to stain for the MVH protein, which is localized in the oocytes of small and early growing follicles. Dye penetration in the tissue is adequate, given that the thickness of day 12 ovaries is not more than 0.5mm. As stressed in the results section, the faint staining in the centre of the ovary is due to

the fact that MVH expression starts to downregulate in the early secondary follicle stage; many of the follicles in the medullar area are close to the secondary stage. These more mature follicles can be visualized in the future, by staining for GDF-9 (Guéripel *et al*, 2006) in addition to the MVH (see GDF-9 expression, 1.5). This would render all the follicle oocytes in the ovary visible when imaging. Additionally, structures like blood vessels and capillaries or neural cells could be stained, following our proposed protocol, to relate the positions of resting and/or growing follicles to these structures in 3D. For example, it would be very interesting to examine the position of an oocyte of an early growing follicle as the network of blood vessels starts to form around it; this would be unfeasible if performed exclusively on histological sections.

A novel efficient way for producing follicle number estimates

One of the main aims of this work was to develop a new method to accurately estimate number of follicles, in parallel to minimizing laboratory time. This was the basis of chapter 4, where we showed that due to biological variability, accurate estimates of follicle number require sampling large numbers of ovaries. Whole mount tissue immunostaining and imaging by means of confocal microscopy, applied on whole juvenile mouse ovaries, is a very promising technique for this purpose. The method was optimized through a series of trials on other types of tissue, before being implemented on juvenile mouse ovaries. On the mouse ovaries, immuno-histochemistry was performed to stain for the MVH protein, which is present in the oocytes of small follicles (primordial up to pre-antral stage). The optical planes that occured from the imaging were used to perform stereologic estimation of the follicle numbers. The results obtained were satisfactory in terms of accuracy of follicle numbers.

This novel approach to estimating follicle number is a combination of the optical and physical disector, albeit without the requirement of performing the time-consuming tasks of tissue embedding and serial sectioning, and most importantly, sections come readily registered due to the nature of the imaging; registration is one of the most time-consuming aspects of the physical disector (unbiased stereologic technique: section 1.9.1). The time required to complete the experiment is a very

important parameter and is the main feature of our method, along with the ability to visualize the 3D volume of the specimen. Using the approach described in this chapter and presented in detail in 9.13 – 9.15, staining and imaging of the tissue took four days. In addition, it was possible to carry out the procedure on many ovaries simultaneously, using culture plates. Due to the small size of the ovary, the amount of chemicals required for each step is not substantial; therefore by placing each ovary into a well of a plate (Nunc, 24 well plate, 1ml suggested volume) the procedures could easily be conducted in parallel. Approximately another half a day would be consumed on the stereologic sampling for each ovary. This would require several weeks to complete following the conventional method of histological examination, even on state-of-the-art stereology microscopes, because of the time-consuming sectioning and histological slide preparation, as described above.

XYZ coordinates

One of the main reasons for the initiation of this study was to extend the spatial analysis of the follicles from 2D to 3D. We demonstrated in chapters 2 and 3 that analysis of the relationships of primordial follicles to their neighbouring follicles within set small distances can be used to infer new signaling mechanisms. This is performed by mapping the *XY* coordinates of the follicles on histological sections (Da Silva-Buttkus *et al*, 2009). This analysis however excluded the follicles located in close proximity but in the space above or below relatively to those examined (see also figure 5.1). To rectify this problem, we had to look beyond the 2D sections, into the 3D volume of the ovary. The method proposed in this chapter brought us one step closer to accomplishing this; however quantification of the exact *XYZ* coordinates of the follicles in the ovary was still not possible.

There are several complications of the method at its current design that do not permit extraction of the follicle coordinates. First of all, as discussed in 5.4.1, the actual numbers of follicles in the whole ovary (>2000 follicles) render such a task extremely time consuming and error prone, if performed manually. Computerised automatic object detection methods in three dimensions are (up to date) not sophisticated to the point where they can be used for accurate follicle recognition and classification. An additional challenge, either to the manual or automatic follicle

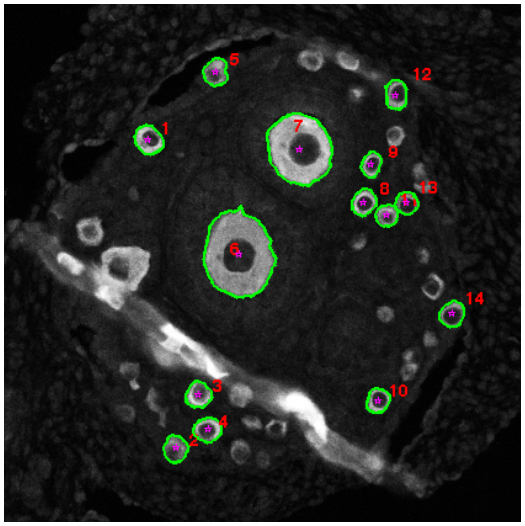
recognition, was introduced by the overlapping follicles created due to the image acquisition method. These follicles, when reconstructed in a volume, were presented with overlapping areas, and their shape was inconsistent (as opposed to having spheres or ellipsoids if optical planes were infinitely thin). This complicated counting, and in addition made the stage determination error-prone. All the above obstacles need to be tackled before *XYZ* coordinates can be determined, to ensure that the resulting analysis will be accurate.

Conclusions

The imaging technique proposed and implemented in this chapter has been used before, for imaging whole embryos (e.g. Zucker, 2006) as well as for imaging whole follicles in rat ovaries (Zucker *et al*, 2000) and exploring 3D morphology whole mouse ovaries (Zucker and Jeffay, 2006). This is the first study to image the whole juvenile mouse ovary, used both for exploring the three dimensional morphology of structures in the ovary, and for quantifying the number of small follicles. We demonstrated that use of the stereologic technique to obtain estimates of follicle numbers has proved accurate. However, not all our aims were achieved, as there are some caveats of the current imaging implementation. In order to complete the 3D approach in the future, improving both visualization and quantification, more advanced imaging techniques are required (such as appropriate use of two-photon microscopy), and improved object recognition algorithms need to be developed. Image segmentation and processing techniques can be used to obtain exact counts of follicle numbers in the ovary, as well as to extract spatial characteristics of the recognized objects; automated recognition will be faster and more precise (seconds or minutes, compared to hours required in applying the stereologic technique). Such a method, developed for 2D objects, is presented in the following chapter.

Chapter 6

Image processing technique for follicle quantification from microscopic images



6.1 Introduction

Reproductive viability is correlated with the number of follicles within the ovaries, which in turn is influenced by genetic predisposition (premature ovarian failure genetics: Fassnacht *et al*, 2006), or externally triggered disruptions (e.g. environmental toxins: Hoyer *et al*, 2007, drugs: Perez *et al*, 1997, radiation: Kundt *et al*, 2009 etc). It is thus a very important task, when assessing the side effects of specific drugs (Tarumi *et al*, 2009) or genetic mutations to assess follicle numbers within the ovaries with adequate accuracy. Accurate assessment of follicle numbers requires the use of several ovaries, which can be time consuming and labour intensive. In chapter 4 (4.2.2) we have presented the stereologic technique, which allows estimating the number of small and growing follicles in the whole ovary more rapidly and accurately compared to traditional techniques (Gundersen and Jensen, 1985, Howard and Reed, 1998). This was applied on optical sections of whole ovaries

in chapter 5, where we demonstrate the accuracy and speed that can be achieved with this technique, when combined with new imaging methods. Nevertheless, it is desirable to establish a counting technique that is accurate and automatic, needing minimal operator's intervention. Such a technique, in combination with the whole ovary imaging method presented in chapter 5, would allow the realisation of studies that require the counting of high number of ovaries within a reasonable time frame.

Counting of ovarian follicles is routinely performed manually by trained operators, and sometimes the results need to be double-checked. In addition, the developmental stage of follicles is assessed and occasionally their diameters and spatial coordinates may be recorded, in order to quantify information regarding their density or spatial arrangement (Da Silva-Buttkus *et al*, 2009, also necessary for the work we presented in chapters 2, 3 and 4). However, these approaches are subjective and are prone to introducing operator's bias. Automating this procedure would significantly increase the efficiency, accuracy and allow sampling higher numbers of ovaries to increase the statistical significance of generated data.

The ideal procedure would involve the reconstruction of the 3-dimensional ovarian volume from the 2-dimensional optical images, and then the application of automatic object recognition algorithms performing counting of follicles. This, however, would require developing state of the art algorithms that would be outside the scope of this PhD. Therefore, it was considered sensible to develop instead a method consisting of an algorithm able to recognise objects (oocytes) on two dimensional images, and coupled it with the stereologic technique to rapidly produce estimates of follicle numbers for the whole ovary. In the following sections we report the working principles of this method and the results of its application on ovarian sections.

6.1.1 Automatic follicle detection: preliminary remarks

When analysing objects in images, it is essential to distinguish the objects of interest from the rest, which is referred to as *background*. In computer vision, the techniques used to find the objects of interest, via a process of partitioning a digital image into multiple sets of pixels, are referred to as *segmentation* techniques (Young *et al*, 1998). It must be stressed at this point that there are no segmentation techniques

that would directly work on any image, and that no segmentation technique is perfect (Young *et al*, 1998). There are currently in the literature techniques for automatic and semi-automatic segmentation and recognition of follicles in ultrasound images. These methods include *Cellular Automata* machines (Viher *et al*, 1998), *Region Growing* techniques (Potocnik and Zazula, 2002), *Watershed segmentation* and *Cellular Neural Networks* (Cigale and Zazula, 2004).

Ultrasound technology is being used to identify large, mature follicles (Dewailly *et al*, 2010), but because of the low resolution of the ultrasound images, is not appropriate for imaging and counting smaller ovarian follicles. For this reason, microscope images are used, which provide satisfactory resolution for follicle identification, as illustrated in figure 6.1. Furthermore, the existing follicle segmentation algorithms for ultrasound images cannot be used for microscope images, due to the differences in resolution. Nevertheless, the general segmentation principles applied there can also be applied for automatic detection of follicles in microscope images.

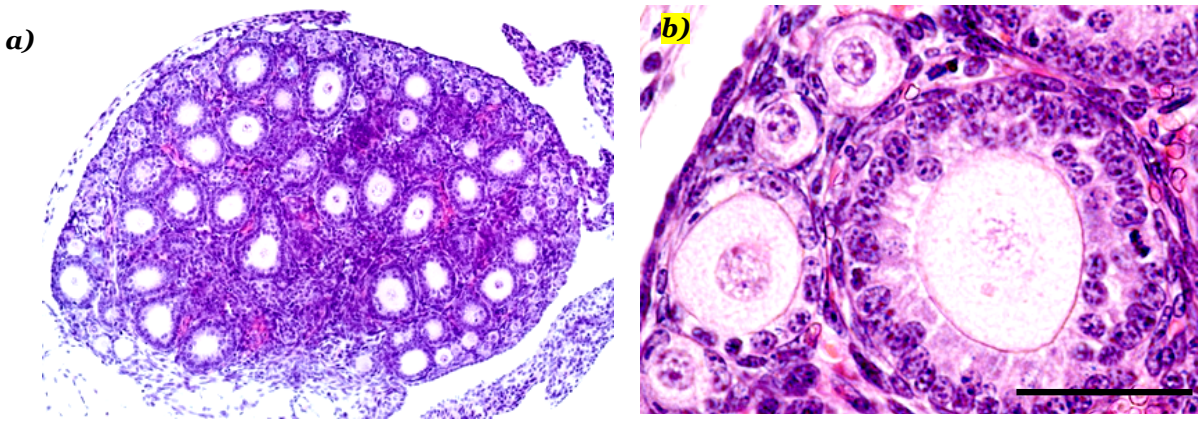


Figure 6.1: Light micrographs of mouse ovary tissue, stained using standard Haematoxylin and Eosin. Oocytes are the ovoid structures, appearing white, surrounded by somatic cells, and can be of various sizes according to their developmental stage. ***a)*** 10x magnification, ***b)*** 60x magnification (bar is 50µm) (appearing in Da Silva Buttkus *et al*, 2008).

One of the major challenges in automating cell recognition in microscope images is the variation in the texture, colour and sometimes the shape of the region of interest; these variations may depend, amongst others, on factors such as the biological structures that are stained, the dye concentration and technical variation in the staining protocol. In addition, the non-standardisation of imaging can also be a source of variation. An example of typical staining is presented in figure 6.1, which

shows Haematoxylin and Eosin (H&E) stained mouse ovaries, acquired using brightfield light at different magnifications. This combination of dyes stains cell nuclei (purple) and intracellular and extracellular protein, as well as cytoplasm (bright pink). H&E staining is among the most popular staining methods in biology.

Various applications have been developed for automatic cell counting (e.g. Volocity, used for 3D reconstruction in chapter 5), which can also be applied to ovarian microscope images; one of these is for instance the open-source CellProfiler tool (Carpenter *et al*, 2006). These applications offer a wide range of image processing tools in the form of modules. Each module performs a specific operation, such as threshold, noise removal, image sharpening etc. The user can tune the individual parameters of each module to perform the analysis required on specific images, using them as a linear processing sequence directly applied to the images. Tuning these modules require significant user intervention, as well as extensive familiarization with the application algorithms, which may not be suitable for a non-expert. Our work is inspired by the fact that these pipelines do not perform well in every possible image context and special modifications are required for different image types. The aim of this work was to develop an automatic algorithm for the detection of oocytes in ovarian sections, requiring minimum input intervention by the user.

In order to improve follicle identification and calculation of spatial properties (size and coordinates on section), it is essential to stain the ovarian sections with a biological marker that can help towards obtaining this kind of information. A suitable procedure is to stain the sections for the MVH protein, which is expressed only in the oocytes of small follicles (Pepling and Spradling, 2001). This is the same marker which has been used in chapter 5 to stain the whole ovary, in order to make the oocytes distinguishable. The stained tissue can be prepared for imaging either by using brightfield light microscopy (figure 6.2*a*) or fluorescence confocal microscopy (figure 6.2*b*). In the latter case, only the fluorescent signal from the MVH marker is collected, obtained as a single separate colour channel (gray-scale). In the case of brightfield imaging, a colour image is acquired and the MVH stained oocytes correspond to the red areas on the image. Typically, all colour images obtained from cameras capturing microscopic images on brightfield microscopes are displayed in the *RGB* (red-green-blue) colorspace, meaning that each pixel has three different values

in order to display the colour (further reading: "Color Image Processing", Lukac and Plataniotis, 2007).

In this work, the automation of oocyte counting is based on image segmentation, using morphological operators and the watershed transform, which is an intensity-based segmentation technique (Roerdink and Meijster, 2001; see also Introduction, figure 1.19). In addition, we propose the use of MVH immunohisto-chemistry as a standard procedure in ovarian tissue staining when assessing numbers of small follicles and their quality (figure 6.2), due to the high signal-noise ratio and minimal variation generated in the image properties.

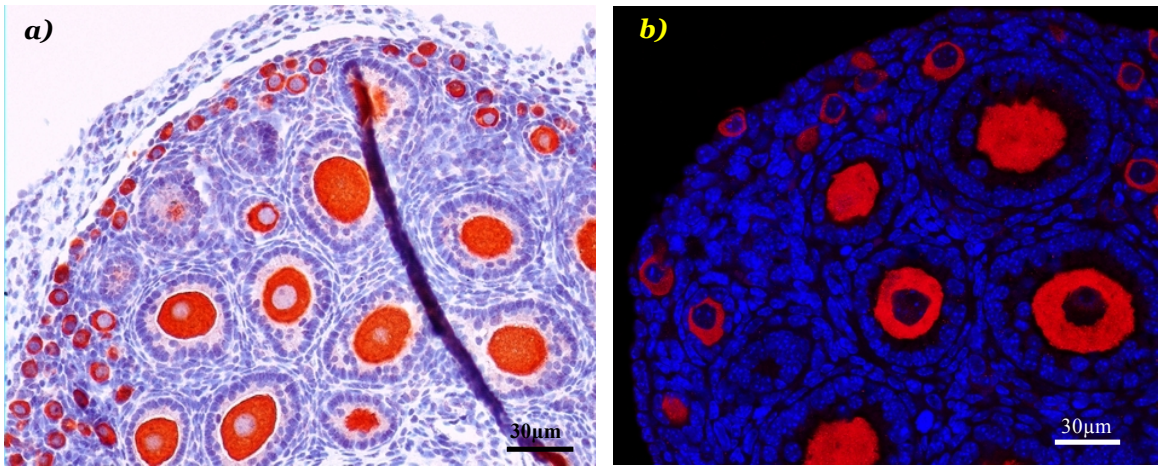


Figure 6.2: Oocytes are stained for mouse vasa homolog (MVH), appearing in red. The procedure can be utilized for both ***a)*** light (counterstain: haematoxylin) and ***b)*** fluorescent microscopy (counterstain: DAPI). It can provide a very clear marker for oocyte size, as well as for oocyte condition, i.e. dead or unhealthy oocytes are not stained.

The remainder of the chapter is organized as follows. The proposed stages for the automatic detection of oocytes and the extraction of morphological and spatial information are explained in section 6.2. The experimental results are presented in section 6.3. The work is concluded with section 6.4, by the discussion of the method, comparisons and suggestions for further improvement.

6.2 The Proposed Method

In this chapter we propose an approach for the automatic detection of oocytes in microscope images (all of which were obtained and kindly provided by Dr Mark

Fenwick) and the estimation of morphological and spatial characteristics, namely the number, the size and the location of the oocytes in an image. The goal of our method is to recognize follicles on images such as the two presented in figure 6.3. The oocytes that should be detected must have a clear nucleus, so that the calculated diameter matches as accurately as possible to the actual one, and the MVH staining has to be clear, which indicates that the follicle is healthy. The proposed detection approach is comprised of three main stages, which include image pre-processing, image segmentation and calculation of morphological and spatial information. The outline of the method is illustrated in figure 6.4. The steps of the algorithm and its implementation in MATLAB are described in detail in the present section.

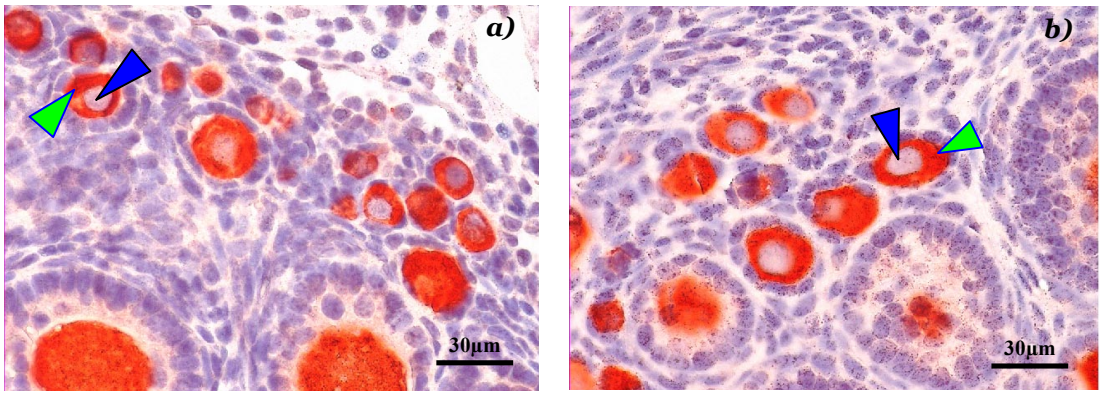


Figure 6.3: Two examples of input images of MVH stained mouse ovarian sections counterstained with haematoxylin. Blue arrow indicates the nucleus and green arrow the oocyte, in each image. These exact images were used throughout the methods, to demonstrate the technique, but the scale bars are not going to be reported for simplicity.

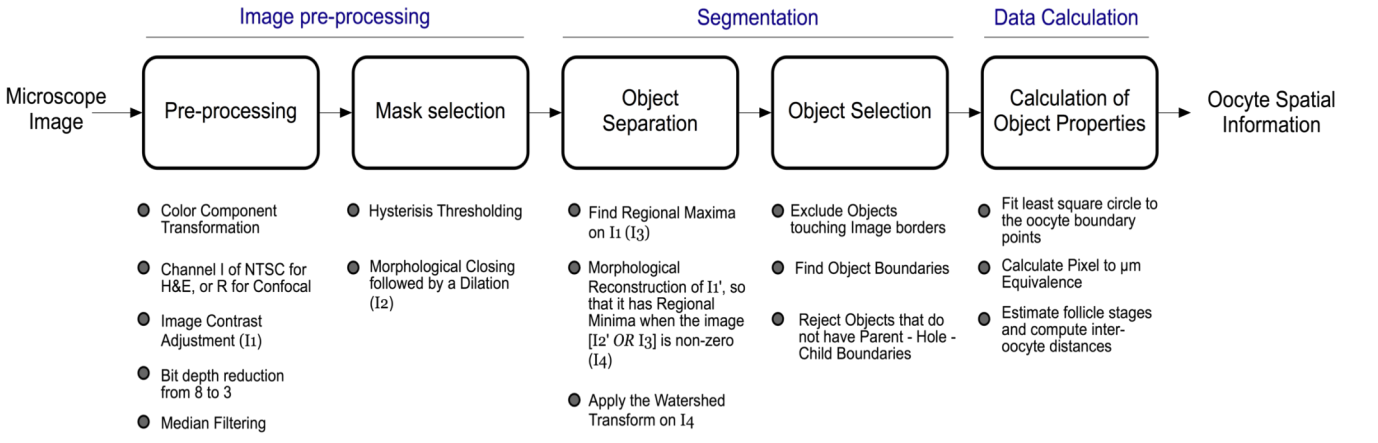


Figure 6.4: Block diagram of the proposed algorithm for oocyte segmentation and feature extraction. Individual steps are extensively explained in the present section.

6.2.1 Pre-processing

Prior to segmenting the microscope images for the oocyte detection, the appropriate image channel has to be selected. The images imported were *RGB* images. At first glance, the channel that best fits our needs wass the blue channel, in which oocytes appeared as completely black areas in a blue background. However, we went on to investigate other color systems such as the *HSV* (Hue - Saturation - Value) and the *YIQ* (Luminance - In-phase - Quadrature), which corresponds to the *NTSC* (National Television System Comittee) color system that is used mainly in the USA to transmit analog color television signal (Gonzalez *et al*, 2004, Lukak and Plataniotis, 2007). The color system that best fitted our needs was the *YIQ*, as the *in-phase* channel provided very clear information of the red stained oocytes (figure 6.5). For the oocyte detection, the *in-phase* channel was converted to a grayscale image and it was represented as *I*.

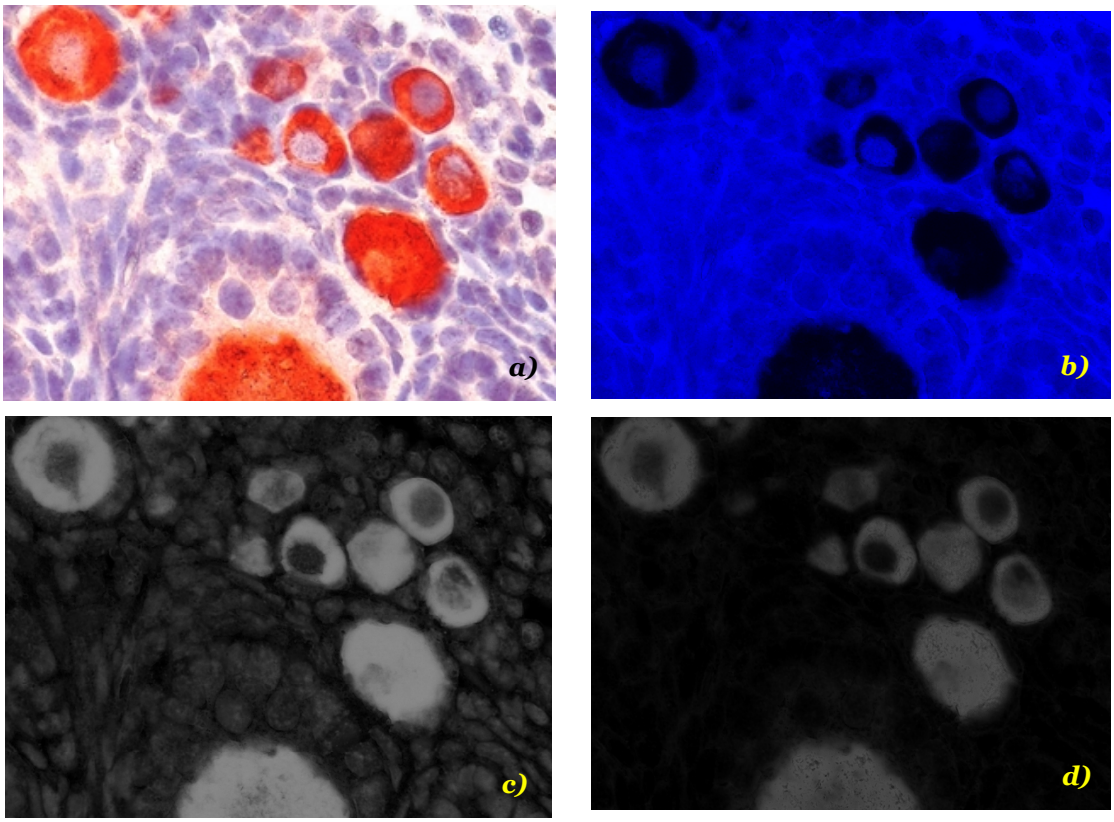


Figure 6.5: ***a)*** *RGB* image, ***b)*** blue channel (*RGB*), ***c)*** *saturation* channel (*HSV*), ***d)*** *in-phase* channel (*YIQ*).

In order to improve the intensity distribution of the grayscale *in-phase* channel image (*I*) and increase the contrast between the oocytes and their background, a contrast enhancement transformation was applied, yielding the image *Iadj* (Gonzalez *et al*, 2004). Figure 6.6 depicts the histogram of the *in-phase* channel for figure 9.5*b*, converted to grayscale, before and after the contrast enhancement. The main goal of adjusting the image contrast was to facilitate the image segmentation process that follows.

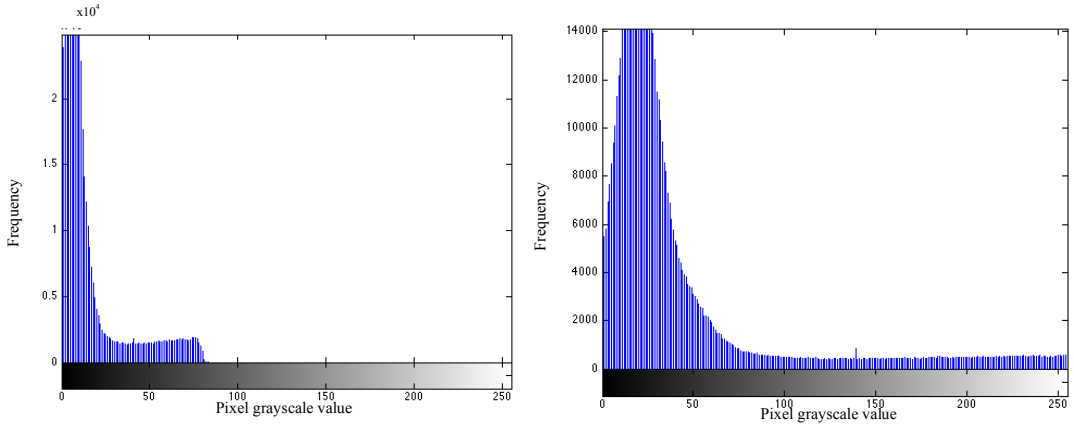


Figure 6.6: Histogram of grayscale *in-phase* channel image of figure 6.5*b*. The original image histogram is presented on the left, while the image histogram after the contrast adjustment is given on the right.

In addition to the contrast adjustment, it has also been recognized that decreasing the bit depth of the grayscale image I_{adj}, from 8 bits (0–255) to 3 bits (0–7) can provide more discrete pixel values, and therefore more discrete areas on the image without distorting the oocyte areas (Viher *et al*, 1998). It has been observed that in the 3-bit image I_{bit} pixels with a value 5–7 belong to oocytes, and pixels with a value 0–1 belong to the background. Pixels with values of 2–4 are candidates for either being part of the oocyte or the background. This can be coupled to the hysteresis thresholding (described in section 6.2.2) to provide a reliable thresholding method. In order to eliminate noise, smoothing of the 3-bit image is performed using a 3x3 median filter[†], resulting in the image I_{smooth}. Figure 6.7 presents the grayscale images after the pre-processing stage.

[†] The median filter is a non-linear digital filtering technique, most commonly used to remove noise while preserving the edges. On an image to be filtered, each pixel is considered and its neighbourhood is examined, in order to replace the pixel's value with the median from all neighbours. (*con't next page*)

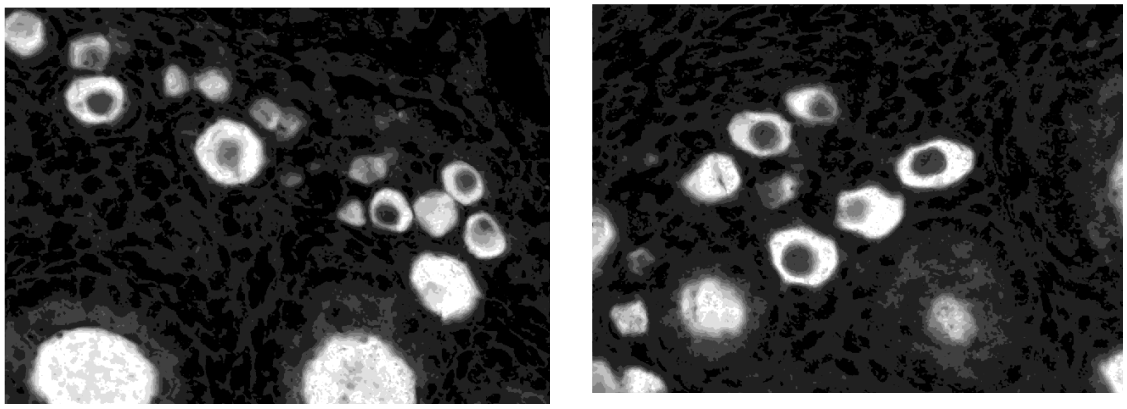


Figure 6.7: Grayscale images of figure 6.3a, 6.3b, after pre-processing, as described in section 6.2.1.

6.2.2 Image Segmentation

Having enhanced the channel intensity image, the next step of the detection algorithm was to isolate the oocytes. From the images shown in figure 6.7, it can be observed that the area of the oocytes corresponds to high intensity values. Therefore, hysteresis thresholding (Canny, 1986) was applied to binarize image I_{smooth}. This hysteresis method employs two threshold values. The high threshold was used to find "seeds" for strong oocyte candidates. These seeds were grown to as large an area as possible, until the image intensity falls below the low threshold value. In the resulted binary image *BW*, the areas that belong to oocytes correspond to the white pixels in a black background as illustrated in figure 6.8.

(*cont'ed from previous page*) In the example illustration, a 3x3 square covers all pixels touching the central pixel. All the values (9 pixels total) are sorted, and the value of the central pixel is replaced by the median of these 9 values.

	125	150	133	100	112
	198	176	143	122	185
	124	114	155	204	124
	165	152	142	179	201
	142	149	155	136	125

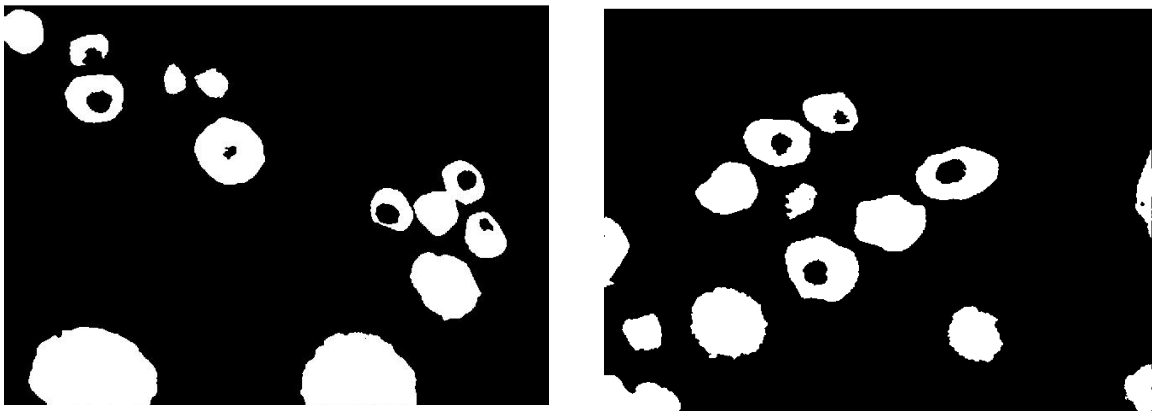


Figure 6.8: Images after the hysteresis thresholding. The high threshold was selected to be 6, and the low to be 3.

In some cases, because of variation in the morphology of the follicle, the oocyte nucleus (black area within oocyte) might be close to (or even touching) the external edge of the oocyte, causing the oocyte to be cut at that edge during the thresholding process. This can be rectified, using morphological processes to close the gap in the binary image. In this case a morphological closing (erosion, followed by a dilation), followed by a further dilation was applied to image *BW*. The structural element used was a disk, of a 2-pixel radius. The results appear in figure 9.9, where the binary images have been superimposed to the original ones, to illustrate the accuracy of the result.

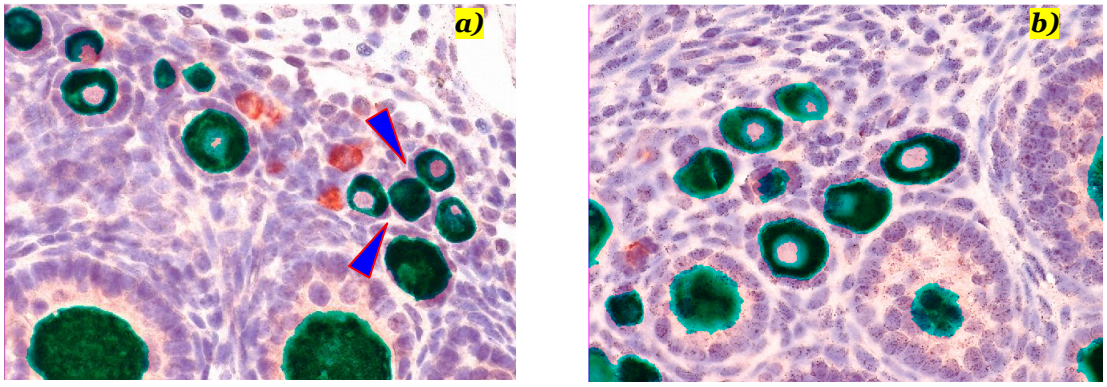


Figure 6.9: Thresholded images overlayed with the original ones (green areas) after filtering and morphological processing (closing, followed by a dilation). Arrows indicate touching objects.

Often, during the image binarization process, the edges of neighboring oocytes were joined and the touching oocytes appeared as a single object (figure 6.9*a*). Separating touching objects in an image is a difficult process. The watershed transform was applied to overcome this problem (Malpica *et al*, 1997, Roerdink and

Meijster, 2001). The watershed transform finds "catchment basins" and "watershed ridge lines" in an image by treating it as a surface where light pixels are high and dark pixels are low.

In order to classify the surface pixels in an image, the extended maxima operator was applied, which is an embedded function in MATLAB (Gonzalez *et al*, 2004, Soille, 1999). This function finds areas (pixel groups) that are significantly higher than their immediate background. This was done in order to avoid "over-segmentation" by the watershed algorithm. This function was applied to the adjusted grayscale image I_{smooth}, as it was before the thresholding. Figure 6.10 illustrates the extended maxima (green areas) superimposed to the binary image.

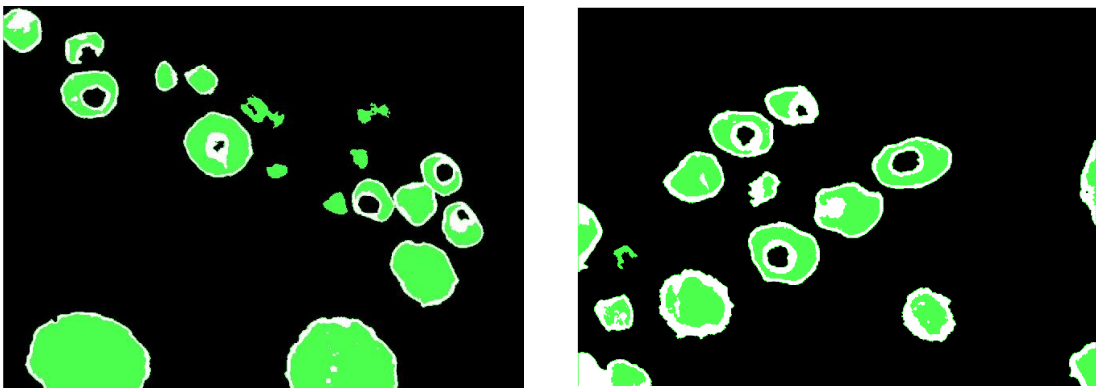


Figure 6.10: The areas (green) identified by the extended maxima operator, whose values are higher than their immediate background. These are superimposed to the binary images.

As the watershed transform identifies low points and not high points, complementin the I_{smooth} image was required as a next step of the method so that the peaks became valleys. The resulting image was then modified so the background pixels and the extended maxima pixels were forced to be the only local minima in the image. This was done using the MATLAB function *imimposemin* (Gonzalez *et al*, 2004), which modified the grayscale image using morphological reconstruction so it only has regional minima wherever the binary image (extended maxima) was nonzero, resulting in image I_{mod}.

After these procedures, image I_{mod} was ready for the application of the watershed transform. The result of the segmentation is presented in figure 6.11, where the different regions were highlighted in different color. Ideally, each of these regions corresponds either to an oocyte or to a nucleus of an oocyte.

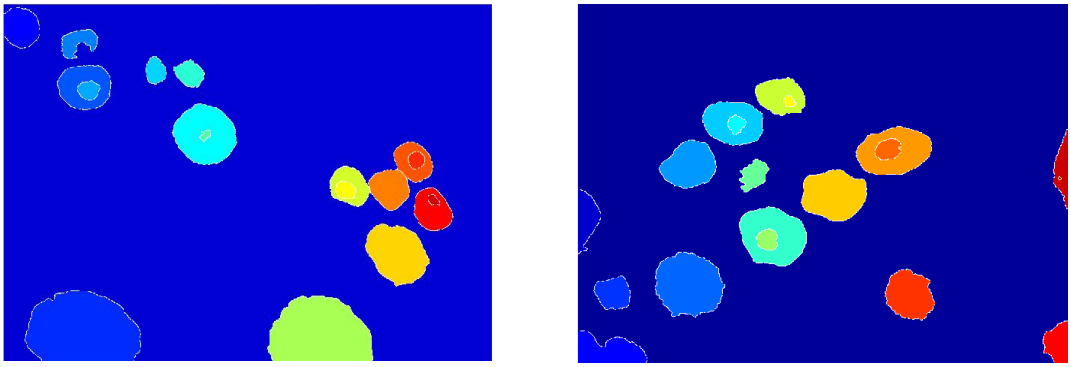


Figure 6.11: The (colorized) regions are segmented using the watershed transform. This is an effective procedure to separate touching objects (oocytes that are very close to each other).

The section has described the main part of the algorithm, and the most challenging aspect. Any modifications to account for different color spaces or different input conditions have to be made in one of the steps reported above. The following part reviews the methods for extracting of the oocyte boundaries and their morphological and spatial characteristics.

6.2.3 Morphological and Spatial Information Extraction

From the set of detected oocyte regions, only some were of interest and had to be kept for further processing. In this work we suggested that the follicles that touch the image boundaries should be ignored, since part of the object was occluded and therefore its morphological characteristics could not be accurately estimated. Furthermore, oocytes of interest were those which contained a clear nucleus. This is because oocytes are approximately spherical, thus the clear nucleus indicates that the oocyte has been cut at its widest part, hence measuring this oocyte gives an accurate estimate of its size. If the nucleus was fuzzy, then after the channel split there would be no hole in the middle of the oocyte, or a very small one that would have been closed, meaning that the oocyte would not be considered. The objects that were touching the boundary were identified in MATLAB as ‘holes’, so using the function *imfill* the oocytes touching the boundary could easily be eliminated.

The last step for the segmentation part of the algorithm was to construct the binary image that would only contain the oocytes. This was done using the logical ‘AND’ operator on the image produced by the watershed segmentation and the image

produced after the elimination of the holes. The resulting images are presented in figure 6.12.

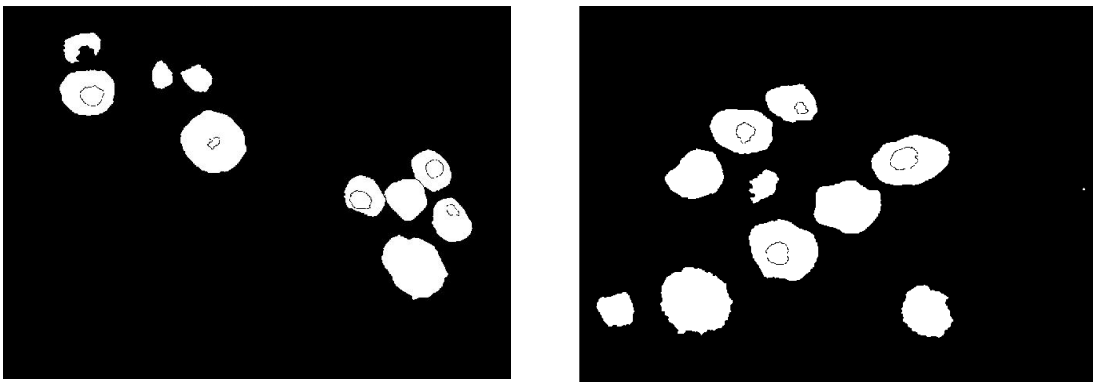


Figure 6.12: Final segmented binary images. These depict the oocytes and their nuclei. Our objects of interest are the oocytes with a nucleus.

The boundaries of the objects within a binary image can be easily retrieved (function *bwboundaries* is employed in MATLAB) (Gonzalez *et al*, 2004). Our final goal though was to keep only the boundaries of the objects (oocytes) that had a nucleus. Figure 6.13 illustrates a simple example of the three categories. MATLAB classifies the boundaries in: *Parent*, *Child* and *Hole*. We were interested in retrieving the boundaries of the objects that were *Parent*, i.e. the ones that included a nucleus (*Child* object, surrounded by a thin black line, which is the *Hole*). The *bwboundaries* function returns a square sparse matrix, which contains the boundary dependencies. We could identify the object which had a child, as its hole boundary would appear twice in this matrix (first time as being enclosed by a boundary -*parent*, and the second time as enclosing a boundary - *child*).

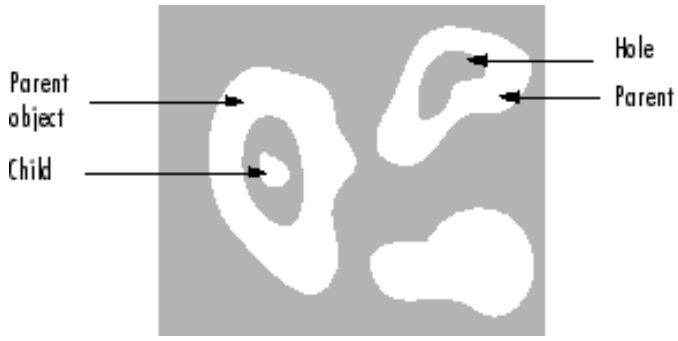


Figure 6.13: Boundary classification by the MATLAB function *bwboundaries*. In images of figure 6.12, the parent object is the oocyte, the hole is the fine black line between the oocyte and nucleus (nuclear membrane), and the child object is the nucleus.

For each of the boundaries identified, a set of properties could be computed. Function *regionprops* was employed in MATLAB. This particular function was used to calculate the coordinates of the center of mass of the detected region, as well as its area. In order to best estimate the diameter of the oocyte, a circle is fitted on to every detected oocyte by calculating the least square differences from each of the detected boundary points. Each boundary is described in MATLAB as a set of contour pixels in a sparse matrix. Once these become available, after the object detection, the procedure to fit a circle was performed as follows:

We started by considering the circle equation:

$$\left(x - x_0\right)^2 + \left(y - y_0\right)^2 = R^2 \tag{6.I}$$

where (x_0,y_0) is the circle center coordinates and R the circle radius.

Eq. 6.I can be written as a polynomial by expanding the parenthesis and isolating the second order terms:

$$ax + by + c = -\left(x^2 + y^2\right) \tag{6.II}$$

where $a = -2x_0$, $b = -2y_0$ and $c = x_0^2 + y_0^2 - R^2$.

We want to estimate parameters a, b and c, based on the contour points that are available. To accomplish this, we can re-write eq. 6.II in matrix form, and use the MATLAB backslash operator to calculate the parameters. This operator is used to solve linear systems of the form $A\psi=B$, ψ being the matrix with the unknown parameters, by setting $\psi=A\backslash B$. If the matrices are not square (which is the case in our example, Eq. 6.III), MATLAB calculates the solution in the least squares sense, by gaussian elimination (further reading: www.mathworks.com). Equation 6.II can be written as follows in matrix form, by considering the boundary contour coordinates (xy pixel position on image of the contour):

$$\underbrace{\begin{pmatrix} a & b & c \end{pmatrix}}_{\psi} \cdot \underbrace{\begin{pmatrix} x_1 & y_1 & 1 \\ \vdots & \vdots & \vdots \\ x_m & y_m & 1 \end{pmatrix}}_{A} = -\underbrace{\begin{pmatrix} x_1^2 + y_1^2 \\ \vdots \\ x_m^2 + y_m^2 \end{pmatrix}}_{B} \tag{6.III}$$

where $x_1 \ldots x_m$ and $y_1 \ldots y_m$ are the coordinates of m pixels of the boundary contour. By performing the backslash operation, as described above, the values of the parameters

a, b and *c* are computed, from where we obtain the least-square fitted circle center coordinates (x_0,y_0) and its radius *R*. Figure 6.14 presents an image where circles are fitted to two detected follicle boundaries. The green follicle contour as well as the fitted red circles and their centers are drawn by the algorithm.

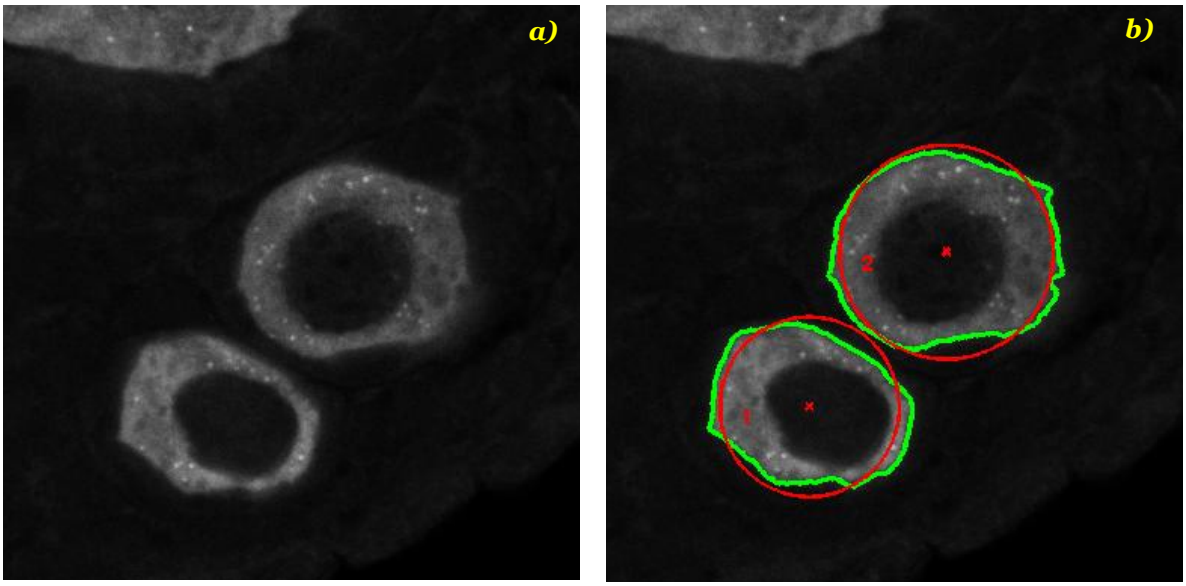


Figure 6.14: ***a)*** Original 60x confocal image of two oocytes on a day 8 mouse ovarian section stained for the MVH protein. ***b)*** Our algorithm recognized the two oocytes (green boundary contours) and fitted a circle on each (red circles with red centers). The fitted circle's diameter is considered as the oocyte's diameter, also used to estimate the follicle's stage.

It has to be noted at this point that the circles radii, as well as any other distance calculated on the screen does not have an actual scale. Due to the fact that pixel coordinates were used for the calculations, all distances were represented in pixel units. In order to convert these distances in μm, a scaling factor was introduced in the program, which needs to be set for every image, so that the scale is correct. This factor can be obtained easily from the microscope images, as it is already embedded in the image information produced by the instrument (in the case of the confocal, where the voxel width and height are displayed in the image metadata). If this information is not directly available (e.g. in the case of the light microscope), it suffices to photograph a known distance for the magnification used, such as a graticule slide. Using an image processing software (such as the free open source ImageJ, available from http://rsbweb.nih.gov/ij/), the distance in pixels between two

parallel lines on the image can be measured and the pixel to distance ratio can easily be calculated, as the distances on the graticule lines are known.

Once the least square circle fitting to all the detected boundaries on the image was completed, the Euclidean distances were calculated between each circle's surface and every other circle on the section, as described in 9.5.1. The center coordinates of the fitted circles were used, as well as their radius, to calculate the surface distances using equation 9.IV. Using the appropriate scaling factor, as described, the distances could be used to produce the number of neighbours each oocyte had within set distances, so that the spatial analysis described in chapters 2 and 3 could be easily reproduced.

6.3 Experimental results

The complete algorithm was tested on microscopic images obtained from imaging neonatal mice up to 12 days of age. The first six images, presented in figure 6.15, were from day 8 mouse ovarian sections, fluorescently stained for MVH and imaged on the confocal microscope. The channel that contains the fluorescent signal from the MVH was used directly in our algorithm, as explained in section 6.2.1 (figure 6.15, d8-Im-1 → d8-Im-6). The final four images in figure 6.15 were from day 12 mouse ovarian sections, prepared for brightfield imaging. Cell nuclei appeared purple (haematoxylin), and oocytes were stained red (MVH). These images were captured on the light microscope using a digital camera, and were imported in our program as *RGB*; the image was split in individual channels, as explained in section 6.2.1, to obtain the correct channel before processing.

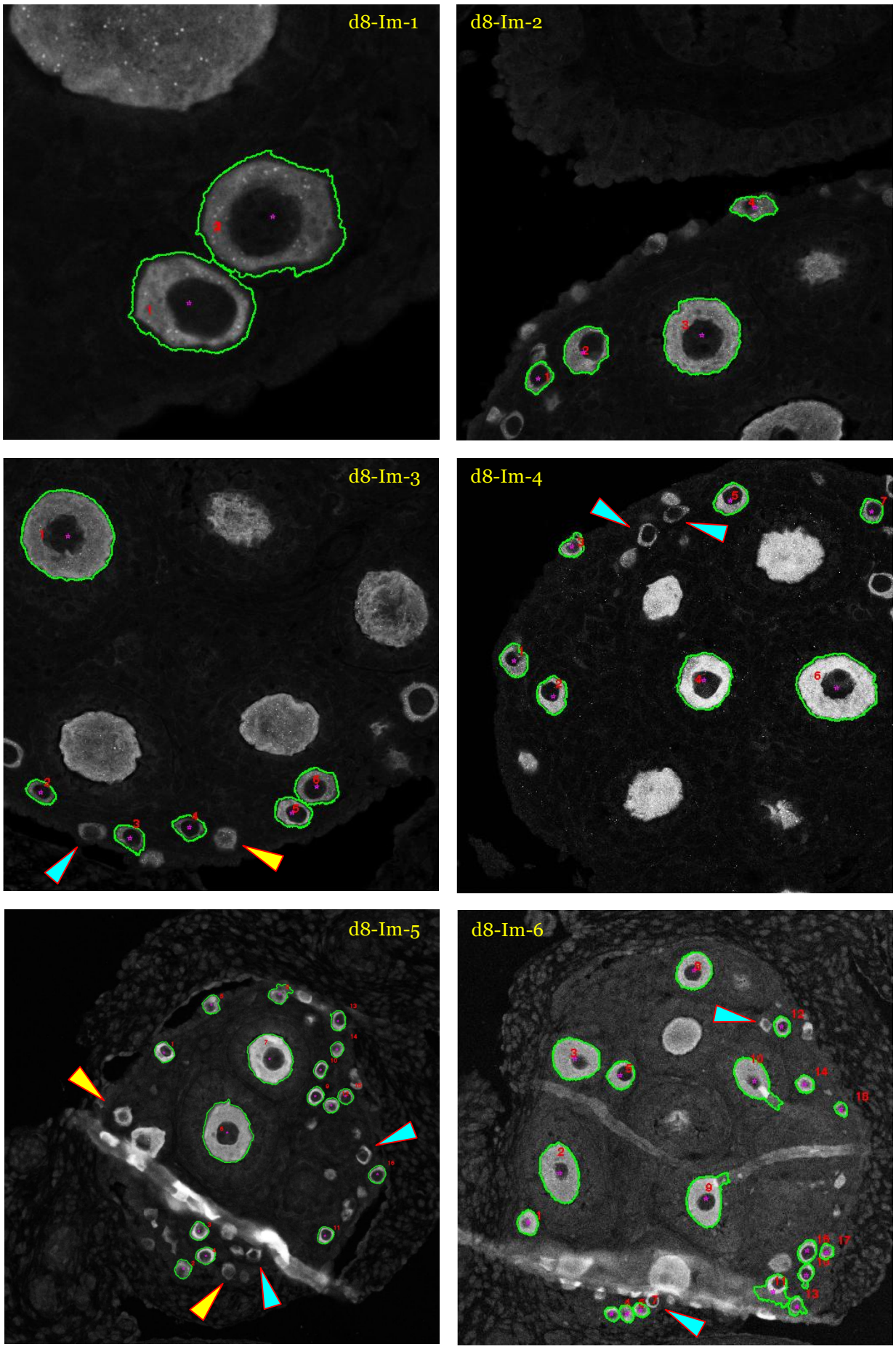


Figure 6.15: See next page for legend

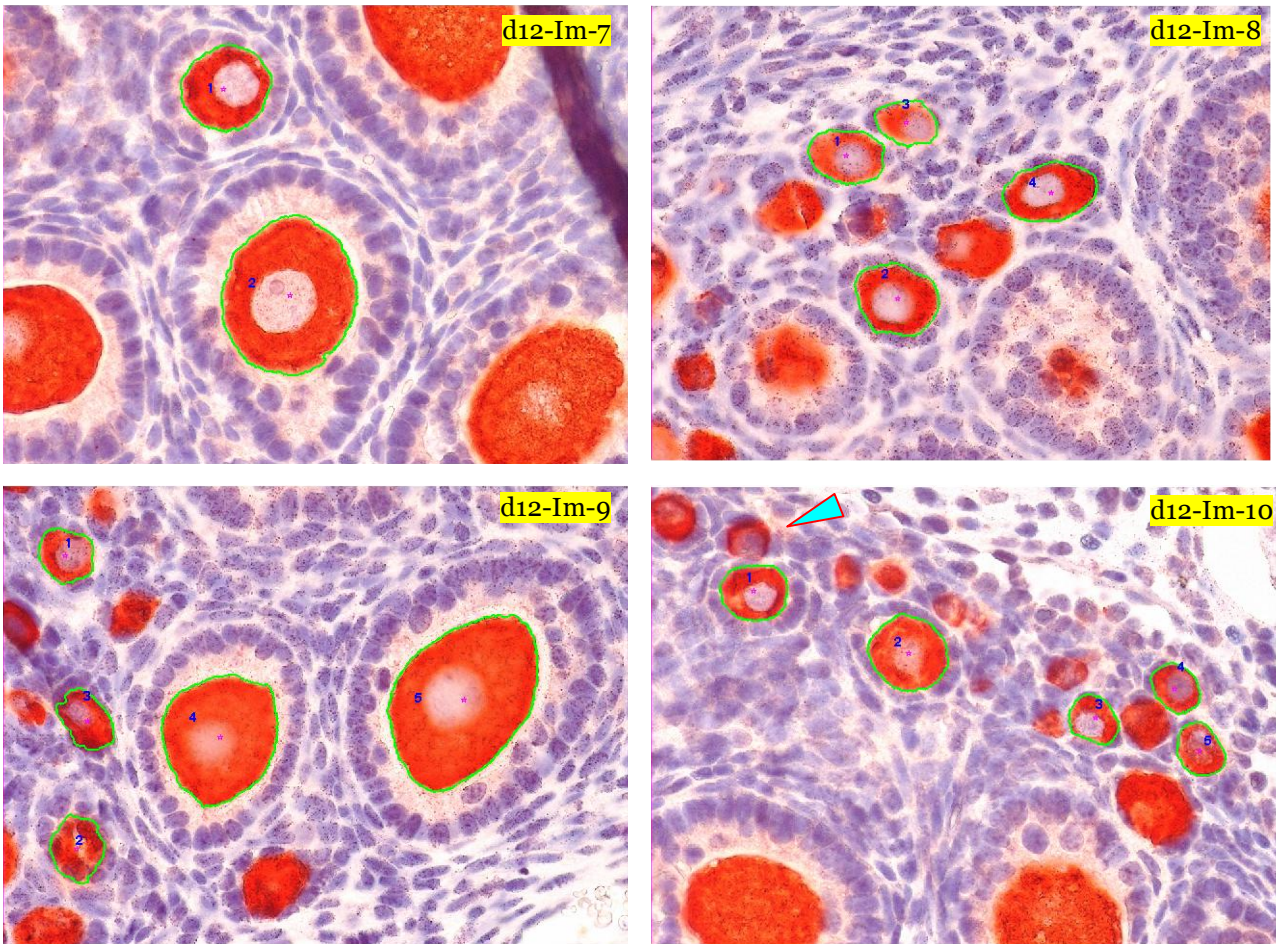


Figure 6.15 \cont'd: Ten ovarian sections used to test the proposed algorithm. The first six images are the MVH channels captured by the confocal microscope; the last four are RGB images obtained from a brightfield microscope, showing the MVH protein in red and the cell nuclei in purple. Green circles surround the oocytes of follicles that have a clear nucleus and are within the image boundaries. Cyan arrows are added manually to point at oocytes missed by the algorithm, because of non-uniform staining; yellow arrows are also added, pointing at oocytes with a fuzzy nucleus. The green boundary lines, as well as the number of each oocyte were automatically generated by the algorithm. The magnification of each image can be found in table 6.1.

The computer program we developed finds the objects of interest by performing the procedure described in the Approach section. Each object that had been recognised had its contour pixels coloured in green. The contours correspond to the actual edge of the oocyte; as next step a circle was fitted on every one of these by the algorithm which was not displayed in this particular figure, as the primary objective of our method was to find the oocytes. Arrows have been manually added to the images to pin-point oocytes missed by the algorithm. Some oocytes appearing as if they were missed, that are touching the edge of the images (figure 6.15, images d8-Im-2 → d8-Im 4) were intentionally excluded from the counting (section 6.2.2). This applies even if a single pixel belonging to the oocyte touched the image edge. The

results of the counting are summarized in table 6.1; first, counts on the sections were manually performed (operator counts), then the algorithm was run and the resulting automatic counts were recorded (algorithm counts).

Table 6.1: Algorithm oocyte counts compared to experimentalist counts on each section of figure 6.15. Note that the magnifications reported here are the objective lenses used, plus the extra zooming occasionally performed on the confocal system, a feature that is not available on light microscopes.

Test Image (figure 6.5)	Magnification	Algorithm counts	Operator counts
d8-Im-1	x63 + zoom x3.4	2	2
d8-Im-2	x63	4	4
d8-Im-3	x63	6	7
d8-Im-4	x63	7	9
d8-Im-5	x20 + zoom x2	16	20
d8-Im-6	x20 + zoom x2	18	20
d12-Im-7	x60	2	2
d12-Im-8	x60	4	4
d12-Im-9	x60	5	5
d12-Im-10	x60	5	6

Overall, the performance of the proposed algorithm was very satisfactory, as there were no false positives, and the oocytes missed were very few compared to those detected (table 6.1 & figure 6.15). False positives could be avoided by ensuring that the staining is uniform, and that there were no defects on the imaged section, such as the folds appearing in images d8-Im-5 and d8-Im-6, figure 6.15, so that the only objects that appear as a ‘bright ring’ are stained oocytes. Regarding the missed oocytes, the algorithm failed to recognize them because either part of the staining was absent (cyan arrows) or their nucleus was quite fuzzy (yellow arrows). Examples of images where follicle parts are missing include images d8-Im-4 and d12-Im-10, whereas in images d8-Im-3 and d8-Im-5 both fuzzy nuclei and partly stained oocytes are present.

6.3.1 Follicle stage estimation

The most important task of the algorithm, which was the most challenging to implement, was to recognize the objects of interest. After completing this process, the feature extraction of the detected object (in our case the spatial properties of the oocytes) was a straightforward task, as it was based solely on calculations performed on the detected objects. These sets of calculations were not image-dependent, like the detection process, they were merely based on the results obtained by the object-detecting algorithm. In section 6.2.3 a detailed explanation of the calculations performed to obtain the oocyte properties and spatial information is given.

Chapters 2 and 3 report specific morphological characteristics of follicle granulosa cells, namely their shape and number of layers formed around the oocyte, which are used to appropriately estimate the follicle's developmental stage. In this case however, the computer program cannot recognize the shapes of the surrounding granulosa cells, a task which can be error prone if automated. Instead, the oocyte diameter can be used as a surrogate measure of developmental stage. Our algorithm takes into consideration only oocytes that have a clear nucleus; therefore the oocyte diameters that were calculated corresponded to an estimation of the largest follicle profile. Consequently, any spatial analysis performed was limited to the follicles that had a clear nucleus, in contrast to the approach implemented in chapters 2 and 3, where all follicle profiles on the section are considered.

The algorithm fits circles onto the boundary of every detected oocyte in a least square sense (section 6.2.3). The oocyte circular diameter is then obtained, which is scaled to correspond to the actual μm units of the section. The results produced by the algorithm were tested by comparing the diameter produced by our program in μm on two of the images we used with the result obtained by manually measuring the oocyte diameters, to verify that the scale of distances calculated is reliable. Figure 6.16 presents two images (d12-Im-7 and d12-Im-10 of figure 6.15) which had the fitted circles drawn in blue by the computer program, with their calculated circular radius values reported on the top left of the oocyte, also printed by the algorithm. The original images were then imported in the LUCIA, where they had their oocyte radii measured, as explained in section 9.3 of chapter 9. The values obtained were added on the images of figure 6.16, at the bottom of every oocyte, and were highlighted in yellow.

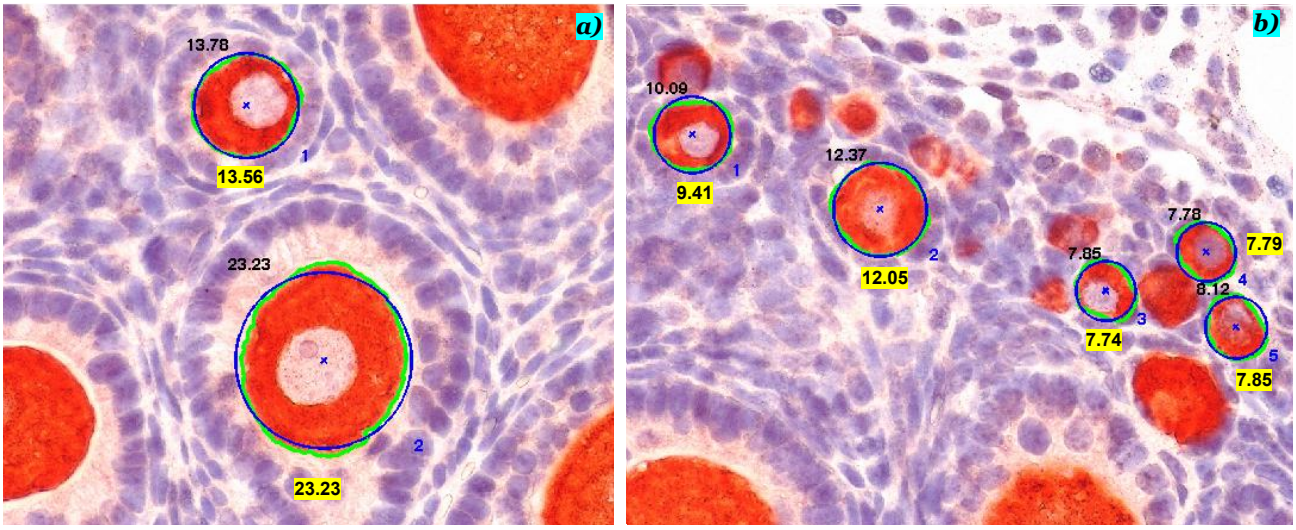


Figure 6.16: Oocytes recognized by the program (green contours) have a circle fitted to their boundary points, using least square fit. The radius of each circle (top left of every oocyte) is scaled according to the image magnification, so that it corresponds to μm. The highlighted bottom values are radii measurements, also in μm, performed in LUCIA (section 9.3) to verify the algorithm's output.

Observing the two radius values for every oocyte of the two images in figure 6.16, it can be safely concluded that the resulting oocyte size estimates from our proposed program compare well with the ones measured experimentally; therefore any distances between follicles, calculated using the Euclidean formula, are also bound to be correct.

The circular diameter of a recognized oocyte corresponds to the diameter of the circle fitted to it, which can be used to estimate the follicle's developmental stage. This was done by setting a threshold between resting and growing oocyte diameter. The threshold is chosen using oocyte diameters of neonatal mice measured in a previous work (Da Silva-Buttkus *et al*, 2009). Table 6.2 presents some statistical information of the oocyte diameters of the primordial follicles collected on day 4, day 8 and day 12 mice. The data from different ovaries were pooled, as they were all normally distributed, and there were no significant differencies (p<0.05) between their means (verified using STATA 8).

Table 6.2: Oocyte diameters of primordial follicles of day 4, day 8 and day 12 ovarian sections. Follicles considered here have a clear nucleus. Assuming that the follicle nucleus is located at the oocyte centre, which means that the diameter appearing on the section, if nucleus is clear, is very close to the actual diameter (Da Silva-Buttkus *et al*, 2009).

Primordial follicle oocyte diameter information	Average	St Dev	Min	Max	Counts
	13.46 µm	2.0	8.1µm	20.65µm	305

From table 6.2 it can be seen that the average oocyte diameter of a primordial follicle in the neonatal mouse ovary is 13.46µm. We want to set a threshold diameter, below which the follicle has high chances of being a primordial (resting). Assuming that the oocyte diameters follow a Gaussian distribution, we consider as threshold t_g:

$$t_g = \mu + 2\sigma = 17.46\,\mu\text{m}$$

where μ is the mean of the distribution and σ the standard deviation. The probability for a primordial oocyte diameter to fall below the chosen threshold is 97%, assuming a normal distribution. Only 8 out of the 305 primordial follicles in our data have a diameter bigger than 17.46µm. This corresponds to a proportion of 97.4%, thus validating our assumption that the selected threshold is reliable. It must be stressed that because it is not possible to automatically assess the exact developmental stage of the follicle, only two developmental categories are going to be considered, *resting* (oocyte diameter < 17.46µm) and *growing* (oocyte diameter ≥ 17.46µm).

As an illustration, the two follicles in image ***a)*** of figure 6.16 are growing (both their diameters are greater than 17.46µm), based on the oocyte size criterion, which is a correct classification according to a visual follicle morphology assessment. Namely, follicle 1 is a primary and follicle 2 is a primary plus (according to morphological criteria presented in section 9.10). In image ***b)***, figure 6.16, follicles 1 and 2 are growing (diameter ≥ 17.46µm), while the remaining three are resting (diameter < 17.46µm). Assessing the morphology of the surrounding granulosa cells, follicles 1 and 2 are classified as transitional, and follicles 3, 4 and 5 are classified as primordial, surrounded by squamous granulosa cells only.

6.3.2 Spatial Analysis

The calculation of the oocyte distances (surface to surface) is also included in the code, which is implemented by calculating the Euclidean distance between surfaces of each oocyte fitted circle (section 6.2.3). For each oocyte, the distance to any other oocyte is calculated, which is used to obtain the number of neighbours of specific developmental stage (resting or growing) within a given radius. As mentioned before, these steps are not image-dependent, so once the oocytes are recognized, the computations for spatial relationships are performed in an automatic way. Note that the spatial analysis in this case does not consider follicle surface-to-surface distances, but rather it is done using oocyte surfaces. This is acceptable, because it was found (Da Silva-Buttkus *et al*, 2009) that there are no significant differences in the spatial analysis results when considering inter-oocyte or inter-follicular distances.

The output of the program is the segmented image with the follicle numbers, as well as a text file containing the spatial information for every oocyte detected. For every oocyte, the computer program calculates its stage, its closest resting follicle, its closest growing, as well as the number of resting or growing follicles within 10, 20 or 50 μm from its surface. This information can be used to apply the logistic regression analysis described in chapters 2 and 3, performed in Stata 8 (Materials and Methods, 9.6), in order to model the proportion of follicles initiating growth in relation to the primordial neighbours. These calculations have been performed on images d8-Im-5 and d8-Im-6 of figure 6.15. These images have chosen for the analysis since they have a high number of detected follicles, and because they represent whole ovarian sections, in contrast to the other images in figure 6.15, which are only parts of sections. We consider groups of oocytes that have 0, 1 and 2 resting neighbours within 10μm from their surface. The proportion of these growing oocytes is computed, by performing logistic regression, and is plotted in figure 6.17. Robust standard errors, clustered by section were used to compute 95% confidence intervals, where the detected proportions are not 0 or 1 (section 9.6). All these calculations were performed in Stata 8; our algorithm does not perform the logistic regression.

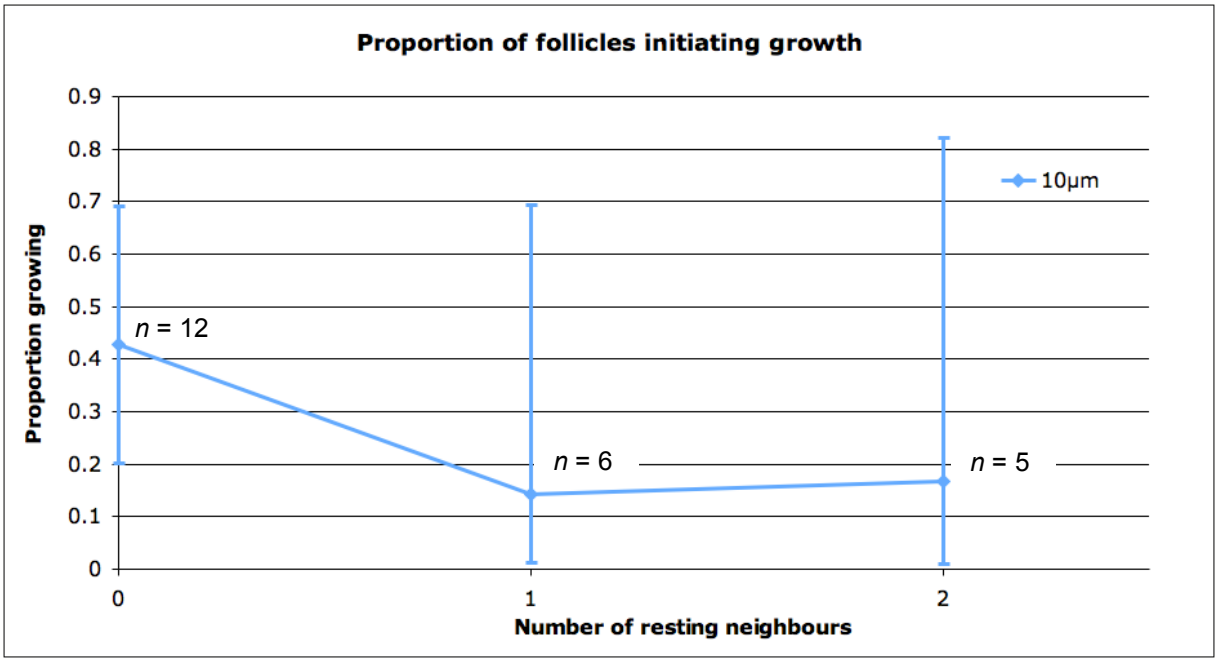


Figure 6.17: Proportion of follicles that have initiated growth in each category of follicles that have 0, 1 or 2 resting follicles within **10μm** of their oocyte surface. Error bars are at 95% confidence intervals. All data collection, as well as the follicle stage classification was performed automatically by our proposed algorithm. The *n* numbers reported next to each proportion are the number of follicles that are included in the analysis, from the two sections that were considered. Large confidence intervals are due to the small *n* numbers.

Figure 6.17 shows the same trend as the one observed in the neonatal mouse in chapter 3, and in the work of Da Silva-Buttkus *et al,* 2009. Namely, if a follicle has at least one other follicle within 10μm from its oocyte surface, the probability of this follicle to be growing drops by at least 50%, as compared to having no neighbours within its proximity. However, the differences presented in figure 6.17 are not statistically significant (confidence interval overlap), mainly due to the fact that there are not many follicles in the sections used. Therefore further tests are required once more tissue becomes available, so that more follicles can be sampled, which should significantly reduce the length of the 95% confidence intervals. Generally, the results are very promising, seeing that the trend is maintained, which corroborates further the hypothesis of local inhibition of follicle growth by the pool of resting follicles.

It must be stressed that the results appearing in figure 6.17 are obtained with minimal user input, and they take less than 10 minutes! The method we formulated recognizes the oocytes and produces the oocyte spatial information from an ovarian section in approximately 10 seconds. Input images are either 1024x1024 pixels, 8-bit, occupying 1MB of disk space, which is a single channel obtained by confocal

microscopy, or *RGB* images captured on the light microscope, 976x716 pixels, occupying 2MB of disk space. Analysis on these images was performed using MATLAB for UNIX, version r2007a, run under X11 on a Macintosh platform with a 2.4GHz dual core processor. The rest of the time is consumed to import the data in Stata 8, perform the logistic regression analysis and plot the results using Excel. Performing the spatial analysis manually, even for the 18 oocytes of image d8-Im-5, figure 6.15, would require more than an hour.

6.4 Discussion

In this chapter we propose a new method for identifying oocytes in ovarian section microscope images, and for calculating their size and coordinates. Although there is a multitude of tools for image analysis, our aim is to automate the process and minimize user intervention, in parallel to reducing operator variability through subjective classification. Our algorithm is based on general segmentation principles (filtering, thresholding, morphological operations, watershed transform etc), and is applied on specially prepared tissue stained for the MVH protein.

The results obtained in terms of counts are very satisfactory, as all the oocytes that have been identified were healthy and well defined. Those oocytes missed by the algorithm were non-isotropically stained, attached to one another or parts of them were dark, and could very easily be missed even by a trained experimentalist. Therefore optimizing the staining with the MVH, to make sure that all oocytes are clearly stained is a crucial requirement. There are occasionally some false positives in the sections where there are folds and the staining is intense. Adding measures of structure circularity, which we have implemented, can eliminate some of these mistakes. These are common problems that have to be dealt with when performing image segmentation (Young *et al*, 1998), due to objects of interest having different morphology.

In terms of follicle classification, using the oocyte diameter to estimate the follicle stage has proved itself to be an efficient way of assessing the developmental stage, without the need of implementing complex and possibly error-prone methods for recognizing the shape of nearby granulosa cells. According to the published data (e.g. Picton, 2001 and Da Silva-Buttkus *et al*, 2008), oocytes start growing

simultaneously to the granulosa cell shape transformation, when the follicle initiates growth. Our algorithm can detect this increase in oocyte size and classify the follicle as being growing. Occasionally, a follicle may appear to be surrounded by flattened granulosa cells, but have an increased size of oocyte. There is high likelihood that there are cuboidal granulosa cells in the surface above and below the visible transect that have been missed, and therefore the follicle will be misclassified. These cases are evaded when using the oocyte diameter for follicle staging. The estimation is based on the diameter of the least square circle fitted to the oocyte contour points. From there, it is straightforward to calculate the number and stage of neighbouring oocytes to each target oocyte, and perform the logistic regression analysis.

The algorithm presented in this chapter has only been applied only on neonatal mouse ovarian section images with the MVH stained oocytes. If it were to be applied to an adult ovary, caution should have been taken as there is a significant number of pre-antral, antral and pre-ovulatory follicles the oocytes of which would not be stained by the MVH antibody. In this case, other markers can be used in combination with the MVH, such as the oocyte-specific protein GDF-9 (Guéripel *et al*, 2006). This would enable the method to count all the follicles present, and would provide with an additional stage-classification measure based not only on the size of the oocyte but also on the marker for which the oocyte is stained.

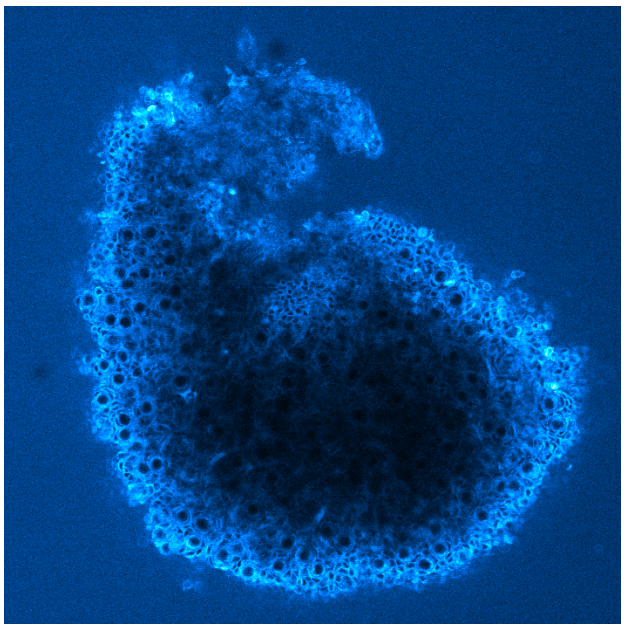
As a future direction, this method can be extended to recognise the MVH stained oocytes on the optical planes obtained from our whole mount imaging method presented in chapter 5. In these images, as reported in chapter 5, oocyte overlapping represents a problem for object recognition. This problem may be solved by means of improving the imaging technique, using for example two-photon microscopy where optical planes are much thinner, as discussed in chapter 5. Additionally, extension of the algorithm is also possible in order to automate counting of follicles using the disector in the stereologic technique. In particular in chapter 5 we presented a fast new method to implement the stereologic technique, based on overlaying two optical planes of two different colours. The algorithm presented here can be easily modified to recognize specific colour information, therefore taking into account only oocytes present in the look-up section. Furthermore, the oocytes recognized would have their diameters accurately computed, instead of the manual estimation currently performed. This would speed up the whole process remarkably.

Conclusions

Automating specific time-consuming tasks in biology, like follicle counting, can facilitate the work of the experimentalists. However, human input is always essential; this program we developed is merely a way of eliminating workload and subjectivity during image analysis. As previously discussed, new methods need to be established for the advancement of follicle counting, that can efficiently and reliably provide results. The technique presented in this chapter can be extended to perform stereologic counts by recognizing a specific colour in two overlayed images (as in figure 5.11), and in combination with the follicle staging using oocyte diameters, improve the results obtained as described in chapter 5. Furthermore, it can be readily used to rapidly obtain follicle sizes and spatial coordinates, which can be either used to conduct spatial analysis (figure 6.17), but using larger section with more follicle numbers, or used as input to construct simulated ovaries.

Chapter 7

Time-lapse imaging of a whole juvenile mouse ovary: A study for follicle motility



7.1 Introduction

Up to date, most of the experiments for the understanding of the ovarian ageing mechanisms are performed in a comparative scheme. This means that ovaries from animals of a specific age after birth, or sometimes at specific points during foetal development, are obtained and fixed. These are then used in various studies for determining follicle numbers, hormones present, protein receptors or any other biological structure or biochemical component. As discussed in chapter 4, all these studies are subject to biological variability, which means that the resulting quantified components vary among tissue of the same species and strain. Each organism is unique, and no results can be safely extracted from a single experiment. Instead, large sample sizes must be studied, in order to draw scientifically equitable conclusions for the broader behaviour of the species (Myers *et al*, 2004, Faddy and Gosden, 2007).

The need for large numbers of experiments could be reduced, if the time parameter is added to the experiments. Valuable information regarding the function of various dynamic processes, such as follicle initiation and growth, could be gathered by monitoring the ovary of an animal in real time, instead of capturing snapshots at different time points, of ovaries from different animals. Such experiments are possible, and their output efficiency is increasing as imaging and tissue staining technologies advance.

Follicle dynamics, examined by means of time-lapse imaging, as in the work by Miller *et al*, 2002, where two-photon microscopy is used to examine the lymph node cells in real time, in combination with appropriate staining, could prove very useful in our study regarding the spatial arrangement of the follicles in the ovary. Currently, our models (eg Da Silva-Buttkus *et al*, 2009) and techniques are implemented based on the assumption that the follicles are immobile and do not rearrange themselves in the live ovary; an assumption that should be tested. Moreover, extrusion of oocytes from the ovarian surface epithelia (Hiura and Fujita, 1977, Wordinger *et al*, 1990, Mackay *et al,* 1992, Kerr *et al*, 2006), which involves follicle repositioning, is an important phenomenon contributing to the overall reduction of follicle numbers in the neonatal mouse ovary, but the aetiology and mechanism behind it remains unknown. A time-lapse experimental approach could provide with further insight into the matters discussed above, which would broaden our understanding of the early follicle pool establishment and progression.

In this chapter, we will attempt to demonstrate how imaging techniques can shed light onto dynamic processes in the neonatal ovary. A culture system is established, capable of sustaining a mouse ovary alive for a short period of time, during which the sample is subject to time-lapse imaging using laser scanning confocal microscopy. We are going to present preliminary results from these experiments regarding basic follicle motility, as well as ovary and cell viability in culture, when subject to laser exposure. Furthermore, potential future experiments are going to be proposed and discussed, which can be an extension to the work presented in this thesis, as part of the effort to understand ovarian ageing. These experiments deviate from the classical approach used for solving these problems; rather, new technologies, combining different scientific disciplines are proposed, giving a multi-disciplinary approach to the experimental design. These experiments could provide

with more information about the dynamics of regulation of follicle growth, which can easily then be modelled. Mathematical modelling, as discussed in chapters 2 and 4 can help significantly by focusing biological research for early follicle growth regulation at specific directions, which is the primary purpose of our research field.

7.2 Materials and experimental design

The culturing, staining and imaging techniques presented in this section have been tested and optimized by conducting the experiments on cultured KK1 granulosa cells, which have been kindly provided by Dr Jalini Joharathnam (originally provided by Professor Ilpo Huhtaniemi). After optimization, the techniques are applied to freshly obtained mouse ovaries. Experimenting with different conditions and materials has been essential in order to compile the set of methods that would ensure maximum survival of the ovaries in the culture, as well as optimal imaging, producing high-quality images of the cultured mouse ovaries. The optimization of media and dye concentrations, as well as imaging times to minimize phototoxicity ensuring a high signal-to-noise ratio consumed a significant amount of the time dedicated to this project. The optimal protocols for culturing, live staining and imaging of a juvenile mouse ovary are presented in detail in section 9.16 of the Materials and Methods chapter. Mouse ovary collection is presented in section 9.12, and was carried out by Dr Mark Fenwick.

7.3 Results

KK1 mouse granulosa cells were cultured and imaged (see section 9.16) before using mouse ovarian tissue, in order to assess viability of cells in the presence of the BODIPY (lipid dye) and DRAQ 5™ (nuclear dye). Cells were cultured in 8 well coverslip chambers as described in Materials and Methods. After 30min incubation, four of these wells had their culture medium replaced by fresh media, without any BODIPY or DRAQ 5™ content. The cells were left to incubate for three days. Every day, the cells were examined using an inverted fluorescent microscope. Most of the cells that did not have their media replaced were dead by the second day of observation, while the rest of them were in good condition (figure 7.1).

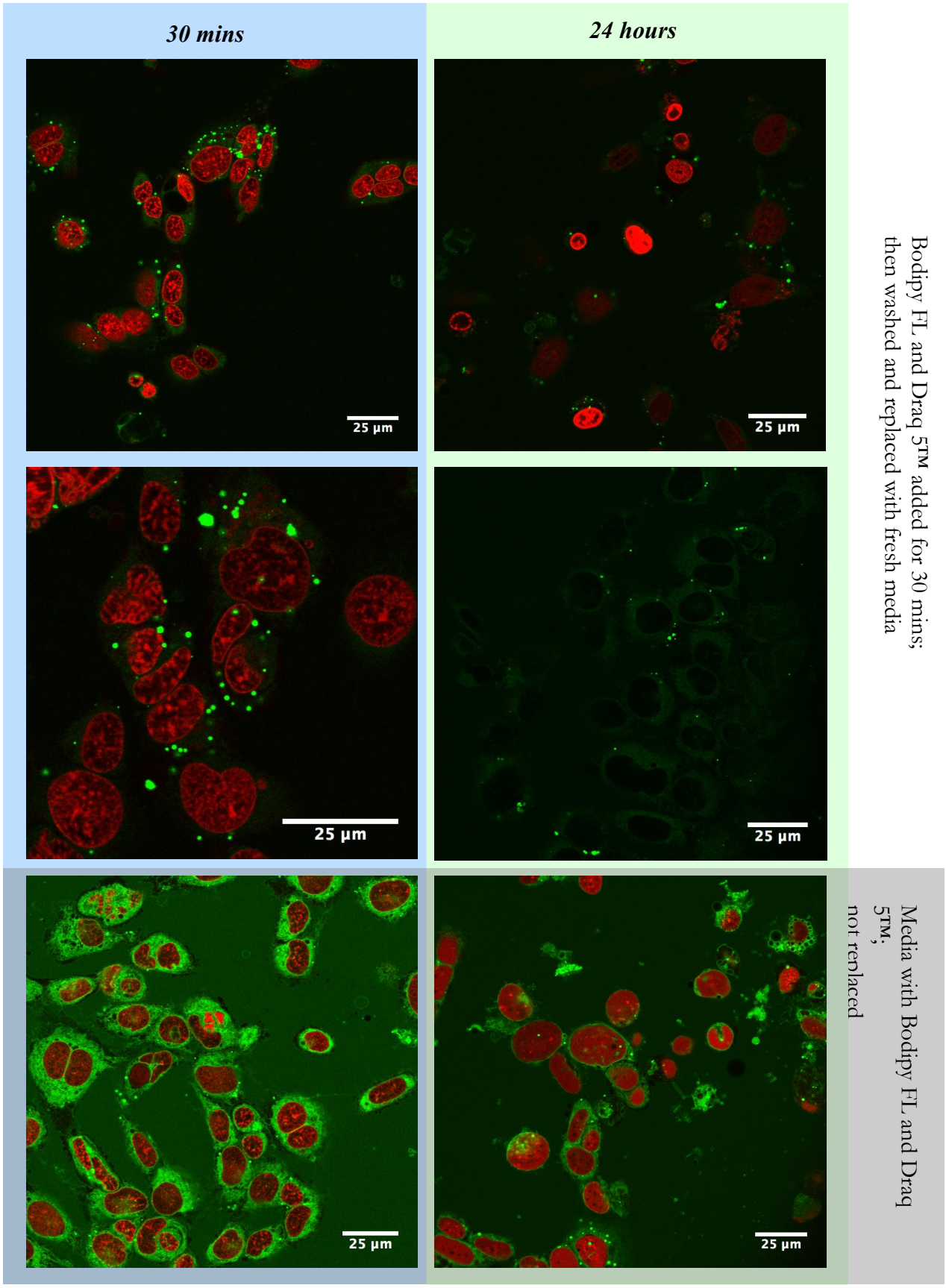


Figure 7.1: Cultured human KK1 cells, stained using the lipid dye BODIPY FL and nuclear stain Draq 5™. Blue column images of cells were obtained 30 min after culture initiation. Green column images were obtained after 24h of culture. Top four images depict cells which had the dyes added to their media, but were washed and had their media replaced by dye-free media before imaging. The two images depict cells which did not have their media replace; these cells were cultured in the presence of both dyes. All images were obtained on a confocal microscope using the same

Figure 7.1 shows that if the dyes are washed from the culture, the intensity of the lipid layer is reduced (figure 7.1, green column), meaning that the laser power needs to be increased in order to obtain good contrast, at the cost of additional phototoxic damage. Some of these cells can survive for up to three days (data not shown). If however the media is not replaced and cells are cultured in the presence of both dyes, the staining intensity does not attenuate (figure 7.1, bottom row); these cells however die by the second day (data not shown). From these tests (figure 7.1), we concluded that the culture medium with the BODIPY and DRAQ 5™ dye could sustain the viability of KK1 cells for at least one day, which is a sufficient incubation time for performing time-lapse imaging. The neonatal mouse ovaries were not going to be cultured for longer than a day, while being imaged. It should be noted at this point that the DRAQ 5™ nuclear dye was not used in the ovarian cultures, as it would not contribute to follicle tracking (see chapter 5, figure 5.5), and would unnecessarily increase tissue laser exposure. The concentration of BODIPY and the laser power used were optimized using the KK1 cells, as well as some whole ovaries; the optimal protocol is reported in section 9.16. It was decided to culture the whole ovaries in the presence of BODIPY, as this would reduce the required laser power for imaging.

Figure 7.2 presents an image of an entire neonatal mouse ovary in culture, captured on the confocal microscope (Materials and Methods 9.16). The optical section reported in Figure 7.2 is taken from the middle of the ovary, using a x10 magnification objective. The dark area in the middle is created due to light scattering in the tissue; a light gradient is created when imaging in large depths inside the tissue (images 7.2*b* & 7.2*c*).

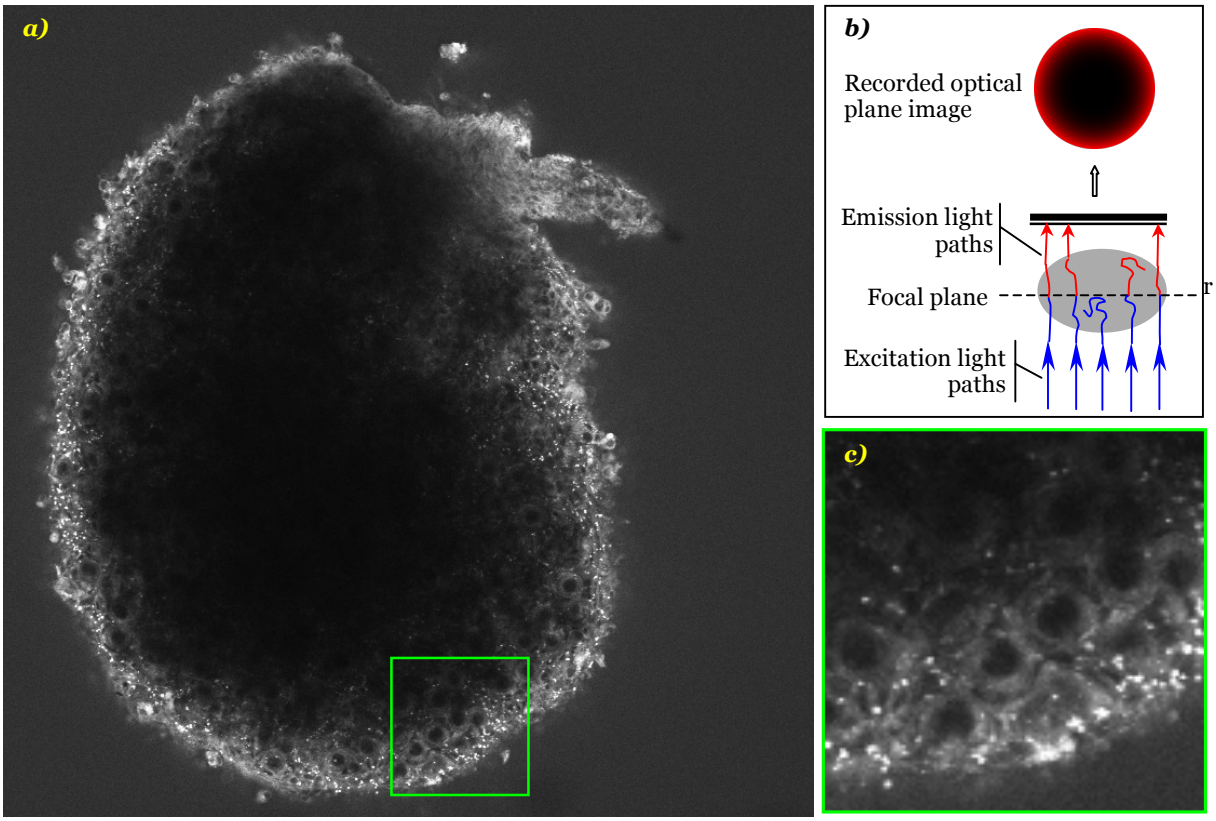


Figure 7.2: ***a)*** Whole live ovary in culture with media containing BODIPY (0.05mM), captured using a x10 magnification objective. Dark area in the middle is due to light scattering in non-cleared tissue volumes, schematically illustrated in ***b)***. Magnified image ***c)*** shows the gradient in detail. There is also additional fluorescence from the media, which contains the dye, but this does not affect the ovarian structure imaging.

Imaging is performed for approximately 12h on every ovary, imaging a small part of the base of the ovary, which is equilibrated on the coverslip at the bottom of the culture well. We found that imaging through the ovary while in culture, at an interval of 9 minutes, obtaining 8 optical sections through the tissue at a 1.8µm step does not significantly affect the whole tissue viability. Due to the frequency of the imaging (and subsequent laser exposure) there is a phototoxic effect on the ovarian tissue; most of the follicles alive at the starting point appear to have degenerated, but because the focus is at a small part of the tissue, near the bottom of the coverslip chamber, this leaves the rest of the ovarian volume unaffected (qualitative assessment of whole mount fixed ovary after imaging, stained with MVH; figure 7.3).

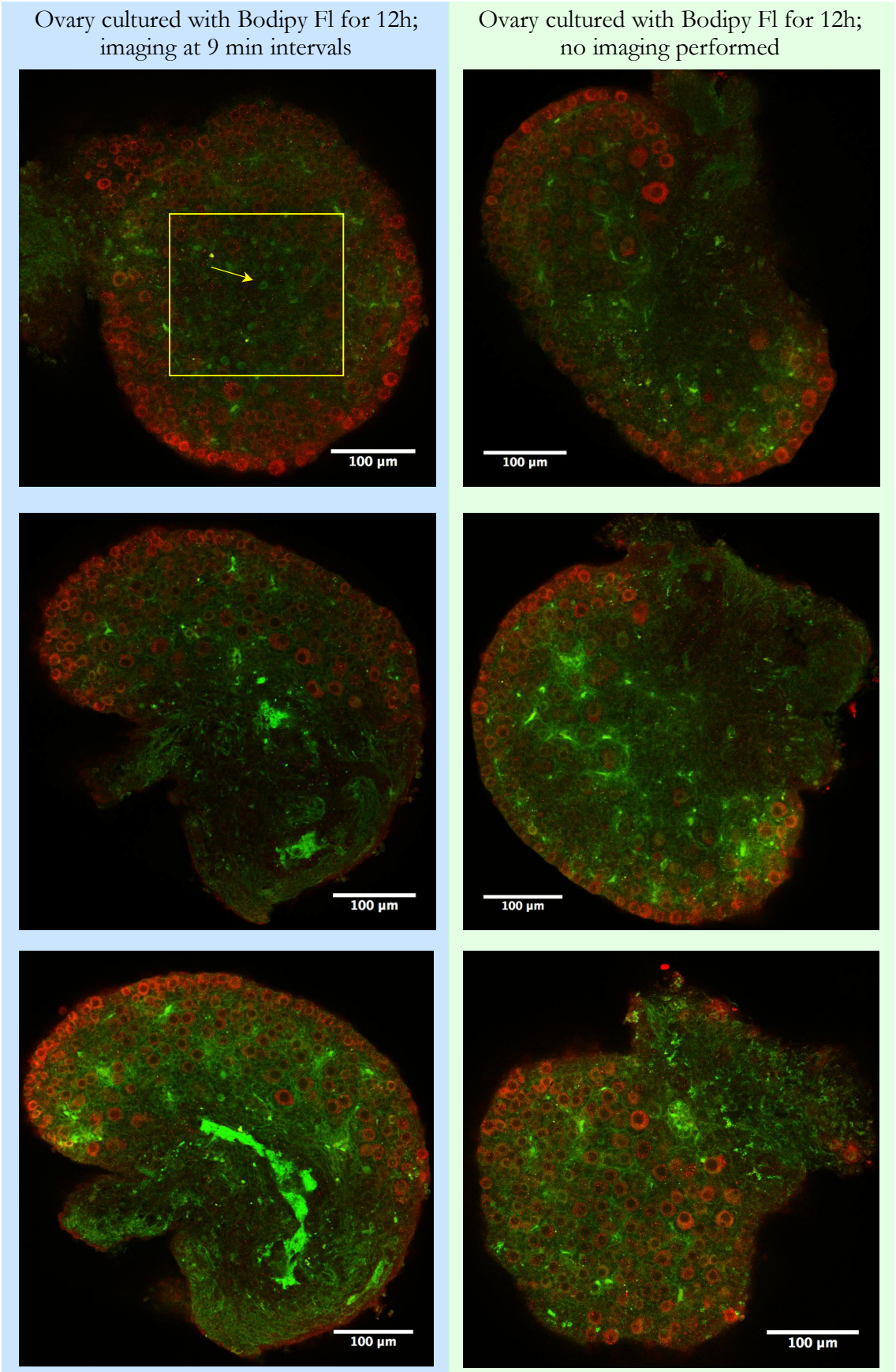


Figure 7.3: Two day 8 ovaries cultured in media with BODIPY FL for 12h. One was taken for live imaging at 9min intervals (blue column), while the other was kept in a dark incubator. After the 12h, both were fixed in Formalin, stained for MVH and imaged using our method (chapter 5). Images are optical planes from whole tissue imaging, as overlays of the BODIPY (green lipid structures) and MVH (red healthy oocytes). In both cases, follicle viability does not seem to be severely affected (visual comparison). The yellow box in the first image shows an area where there are lots of degenerated follicles (green structures – similar to the one marked with a yellow arrow). This may have been the site of the time-lapse imaging. All optical sections can be found in supplementary material

Figure 7.3 reports optical planes of two day 8 ovaries; one was taken for time-lapse confocal imaging as described, obtaining 8 optical planes every 9 minutes, using the 488nm argon laser. The other ovary was kept in a dark incubator, under the same culturing conditions. Both were cultured in the presence of BODIPY FL. These were fixed in Formalin after 12h of culture, and following the procedure presented in chapter 5, were stained for MVH, chemically cleared and imaged on the confocal microscope. Because of the BODIPY presence in the culture media, lipid structures could also be observed (green on images of figure 7.3), together with the MVH (red oocytes).

By qualitatively comparing the optical planes of the two ovaries, one can conclude that the effect of the time-lapse imaging did not have an extreme effect on the overall follicle health. There are some peculiar structures appearing inside the time-lapse imaged ovary (figure 7.3, third image in blue column), but may be a stain artefact. It is interesting to examine the first image in the blue row of figure 7.3, where there is an area rich in degenerated small follicles (yellow box, degenerated follicles are similar to the one pointed by the yellow arrow). This optical plane was obtained close to the edge of the ovary; there is a good chance that the marked area is within the volume that was being imaged during the time-lapse experiment. As mentioned before, by the end of the time-lapse imaging there are a lot of degenerated follicles (also discussed in the following section).

7.3.1 Observing live follicle morphology and behaviour

Images are obtained using single photon laser scanning confocal microscopy through a small volume in the cultured tissue. No optical clearing was performed for the time-lapse imaging, as this is a cytotoxic procedure. Therefore significant light attenuation happens while imaging the living tissue (figure 7.2); this still enables images to be recorded, displaying follicles sufficiently clearly, but imaging is much more effective at small depths through the ovary. Figure 7.4 presents two optical planes of a d10 mouse ovary at the time the imaging is initiated, as well as the same optical planes when the imaging is terminated after 12 hours. The focal planes presented in this figure are the starting optical sections at approximately 2 – 3μm

inside the tissue (7.4*a*, 7.4*c*) and the final optical section 12.6μm away from the starting section (7.4*b*, 7.4*d*).

Images 7.4*a* and 7.4*b* show that a clear morphology of the ovary can be obtained using the BODIPY lipid stain. Images *a)* and *b)* are captured approximately 20 minutes after the tissue was placed in the culture media; the BODIPY hasn't diffused completely in the entire tissue. In images *b)* and *d)*, the overall image intensity is much higher, as the staining of the tissue is saturated, after 12h. Moreover, as imaging progresses further inside the tissue, the emitted light attenuates significantly. The images that are obtained at approximately 15μm inside the ovary have dark areas, where follicles are difficult to track; therefore extending the imaging at greater depths would be futile. Nevertheless, because of less light scattering around the ovarian edge (image 7.2*b*), the area close to the ovarian surface appears to be of similar intensity to the images of the initial optical sections, allowing the observation of follicle activity.

Images obtained are much clearer during the first 2h of imaging, as the BODIPY stained cell membranes and lipid structures are subtler. The bright spots appearing in the cells are most probably lipid vesicles, and as time progresses, their fluorescence intensity increases since the whole sample is soaked in the BODIPY stain, until they are saturated (images 7.4*c* and 7.4*d*). In addition, at the beginning of imaging most follicles are in good condition. This can be observed in images *a)* and *b)* of figure 7.4, where green arrows are drawn to point at two healthy follicles, recognizable by the dark circular nuclei, surrounded by the lightly stained oocyte and spotted granulosa cells. When follicles are about to die, the dark nucleus becomes blurry, as the follicle breaks down and shrinks. Furthermore, their staining in our images appears brighter as more BODIPY stained lipid vesicles accumulate in the dying follicle volume (Escobar *et al*, 2008). Dead follicles are marked with a yellow arrow on figure 7.4. A well-shaped live follicle, followed until it died, is shown in figure 7.5. Images in figure 7.5 are obtained from d10 mice, at the lowest focal plane.

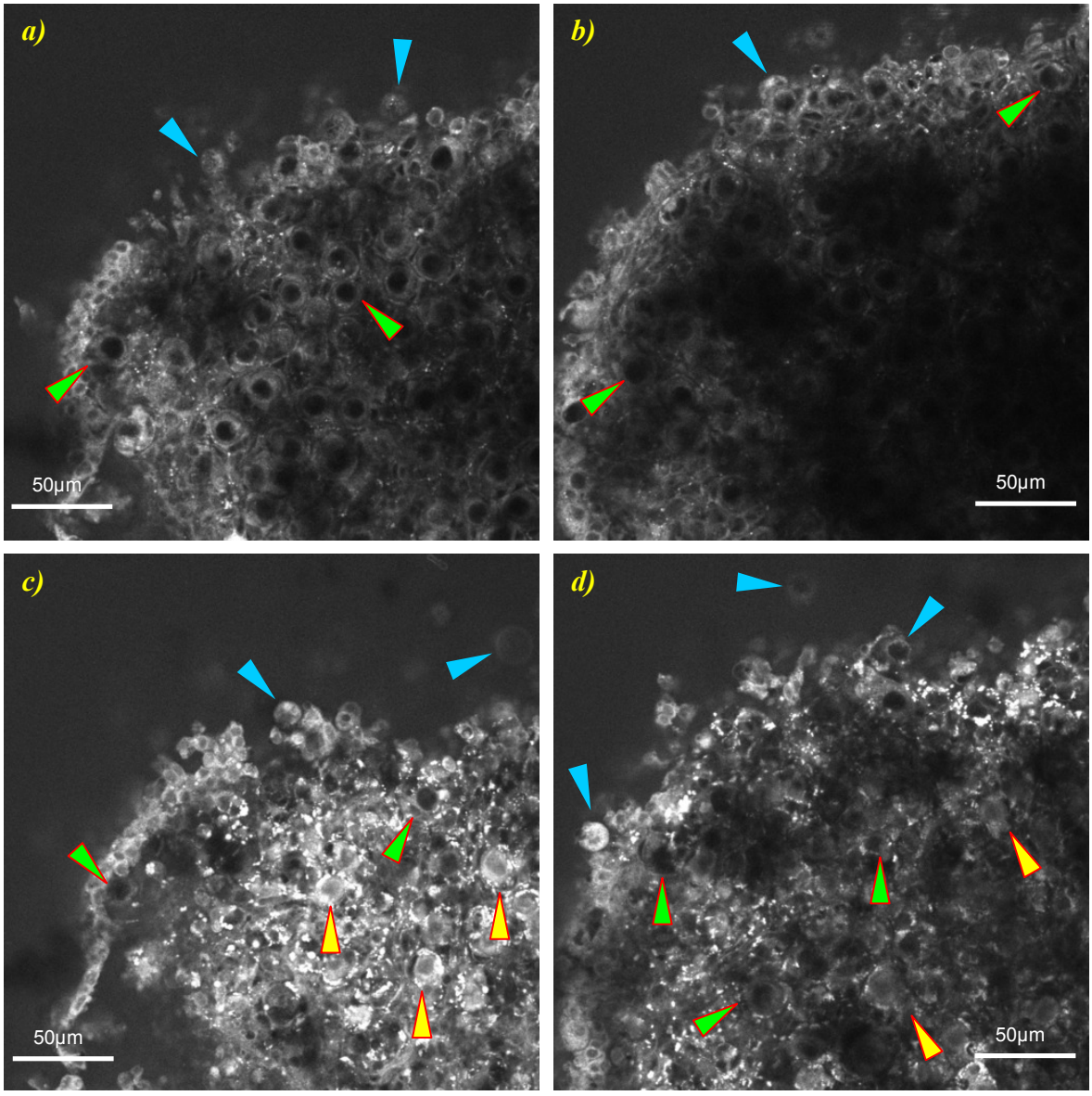


Figure 7.4: Confocal images of a cultured ovary in BODIPY containing media (0.05mM). Images ***a)*** and ***b)*** are obtained at the beginning of the culturing, while ***c)*** and ***d)*** are the last images captured, after 12h. Images ***a)*** and ***c)*** are the starting focal plane, approximately 10µm in the tissue; ***b)*** and ***d)*** are 12.6µm deeper. Cyan arrows point at oocytes discarded from the ovary, green arrows point at healthy follicles and yellow arrows point at dead follicles.

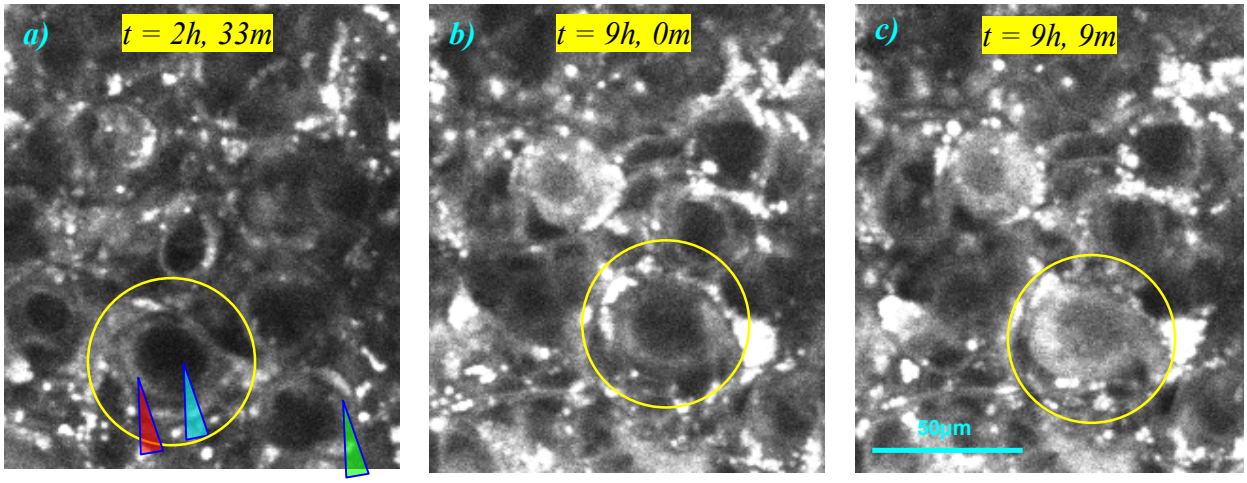


Figure 7.5: Parts of day 10 cultured mouse ovarian tissue, imaged for 12h. All three images are obtained at the same focal depth, with the same laser intensity. Healthy follicles have dark circular nuclei (blue arrow) and faded oocytes (red arrow). Sometimes, vesicles in granulosa cells can make some of them visible (green arrow). Circled follicle is the same in all images, shown after 2h and 33mins in culture in image ***a)***, after 9h in image ***b)*** and after 9h and 9mins in image ***c)***, where it died. Follicle is not in the same position, as there is constant slight re-arrangement of follicles in the ovary, which ceases as soon as a follicle dies. All three images are of the same scale (scale bar appears in image ***c)***).

An interesting finding that is shown in figure 7.5 is that follicles do slightly rearrange themselves in the ovary, which appears to be a dynamic system with the follicles not staying still. However, this movement is not significant, it is more of a 'wobbling' of the follicles as the images are captured in different time-points (yellow cirled follicle is in different position after ~6,5h). Therefore this random follicle movement should not affect the results obtained from the spatial analysis performed in chapters 2 and 3. In supplementary material the optical planes can be additionally found in the form of animations, one animation for each optical plane, and for each ovary imaged. These animations show clearly this random follicle movement. A few images from an image sequence from a day 9 juvenile mouse have been selected and shown in figure 7.6, to demonstrate the magnitude of follicle movement; it shows that movement is confined to a few micrometers within its neighbourhood (green and cyan ellipses in figure 7.6). More specifically, follicles 'wobble' around a small area, in a random manner, without travelling to a specific direction. This was the case in all cultures and all optical planes of the ovaries that were cultured: there is no significant translocation of follicles from one place to the other.

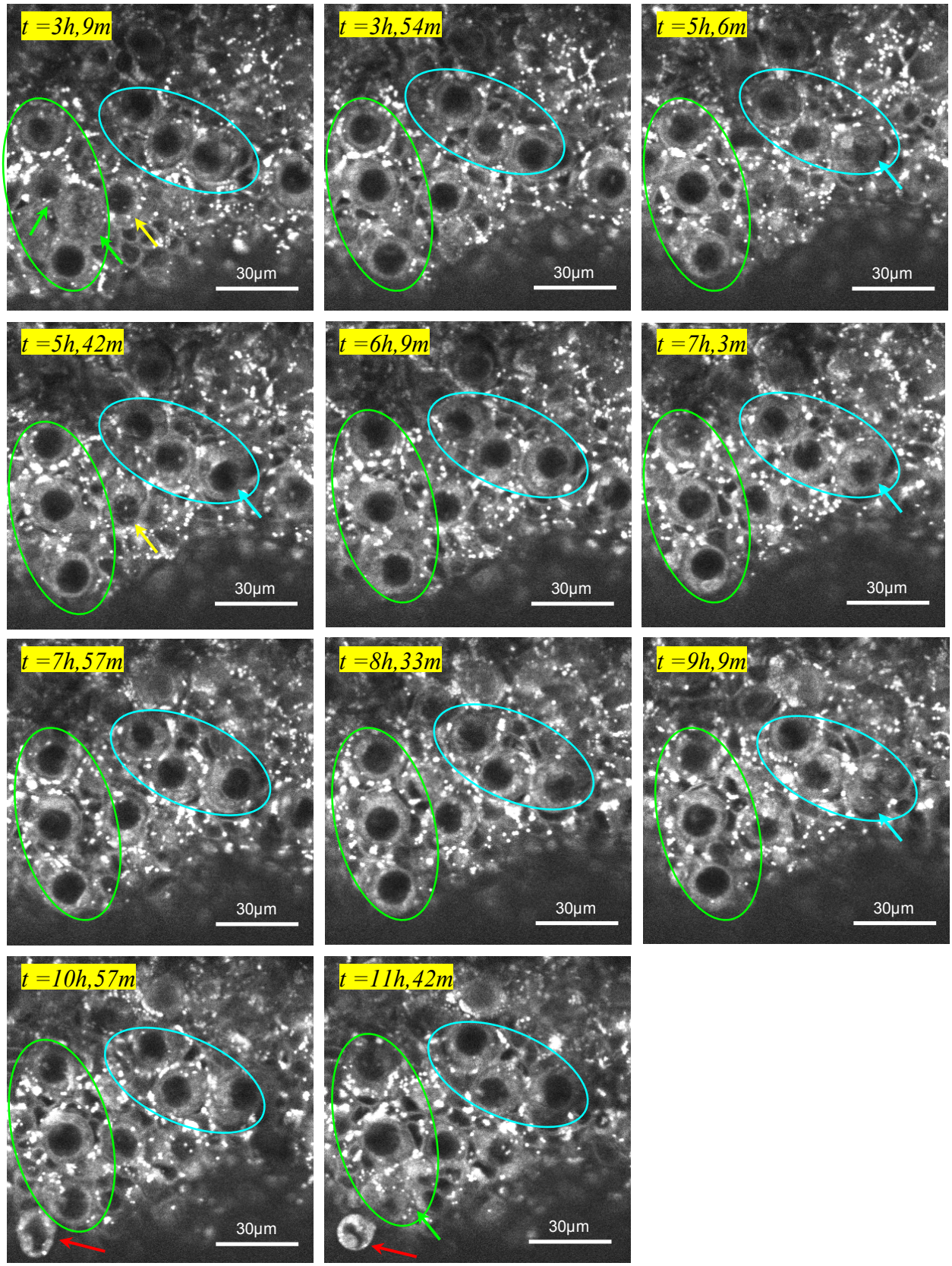


Figure 7.6: Time-lapse optical planes from a cultured day 9 mouse ovary. Depth of imaging is approximately 21µm inside the tissue. Two ellipses (height of the green ellipse is approximately 60µm) have been drawn to mark groups of follicles in various timepoints. Ellipses are of same size in all images, showing that relative movement of follicles in present but minor (less than 5µm), over approximately 9 hours. Yellow, green and cyan arrows show follicles that moved to the optical plane above or below the current. Red arrows show an extruded oocyte. All time steps are available in supplementary material.

Another intriguing and frequently occurring phenomenon that can be observed from the animations in the supplementary material, also pinpointed in figure 7.6 by the red arrows, is oocytes being expelled from the ovarian surface epithelium. This is an event that has been mentioned in the literature for a long time in a descriptive manner, by observing sections where oocytes are located into the peritoneal cavity (Hiura and Fujita, 1977, Wordinger *et al*, 1990). Up to date, there is no published work in the literature that reports time-lapse imaging of this process, therefore this is the first time the phenomenon is recorded in real time. In the next section we will give a more detailed description of this phenomenon.

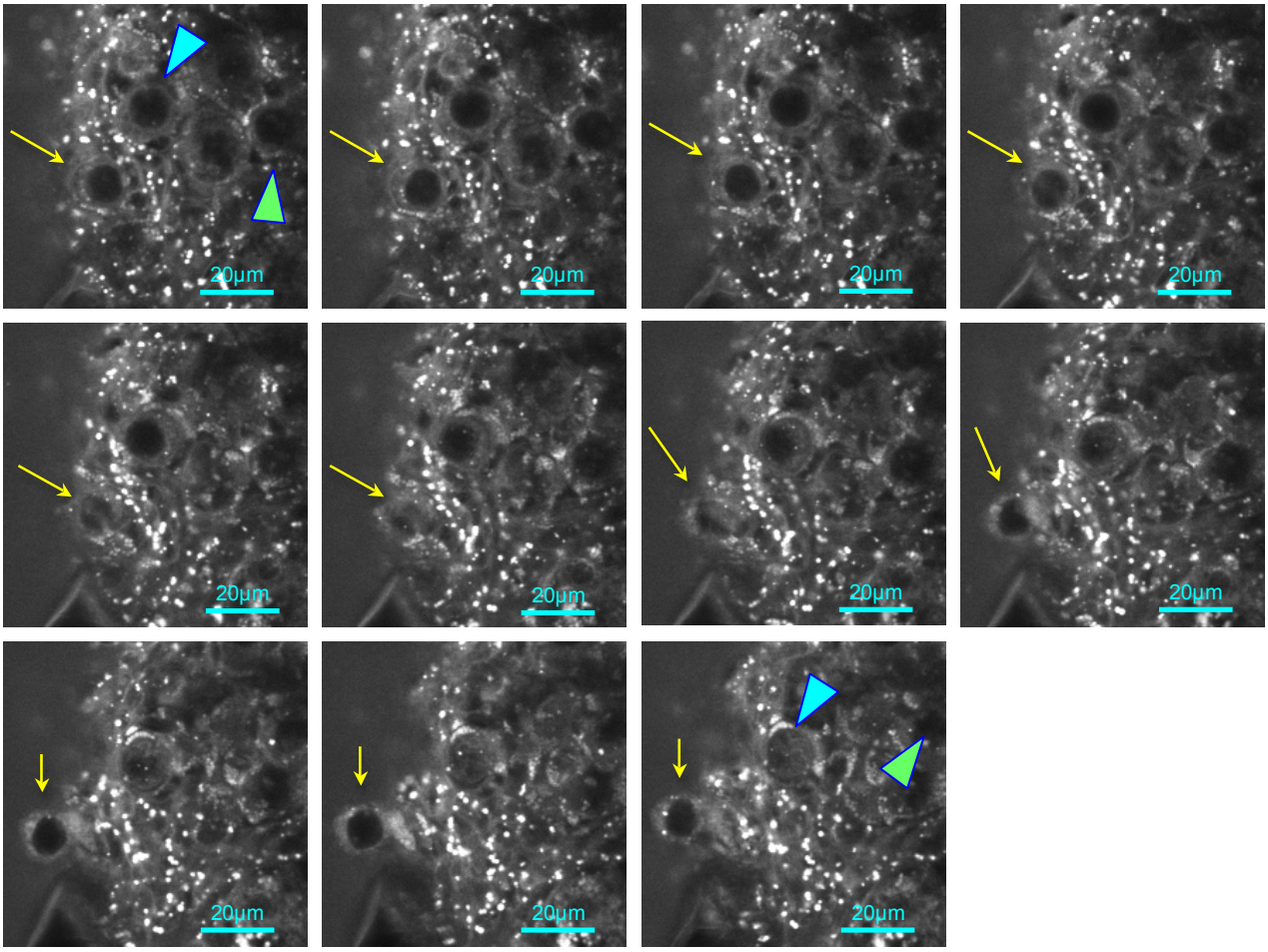


Figure 7.7: Image sequence showing an oocyte being expelled from a neonatal mouse ovary. Imaging here is not performed every 9 minutes, rather every 30 seconds (each frame is 30 sec later than the previous), so that the phenomenon can be recorder in detail. Yellow arrows point at the follicle that is discarded; arrowheads point at two follicles that slightly rearranged. Animation from which the sequence is obtained can be found in supplementary material.

7.3.2 Follicle motility

Our imaging technique can provide insight into follicular motility, as it is able to show the repositioning of the small follicles as time progresses. As shown in figure 7.6, follicles do move, but the movement is minor and random. There is no significant repositioning or movement over distances greater than 5μm. In the first image of figure 7.6, two follicles in the green ellipse are presented with a clear nucleus (black circle), and there are two others pointed by green arrows that have a fuzzy nucleus, indicating that they are in the plane above or below. 45minutes later (second image) one of these follicles comes into focus, while the other one disappears. A similar scheme can be observed in the last image of figure 7.6, where the follicle pointed by the green arrow is just moving to the plane below. Similar behaviours can be seen when following the follicles in the cyan ellipse, or the follicle pointed by the yellow arrow at the beginning of the images in figure 7.6.

Arrowheads have been added on figure 7.7 as well, at the starting and finishing image, to point at follicles which changed position. The cyan arrowhead points at a follicle where the nucleus is clearly visible (dark circle), but as time progresses, it slowly moves towards the z direction, out of the focal plane. This can be verified by examining the second row of images on figure 7.7, where the dark circular nucleus slowly becomes blurry, as the nucleus leaves the focal plane and the surrounding oocyte comes into focus, until the nucleus completely disappears, at the final image. At this point it should be noted that the follicle is not dead, as opposed to the follicle circled in figure 7.5, image *c)*, which has much brighter staining and is deformed. The green arrowhead in figure 7.7 points at a follicle that changed position in the z direction (dark nucleus appears smaller in the final image) and also moved towards the edge of the image.

Interestingly, the dead follicles can be recognized in all the animations presented in supplementary material, as they cease to wobble around, and they stay still at the same place, which is not the case for the live ones, as we reported earlier. It has been suggested that oocyte movement could be passive, caused by overcrowding of oocytes in the young mouse ovary (Wordinger *et al*, 1990). Our results show that this is not the case. Alive follicles exhibit a dynamic behaviour, rearranging themselves in the cortical area over very small random directions (>5μm), whereas the ones that died are completely immobile, something which would not be observed

if the follicle movement was passive. Unfortunately, due to the limitations of the single photon laser scanning confocal imaging, it is impossible to examine the behaviour of larger follicles that are located in the inner cortical area.

7.4 Discussion and future research potential directions

Follicle extrusion

Using our proposed experiment, the follicle extrusion process can be recorded while actually occurring. In the image sequence reported in Figure 7.7, an egg is shown to be expelled in the extraovarian environment. The description of the phenomenon by other groups (Hiura and Fujita, 1977, Wordinger *et al*, 1990, Macay *et al*, 1992) that used fixed sections and samples corresponds to what observed in our *ex-vivo* samples, namely the recorded oocyte ejection is not due to the culturing, but also occurs in the live animal as well. What may be variable is the number of follicles extruded from the *ex vivo* ovary, as this mechanism may be affected by the culturing.

The mechanics of the oocyte extrusion are studied extensively in the work presented by Hiura and Fujita (1977), also reported in the work of Wordinger *et al* (1990), where ultrastructural changes of the cells at the site of the extrusion are observed by electron microscopy and described. In the cited work, a four-step mechanism is proposed, which involves primordial follicle migration close to the peritoneal epithelium (ovarian surface), disappearance of the follicle's basal lamina, invasion of the follicle between the ovarian surface epithelium cells, breaking the tight-junctions between them and finally opening of the intercellular space of the peritoneal epithelium to extrude the oocyte to the extra-ovarian cavity. These steps can be observed in the image sequence of figure 7.7 as time progresses. The resemblance between the predicted mechanisms described here, also presented schematically in figure 7.8, and to the phenomenon seen in the animations is very striking.

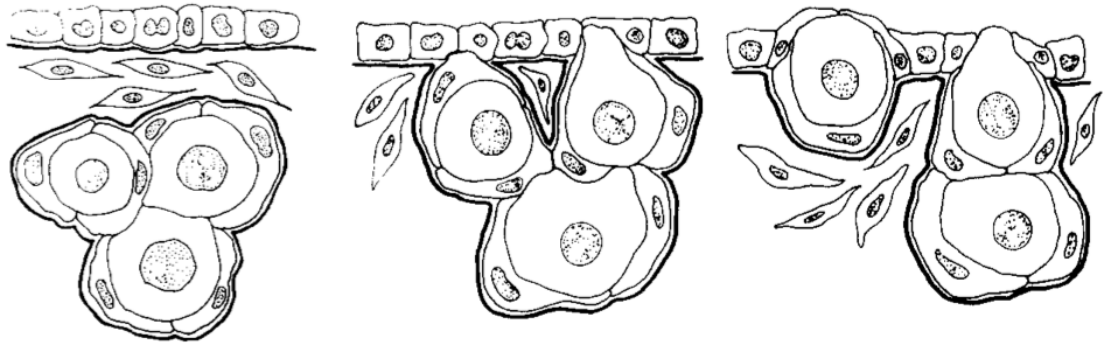


Figure 7.8: Schematic representation of the postulated oocyte extrusion process through the ovarian surface epithelium. Image obtained from Hiura and Fujita (1977). Oocytes are breaking through basal lamina that the ovarian surface epithelium is sitting on.

All the proposed mechanisms for follicle expulsion suggest that there is primordial follicle migration closer to the ovarian surface. Wordinger *et al* (1990) report that pseudopodia-like cell processes are observed prior to oocyte extrusion, using electron microscopy. However, it has not been possible to verify whether follicles rearrange themselves constantly, and what sort of movement is performed, as the physicochemical mechanisms responsible for the follicle movement are not as yet known (Wordinger *et al,* 1990). The migratory capability of oocytes has been studied in the work of Macay *et al* (1992). The authors report motility features on the extruded oocytes, detected using scanning electron microscopy; motile capability however is postulated to be lost as the ovary ages, beyond approximately one week of age.

Another reason for follicle loss could be the destruction of the fragile ovarian surface epithelium during ovary harvest and culture. Breakage of the ovarian surface could be responsible for the observed follicle loss, however extra care was taken with tissue handling, by using only sterile pasteur pipettes and no forceps whatsoever, in order to sustain tissue morphology. All procedures were consistently repeated for every ovary that was cultured. Arguments against the possibility of ovarian surface epithelium destruction come from imaging day-10 to day-12 mouse ovaries, where no follicle extrusion was observed (see supplementary material – not shown here), in contrast to younger ovaries (figures 7.6 and 7.7). Therefore in all probability the recorded follicle extrusion is not due to the culturing or ovary handling, and the phenomenon duration is consistent with that of the published work (Macay *et al*, 1992).

7.4.1 Live imaging and GFP tagging

The importance of obtaining time-series images when studying a dynamic system such as the ovary is pivotal, as it allows for real-time monitoring of specific processes, which can be visualized by appropriate staining. In this chapter, we used a general lipid membrane marker (BODIPY FL), which helped acquire very interesting results that were presented in the previous sections. However, fluorescent tagging of specific structures of interest in the ovary would provide with much more detailed information on their evolution through time. The most successful way to implement such a tagging is to use green fluorescent protein (GFP) transgenic animals. The GFP coding sequence can either be used as a reporter molecule, which can be considered as a fluorescent probe to monitor gene expression, or can be inserted into the beginning or end of the protein of interest coding sequence (Pepling *et al*, 2010). These methods are both accomplished using recombinant DNA technology to create transgenic animals (Alberts *et al,* 2008). When GFP is used as a reported molecule, the GFP coding sequence is placed under transcriptional control of the gene of interest, meaning that every time the gene is transcribed, a GFP protein is also generated. Imaging of such cells can reveal the gene-of-interest's expression patterns. Similarly, if the GFP sequence is attached to the beginning or end of another gene, a chimeric protein is created, which can be seen as the fluorescent version of the normal protein. Most of the times, the chimeric proteins are functional just like the normal ones, the location of which can then be revealed by fluorescent imaging. In general, GFP tagging is the clearest and most unambiguous way of showing the distribution and dynamics of a protein in a living organism (Alberts *et al,* 2008).

In order to reduce light induced phototoxicity (toxicity by production of free oxygen radicals, due to non-radiative energy transfer) to the tissue from the laser light for exciting the GFP fluorophore, two-photon confocal microscopy can be used (chapter 5), which uses infrared photon ultrashort pulses. Infrared photons do not promote photoreactivity, as opposed to visible light photons, if correctly applied (Koester *et al*, 1999). Moreover, as discussed in chapter 5, one of the benefits of using multi-photon lasers is that the depth of imaging can be increased. Therefore, combination of two-photon microscopy and GFP tagging can yield substantially good tissue viability and specific protein or ligand monitoring in real time.

Certain structures (such as oocytes (Pepling, 2010), endothelial cells (Haisma *et al*, 2010), neural cells (Shneider *et al*, 2009) etc, depending on the experiment) can be therefore stained in GFP transgenic mice ovaries, which can then be cultured using the proposed methods presented in this chapter and detailed in section 9.16. The culture conditions can be improved in the future as well, by introducing new supplements in the media that would extend tissue viability. However, this requires significant experimentation time and technical skills. A very useful addition to our culturing system would be to find a means of keeping the tissue immobile, while having access to the media from its entire surface and being free to develop. The use of supporting matrices, such as the Alginate hydrogel or agarose gels should be avoided as it causes light aberrations. A promising technique, presented in the work of Supatto *et al* (2009) would be to use a water immersion objective with an upright confocal microscope and glue the sample to the bottom of the culture chamber. The ovary could then be imaged from above, by immersing the water objective to the culture medium. Again, this required significant time for experiment optimizations.

A bigger volume of the ovary can be imaged using two-photon microscopy, at a much greater imaging frequency (seeing that there is no photobleaching or phototoxicity), for example one stack per 2 – 3 minutes. This can provide with very useful information about the dynamics and behaviour of the stained structure, and a period of time long enough to observe processes of interest. An example of experimenting with GFP transgenic mice and two-photon excitation microscopy is the work done by Kim *et al* (2009), where they examine progenitor cell and migratory neuroblast motility by doing time-lapse imaging.

The spatial analysis we performed in chapters 2 and 3 can also be applied in the case of the live ovary imaging. Follicle positions can be analysed, and have their spatial coordinates and developmental stages assessed, in order to conduct the logistic regression analysis to calculate the proportion of follicles that initiate growth in relation to the number of resting follicles within a set distance. It would be possible then to assess whether the observed patterns would change as the follicles reposition themselves as time progresses. In order to more accurately assess developmental stages and position of follicles, tagging specific follicle markers such as the MVH protein (also used in chapters 5 and 6) is necessary. This can be accomplished by producing GFP transgenic animals, assuming that the functionality of the MVH or

any other tagged protein would not be severely affected by the attachment of the GFP protein to it. Furthermore, two-photon microscopy should be employed to visualise follicles deeper in the tissue, as imaging using the method presented in this chapter only allows visualization of small follicles in a small cortical region.

A step further to this analysis would be to optimize our oocyte recognition algorithm, presented in chapter 6, to recognise not only the spatial coordinates from a single image, but to also process image sequences (animation) from the time-lapse experiments. The algorithm is able to recognise the MVH stained oocytes on captured images of fixed sections. Optical sections from live tissue with MVH stained using GFP should have similar characteristics, and therefore the algorithm could be used, without major modifications, to find follicles. This can be done in each captured image, so that oocytes can be tracked (black circular nuclei). It could then be quantitatively assessed how the relationship of each follicle to its neighbours changes as the follicles and neighbours move, and as the ovary is maturing in culture. A more ambitious approach would require dramatic extension of the object recognition algorithm to be able to detect 3D structures. A volume from the live imaging could then be reconstructed, so that z-direction movement could be easily detected as well. The spatial analysis could then be applied in three dimensions among the detected oocytes that could be represented as spheres, so that every possible neighbour to a target follicle within a set spherical radius can be considered for the analysis.

At the end of the culturing and time-lapse imaging, the ovary can be fixed for whole-mount imaging, as described in chapter 5 (methods detailed in sections 9.13 – 9.15). The GFP labeled MVH should still be visible when excited, so the tissue can be cleared and imaged immediately, within one day from the end of culturing. However, should the experimentalist wishes to study additional structures, such as blood vessels and capillaries, or neuron cells, within the whole ovary, the tissue can be processed for immunostaining, as explained in 9.13. Whole tissue imaging using the two-photon microscope, if possible, can yield optical slices that can be reconstructed to an ovarian volume, and follicle numbers can be quantified. Quantification of exact numbers however is a rather ambitious scenario, because as explained in section 5.4.1 and discussed in section 5.5, follicle quantification in a volume is presented with certain difficulties that need to be addressed before methods can be available to experimentalists.

7.4.2 Modeling using the Simulated Ovary

The movies captured in our work and presented in this chapter can provide a preliminary understanding of the dynamics in the ovary over short periods of time. Movies can be improved, as explained in the previous section, using transgenic animals and two-photon microscopy, but the full picture of the ovarian behaviour over extended time periods would still be missing. Modelling of the observed dynamic processes could not only corroborate the experimental findings, but would also provide insight into the system's behaviour in later ages. It has been demonstrated in chapter 5 (section 5.4.2) how the simulated ovary (presented in Chapter 4) can be used to validate the results obtained from counting experiments. The data collected from experiments such as the ones proposed in the previous sections can be incorporated into our simulated ovary model, resulting in a 'real time' simulated ovary, where the follicle dynamics could be simulated as the ovary ages.

Furthermore, follicle elasticity that can be measured from isolated follicles using atomic force microscopes which could be a very useful addition to the simulated ovary, as this would enable additional simulation of the follicle–follicle interactions and follicle–ovarian surface interactions, using simple assumptions. Spatial patterns that could be studied in the live GFP tagged ovary could also be used in the simulated ovary in combination with tissue mechanics that can be incorporated using the data from the atomic force microscopes. This could provide with enough data to model the follicle arrangement as time progresses, which involves antral follicle dilation in 3D, nudging smaller follicles located close to it, resting follicle extrusion and minor random rearrangement, ovarian surface epithelium expansion etc. Simulating follicle elasticity, based on simple assumptions, could also provide insight as to if there is influence from inter-follicular mechanical forces that can affect follicle growth, or whether oocyte extrusion in early neonatal life is due to follicle overcrowding in the ovary.

Ultimately, building a model of the neonatal mouse ovary based on our simulated ovary, enriched with additional experimental data from proposed experiments, could help expand the understanding of the ageing process, by simulating the time progression of the system. At this point, it is not possible to predict the amount of time that would be required to perform model parameter optimizations, but this is a very important as well as an extremely time-consuming

task. It should be stressed yet again that solid answers to biological questions and hypotheses can only be given from direct biological experimentation. The modelling presented in this work, or the potential future modelling work, is merely a means of understanding dynamical mechanisms and systems. The exact function of genes and cell signaling can only be verified using traditional biological experiments, which can be usefully directed by mathematical modelling.

7.4.3 Conclusions

In this chapter, we make use of existing imaging tools to demonstrate the usefulness of the results that can be obtained from time-lapse experiments. We showed that ovaries could be sustained in culture for at least 24h, using traditional culturing techniques but without the use of any supporting matrices such as Matrigel or floating filters (section 9.8). This provides with enough time to perform time-lapse imaging in regular time intervals using confocal laser scanning microscopy. Follicle dynamics can be then monitored in individual focal planes, with the aid of live stains such as the BODIPY lipid stain, which renders the cell membranes visible. This in addition minimizes the laser power required for imaging. Unfortunately, only a small volume of the ovary (up to 20μm inside the tissue) was visible using single photon microscopy, but the results we obtained were nonetheless useful.

The work presented in this chapter demonstrates how a simple to implement technique can be used to record phenomena such as the oocyte extrusion, or the small follicle motility in the ovary, as presented in section 7.3 (figures 7.6, 7.7). In the future, the same experiment can be used to conduct survival studies of the oocytes within a specific area on a focal plane, by marking all the healthy follicles at the beginning of the imaging, and recording the time of death for each follicle as time progresses. In addition, recorded oocyte extrusion from a small area of the ovary can be used to estimate the number of follicles lost during the mouse neonatal life from the entire ovary, by extrapolating to the whole volume.

There are however several limitations of the method presented in this chapter. The most important comes from the fact that the imaging depth within tissue, using single-photon confocal microscopy, cannot exceed 30μm. Chemical clearing is cytotoxic and cannot be used for refractive index matching, increasing the imaging

depth significantly, as presented in chapter 5. Multiphoton microscopy can improve imaging depth up to more than 100μm (Zhinov *et al*, 2008), but infrared photons will severely increase heat within the cultured tissue. In addition, the culture conditions used are not optimal, as the components used are identical to those used for chapter 3 cultures (see 3.4 for more details on the problems of culturing). Therefore, as a future direction, multiphoton microscopy imaging should be optimized for *ex vivo* imaging, together with culture conditions optimizations to permit longer culturing and the development of more mature follicles. Then the method could be used for species with larger ovarian volume, such as ruminant or human.

In order to extend our knowledge regarding primordial follicle initiation and growth within the cortical area of the ovary, biological research is essential. As it was discussed in chapters 2 and 3, mathematical and generally non-traditional biological methods by themselves cannot provide explicit answers to biological questions, but can significantly assist biologists by focusing experimental research to a specific direction. In the rest of this section, we are going to propose different approaches that can be employed to study primordial follicle initiation and ovarian ageing, as opposed to conventional biological research, which could be a potential future extension to the methods presented in this thesis.

Chapter 8

Discussion

8.1 Synopsis of the results and discussion

In this work, non-conventional approaches were developed to extend the understanding of cell signaling within an important biological system: the mammalian ovary. Computational and mathematical approaches were employed to gain insight into follicle initiation and growth, as well as to determine the number of small follicles in the young ovary in an efficient and accurate manner. The exact mechanism that precipitates the activation of follicles in the quiescent pool (the primordial follicles) is, to date, unknown. Recent work showed that activation of the primordial pool may be regulated by a number of locally produced growth factors, as well as by the PI3 kinase pathway, by which several growth factors act. Nevertheless, the process behind the selection of a few primordial follicles to grow, keeping the others in the quiescent state, is still unknown.

As a first step to address these questions, we implemented a 2D-analysis of imaging data from microscopic sections. Previous studies conducted in our laboratory on neonatal mice quantified the spatial positions of the follicles in the ovary and it was concluded that the regulation of primordial follicle initiation is highly likely to be via (inhibitory) paracrine signaling between quiescent follicles. This approach has been extended in this project to adult human ovarian sections. Our work has established that a similar inhibitory mechanism applies in the human, notwithstanding the age, size and morphology of the adult human ovarian section. Specifically, quantification of the primordial follicle positions on the section, led to the conclusion that there is a signal (a diffusable ligand) secreted by primordial follicles and acting on neighbouring primordial follicles to keep them in a quiescent state. This was found in both normal and polycystic ovaries, and explains the observation of clusters of primordial follicles in adult human ovarian sections. The strength of the predicted signal in adult humans is weaker than the one detected in the neonatal mouse. This may be due to the sparse distribution of follicles in the adult human ovary.

Additionally, this may indicate that the mechanism may be less effective in the adult ovary, and it may be supplemented or replaced by others (eg signals from growing follicles) in the regulation of follicle initiation.

Furthermore, application of our approach to cultured neonatal mouse ovarian sections (lacking a blood supply), confirmed that the predicted mechanism for primordial follicle activation is truly originating from local sources and not from the blood supply. The strength of the primordial follicle signal, preventing them from entering the transitional stage of development, is found to have the same inhibitory effect as in the *in vivo* ovary.

Another important aim of this project was to address the issue of adequate sample sizes when numbers of follicles are quantified. In ovarian biology, accurate estimation of the number of follicles present at a specific time point or after an experiment is of critical importance, in order to assess ovarian follicle reserve and fertility of a female. Specific examples include studies of knocking out certain genes which cause follicle depletion in mice, where the experimentalist must accurately determine the reduction in the number of follicles in comparison to a control group of ovaries, by estimating follicle number in both groups of animals. Another example is the "follicle renewal" hypothesis of Tilly and colleagues (Johnson *et al*, 2004), which was apparently supported by the finding of lack of depletion of non-growing follicles in juvenile mice, reported by Kerr *et al* (2006). A careful analysis showed, however, that this effect was statistically insignificant (Faddy and Gosden, 2007), because an insufficient number of animals was used.

We developed a novel tool, the "Simulated Ovary", to quantify the error in counting follicles due to biological variability amongst ovaries of the same species. The generation of these ovaries is based on actual data obtained from the neonatal mouse ovaries and allow for an infinite number of counting experiments to be conducted *in silico*. Our study has quantitatively shown that it is very important to have an adequate number of ovaries when estimating follicle numbers. The sampling frequency of sections within an ovary does not play such big a role and can be moderated. We indicated that real experiments for counting follicles need to use at least 10-15 ovaries, otherwise conclusions drawn from estimates of follicle numbers may not be accurate.

Examination of large sample sizes however is a time-consuming and laborious task. Currently, even state-of-the art techniques can be tedious and intensive and if carried out by many investigators, experimentalist bias can be introduced. Therefore faster and more accurate estimating techniques need to be developed. In the present study, a new method is proposed for fast estimation of follicle numbers, using the stereologic technique and whole tissue imaging by laser scanning confocal microscopy. This procedure exhibits excellent tissue morphology in optical sections, in parallel to being optimal for batch processing of a large number of ovaries. We showed that the quantification of follicles by means of stereologic counting is fast and we tested its accuracy using the Simulated Ovary.

The proposed method, though faster, still requires experimentalist assessment of follicle numbers and developmental stages. In order to eliminate investigator bias, and to automate simple but time-consuming tasks such as the spatial coordinate assignment, automated techniques based on object recognition need to be introduced. Computer vision technology has not yet evolved to the point where the computer can recognize complex structures such as the follicles, and assess their developmental stage using morphological criteria. More simplistic approaches to biological object recognition are commercially available, but are usually very expensive and require training and expertise to be used, to the point where most experimentalists opt to perform the tasks manually. In this project, a simple image-processing tool was developed, which can recognize MVH stained oocytes on histological sections, and assess their developmental stage based on the oocyte size. This computer programme is shown to reproduce the results of the spatial study in the juvenile mouse, but more quickly, demonstrating the possibility for developing automated methods to assist analysis of high-throughput biological technologies.

Finally, an extension of this work in 4D was presented; we showed that the inclusion of the time dimension allows testing simple hypotheses (such as whether follicles are motile) and provides new information and insight into the dynamics of the ovary. More specifically, results obtained from time-lapse imaging of whole ovarian cultures using single photon confocal microscopy were presented, showing that the ovary exhibits a dynamic behaviour, with follicles shifting their positions slightly in a random manner. This movement is not significant over time, and does not affect the validity of the results presented in chapters 2 and 3 where spatial

distributions were examined. Resulting animations also show the phenomenon of follicle loss by extrusion from the ovarian surface epithelium during the neonatal life of a mouse, which ceases after a certain age.

The exploration of the initiation of the primordial follicle started over a century ago, with new tools and methods constantly being developed. The need for unveiling the mechanism of primordial follicle activation is compelling: there are practical implications for contraception, alleviation of infertility and potentially modifying the rate of follicle depletion, to delay the upcoming menopause. Yet, to date, as the literature on this field asserts, "this mechanism still remains obscure". It is evident that this phenomenon needs to be examined from a different perspective, other than classic biological research. In our project, we seek to provide new tools and methodologies to address these issues so that the problem can be solved.

8.2 Novelties, caveats and future directions

This project demonstrates how modeling approaches can be applied to 2D and progressively to 3D and 4D data, increasing the complexity and quantity of information to analyse. The novelty of this work is the perspective by which various hypotheses are addressed. Follicle developmental patterns have been quantified, both in adult human and cultured juvenile mouse ovarian sections; the novel techniques we developed can detect subtle differences in case-control morphology, such as the "developmental gradient" visually observed in both live and cultured ovarian sections, or in any given histological section. However, our approach alone does not provide any explicit information on the nature of signals, which need to be examined using experimental biological techniques. For example, stimulation by kit-ligand produced by the granulosa cells, activates the PI3K pathway, leading to primordial follicle initiation. Our predicted signal may therefore be continuously blocking the pathway, by means of antagonizing kit-ligand or some other growth factor, such as the BMPs. The action of such factors must be local, within a small range. Research in our laboratory (Dr Mark Fenwick and Ms Jossie Mora) is currently focused in identifying BMP antagonists as candidates which could potentially inhibit primordial follicle activation. These could be specifically examined using isolated viable primordial follicles in culture, a procedure which is very delicate and challenging due to the

small size and fragility of the primordial follicle and which is currently being developed (already possible for sheep primordial follicles and lamb early growing follicles; Muruvi *et al*, 2005, Muruvi *et al*, 2009). Attempts in our laboratory over a decade ago to culture early human follicles failed due to the oocyte extruding from the follicle (Abir *et al*, 1997) possibly due to the lack of tensile strength in the enveloping single layer of flattened granulosa cells. However, it may be possible to achieve follicle-specific examination for BMP antagonists using laser microdissection of areas of sections rich in primordial follicles, and carry out rt-PCR of mRNA from these dissected sections.

The model was further extended into the three-dimensional simulated ovaries. These ovaries are essentially a set of follicle coordinates and diameters, assigned in the *XYZ* Cartesian plane. The added complexity of this model serves the purpose of being much more realistic and accurate. This model is used to simulate counting experiments *in silico*, a process lasting no longer than a few seconds, without requiring any additional tissue, other than the one used to obtain the data for constructing the simulated ovaries. This model can easily be used by ovarian biologists for efficient planning of experiments, in order to achieve optimal use of the available tissue and animals. In the future, the programme can also be developed as a web-based resource, so that it can be more widely and easily accessible.

In this work, analyses have been extended to three dimensions, as demonstrated by the imaging of whole ovarian tissue, and techniques were advanced to high-throughput methods, allowing for a significant amount of tissue to be processed and imaged in parallel. This project was achieved to the extend of providing very clear images of whole tissue very fast, but *XYZ* analysis was not developed, as discussed in chapter 5. In order to complete this, new imaging techniques are required (optimization of multi-photon imaging or optical projection tomography) to overcome problems of optical plane overlapping, which could compromise the accuracy of the *XYZ* analysis.

As datasets are becoming larger, their processing should be automated using new methods; this is to eliminate variations due to experimentalist bias (e.g. when qualitatively assessing follicle stage) and to speed up processes that are tedious and time-consuming. The image processing technique presented in this project shows how new computational methods can improve the efficiency and the accuracy of high-

throughput biological techniques. However, these imaging techniques still need significant amount of development to be applied in a more global scale in the future, namely to be able to recognize and count three dimensional objects. Meeting this aim in the future is linked to the completion of the *XYZ* analysis of follicles in the whole ovary, which requires the use of automated methods to be realized, not only due to the large number of follicles (more than 2000), but also due to the variation that experimentalists would introduce to such measurements.

Further advancing research in four dimensions by examining the spatiotemporal dynamics of follicles in culture can provide valuable insight on ovarian ageing. In this project, a simple implementation using whole ovarian cultures was presented. The method is easy to apply and can yield very interesting results in a short amount of time. If combined with appropriate staining (e.g. GFP tagging) and two-photon imaging, the resulting image (or volume) sequences could provide very specific answers to hypotheses regarding follicle dynamic behaviour. This method can also be applied to cultures of isolated follicles, where specific trafficking of components can be monitored in real-time.

Overall, the general aims of this thesis have been achieved, apart from the extension of the follicle spatial distributions to three dimensions. In order to achieve an end point of the work presented in this thesis, further experiments and method optimizations are required. First of all, biological investigation in search of the primordial inhibitor is essential. The *XY* analysis presented in chapters 2 and 3 must be extended to three dimensions in the future, using the whole tissue imaging techniques presented in chapter 5, with further optimizations. These need to be combined with new image recognition tools (extended from those presented in chapter 6) in order to be time efficient and accurate. From there, a more realistic local signaling pattern will result, which may provide with more insight for biological research. Furthermore, real *XYZ* distributions of follicles can be used as input to the simulated ovary, improving the current model which is only based on section *XY* data. Ideally, completion of all the projects presented in this thesis would provide the experimentalists with the following tools:

- Use of 3D tissue imaging techniques to image an adequate number of ovaries (eg 10), count the follicles and analyze their spatial arrangement automatically.

- Use simulated ovaries, created by the data obtained, to check whether additional tissue is required in order to make their analysis more robust.

8.3 Conclusions

Mathematical and computational modeling in biology is a powerful tool, offering new insights into biological systems. Models are used to describe, simulate, analyse and predict the behaviour of biological systems (Kirschner and Linderman, 2009). Proper adaptation of biological data into a set of equations or logical rules offers an infrastructure by which the system can be described and ultimately understood. It is often said in the literature that in the ovary, mechanisms governing the follicle initiation of growth are hidden behind complex processes. Using models and new approaches, such as the ones presented in this work, one can realise that complexity can be due to a very large number of simple processes, interacting with each other. This is by no means implying that biological systems are simplistic; rather understanding simple processes and representing them through modeling can lead to the understanding of their complex functions.

The data used in our models are obtained from microscope images. Imaging is a compelling and versatile tool in biology and medicine, combining the power and beauty of direct observation with newly developed implements such as the Förster Resonance energy Transfer (FRET), the Fluorescence Recovery After Photobleaching (FRAP), the Fluorescence Lifetime Imaging (FLIM) (McGinty *et al*, 2008) and many more (Engel *et al*, 2010). In addition to the advances in labeling methods during the past decade, there has been an explosion of microscopy-based approaches, from *in vivo* visualization to imaging protein dynamics, producing a vast amount of information to be analyzed (high-throughput fluorescence microscopy) (Wang *et al*, 2008). These methods continuously evolve to generate new insight into fundamental biological questions, in combination with established biological experimentation, such as quantitative PCR or blotting. Imaging allows us to relate focused molecular analyses to the 2D and 3D relationships between organelles, cells, structures within organs, as well as between cell types, such as the oocyte or granulosa cells.

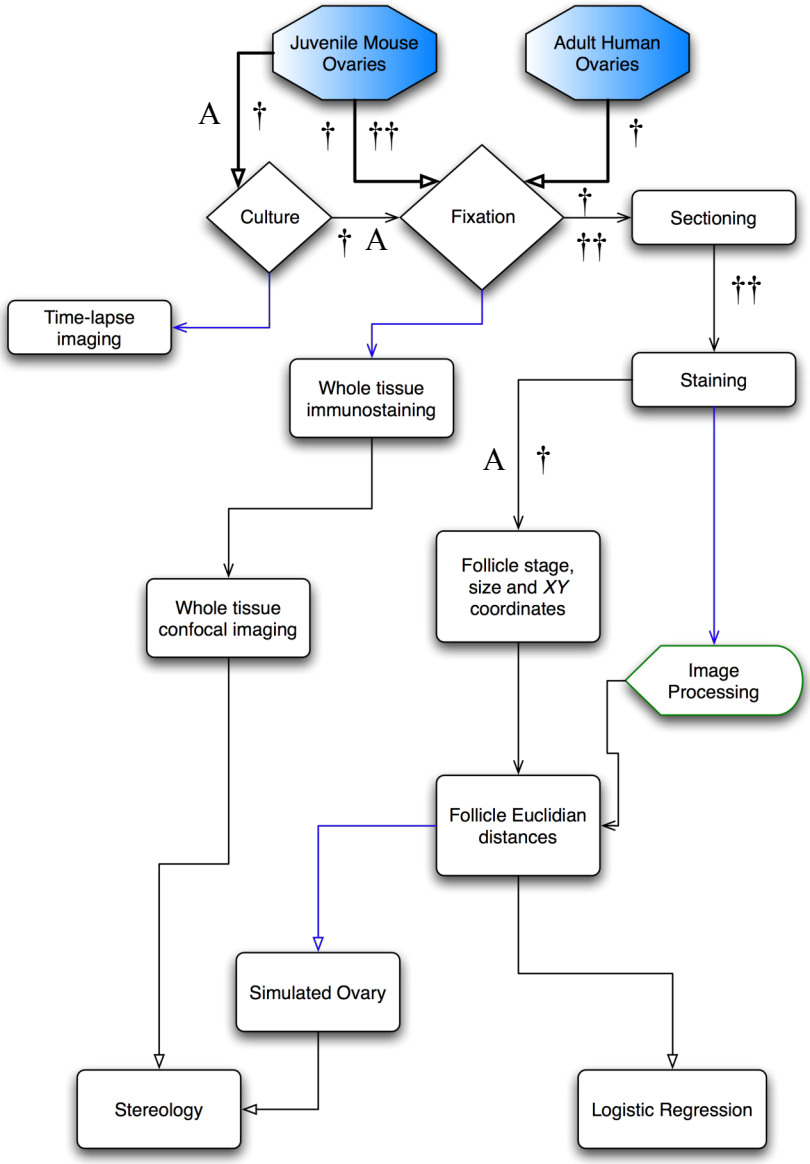
Interdisciplinary approaches to classical problems are gradually becoming preferable over conventional methods, as new tools are being developed and applied

to address specific problems more efficiently. In addition, the use of computational modeling approaches that can describe and simulate specific mechanisms or systems generates a positive feedback loop that guides new experimentation towards obtaining more meaningful data, which ultimately leads to important breakthroughs.

Chapter 9

Materials, methods and algorithms

An overview of the processes and experiments performed for this project appears in the figure. In the present chapter, all the methods and algorithms are analytically described. The sections marked in their title with a dagger symbol (†) indicate procedures carried out by Dr Sharron Stubbs; methods marked with two daggers (††), were performed by Dr Mark Fenwick.



Flowchart 9.1: Summary of the experimental processes carried out in the project. Blue lines denote subsequent processes that are performed on mouse ovary only. One dagger (†) denotes procedures carried out by Dr Stubbs, two daggers (††) denote procedures carried out by Dr Fenwick and (A) is used to mark procedures carried out by myself when someone else also performed the same experiments, otherwise the (A) is omitted.

9.1 Human Ovarian Tissue Collection (†)

Whole ovary tissue samples (formalin fixed and paraffin embedded), from patients who had undergone oophorectomy for nonmalignant gynecological disorders between 1993 and 2000, were obtained from the histopathology tissue bank at St. Mary's Hospital NHS Trust. Ethical approval for the use of this tissue was obtained from the Local Research Ethics Committee, and the tissue had been removed with informed surgical consent. For another study in our laboratory 5µm sections were mounted on poly-l-lysine slides. Immunohistochemistry was undertaken to identify MCM-2 (mini-chromosomal maintenance-2), which is a replication-licensing protein, using a mouse MCM-2 antibody (clone D1) (Stubbs *et al*, 2005, 2007). The ovary samples were histologically classified as normal, or polycystic (PCO) if in the section there were at least 10 follicles bigger than 2mm in diameter and either had increased density of stroma, and/or had thickened tunica (Stubbs *et al*, 2005, 2007). In the present study, five normal and nine polycystic ovulatory ovaries from the archive were used for spatial analysis. In table 9.1, the clinical information of the ovaries used is displayed. It must be stressed that the individual experimental procedures described here had already been performed for the published work referenced (Stubbs *et al*, 2005 & 2007), and the sections I used were readily available to me, without any additional processing required. The experiments were not repeated for my thesis. Therefore detailed protocols and positive and negative stainings can be found in these papers, or can be requested from the corresponding author.

Table 9.1: Clinical details of subjects donated the ovaries used for MCM-2 immunohistochemistry, used in this project (adapted from Stubbs *et al*, 2005).

Classification	Code	Age (yrs)	BMI	Ultra-sound	Ovarian volume (ml)	Menstrual cycle history[a]
Normal	N1	34	20.2	normal	4.4	regular (2/28)
Normal	N2	33	17.5	normal	6.4	regular (5-7/21, prev 5/28)
Normal	N3	26	27	normal	2.5	regular (4/28)
Normal	N4	30				Normal histology[b]
Normal	N5	34	23.9	normal	—	regular (7/30)
Mean (sem)		31.4 (1.5)	22.2 (2.1)		4.4 (1.1)	
OvPCO	P1	30	24.8	PCO	—	regular (5/28-31)
OvPCO	P2	34	29.4	PCO	7.3	regular
OvPCO	P3	35	23.4	PCO	12.6	regular (7/33)
OvPCO	P4	35	18.4	PCO	14.5	regular (5-6/30-32)
OvPCO	P5	31	—	—	—	corpus luteum and corpora albicans on histology[d]
OvPCO	P6	30	19.3	PCO	9.6	regular (5/28)
OvPCO	P7	33	26.8	PCO	9.2	regular (7/28)
OvPCO	P8	34	26.8	PCO	9.3	regular (7/28)
OvPCO	P9	24	—	—	—	corpora albicans on histology[c]
Mean (sem)		31.8 (1.2)	24.1 (1.5)		10.4 (1.1)	

[a] (#/#) days of bleeding/cycle length. [b-d] no cycle history or ultrasound available; classified according to histology alone: [b] normal, [c and d] PCO with evidence of recent ovulation

9.2 Sample Examination and Data Collection

The sections described above were examined using a Nikon E600 Eclipse microscope (Nikon UK Ltd., Kingston-Thames, UK). Using the 10x objective lens, the sections were scanned in search of areas rich in follicles. The follicles were later analysed to establish their developmental stage, size and relative position.

The follicle types considered for the present analysis are *primordial*, *transitional, primary and secondary*. Follicles are classified into one of the categories according to the well-established morphological characteristics reported in (Stubbs *et al*, 2005, 2007).

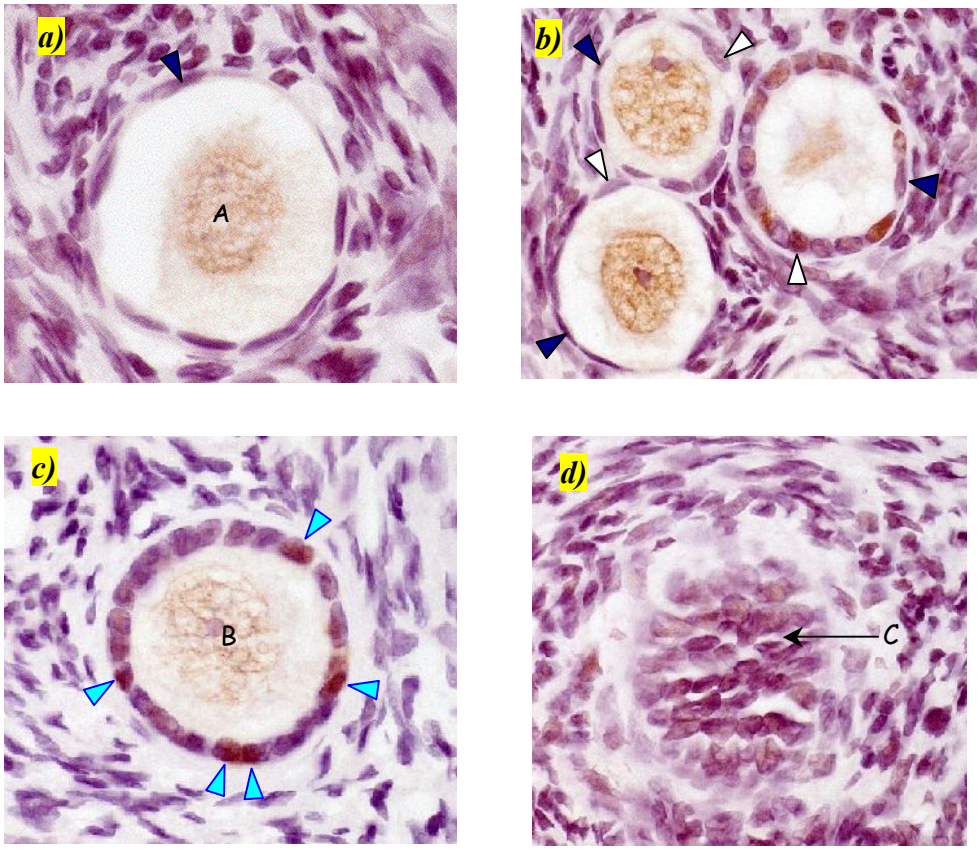


Figure 9.1: Light micrographs of sections of human ovarian tissue (x60 magnification).

a) Primordial follicles have only flattened granulosa cells (GC). The nucleus (A) is clearly shown. Examples of flattened cells are identified with the filled arrow.

b) Transitional follicles have at least one but not all cuboidal GCs. Flattened GCs are pointed with the filled arrow and cuboidal GCs with the white arrow

c) Primary follicles have a single layer of cuboidal GCs. The nucleus (B) is fuzzy. The brown GCs (cyan arrowheads) are positive to the MCM-2 marker, meaning that they are in the cell cycle.

d) Only the external surface (C) of this follicle is visible. The oocyte is not visible, thus the follicle is classified as a cluster of granulosa cells.

Figure 9.1 presents a few examples of human follicles classified into appropriate developmental categories, by satisfying one of the following criteria.

- The follicle were classified as *primordial* if a single layer of only flattened granulosa cells surrounded the oocyte.
- Follicles in which at least one, but not all, granulosa cells are cuboidal were classified as *transitional*.
- Follicles in which a single layer of only cuboidal granulosa cells surrounds the oocyte were classified as *primary*.
- Follicles with more than one layer of cuboidal granulosa cells were classified as *secondary*.

Each follicle within every section examined was assigned a unique number, classified into one of the categories stated and had its diameter measured. All measurements were inserted into an Excel spreadsheet. The information for each follicle included the following specifications:

- Unique *follicle number* in each ovarian section.
- *Follicle type*, represented as a number in the following scheme: Primordial → 1, Transitional → 2, Primary → 3, Secondary → 4.
- *Nucleus state*, represented again by a number: Nucleus absent → 0, nucleus present but fuzzy → 1, nucleus clearly shown →2.
- *Follicle diameter*, measured in *μm* in the image analysis software.
- *Follicle condition*, 0 if the follicle was regular in shape or 1 if it was deformed for any reason.
- Some follicles can be sectioned just at the edge of the follicle surface. In this case, the oocyte was not visible, and a 0 entry was assigned to the follicle, whereas if the egg was visible a 1 entry was assigned.
- *MCM-2* positive (1) or negative (0) follicle. When at least one of the granulosa cells was positive for the MCM-2 marker, the follicle was classified as positive. This set of measurements was obtained using captured section pictures from the archive, as part of a different study (Stubbs *et al*, 2007).

The appearance of the oocyte nucleus is taken into account if it is necessary to estimate the average follicle diameter of each developmental category (chapter 2, table 2.1). Oocytes and follicles are assumed to be spherical. The actual follicle diameter was matched most accurately when the follicle was sectioned at its widest part, which is when the oocyte nucleus was clearly visible on the ovarian section (figure 9.2). Note that in order to conduct the spatial analysis, which involved relating each follicle to its neighbour on the section by calculating their surface-to-surface distance, all follicle diameters were recorded.

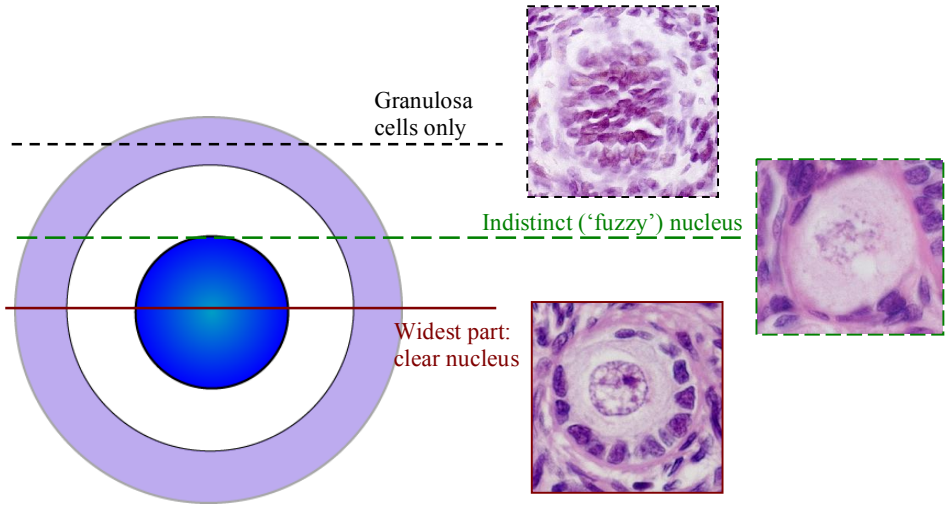


Figure 9.2: Schematic diagram of a follicle sectioned through three different loci; the granulosa cell layer(s) (black dashed line), the oocyte (green dashed line) and through the nucleus (red line). Corresponding histological images depict the actual effect in each case. Follicles, oocytes and nuclei are considered to be spherical.

9.3 Human histological section imaging by light microscopy

A digital camera (DXM 1200, Nikon), which was attached to the Nikon Eclipse E600 light microscope, was used to capture regions of interest on the histological sections. The 10x magnification objective was selected to capture images of broad areas on the ovarian sections, as this provided enough detail to see the follicles clearly. Images were obtained so that all the follicles on each ovarian section were photographed. Once a follicle cluster (area rich in follicles, usually more than five follicles) has been identified within a region of the ovary, several 10x pictures may be required to cover the cluster. The images of this cluster were captured so that there was at least one easily identifiable part between two images. The assembly of the 10x overlapping images for each cluster was done using a stitching application on a Macintosh platform (DoubleTake 2.0.5).

After obtaining all follicles available on the section on 10x images, the whole ovary was then photographed using lower magnification. The same region overlapping method was applied to low magnification (2x) images, captured to cover the whole ovarian section, because attempting to cover the entire section with 10x images would require more than 50 images. The 2x images were stitched, to

reconstruct the whole ovarian section. This was done so that every follicle in the clusters could be related to the whole ovary, as will be discussed in the following sections.

Follicle sizes

Each follicle on every human ovarian section was assigned a unique number and classified into a developmental stage, according to the morphological criteria presented in 9.2. Using a 60x magnification objective, the diameter of each follicle was measured, using the software accompanying the microscope (LUCIA, Nikon). The follicles are regarded as spherical, so the diameter assigned was calculated by averaging the follicle width and height measurements (figure 9.3).

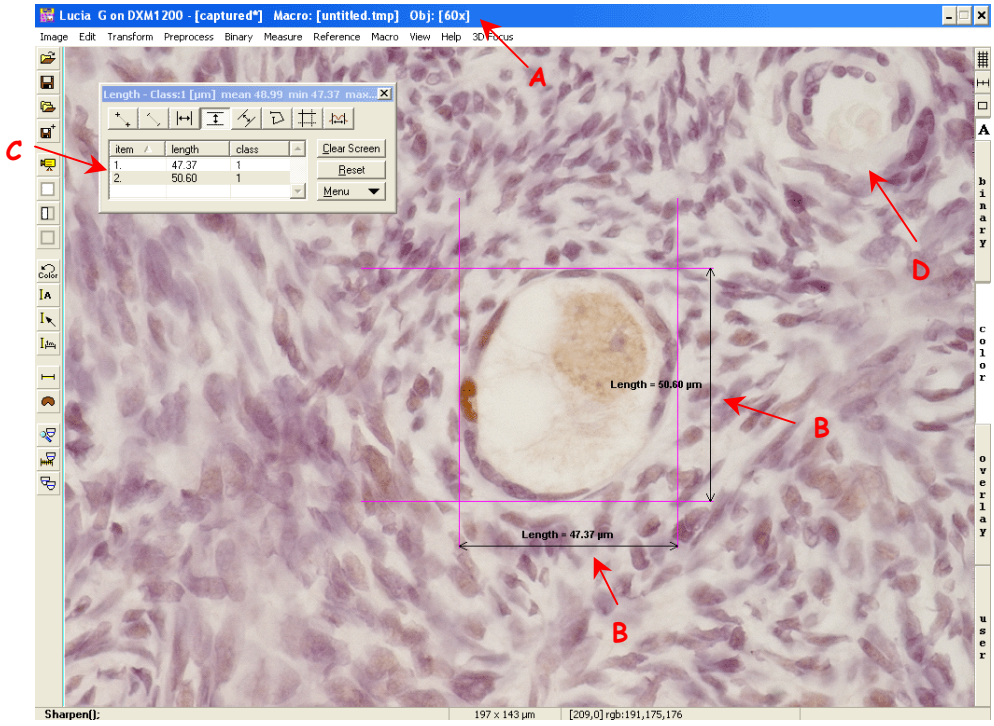


Figure 9.3: Screenshot of the image analysis software LUCIA, with a 60x image loaded. *A:* The magnification used was set so that sizes are displayed correctly. *B:* Each follicle has its width and height measured. *C:* The follicle diameter was the mean value of the width and height. *D:* Caution should be taken with some blood vessels that may be mistaken for follicles in the adult ovary.

9.4 Follicle XY coordinates

Ultimately, the images captured were assembled together to relate the position of all follicles in a section to a common coordinate system. For this purpose, another application was used (Graphclick, obtained from http://www.arizona-software.ch), in order to assign coordinates to each follicle (figure 9.4). Its principal function is to provide the coordinates of points on a loaded image, corresponding to a scale that the user defines. Using the Lucia software, we could measure the width of the entire frame that was captured to an image, which could then be used to initialise the scales within GraphClick. Each follicle's position on the image was represented by a set of *XY* coordinates. Of course, as is going to be explained later, the coordinates of the follicles within each individual image that were obtained need to be transformed to relate to the whole ovary. Figure 9.4 presents the Graphclick application and the functions used for our project.

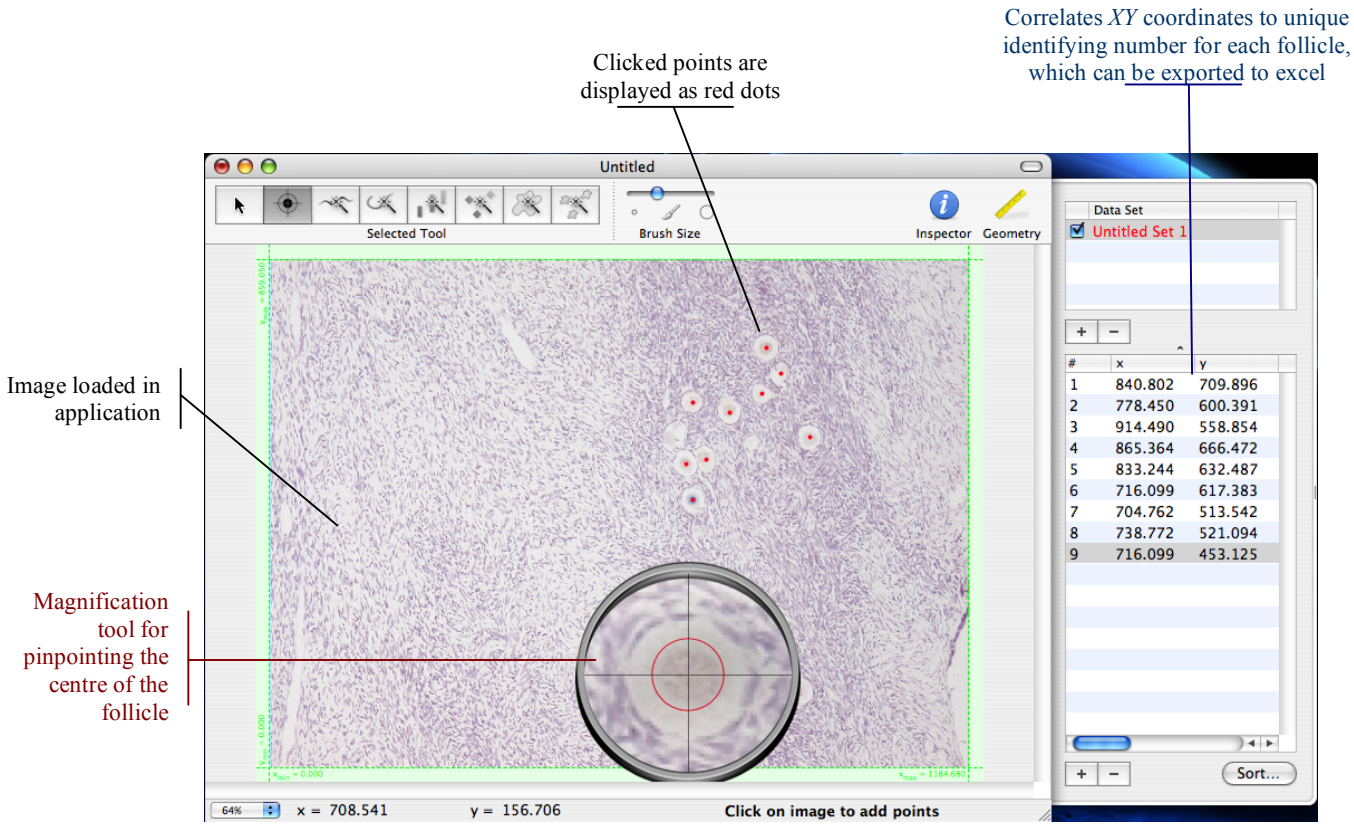


Figure 9.4: Screenshot of the Graphclick application, used to obtain *XY* coordinates of follicles in each image or stitched images.

9.4.1 Transforming image Coordinates

In order to conduct the spatial analysis on the adult human ovary sections, all the follicles coordinates had to refer to the same coordinate system, which would be that of the whole section. The whole ovarian section could be reconstructed by stitching the 2x images, creating a "collage", as shown in figure 9.5.

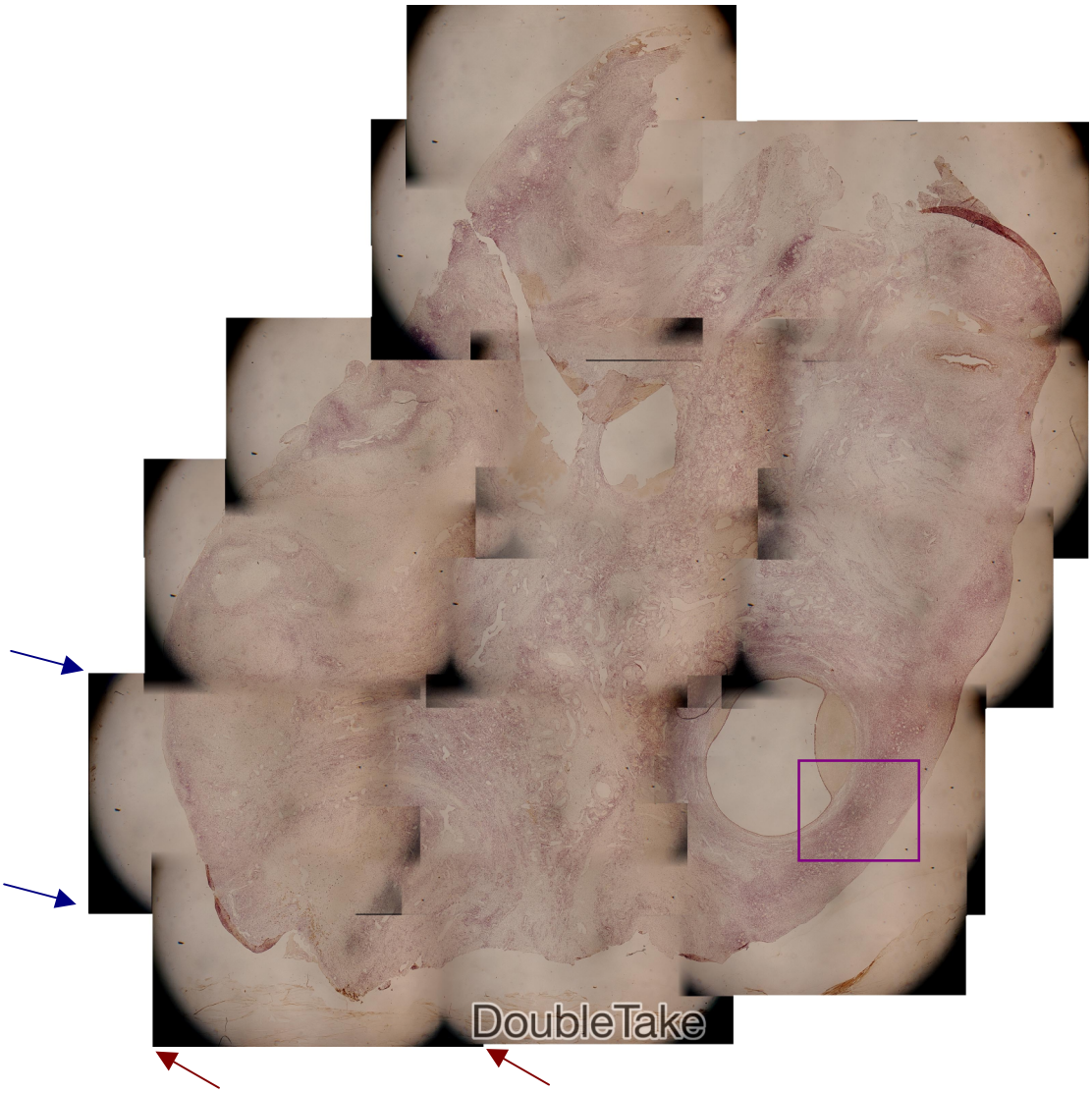


Figure 9.5: Whole adult human ovarian section, presented as a "collage" of stitched 2x magnification images. Stitching was done using DoubleTake programme. Blue arrows denote vertical image boundaries and red arrows denote horizontal image boundaries. Those boundaries are required in order to assign the coordinate system in Graphclick, which is the global coordinate system for the specific ovarian section. The purple box shows an area rich in small follicles which are practically invisible, next to a big antral.

The coordinate system can be assigned on this collage for the whole ovary using Graphclick, as the size of each image of the collage was known and was kept constant, and the boundaries were easy to be identified on it, due to the dark areas created by the microscope iris when using the 2x objective (arrows, figure 9.5). The follicle *XY* coordinates that were assigned on individual 10x magnification images, which are much more detailed, needed to be transformed accordingly, in order to relate to the collage coordinate system (figure 9.6).

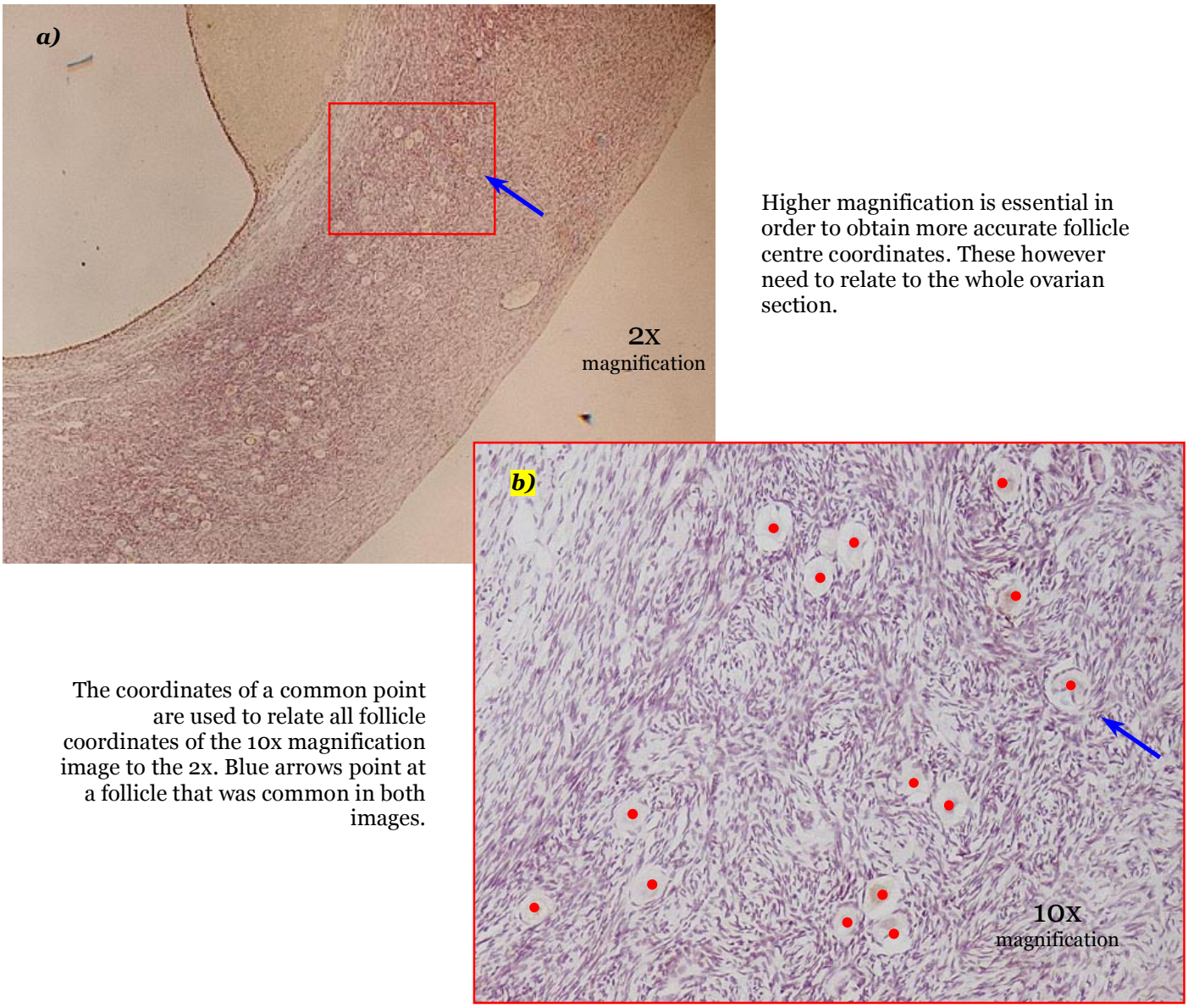


Figure 9.6: ***a)*** Part of a 2x image of a cluster of follicles on a human ovarian section (purple box in figure 9.5). ***b)*** Part of this cluster in 10x magnification, suitable for assigning follicle coordinates in Graphclick (figure 9.4). All follicle coordinates, which refer to the origin of the individual 10x image(s), need to be transformed to refer to the whole ovarian section.

In order to transform the *XY* follicle coordinates from any 10x image to the 2x images, a common point across the two images had to be identified. Figure 9.6a shows an area rich in follicles, marked in figure 9.5 with a purple square. Figure 9.6b is part of a 10x image, which was used to obtain the follicle coordinates using Graphclick, as the detail in these images was superior to the 2x. The transformation method for the *XY* coordinates from the 10x image reference system to the 2x reference system, will be presented using images 9.6*b* (10x) and 9.6*a* (2x) as example. The same method can be used for all cases, e.g. for transforming the coordinates of a collage of 10x images to the 2x whole ovary collage.

At first, a common point P_A was identified among the two images (figure 9.6, blue arrows). We are going to examine in detail how the coordinates of a follicle on the 10x image, $F(x_2,y_{2,})$ will be transformed, relating to the new coordinate system of the collage. Ultimately, all the follicles of the 10x image will be transformed similarly to relate to the same coordinate system. Figure 9.7 illustrates a simplified schematic representation of figure 9.6, marking the two coordinate systems.

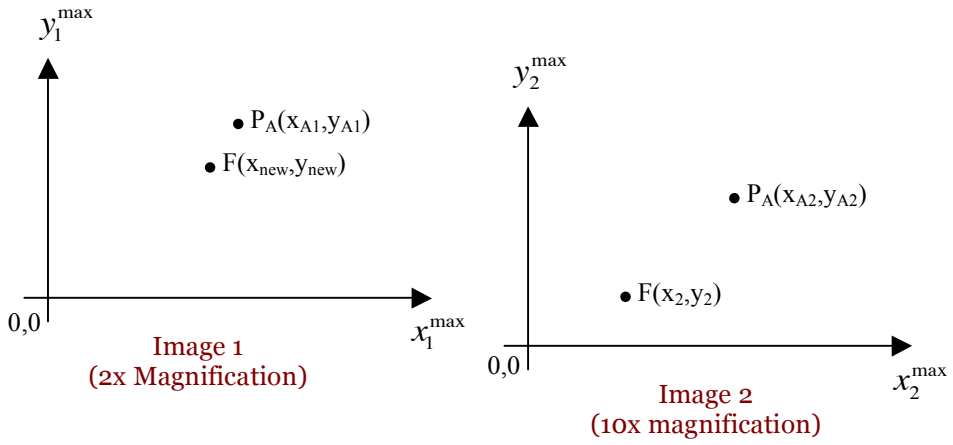


Figure 9.7: Schematic representation of the images appearing in figure 9.6, as two individual coordinate systems. The illustration is simplified to include only two follicles in each image, defined by the coordinates of their centres, on each image. The common point between the two images is the centre of follicle P_A. Follicle F coordinates will be transformed to refer to Image 1.

In brief, the transformation will be done as follows: The coordinates of F in Image 2, figure 9.7 are assigned referring to the origin (0,0) of the Image 1 coordinate system. These coordinates will be transformed to refer point F, instead of the origin, to the point P_A. The points P_A are common in the two images, thus the point F also

refers to Image 1, figure 9.7. Thus by transforming the new coordinates of point F one more time, referring them to the origin of Image 1, will provide with the coordinates of F_{new}. Point F and F_{new} are the same follicle, in two different images, but we can only measure the coordinates of F accurately (being in a higher magnification image), and by applying the transformation we can obtain the coordinates of F_{new}. Below the steps of the transformation are explained in more detail.

As a first step, the origin of the coordinate system of Image 2 (10x) will be shifted on to $P_A(x_{A2},y_{A2})$. So, the coordinates of follicle F in Image 2 will be transformed as:

$$\begin{aligned} x_2^{'} &= x_2 - x_{A2} \\ y_2^{'} &= y_2 - y_{A2} \end{aligned} \tag{9.I}$$

where $F'\left(x_2^{'}, y_2^{'}\right)$ are the new transformed coordinates for F, referring to the common point P_A. Next, in order to refer point F to Image 1 (2x), the reference system must be moved from P_A to the origin of this image. Since point P_A is common to both images, all we need to do is shift the origin again, to match the origin of Image 1. Thus the transformation for $F'\left(x_2^{'}, y_2^{'}\right)$ is done as shown below:

$$\begin{aligned} x_{new} &= x_2^{'} + x_{A1} \\ y_{new} &= y_2^{'} + y_{A1} \end{aligned} \tag{9.II}$$

where $F_{new}\left(x_{new}, y_{new}\right)$ are the final transformed coordinates of F′.

To sum up, each follicle coordinates on the 10x magnification image were transformed to a different coordinate system that of the stitched 2x image, based on a common point between the two images. The new *XY* coordinates were calculated using the formulas below:

$$\begin{aligned} x_{new} &= x_2 - x_{A2} + x_{A1} \\ y_{new} &= y_2 - y_{A2} + y_{A1} \end{aligned} \tag{9.III}$$

The transform was applied to all the follicle coordinates of the 10x images respectively, using an algorithm implemented in MATLAB, referring them to the stitched 2x image of the whole ovarian section, providing with a complete set of coordinates for all the follicles, which were mapped to the whole ovarian section.

9.5 Euclidian distances

9.5.1 Inter-follicular distances

The follicle *XY* coordinates were used to calculate inter-follicular distances, as well as distances between the follicles and the ovarian surface. Assuming d_1 as the diameter of a follicle A, with centre coordinates (x_1, y_1), and d_2 the diameter of a follicle B, with centre coordinates (x_2, y_2), the Euclidean distance of the two follicles, surface to surface, was calculated in the following way :

$$D_{AB} = \sqrt{(x_1 - x_2)^2 + (y_1 - y_2)^2} - \frac{d_1}{2} - \frac{d_2}{2} \qquad (9.IV)$$

In some cases, the distance D_{AB} is negative, due to the fact that the follicle was considered as perfectly circular, with its diameter being the average of the vertical and horizontal diameter measured. The distance was then regarded as 0, i.e. the two follicles were touching. The distances between pairs of follicles for every follicle within the section were calculated, using a computer programme coded in Fortran 77.

Assuming that the putative local inhibitory signal has an effect within a given radius, the programme computes the number of follicles (seen as potential signal sources) within this radius from a target follicle. This was done in order to investigate the effect of the neighbouring follicles within a short distance (10μm in the juvenile mouse, 25μm – 100μm in human) on the target follicle.

9.5.2 Euclidian distances of follicles from the ovarian surface

The GraphClick software was additionally used to map the *XY* coordinates of the ovarian surface, in order to calculate the distance between follicles and the surface. This was done by obtaining the coordinates of a set of points on the ovarian section edge, at regular intervals, and consequently connecting the points using straight lines. Each line segment was divided into another 100 points, resulting in an adequate approximation of the ovarian surface. All the calculations are embedded into the Fortran programme. The Euclidean distance D_{AW} between the surface of a follicle A(x_1,y_1) of diameter d_1 and a point on the ovarian wall W(x_w,y_w) was calculated using Eq 9.V:

$$D_{AW} = \sqrt{\left(x_1 - x_w\right)^2 + \left(y_1 - y_w\right)^2} - \frac{d_1}{2} \quad (9.V)$$

For each follicle, the programme calculates a pair of distances for every point on the ovarian surface. The distance of the follicle to the ovarian surface was the minimum of these distances. When this distance was negative, as explained before, we assumed that the follicle touches the surface, and the distance was set to 0.

9.6 Follicle proportions

9.6.1 Follicle proportions calculation using Logistic Regression

Logistic regression is used for predicting the probability of occurrence of an event by fitting the input data to a logistic curve. The logistic function is written as:

$$f(z) = \frac{1}{1 + e^{-z}} \quad (9.VI)$$

The input value z can range from negative infinity to positive infinity, whereas the output $f(z)$ is confined to values between 0 and 1. Therefore z is used to represent the certain set of conditions, and the resulting $f(z)$ represents the probability of a particular outcome, given the set of conditions. The variable z can be defined as:

$$z = \beta_0 + \beta_1 x_1 + \beta_2 x_2 + \ldots + \beta_k x_k \quad (9.VII)$$

where β_0 is the intercept and β_1, β_2, β_3 etc are called regression coefficients of x_1, x_2, x_3 etc.

Logistic regression is a useful way of describing the relationship between one or more factors (such age, sex, smoking etc / zero, one, two etc primordial neighbours) and an *outcome* that has only two possible values (not dead, dead / not growing, growing). This was implemented in our project using Stata 8 statistical software (Stata Inc).

Stata performs logistic regression with the *logit* function. The function presents the regression coefficients (coefficients of independent variables), measured in logged odds. In order to get the predicted probabilities (proportions) from the computed coefficients, and the 95% confidence intervals, we used the *adjust* command. Furthermore, when using the *logit* command, we also used the *cluster*

option, which specifies that the observations are independent across clusters, which are the ovaries in our case. The *cluster* command affects the estimated standard errors, but not the estimated logistic regression coefficients. Robust variance estimates are also obtained when using the *cluster* command, in the place of traditional error calculation that Stata performs. This is a very important point to stress, as making use of the *cluster* command, it is assumed that each ovary is a discreet case; therefore the results were individually compared. Specifically, there are n=14 ovarian sections from 14 different human subjects considered for the analysis; using the *cluster* command,

Further reading: Stata online manuals (http://www.stata.com/) and Stata 8 reference manuals (Stata Press).

9.6.2 Testing for statistical significance

In order to test whether the parameters of the most recently fitted model were different, we use the *test* command in Stata 8, which performs Wald tests. The Wald test is a parametric statistical test with a great variety of uses. Whenever a relationship within or between data items can be expressed as a statistical model, with parameters to be estimated from a sample, the Wald test can be used to test the true value of the parameter based on the sample estimate. The *test* command in Stata 8 performs Wald tests for simple and composite linear hypotheses about the parameters of the most recently estimated model, which in our case was the logistic regression.

9.6.3 Example of proportion calculation in Stata 8

Here we present an example workflow for calculating the proportion of follicles initiating growth in each group of follicles that have a set number of primordial neighbours (0, 1, 2, etc) within e.g. 25μm from their surface (see section 2.3, figure 2.3).

After importing in Stata the spreadsheet containing all our data, we generated a new variable for each follicle which was set to 0 if the follicle was resting or 1 if the follicle was growing, i.e. its stage was transitional or above.

```
.gen growing = 1
.replace growing = 0 if stage!= "Primordial"
```

Logistic regression was then used to describe the relationship between the number of primordial follicles within 25µm and the probability of the follicle to be growing. Stata also calculated robust standard errors, clustered by ovary, meaning that data are considered as independent for each ovarian section, as previously explained.

```
.xi:logit growing I.primordial_neighbours, cluster (ovary)
.adjust, by (primordial_neighbours) pr ci
```

Using the *adjust* command, a table was produced, with the proportions and their associated 95% confidence intervals. By plotting the proportions, connecting points with straight lines and adding the confidence intervals on each point, we obtain the blue line in figure 2.6. Since the confidence intervals were available, one can visually assess the differences among any pair of proportions, which were highly significant statistically when the confidence intervals range did not overlap (Cumming *et al*, 2007).

If we want to test whether proportions for different cases (different number of primordial neighbours) are significantly different statistically, we can use the *test* command on the parameters calculated from the *logit* command (9.6.1):

```
.test _Iprimord~1 = _Iprimord~2
```

The *p*-value resulting from the Wald test is the confidence by which we can reject the null hypothesis, which is that the two proportions are not different. If *p*-value < 0.05 then we considered the two proportions significantly different (represented as one star above the appropriate line segment on the figures). If *p*-value < 0.01 then we considered the difference highly significant (represented as three stars above the corresponding line segment on the figures 2.3 – 2.5, chapter 2).

9.7 Neonatal mouse ovary collection (†)

C57BL/6 mice were obtained on day 4pp and day 12pp (Harlan Olac Ltd, UK). Ovaries at day 4 (*n*=3) and day 12 (*n*=3) were dissected and fixed immediately as *in vivo* control samples. Ovaries from 6 day 4pp mice were collected in Dulbecco Modified Eagle medium/F12 (DMEM/F12) with HEPES (Invitrogen Ltd, Paisley, UK) and then cleanly dissected from bursa membrane, fat and oviduct under a SMZ 1500 stereo microscope (Nikon Ltd, Kingston, UK). The pairs of ovaries were then allocated to one of 2 culture conditions, one of them with a Matrigel® tissue support matrix (Wright *et al*, 1999), and one without any support (floating filters; Eppig and O'Brien, 1996).

9.8 Culture conditions for neonatal mouse ovaries (†)

The tissue was cultured on plate inserts (Millicell-CM12mm diameter, 0.4μm pore size, Millipore, Bedford, MA, USA) in a 24 well plate (Nunclon, Roskilde, Denmark). 1 ovary from each animal was cultured in a floating filter system, and the other ovary was cultured on an insert that was coated with an artificial extra-cellular matrix containing minimal growth factors (growth factor reduced Matrigel; Becton Dickenson). The growth factor reduced Matrigel was diluted, according to the guidelines, 1:3 in Earles balanced salt solution (EBSS; Invitrogen). 100μl was then layered onto the base of the plate insert and this was then incubated at 37°C for between 30 minutes to 1 hour prior to the tissue being added, to allow the Matrigel to set.

The basic medium used for the culture was DMEM/F12 without Hepes (Invitrogen) containing 0.1% w/v bovine serum albumin (BSA; Sigma-Aldrich Compnay Ltd, Dorset, UK), 0.1% v/v Albumax (Invitrogen), 2.75μg/ml transferrin (Invitrogen), 6.7ng/ml sodium selenite (Sigma) and antibiotics (penicillin/streptomycin, 50IU/50μg/ml; Invitrogen). 100μl of filter sterilised pre-conditioned media was placed over the tissue in each insert so it formed a meniscus, and 400μl was placed around the insert, in the well of the plate. The plates were then incubated at 37°C under 5% CO2 for 8 (n = 6 ovaries) or 12 (n = 6 ovaries) days. The medium was removed every 2 days and replenished with fresh medium.

9.9 Ovarian histology for neonatal mouse (†)

After 8 or 12 days in culture the tissue was fixed in Bouins fixative (Sigma) for 4 hours and kept in 70% ethanol until processed. The tissue was then dehydrated through a series of ethanol (70%, 90% for 1 hour each, 100% x3, 1.5 hour each), and cleared using a xylene substitute (Histoclear; National Diagnostics). The tissue was then submerged in molten paraffin wax and the wax block was cooled on ice. The whole of the sample was serially sectioned (5μm) on a Leica microtome until there was no tissue left in the block. To visualise the sections of ovary, the nuclei of the cells was stained with haematoxylin and the cytoplasm of the cells were stained with aqueous eosin solution.

The slides were dewaxed in 2 changes of Histoclear (5 min each) and rehydrated through an alcohol series (100%, 100%, 70%, 2 min each). The slides were then stained with Erlichs haematoxylin (Fisher) for about 15 minutes. The haematoxylin was washed off with tap water and then differentiated with 1% acid alcohol (1ml HCl in 100ml 70% v/v ethanol) for a few seconds. The sections were washed in tap water until the stain had taken on a blue colour. The slides were then stained in aqueous eosin (Fisher) for 5 minutes and then washed in tap water before rapid dehydration in ethanol (70% v/v few seconds, 100%, 100%, 1 minute each maximum). The slides were then transferred to Histoclear (5 min x 2) and then mounted with Distyrene Plasticizer and Xylene mountant (VWR, Lutterworth, UK).

9.10 Morphological analysis of mouse follicles (†)

Ovarian cortical sections were viewed on an E600 microscope at 60x magnification, and images were taken with a DXM 1200 digital camera and captured using the Lucia™ image analysis system (Nikon Ltd). Follicles were classified as healthy or as having signs of atresia. An atretic follicle was described as a follicle that had 2 or more of the following criteria; 1. pyknosis of the nuclei of the granulosa cells or oocyte, 2. vacuoles in the oocyte cytoplasm, 3. condensation of nuclear or cytoplasmic material, 4. shrinkage or blebbing of the membrane (Webber *et al*, 2003).

Healthy follicles were classified according to the stage of development, primordial follicles having 100% flattened granulosa cells, transitional follicles were

described as having at least 1 cuboidal granulosa cell, primary follicles having a complete layer of cuboidal granulosa cells, primary + having the beginning of a second layer of cuboidal granulosa cells, and secondary follicles having 2-5 layers of cuboidal granulosa cells. Under the culture conditions used in these experiments the follicles rarely progress beyond the secondary stage during the time of culture or indeed in the day 12 in vivo samples. The diameters of the oocyte and follicle were analysed by taking a mean of the perpendicular measurements from the oocyte membranes and basal laminae respectively, and the number of granulosa cells surrounding the oocyte was noted (Stubbs *et al*, 2007).

9.11 Data collection for spatial analysis (†)

Images of entire sections were captured using a camera mounted on the light microscope (Nikon Eclipse with DXM 1200 digital camera). The sections were either included on a single image, or if they were too large, two or more overlapping images were captured and then stitched together (DoubleTake application) into one containing the whole section. The image was then imported into GraphClick (Arizona Software, see 9.4) for mapping the *XY* coordinates of the centre of each follicle on the section, as well as for recording the ovarian surface epithelium coordinates (as described in 9.5.2). The definition of scale was extremely important in order to conduct correct mapping of coordinates, so the GraphClick programme was initialized using the width and height of the whole section (or specific part of it), measured on the microscope analysis software (LUCIA, section 9.3).

9.12 Neonatal mouse ovary collection for fixation or culture (††)

Mice were housed in accordance with the Animals (Scientific Procedures) Act of 1986 and associated Codes of Practice. Ovaries were fine dissected from bursa membrane, fat and oviduct under a SMZ 1500 stereo microscope (Nikon Ltd, Kingston, UK) from neonatal mice (C57BL/6, Harlan), up to day 12 *post partum*. The ovaries were either fixed in Formalin, for at least 24h, or immediately placed into collection media (DMEM/F12 with HEPES, Invitrogen #31330, gassed and pre-warmed to 37^{o}C) to prepare for culturing.

9.13 Whole ovary immunohistochemistry

Standard immunohistochemistry was used for specific staining in whole ovaries. Antibodies, despite their considerable molecular weight and size, were able to diffuse inside the tissue without any complications. A simple protocol was formulated to immunostain for the Mouse Vasa Homologue (MVH) protein (the antibody donated to us was raised in rabbit, therefore it is a polyclonal antibody) within the ovarian oocytes. The same procedure can be followed to stain for any object of interest.

Formalin-fixed juvenile mouse ovaries were dehydrated through absolute Methanol and equilibrated on ice for at least 1 hour. These samples can also be stored for extended periods in Methanol. Tissue cell basement membrane permeabilization followed dehydration, which is a crucial step that promotes antibody penetration in the whole volume of the tissue, and additionally quenches autofluorescence, which is usually an unwanted property of the tissue. This was done by treating the ovary through a series of solutions, namely Methanol for 1h, Methanol:DMSO, 4:1 v/v for 1h and Methanol:DMSO:H_2O_2, 7:2:1 v/v for 1h (Dimethyl Sulphoxide – DMSO was purchased from Sigma). Tissue was then re-hydrated through a series of Methanol and Phosphate Buffered Saline (PBS) solutions[†]. Methanol v/v concentrations are 100%, 75%, 50%, 25% and 0%, and the tissue was treated in each solution for 10mins.

Before introducing the primary antibody in the tissue, non-specific binding sites were blocked by transferring the sample into CAS-Block™ (a universal commercial blocking agent; Zymed Laboratories, Inc) for an hour. Tissue was then incubated for more than 12h (overnight), at 4ºC into the primary MVH targeting antibody (rabbit anti-mouse *vasa* homologue; courtesy of Dr T Noce of the Mitsubishi Kagaku Institute of Life Sciences, Tokyo, Japan). The concentration of the primary antibody used was 1:5000 v/v, diluted in CAS-Block.

The ovary was then thoroughly washed in PBS (5 x 1h, optional shaking) before incubating into the secondary antibody; the antibody was raised in goat to target the primary antibody (rabbit). The secondary antibody was diluted in CAS-Block in 1:300 v/v concentration. The fluorophore that is conjugated to the secondary antibody is a goat anti-rabbit IgG Alexa fluor 633 (Invitrogen, #A21070, excitation

[†] PBS used: 0.14M NaCl, 2.68mM KCl, 8.1mM Na_2HPO_4, 1.66mM NaH_2PO_4; pH: 7.3±0.2 @ 25^0C

and emission spectra appear in figure 9.8), which worked flawlessly with the MVH primary antibody, whereas same Alexa 405 and 488 fluorophores that were tested did not yield results as satisfactory (data not shown). Tissue was incubated overnight at 4ºC in the secondary antibody, with gentle rocking.

9.14 Whole tissue mounting and chemical clearing

Tissue was washed in PBS (3 x 30mins) after the secondary antibody incubation. The sample was then set into 1% Low Melting Point Agarose, prewarmed to 37ºC, and then was left at room temperature to set, forming a gel block. The block was then transferred into 100% Methanol for 2h to dehydrate. In order to ensure that there was no water residue whatsoever, the Methanol was replaced after 2h with fresh Methanol (100%); tissue was stored in that overnight – for at least 12h. The container must be kept in the dark to ensure that there will be no fluorescence photobleaching from ambient lights. Note that the tissue can be stored in the dark for extended periods of time at 4ºC in Methanol without loss of fluorescence intensity.

The agarose mounted tissue was then optically cleared using a mixture of 1:2 v/v Benzyl Alcohol : Benzyl Benzoate (both obtained from Sigma) for at least 4h. BABB-cleared agarose block was positioned within a coverslip chamber (nunc LabTek chambered coverglass system #155411), with an additional small quantity of BABB to account for any evaporation, and it was taken for imaging on a Leica SP5 inverted confocal microscope. The refractive index of BABB is 1.54, and is almost identical to that of the cleared block of tissue, thus reducing optical distortion (Zucker, 2006, Zucker and Jeffay, 2006). It is critical that the tissue was completely equilibrated in 100% Methanol before submerging it in the BABB solution, as any residual water would cause precipitation in the tissue, making it opaque.

It must be noted at this point that BABB dissolved most adhesives and plastics within a couple of hours, including nail polish, causing dangerous leakages. This chemical is very harmful to microscope objective lenses and to human skin and eyes (Zucker, 2006). We found that using the commercially available coverslip chambers obtained from nunc there were no leakages within a minimum of 3 hours, which was safe to allow imaging for multiple ovaries. Therefore, the time BABB takes to

dissolve any chambers containing the tissue must be taken into account when imaging for extended periods of time.

9.15 Whole tissue imaging using laser scanning confocal microscopy

Leica inverted SP5 Confocal Microscope

The system we used for imaging consists of an inverted Leica SP5 microscope and some assorted lasers, from which we utilized the HeNe laser with excitation of 633 nm, collecting the emission of the Alexa 633 antibody to the range of 640 nm – 750 nm (figure 9.8). The objective lenses of our choice for the imaging were the 10x (fluotar 10.0x dry, numerical aperture 0.3, working distance 11000μm) and the x20 (fluotar x20.0 dry, numerical aperture 0.5, working distance 1500μm) zooming appropriately so that the widest part of the ovary could fit within the scanning frame. The working distance of these objectives is big enough to allow imaging through an entire neonatal ovary; their diameter can be around 500μm (own observations). Zooming allows for more detail to be captured with a given objective. It can be performed in most modern confocal microscopes, by confining the laser scanning to a specific area of the sample, which is selected by the user. The selected area is scanned and captured at the same resolution (e.g 512x512 pixels) as the original full scale image, effectively resulting in a zoomed part of the sample.

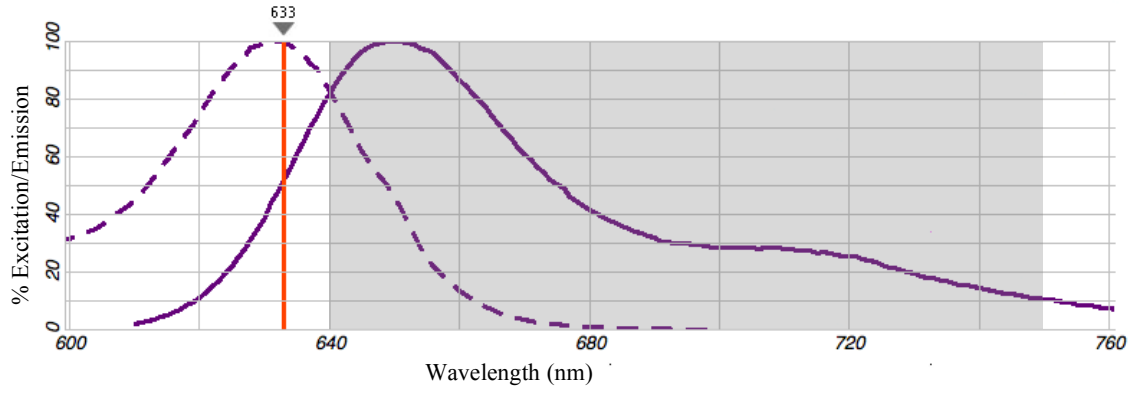


Figure 9.8: Alexa 633 excitation (dashed line) and emission spectra (continuous line). The fluorophore is excited using a HeNe laser at 633 nm, and the emission is collected between 640 nm to 750 nm (gray area).

The resolution of the image was set to 1024 by 1024 pixels, of 256 gray levels of intensity (8-bit), to ensure that fine details of the sample were preserved on the focal plane. As a general rule to obtain good contrast and scientifically equitable images when using laser scanning confocal microscopy was to offset all pixel grayscale values slightly above 0 and saturate them just below the 255. Optical slices were obtained at a sample depth interval of 2.5 or 3.0 μm, covering the entire volume of the ovary. Each frame was scanned with a pinhole of either 1 or 0.5 Airy Units (system minimum), in order to limit as much as possible the background fluorescence occurring from the out-of-focus laser beam illumination of the rest of the tissue.

To improve image clarity, each acquisition on every focal plane was averaged 4 times. This is a very important function of the confocal microscope, which involved scanning each line of pixels or the entire image frame *n* times, and finally reconstructing the image by assigning to each pixel the average value of the *n* obtained. The signal-to-noise ratio of the image was improved by averaging, but if overused, it can cause the fluorescent dye to photobleach.

Leica inverted SP5 Confocal Microscope with multi-photon laser

Imaging was also performed on a similarly configured Leica SP5 inverted confocal microscope, which featured a shared Ti:Sapphire infrared pulse laser, tunable from 690nm to 1020 nm (Mai Tai HP:IR ps multi-photon laser, Spectra-Physics, Mountain View, CA). Tissue was prepared as explained in 9.13 & 9.14, only this time Alexa 488 (Invitrogen #A11008) secondary antibody was used, which can be excited at its maximum by 500nm wavelength radiation. The multi-photon laser was tuned to emit photons at 1000nm wavelength in order to excite the fluorophore (see Introduction 1.8.3, two-photon excitation). Emission of the Alexa 488 was collected at the range of 500nm-570nm. The Alexa 633 antibody that was normally used would require tuning the laser to emit photons at around 1300nm wavelength, which exceeds the instrument capabilities.

Furthermore, trials have been performed to assess the results obtained using multi-photon system with tissue immunostained using secondary antibodies conjugated to quantum dots (see Introduction, 1.11.1) (Pawley, 2006). The quantum dots of our choice were the Qdot 625 (Qdot 625 goat anti-rabbit, Invitrogen

#A10194), which were excited by light in the near UV spectrum (~50% excitation at 400nm) and emitted at 625nm (far red spectrum). The dye was excited by tuning the multi-photon laser to emit 800nm infrared photon pulses. The staining protocol followed was exactly the same as described in sections 9.13 & 9.14. However, the results of this staining were not satisfactory, as it was found later that the Qdots were unstable if used with PBS.

Autofluorescence

When examining the tissue morphology, the naturally induced fluorescence, or autofluorescence, can be very informative (autofluorescence; Introduction, 1.11.1). Samples used in this case were unstained, transferred from Formalin to Methanol and then cleared as described in 9.13 & 9.14. In order to determine the optimal excitation and emission spectrum for autofluorescence, λ-scans were performed on the Leica SP5 confocal microscope. Each time, a laser line was selected to excite the unstained sample, and emission was collected on the entire visible spectrum of greater wavelength than the laser emission wavelength, according to the Stokes shift principle. For example, when using the 488 laser line as an excitation source, emission is investigated in the spectrum of 495nm (8nm away from the excitation light) and 700nm. The λ-scan essentially captures images within set intervals within the band of the spectrum specified. This was repeated for all the laser lines available, at the same power level. After this process was completed, the image offering the best contrast in the tissue among those obtained denotes the maximum emission wavelength of the autofluorescence, for a specific excitation laser line. We found the best images are obtained using the 488 laser, at around 20% power, collecting the emission of the autofluorescence in the range of 495nm-550nm.

Object visualization

The entire sample volume could be computationally reconstructed using the optical planes captured by the confocal microscope. To accomplish this, we used the Volocity software (Improvision Volocity, Perkin Elmer, Cambridge, UK), which offers a wide variety of volume reconstructing options. The optical planes were inserted in the programme and intensity rendering was performed, so that the internal

components of the tissue were visible. The reconstructions at this point were mainly performed for illustrative purposes, and for tissue morphological assessment. There are no options for sophisticated object recognition methods within the Volocity programme available up to date, which could be used for automated oocyte counting.

9.16 Live imaging of neonatal mouse ovaries in culture

Collection media was prepared for tissue maintenance, during tissue transportation from dissection room to the sterile hood, and until the tissue was placed into culture. This media was the DMEM/F12 solution with HEPES (Invitrogen, #31330), which was pipetted into sterile 5ml collection tubes and placed into an incubator maintaining a 37ºC temperature and air with 5% CO2 concentration, to warm and gas, before it coulb be used.

9.16.1 Culture media

Culturing was performed at 37°C, in presence of 5% CO_2 air. The ovaries were cultured in specially prepared media, without any added growth factors; additional components that promote tissue development and improve survival in culture were necessary though, but these did not affect follicle development (such as antibiotics and serum). Reported in Table 9.2 are the ingredients used to prepare the culture media, and their concentrations.

Table 9.2: Culture media solution components.

Ingredient	Concentration required	Content in 10ml solution
DMEM/F12 without HEPES (Invitrogen, #21041)	Use as is	9.75ml
Bovine Serum Albumin (BSA) (Sigma)	0.10% (w/v)	0.01g
Albumax (Invitrogen)	0.10 % (w/v) (stock at 0.1g/ml)	0.1ml
Transferrin (Invitrogen)	2.75µg/ml (stock at 4mg/ml)	6.9µl
Sodium Selenite (Sigma)	6.7ng/ml (stock at 2µg/ml)	33.5µl
Penicillin/Streptomycin (Invitrogen)	50IU P + 50µg/ml S	0.1ml

All components were prepared and mixed into a solution in a sterile environment, to avoid any infections. The solution was additionally passed through a 0.2μm sterile syringe filter (Millipore, Bedford, MA, USA) into a sterile tube, and then placed into an incubator to warm to 37ºC, before tissue collection.

In order to improve live tissue visualization, a lipophilic dye (BODIPY FL C12, Invitrogen #D-3822) that stains lipid bi-layers which can be used as a general membrane marker, was added in the culture media, in 0.05mM concentration. The amount of BODIPY to be added to 1ml of media can be calculated using the two fundamental formulae:

$$n = \frac{m}{mw} \tag{9.VIII}$$

$$C = \frac{n}{V} \tag{9.IX}$$

where: n is the number of moles, m is the mass, mw is the molecular weight, C is the concentration and V is the volume The molecular weight of the specific BODIPY molecule is 418.33. In 1ml of culture media, the volume of BODIPY that needs to be added is 21μl, in order to have a 0.05mM concentration solution. Ovaries were cultured for approximately a day in this culture media. The presence of BODIPY in the reported concentration does not disrupt tissue viability for such a short culturing time.

DRAQ 5™ counterstaining

DRAQ 5™ (Biostatus limited) is a far-red fluorescent DNA specific dye that can be used in both live and fixed cells. It was preferred over commonly used fluorescent dyes such as Hoescht or DAPI, which also label DNA, because it is extremely photobleaching resistant. In addition, it is excited by red light (633nm HeNe laser); this light caused much less photo-damage to the cells or tissue than UV light used to excite Hoescht and DAPI. In 0.5ml of solution, 1μl of DRAQ 5™ was added, both when culturing KK1 granulosa cells or juvenile mouse tissue. Tissue could then be fixed, chemically cleared and imaged on the confocal microscope; the DRAQ 5™ was still adequately detectable.

9.16.2 Culture set-up

C57BL/6 mice were obtained on various ages up to day 8pp (Harlan) (section 9.12), as part of various experiments; one of the two ovaries was offered for the time-lapse culture experiment. Tissue was cultured in coverslip chamber slides (nunc Lab-Tek coverglass system, 8 chamber, #155411), in order to be imaged on the confocal microscope.

DMEM/F12 culture media supplemented with BSA, Albumax, Transferrin, Sodium Selenite, Penicillin and Streptomycin (concentrations and preparations described in 9.16.1) including the BODIPY dye, was added in the slide chamber. This was filled with a quantity of approximately 800μl. The ovary was then positioned inside the chamber, which had a thin coverslip bottom, so that it could be imaged on the inverted microscope properly. A few drops of mineral oil (Sigma) were added before imaging in the chamber where the ovary was cultured, creating a protective surface on the well that allowed gas exchange but prevented media evaporation while the tissue was in the microscope incubator. As an additional precaution to prevent media evaporation, the rest of the chambers were filled with any surplus prepared culture media, before covering the slide chambers.

No supporting materials were used for the culture, such as Matrigel or filters (as done in method described in section 9.8), as this would interfere with the live imaging. We did run some tests using alginate hydrogels as a supporting matrix for our ovary cultures (methods: Xu *et al*, 2008). Although the gel did not significantly interfere with light, there were problems with the tissue constantly shifting inside the alginate. Therefore the hydrogel method was abandoned. We found that tissue sitting at the bottom of the coverslip slide chamber filled with culture media could be cultured without any problems with gas or nutrient diffusion into the tissue, for such a short time (up to 1 day). The ovary was left to equilibrate at the bottom, so that it stayed immobile for imaging. Caution must be taken, after placing the ovary for imaging on the microscope, to avoid any movement of the chamber slide or any vibrations, otherwise the time-lapse imaging would be affected.

9.16.3 Time-lapse imaging

The slide chamber was positioned inside the timelapse incubator of an inverted Leica SP5 confocal microscope. The incubator was maintained at 37ºC temperature, and there was a continuous supply of air containing 5% CO_2 in a small area in the incubator where the culture slide chamber was located. Images of the ovary were acquired using either a dry 20x magnification objective (Fluotar 20.0x dry, numerical aperture 0.5, working distance 1500μm) or a 10x objective (Fluotar 10.0x dry, numerical aperture 0.3, working distance 11000μm), zooming appropriately so that follicles were in clear view (see also Chapter 5, 5.2.4). Image resolution was set to 1024x1024 pixels, 256 grayscale values. Eight optical slices, around 1.8μm apart were acquired at a maximum frequency of every 9 minutes, for at least six hours, averaging each line of the frame 4 times. The 488nm line of an Argon laser was used, exciting the BODIPY fluorophore at 56% and collecting the emission in the range of 500nm – 550nm. The Argon laser power was set to 20%, and the output power of the 488 line was set to 7%. The final 488 laser output using the 20x objective was measured at 19μW maximum. If autofluorescence was to be used, as described in chapter 5, the required power of the 488 laser would reach at least 0.4mW, which would induce severely more light toxicity. In order to further reduce laser induced toxicity on the tissue, scanning was set to 1000Hz frequency, bidirectional, meaning that 1000 lines of the sample are scanned every second, in both directions (laser does not only scan one direction and then returning to scan the next line, but scans also on its way back, which doubles the scanning speed). The minimum zoom setting for the 1000Hz frequency was x3, which proved useful in our case, as the follicles were more clearly displayed using the 10x objective. After the completion of the time-lapse imaging, ovaries were fixed in Formalin and prepared for whole tissue imaging, following the procedure described in sections 9.13 – 9.15. This method enables the experimentalist to assess their state at the end of the culturing.

9.17 The Simulated Ovary algorithm

It must be emphasized that the data used to produce the simulated ovaries are from real data, extracted from mouse ovarian sections. These data were part of

previous studies, investigating the spatial relationships of follicles in the neonatal mouse ovary (Da Silva-Buttkus *et al*, 2009). The computer programme to generate the simulated ovaries was coded in Fortran 77 (GNU g77 v3.4 compiler was used to compile the programme).

Using statistical analysis software (STATA 8), we calculated the mean value and standard deviation of the follicle, oocyte, nucleus and nucleolus diameters for each follicle type and for each age, using two ovarian sections per age group (i.e. day 4, day 8 and day 12 mouse ovaries). We used these values to calculate the ratio between the mean follicle diameter and the mean diameter from the other structures (oocyte, nucleus and nucleolus, respectively) reported in Tables 9.3 and 9.4. The mean and standard deviation of the follicle distance to the ovarian surface for each follicle type and for each ovarian age were also calculated (Table 9.5).

Table 9.3 Follicle *diameter* data from neonatal mouse ovarian section analysis.

Follicle Type	Day 8	Day 12
Primordial (Mean± Std Dev) (µm)	20 ± 5 (*n*=79)	18 ± 5 (*n*=136)
Primary (Mean± Std Dev) (µm)	48 ± 5 (*n*=6)	51 ± 10 (*n*=5)
Secondary (Mean± Std Dev) (µm)	–	79 ± 7 (*n*=4)

Table 9.4 Ratios between oocyte, nucleus and nucleolus diameter and the follicle diameter.

Follicle Stage	Oocyte	Nucleus	Nucleolus
Primordial	0.78	0.38	0.16
Primary	0.64	0.26	0.08
Secondary	0.54	0.21	0.06

Table 9.5 Follicle *distance* to ovarian wall. (Data from neonatal mouse ovarian sections).

Follicle Type	Day 8	Day 12
Primordial (Mean± Std Dev) (μm)	30 ± 25	24 ± 17
Primary (Mean± Std Dev) (μm)	69 ± 29	70 ± 29
Secondary (Mean± Std Dev) (μm)	–	174 ± 77

Table 9.6 Follicle numbers in whole neonatal mouse ovaries: data reported by Kerr *et al* (2006).

Age in days	Total Primordial follicles ± *SEM*	Total Primary follicles ± *SEM*	Total Secondary follicles ± *SEM*
7	1987 ± 203	569 ± 35	5 ± 4
12	2317 ± 289	362 ± 34	328 ± 34

The data in tables 9.3 to 9.6 were used to construct simulated ovaries. These were assumed to be spherical. The same holds for all follicles contained within the ovaries. More precisely, each follicle was constructed with co-centric spherical oocyte, nucleus and nucleolus. We adopted these spherical structures for reasons of simplicity.

The diameter of each follicle in the simulated ovary was randomly chosen from a Gaussian distribution (Press *et al*, 2007– Numerical Recipes, Chapter 7), the mean and the standard deviation of which were taken from Table 9.3. We considered two numbers coinciding with the maximum and minimum follicle diameters measured from the ovarian sections and when a value pulled from the distribution was not within the range of these two numbers, it was rejected and a new one was generated. The diameters of the remaining structures (oocyte, nucleus and nucleolus, respectively) for each follicle were assigned according to the ratios reported in Table 9.4. Once all follicles were assigned a diameter, they need to be inserted in the spherical ovary. For this purpose, the volume of the ovary needs to be chosen as a proportion, $a>1$, of the total volume occupied by the follicles:

$$a = \frac{V_{\text{ovary}}}{\sum_{1}^{N} V_{follicle}} \qquad (a > 1) \qquad (9.X)$$

The ovary diameter can be calculated by the formula:

$$d_{\text{ovary}} = \sqrt[3]{\frac{6}{\pi} a \sum_{i=1}^{N} V_i} \qquad (9.XI)$$

where N is the total number of follicles, V_i is the volume of follicle i (spherical volume).

In order to insert a given follicle in the ovary, a random point was chosen on the spherical surface of the ovary (page 111, Howard and Reed 1998). The follicle was placed in the direction of the random point chosen on the spherical surface, along the ovarian radius, at a specific distance from the ovarian wall. This distance was randomly picked from a Gaussian distribution, the mean and the standard deviation of which were taken from table 9.5. If a negative number was generated, then the distance was rejected and a new one was generated. If the new follicle inserted overlaps with any of those previously inserted, a new point on the surface was picked, while the distance to the wall was kept constant, in order to preserve the Gaussian distribution, until an available spot is found. This procedure was iterated for a number of times t. If after t attempts no available spots are found, the procedure was repeated from the beginning, i.e. a new distance to the ovarian wall is chosen, together with a new random point on the spherical surface. It is worthwhile to stress that the value of t chosen affects the mean follicle distance from the ovarian surface.

Once all the follicles are inserted, the follicle profile density, $\rho_{profile}$, was calculated for the equatorial cross-section as:

$$\rho_{profile} = \frac{\sum_{i=1}^{N_p} A_{profile}}{A_{\text{sec}tion}} \qquad (9.XII)$$

where $A_{profile}$ is the area occupied by each profile (follicle cross-section), $A_{section}$ is the area of the cross-section and N_p is the number of profiles on an equatorial cross-section. If the profile density was within 10% of the one from the real sections, the

ovary is accepted; otherwise a new ovary is generated. The success rate in generating acceptable ovaries depends strongly on the value of *a* chosen. We found that for *t=10,000* and for the values of *a* (Eq 9.X) reported in table 9.7, we not only had a high success rate, but also the mean distance from the ovarian surface of follicles within an equatorial section well reproduced the experimental mean distance (Table 9.5).

Table 9.7: Profile density, $\rho_{profile}$, calculated from the actual ovarian sections and volume proportion, *a*, used to generate simulated ovaries.

Ovary age	Actual $\rho_{profile}$ (Eq. 9.XII)	Volume proportion, *a*
Day 7	0.47	2.4
Day 12	0.64	2.5

We generated simulated ovaries of two different ages, namely day 7 and day 12 post natal. Each of these ovaries was randomly assigned a number of primordial follicles, as well as primary and secondary follicles, according to a normal distribution. We chose one Gaussian distribution for each age and follicle stage, the mean and the standard deviation of which were selected according to the data reported by Kerr *et al*, 2006 and shown in table 9.8. This means each ovary had a different random number of primordial, primary and secondary follicles, picked from Gaussian distributions (Press *et al*, 2007 – Numerical Recipes, Chapter 7) different for every type of follicle. The position of each follicle in an ovary was assigned according to the procedure explained above. We generated 350 ovaries for each age, since we checked that this number adequately samples the chosen distributions (see section 4.2.3).

Table 9.8: Mean and standard deviation of the various Gaussian distributions used to generate the follicle numbers for each stage and age. The data have been obtained and adjusted taken from Kerr *et al.* 2006 (see table 9.6)

Age	Primordial (*mean* ± *Std Dev*)	Primary (*mean* ± *Std Dev*)	Secondary (*mean* ± *Std Dev*)
Day 7	2000 ± 490	570 ± 86	5 ± 4
Day 12	2300 ± 770	360 ± 90	330 ± 90

In order to generate the follicle spatial distribution of day 7 ovaries, we used the data of day 8 ovaries, in absence of day 7 sections, assuming that follicle distributions from the two ages were similar (see 4.2.1).

REFERENCES

Abercrombie M.
Estimation of nuclear population from microtome sections.
Anatomical Records, Vol 94, pp 239–247, 1946

Abir R, Franks S, Mobberley MA, Moore PA, Margara RA, Winston RM.
Mechanical isolation and in vitro growth of preantral and small antral human follicles.
Fertility and Sterility, Vol 68, No 4, pp 682-8, 1997

Abir R, Roizman P, Fisch B, Nitke S, Okon E, Orvieto R, Ben Rafael Z.
Pilot study of isolated early human follicles cultured in collagen gels for 24 hours.
Human Reproduction, Vol 14, No 5, pp 1299-301, 1999

Adhikari D, Liu K.
Molecular mechanisms Underlying the Activation of Mammalian Primordial Follicles.
Endocrine Reviews, Vol 30, No 5, 438-464, 2009.

Alanentalo T, Lorén C E, Larefalk A, Sharpe J, Holmberg D, Ahlgren U.
High-resolution three-dimensional imaging of islet-infiltrate interactions based on optical projection tomography assessments of the intact adult mouse pancreas.
Journal of Biomedical Optics, Vol 13, No 5, 054070, 2008

Alberts B, Johnson A, Lewis J, Raff M, Roberts K, Walter P.
Molecular Biology of the Cell.
Garland Science, 5th edition, ISBN: 978-0-8153-4105-5, 2008

Andres JL, DeFalcis D, Noda M, Massagué J.
Binding of two growth factor families to separate domains of the proteoglycan betaglycan.
Journal of Biological Chemistry, Vol 267, No 9, pp 5927-30, 1992

Aravindakshan J, Chen X, Sairam MR.
Differential expression of claudin family proteins in mouse ovarian serous papillary epithelial adenoma in aging FSH receptor-deficient mutants.
Neoplasia,.Vol 8, No 12, pp 984-94, 2006

Arici A, Oral E, Bahtiyar O, Engin O, Seli E, Jones EE.
Leukaemia inhibitory factor expression in human follicular fluid and ovarian cells.
Human Reproduction, Vol 12, No 6, pp 1233-9, 1997

Baker T G.
A quantitative and cytological study of germ cells in human ovaries.
Proceedings of the Royal Society of London, Vol 158, pp 417-33, 1963

Baker TG
Oogenesis and ovarian development.
In Reproductive Biology (Ed. H. Balin & S. R. Glasser), pp. 398-437. Amsterdam: Excerpta Medica, 1972

Baker T G, Franchi L L.
The fine structure of oogonia and oocytes in human ovaries.
Journal of Cell Science, Vol 2, No 2, pp 213-24, 1967

Baker J, Hardy MP, Zhou J, Bondy C, Lupu F, Bellvé AR, Efstratiadis A.
Effects of an Igf1 gene null mutation on mouse reproduction.
Molecular Endocrinology, Vol 10, No 7, pp 903-18, 1996.

Balen A, Homburg R, Franks S.
Defining polycystic ovary syndrome.
BMJ, Vol 338, p a2968, 2009

Bankman I N.
Medical image processing and analysis.
ISBN: 978-0-12-373904-9, © Elsevier Inc, 2009

Barber TM, Bennett AJ, Groves CJ, Sovio U, Ruokonen A, Martikainen H, Pouta A, Hartikainen AL, Elliott P, Lindgren CM, Freathy RM, Koch K, Ouwehand WH, Karpe F, Conway GS, Wass JA, Järvelin MR, Franks S, McCarthy MI.
Association of variants in the fat mass and obesity associated (FTO) gene with polycystic ovary syndrome.
Diabetologia, Vol 51, No 7, pp 1153-8, 2008

Barbieri RL, Makris A, Ryan KJ.
Effects of insulin on steroidogenesis in cultured porcine ovarian theca.
Fertility and Sterility, Vol 40, No 2, pp 237-41, 1983

Benedict JC, Lin TM, Loeffler IK, Peterson RE, Flaws JA.
Physiological role of the aryl hydrocarbon receptor in mouse ovary development.
Toxicological Sciences, Vol 56, No 2, pp 382-8, 2000

Block E.
Quantitative morphological investigations of the follicular system in women; variations at different ages.
Acta Anatomica, Vol 14, No 1-2, pp 108-23, 1952

Boland NI, Humpherson PG, Leese HJ, Gosden RG.
Pattern of lactate production and steroidogenesis during growth and maturation of mouse ovarian follicles in vitro.
Biology of Reproduction, Vol 48, No 4, pp 798-806, 1993

Bottaro DP, Rubin JS, Ron D, Finch PW, Florio C, Aaronson SA.
Characterization of the receptor for keratinocyte growth factor. Evidence for multiple fibroblast growth factor receptors.
The Journal of Biological Chemistry, Vol 265, No 22, pp 12767-70, 1990

Bristol-Gould SK, Kreeger PK, Selkirk CG, Kilen SM, Cook RW, Kipp JL, Shea LD, Mayo KE, Woodruff TK.
Postnatal regulation of germ cells by activin: the establishment of the initial follicle pool.
Developmental Biology, Vol 298, No 1, pp 132-48, 2006

Broekmans F J, Knauff E A, te Velde E R, Macklon N S, Fauser B C.
Female reproductive ageing: current knowledge and future trends.
Trends in Endocrinology and Metabolism, Vol 18, No 2, pp 58-65, 2007

Byskov A, Guoliang X, Andersen C.
The cortex–medulla oocyte growth pattern is organized during fetal life: an in-vitro study of the mouse ovary.
Molecular Human Reproduction, Vol 3, no 9, pp 795–800, 1997

Canning J, Takai Y, Tilly J.
Evidence for genetic modifiers of ovarian follicular endowment and development from studies of five inbred mouse strains.
Endocrinology, Vol 144, pp 9-12, 2003

Canny J.
A computational approach to edge detection.
IEEE Transactions on Pattern Analysis and Machine Intelligence, vol 8, pp. 679–698, 1986.

Cantley LC.
The phosphoinositide 3-kinase pathway.
Science, Vol 296, No 5573, pp 1655-7, 2002

Cao Y, Xing Q, Zhang ZG, Wei ZL, Zhou P, Cong L.
Cryopreservation of immature and in-vitro matured human oocytes by vitrification.
Reproductive Biomedicine Online, Vol 19(3), pp 369-73, 2009

Carabatsos MJ, Elvin J, Matzuk MM, Albertini DF.
Characterization of oocyte and follicle development in growth differentiation factor-9-deficient mice.
Developmental Biology, Vol 204, No 2, pp 373-84, 1998

Carpenter A, Jones T, Lamprecht M, Clarke C, Kang H I, Friman O, Guertin D, Chang H J, Lindquist R, Moffat J, Golland P and Sabatini D.
CellProfiler: image analysis software for indentifying and quantifying cell phenotypes.
Genome Biology, vol 7, 2006

Chabot B, Stephenson DA, Chapman VM, Besmer P, Bernstein A.
The proto-oncogene c-kit encoding a transmembrane tyrosine kinase receptor maps to the mouse W locus.
Nature, Vol 335, No 6185, pp 88-9, 1988

Charleston S J, Hansen R K, Thyer C A, Charleston B L, Gougeon A, Siebert R J, Soules R M, Klein A N.
Estimating human ovarian non-growing follicle number: the application of modern stereology techniques to an old problem.
Human Reproduction, Vol 22, No.8, pp 2103-2110, 2007

Chen K, Perelman TL, Zhang Q, Dasari RR, and Feld SM.
Optical computed tomography in a turbid medium using early arriving photons.
Journal of Biomedical Optics, Vol 5, No 144, 2000

Chia TH, Levene MJ.
Microprisms for in vivo multilayer cortical imaging.
Journal of Neurophysiology, Vol 102, No 2, pp 1310-4, 2009

Cigale B and Zazula D.
Segmentation of ovarian ultrasound Images using cellular neural networks.
International Journal of Pattern Recognition, Vol 18, pp 563-581, 2004.

Cumming G, Fidler F, Vaux D L.
Error bars in experimental biology.
Journal of Cell Biology, Vol 177, pp 7-11, 2007

Cundiff ST and Ye J.
Colloquium: Femtosecond optical frequency combs.
Reviews of Modern Physics, Vol 75, pp 325 - 342, 2003

Da Silva-Buttkus P, Jayasooriya GS, Mora JM, Mobberley M, Ryder TA, Baithun M, Stark J, Franks S, Hardy K.
Effect of cell shape and packing density on granulosa cell proliferation and formation of multiple layers during early follicle development in the ovary.
Journal of Cell Science,Vol 121, Pt 23, pp 3890-900, 2008

Da Silva-Buttkus P, Marcelli G, Franks S, Stark J, Hardy K.
Inferring biological mechanisms from spatial analysis: Prediction of a local inhibitor in the ovary.
PNAS, Vol 106, pp 456-461, 2009

Danilovich N, Sairam MR.
Haploinsufficiency of the follicle-stimulating hormone receptor accelerates oocyte loss inducing early reproductive senescence and biological aging in mice.
Biology of Reproduction, Vol 67, No 2, pp 361-9, 2002

Derynck R, Lindquist PB, Lee A, Wen D, Tamm J, Graycar JL, Rhee L, Mason AJ, Miller DA, Coffey RJ, et al.
A new type of transforming growth factor-beta, TGF-beta 3.
EMBO J, Vol 7, No 12, pp 3737-43, 1988

Dewailly D, Catteau-Jonard S, Poncelet E.
Which morphological investigations and how to interpret them to make the diagnosis of PCOS?
Annales d'Endocrinologie (Paris), Vol 71, No 3, pp 183-8, 2010

Dong J, Albertini DF, Nishimori K, Kumar TR, Lu N, Matzuk MM.
Growth differentiation factor-9 is required during early ovarian folliculogenesis.
Nature, Vol 383, No 6600, pp 531-5, 1996

Dupont J, Holzenberger M.
Biology of insulin-like growth factors in development.
Birth Defects Research - part C Embryo Today, Vol 69, No 4, pp 257-71, 2003

Durlinger AL, Gruijters MJ, Kramer P, Karels B, Ingraham HA, Nachtigal MW, Uilenbroek JT, Grootegoed JA, Themmen AP.
Anti-Müllerian hormone inhibits initiation of primordial follicle growth in the mouse ovary.
Endocrinology, Vol 143, No 3, pp 1076-84, 2002

Durlinger AL, Gruijters MJ, Kramer P, Karels B, Kumar TR, Matzuk MM, Rose UM, de Jong FH, Uilenbroek JT, Grootegoed JA, Themmen AP.
Anti-Müllerian hormone attenuates the effects of FSH on follicle development in the mouse ovary.
Endocrinology. Vol 142, No 11, pp 4891-9, 2001

Durlinger AL, Kramer P, Karels B, de Jong FH, Uilenbroek JT, Grootegoed JA, Themmen AP.
Control of primordial follicle recruitment by anti-Müllerian hormone in the mouse ovary.
Endocrinology, Vol 140, No 12, pp 5789-96, 1999

Durlinger A L, Visser J A, Themmen A P.
Regulation of ovarian function: the role of anti-Müllerian hormone.
Reproduction, Vol 124, No 5, pp 601-9, 2002

Eckert JJ, Fleming TP.
Tight junction biogenesis during early development.
Biochimica et Biophysica Acta, Vol 1778, No 3, pp 717-28, 2008

Elvin JA, Yan C, Matzuk MM.
Oocyte-expressed TGF-beta superfamily members in female fertility.
Molecular.and Cellular Endocrinology, Vol 159, No 1-2, pp 1-5, 2000

Engel S, Scolari S, Thaa B, Krebs N, Korte T, Herrmann A, Veit M.
FLIM-FRET and FRAP reveal association of influenza virus haemagglutinin with membrane rafts.
The Biochemical Journal, Vol 425, No 3, pp 567-73, 2010

Eppig JJ.
Mouse oocyte development in vitro with various culture systems.
Developmental Biology, Vol 60, No 2, pp 371-88, 1977

Eppig J J, O'Brien M J.
Development in vitro of mouse oocytes from primordial follicles.
Biology of Reproduction, Vol 54, pp 197-207, 1996

Erickson F G, Shimasaki S.
The spatiotemporal expression pattern of the bone morphogenetic protein family in rat ovary cell types during the estrous cycle.
Reproductive Biology and Endocrinology, 1:9, 2003

Fabbri R, Pasquinelli G, Montanaro L, Mozzanega B, Magnani V, Tamburini F, Venturoli S, Keane D.
Healthy early preantral follicle can be obtained in a culture of frozen-thawed human ovarian tissue of 32 weeks.
Ultrastructural Pathology, Vol 31, No 4, pp 257-62, 2007

Faddy M
Follicle dynamics during ovarian ageing.
Molecular and Cellular Endocrinology, Vol 163, pp 43-48, 2000

Faddy M, Gosden R.
Numbers of Ovarian Follicles and Testing Germ Line Renewal in the Postnatal Ovary: Facts and Fallacies.
Cell Cycle, Vol 6, p 15, 2007

Faddy MJ, Gosden RG, Edwards RG.
Ovarian follicle dynamics in mice: a comparative study of three inbred strains and an F1 hybrid.
Journal of Endocrinology, Vol 96, No 1, pp 23-33, 1983

Faddy MJ, Telfer E, Gosden RG.
The kinetics of pre-antral follicle development in ovaries of CBA/Ca mice during the first 14 weeks of life.
Cell of Tissue Kinetics, Vol 20, No 6, pp 551-60, 1987

Falender E A, Shimada M, Lo K Y, Richards S J.
TAF4b, a TBP associated factor, is required for oocyte development and function.
Developmental Biology, Vol 288, pp 405-419, 2005

Fassnacht W, Mempel A, Strowitzki T, Vogt PH.
Premature ovarian failure (POF) syndrome: towards the molecular clinical analysis of its genetic complexity.
Current Medicinal Chemistry, Vol 13, No 12, pp 1397-410, 2006

Finlayson A, Sanders S
Endocrine and Reproductive systems.
Elsevier Ltd, 3rd edition, ISBN: 978-0-7234-3427-6, 2007

Flaws JA, Hirshfield AN, Hewitt JA, Babus JK, Furth PA.
Effect of bcl-2 on the primordial follicle endowment in the mouse ovary.
Biology of Reproduction, Vol 64, No 4, pp 1153-9, 2001

Forabosco A and Sforza C.
Establishment of ovarian reserve: a quanitative morphometric study of the developing human ovary.
Fertility and Sterility, Vol 88, no 3, pp 675 – 683, 2007

Franks S, Stark J, Hardy K
Follicle dynamics and anovulation in polycystic ovary syndrome.
Human Reproduction Update, Vol 14, no 4, pp 367–378, 2008

Galloway SM, McNatty KP, Cambridge LM, Laitinen MP, Juengel JL, Jokiranta TS, McLaren RJ, Luiro K, Dodds KG, Montgomery GW, Beattie AE, Davis GH, Ritvos O.
Mutations in an oocyte-derived growth factor gene (BMP15) cause increased ovulation rate and infertility in a dosage-sensitive manner.
Nature Genetics, Vol 25, No 3, pp 279-83, 2000

Gonzalez C R, Woods E R and Eddins L S.
Digital Image Processing Using MATLAB
Prentice Hall, 2004.

Gosden RG, Wade JC, Fraser HM, Sandow J, Faddy MJ.
Impact of congenital or experimental hypogonadotrophism on the radiation sensitivity of the mouse ovary.
Human Reproduction, Vol 12, No 11, pp 2483-8, 1997

Gougeon A.
Dynamics of follicular growth in the human: a model from preliminary results
Human reproduction, vol 1, pp 81-87, 1986

Gougeon A and Chainy G.B.N.
Morphometric studies of small follicles in ovaries of women at different ages,
Reproduction and Fertility, Vol 81, pp 433-442, 1987

Gougeon A, Lefèvre B, Testart J.
Influence of a gonadotrophin-releasing hormone agonist and gonadotrophins on morphometric characteristics of the population of small ovarian follicles in cynomolgus monkeys (Macaca fascicularis).
Journal of Reproduction and Fertility, Vol 95, No 2, pp 567-75, 1992.

Gougeon A, Ecochard R, Thalabard J C.
Age-related changes of the population of human ovarian follicles: increase in the disappearance rate of non-growing and early-growing follicles in aging women.
Biology of Reproduction, Vol 50, No 3, pp 653-63, 1994

Gougeon A.
Regulation of Ovarian Follicular Development in Primates: Facts and Hypotheses.
Endocrine reviews, Vol 17, no 2, pp 121-155, 1996

Guéripel X, Brun V, and Gougeon A.
Oocyte Bone Morphogenetic Protein 15, but not Growth Differentiation Factor 9, Is Increased During Gonadotropin-Induced Follicular development in the Immature Mouse and Is Associated with Cumulus Oophorus Expansion.
Biology of Reproduction, Vol 75, no 6, pp 836-843, 2006

Gregor T, Wieschaus EF, McGregor AP, Bialek W, Tank DW.
Stability and nuclear dynamics of the bicoid morphogen gradient.
Cell, Vol 130, No 1, pp 141-52, 2007.

Gundersen HJ, Jensen EB.
Stereological estimation of the volume-weighted mean volume of arbitrary particles observed on random sections.
Journal of Microscopy, Vol 138, pp 127-142, 1985

Gundersen HJ.
Stereology of arbitrary particles. A review of unbiased number and size estimators and the presentation of some new ones, in memory of William R. Thompson.
The Journal of Microscopy, Vol 143, pp 3-45, 1986

Haisma HJ, Kamps GK, Bouma A, Geel TM, Rots MG, Kariath A, Bellu AR.
Selective targeting of adenovirus to alphavbeta3 integrins, VEGFR2 and Tie2 endothelial receptors by angio-adenobodies.
International Journal of Pharmaceutics, Vol 391, No 1-2, pp 155-61, 2010

Halpin DM, Jones A, Fink G, Charlton HM.
Postnatal ovarian follicle development in hypogonadal (hpg) and normal mice and associated changes in the hypothalamic-pituitary ovarian axis.
Journal of Reproduction and Fertility, Vol 77, No 1, pp 287-96, 1986

Hansen K R, Soules M R.
Counting ovarian follicles is not without its challenges.
Fertility and Sterility, Vol 89, No 4, pp 1028-9, 2008

Hansen K R, Knowlton N S, Thyer A C, Charleston J S, Soules M R, Klein N A.
A new model of reproductive ageing: the decline in ovarian non-growing follicle number from birth to menopause.
Human Reproduction, Vol 23, pp 699-708, 2008

Hedreen JC.
What Was Wrong With the Abercrombie and Empirical Cell Counting Methods? A Review.
The Anatomical Record Vol 250, pp 373–380, 1998.

Hedreen JC. (†)
Lost caps in histological counting methods.
The Anatomical Record, Vol 250, No 3, pp 366-72, 1998.

Heise M, Koepsel R, Russel J A, McGee A E.
Calcium alginate microencapsulation of ovarian follicles impacts FSH delivery and follicle morphology.
Reproductive Biology and Endocrinology 2005, 3:47

Hemadi M, Abolhassani F, Akbari M, Sobhani A, Pasbakhsh P, Ährlund-Richter L, Modaresi M and Salehnia M.
Melatonin promotes the cumulus–oocyte complexes quality of vitrified–thawed murine ovaries; with increased mean number of follicles survival and ovary size following heterotopic transplantation.
European Journal of Pharmacology, 2009

Henderson S A, Edwards R G.
Chiasma frequency and maternal age in mammals.
Nature, Vol 218, No 5136, pp 22-8, 1968.

Hirobe S, He WW, Lee MM, Donahoe PK.
Mullerian inhibiting substance messenger ribonucleic acid expression in granulosa and Sertoli cells coincides with their mitotic activity.
Endocrinology, Vol 131, No 2, pp 854-62, 1992

Hiura M, Fujita H.
Electron microscopic observations on the elimination of the oocyte through the peritoneal epithelium in the neonatal mouse ovary.
Cell and Tissue Research, Vol 187, No 1, pp 73-9, 1977

Howard V.C. and Reed G.M.
Unbiased Stereology. Three - Dimensional Measurement in Microscopy.
© BIOS Scientific Publishers Limited, 1998

Hoyer B P, Sipes G.
Development of an Animal Model for Ovotoxicity Using 4-Vinylcyclohexene: A Case Study
Birth Defects Res (Part B) 80:113–125, 2007

Hreinsson JG, Scott JE, Rasmussen C, Swahn ML, Hsueh AJ, Hovatta O.
Growth differentiation factor-9 promotes the growth, development, and survival of human ovarian follicles in organ culture.
The Journal of Clinical Endocrinology and Metabolism, Vol 87, No 1, pp 316-21, 2002

Huang EJ, Manova K, Packer AI, Sanchez S, Bachvarova RF, Besmer P.
The murine steel panda mutation affects kit ligand expression and growth of early ovarian follicles.
Developmental Biology, Vol 157, No 1, pp 100-9, 1993

Huang EJ, Nocka KH, Buck J, Besmer P.
Differential expression and processing of two cell associated forms of the kit-ligand: KL-1 and KL-2.
Molecular Biology of the Cell, Vol 3, No 3, pp 349-62, 1992

Hussein TS, Froiland DA, Amato F, Thompson JG, Gilchrist RB.
Oocytes prevent cumulus cell apoptosis by maintaining a morphogenic paracrine gradient of bone morphogenetic proteins.
Journal of Cell Science, Vol 118, Pt 22, pp 5257-68, 2005

John GB, Gallardo TD, Shirley LJ, Castrillon DH.
Foxo3 is a PI3K-dependent molecular switch controlling the initiation of oocyte growth.
Developmental Biology, Vol 321, No 1, pp 197-204, 2008

Johnson M H
Essential Reproduction
ISBN: 978-1-4051-1866-8, ©2007 M.H. Johnson and B.J. Everitt

Johnson J, Canning J, Kaneko T, Pru K J, Tilly L J.
Germline stem cells and follicular renewal in the postnatal mammalian ovary.
Nature, Vol 428, pp 145 – 150, 2004

Jones JI, Clemmons DR.
Insulin-like growth factors and their binding proteins: biological actions.
Endocrine Reviews, Vol 16, No 1, pp 3-34, 1995

Jones EC, Krohn PL.
The relationships between age, numbers of ocytes and fertility in virgin and multiparous mice.
Journal of Endocrinology, Vol 21, pp 469-95, 1961

Jünger MA, Rintelen F, Stocker H, Wasserman JD, Végh M, Radimerski T, Greenberg ME, Hafen E.
The Drosophila forkhead transcription factor FOXO mediates the reduction in cell number associated with reduced insulin signaling.
Journal of Biology, Vol 2, No 3, p 20, 2003

Kezele P R, Nilsson E E and Skinner M K.
Cell – Cell Interactions in Primordial Follicle Assembly and Development.
Frontiers in Bioscience, Vol 7, pp 1990-6, 2002

Kezele P R, Nilsson E E, Skinner M K. (†)
Insulin but not insulin-like growth factor-1 promotes the primordial to primary follicle transition.
Molecular and Cellular Endocrinology, Vol 192, No 1-2, pp 37-43, 2002

Kezele P, Nilsson EE, Skinner MK.
Keratinocyte growth factor acts as a mesenchymal factor that promotes ovarian primordial to primary follicle transition.
Biology of Reproduction, Vol 73, No 5, pp 967-73, 2005

Kerr JB, Duckett R, Myers M, Britt KL, Mladenovska T, Findlay JK.
Quantification of healthy follicles in the neonatal and adult mouse ovary: evidence for maintenance of primordial follicle supply.
Reproduction, Vol 132, No 1, pp 95-109, 2006

Kherlopian AR, Song T, Duan Q, Neimark MA, Po MJ, Gohagan JK, Laine AF.
A review of imaging techniques for systems biology.
BMC Systems Biology, Vol 2, p 74, 2008

Kim Y, Comte I, Szabo G, Hockberger P, Szele F G.
Adult mouse subventricular zone stem and progenitor cells are sessile and epidermal growth factor receptor negatively regulates neuroblast migration.
PLoS One, Vol 4, No 12, e8122, 2009

Kirschner DE, Linderman JJ.
Mathematical and computational approaches can complement experimental studies of host-pathogen interactions.
Cellular Microbiology, Vol 11, No 4, pp 531-9, 2009.

Koester HJ, Baur D, Uhl R, Hell SW.
Ca2+ fluorescence imaging with pico- and femtosecond two-photon excitation:signal and photodamage.
Biophysical Journal Vol 77, pp 2226–2236, 1999

Kundt MS, Martinez-Taibo C, Muhlmann MC, Furnari JC.
Uranium in drinking water: effects on mouse oocyte quality.
Health Physics, Vol 96, No 5, pp 568-74, 2009.

Kwintkiewicz J, Giudice LC.
The interplay of insulin-like growth factors, gonadotropins, and endocrine disruptors in ovarian follicular development and function.
Seminars in Reproductive Medicine, Vol 27, pp 43-51, 2009.

Lee WS, Otsuka F, Moore RK, Shimasaki S.
Effect of bone morphogenetic protein-7 on folliculogenesis and ovulation in the rat.
Biol Reprod. 2001 Oct;65(4):994-9.

Lee WS, Yoon SJ, Yoon TK, Cha KY, Lee SH, Shimasaki S, Lee S, Lee KA.
Effects of bone morphogenetic protein-7 (BMP-7) on primordial follicular growth in the mouse ovary.
Molecular Reproduction and Development, Vol 69, No 2, pp 159-63, 2004.

Linderstrøm-Lang K, Holter H and Ohlsen A S.
The distribution of enzymes in the stomach of pigs as a function of its histological structure.
Studies on enzymatic histochemistry: XIII, Comptes-rendus du Lab, Carlsberg, Vol 20, pp 66-125, 1935.

Lintern-Moore S, Peters H, Moore GP, Faber M.
Follicular development in the infant human ovary.
Journal of Reproduction and Fertility, Vol 39, No 1, pp 53-64, 1974

Louhio H, Hovatta O, Sjöberg J, Tuuri T.
The effects of insulin, and insulin-like growth factors I and II on human ovarian follicles in long-term culture.
Molecular Human Reproduction, Vol 6, No 8, pp 694-8, 2000.

Lukac R and Plataniotis N K.
Color Image Processing: Methods and Applications
CRC Press, 2007.

Mackay S, Smith R A, Haig T.
An investigation of the migratory potential of mouse oocytes in vitro.
Journal of Anatomy, Vol 181, pp 437-46, 1992

Maciel GA, Baracat EC, Benda JA, Markham SM, Hensinger K, Chang RJ, Erickson GF
Stockpiling of Transitional and Classic Primary Follicles in Ovaries of Women with Polycystic Ovary Syndrome.
The Journal of Clinical Endocrinology & Metabolism, Vol 89, No 11, pp 5321–5327, 2004

Malpica N, Ortiz de Solorzano C, Vaquero J J, Santos A, Vallcorba I, Garcia-Sagredo M J and del Pozo F.
Applying Watershed Algorithms to the Segmentation of Clustered Nuclei.
Cytometry, vol 28, pp 289-297, 1997.

Mani AM, Fenwick MA, Cheng Z, Sharma MK, Singh D, Wathes DC.
IGF1 induces up-regulation of steroidogenic and apoptotic regulatory genes via activation of phosphatidylinositol-dependent kinase/AKT in bovine granulosa cells.
Reproduction, Vol 139, No 1, pp 139-51, 2010.

Marlies E K, Meerasahib F M, Kramer P, van de Lang-Born M N B, de Jong H F, Groome P N, Themmen N P A, Visser A J.
Serum Anti-Müllerian Hormone Levels Reflect the Size of the Primordial Follicle Pool in Mice.
Endocrinology, Vol 147, pp 3228 –3234, 2006

Martinovitch P N.
The development *in vitro* of the mammalian gonad. Ovary and ovogenesis
Proceedings of the Royal Society of London. Series B, Biological Sciences, Vol. 125, No. 839, pp. 232-249, 1938

Masters B R.
Confocal microscopy and multiphoton excitation microscopy : the genesis of live cell imaging.
©2006 The society of Photo-Optical Instrumentation Engineers
ISBN: 0-8194-6118-0

McGee E A, Hsueh A J.
Initial and cyclic recruitment of ovarian follicles.
Endocrine Reviews, Vol 21, No 2, pp 200-14, 2000.

McGinty J, Tahir K B, Laine R, Talbot C B, Dunsby C, Neil M A, Quintana L, Swoger J, Sharpe J, French P M.
Fluorescence lifetime optical projection tomography.
Journal of Biophotonics, Vol 1, No 5, pp 390-4, 2008.

McGrath SA, Esquela AF, Lee SJ.
Oocyte-specific expression of growth/differentiation factor-9.
Molecular Endocrinology, Vol 9, No 1, pp 131-6, 1995.

McGurk L, Morrison H, Keegan P L, Sharpe J, O'Connell A M.
Three-Dimensional Imaging of Drosophila melanogaster.
PLoS ONE 2(9): e834, September 2007.

McLaughlin E, Mclver S.
Awakening the oocyte: controlling the primordial follicle development.
Reproduction, Vol 137, pp 1-11, 2009.

Meredith S, Doolin D.
Timing of activation of primordial follicles in mature rats is only slightly affected by fetal stage at meiotic arrest.
Biology of Reproduction, Vol 57, No 1, pp 63-7, 1997.

Meredith S, Dudenhoeffer G, Jackson K.
Single-section counting error when distinguishing between primordial and early primary follicles in sections of rat ovary of different thickness.
Journal of Reproduction and Fertility, Vol 117, No 2, pp 339-43, 1999.

Miller B P, Charleston S J, Battaglia E D, Klein A N, Soules R M.
An Accurate, Simple Method for Unbiased Determination of Primordial Follicle Number in the Primate Ovary.
Biology of Reproduction, Vol 56, pp 909 – 915, 1997.

Miller C E, Thompson R P, Bigelow M R, Gittinger G, Trusk T C, Sedmera D.
Confocal imaging of the embryonic heart: how deep?
Microscopy and Microanalysis, Vol 11, No 3, pp 216-23, 2005

Miller M J, Wei S H, Parker I, Cahalan M D.
Two-photon imaging of lymphocyte motility and antigen response in intact lymph node.
Science, Vol 296, No 5574, pp 1869-73, 2002

Monget P, Bondy C.
Importance of the IGF system in early folliculogenesis.
Molecular and Cellular Endocrinology, Vol 163, No 1-2, pp 89-93, 2000

Monici M.
Cell and tissue autofluorescence research and diagnostic applications.
Biotechnology Annual Review, Vol 11, pp 227-56, 2005

Monk M, McLaren A.
X-chromosome activity in foetal germ cells of the mouse.
Journal of Embryology and Experimental Morphology, Vol 63, pp 75-84, 1981

Morita Y, Manganaro TF, Tao XJ, Martimbeau S, Donahoe PK, Tilly JL.
Requirement for phosphatidylinositol-3'-kinase in cytokine-mediated germ cell survival during fetal oogenesis in the mouse.
Endocrinology, Vol 140, No 2, pp 941-9, 1999

Muruvi W, Picton HM, Rodway RG, Joyce IM.
In vitro growth of oocytes from primordial follicles isolated from frozen-thawed lamb ovaries.
Theriogenology, Vol 64, No 6, pp 1357-70, 2005

Muruvi W, Picton HM, Rodway RG, Joyce IM.
In vitro growth and differentiation of primary follicles isolated from cryopreserved sheep ovarian tissue.
Animal Reproduction Science, Vol 112, No 1-2, pp 36-50, 2009

Myers M, Britt KL, Wreford NG, Ebling FJ, Kerr JB.
Methods for quantifying follicular numbers within the mouse ovary.
Reproduction. Vol 127, No 5, pp 569-80, 2004

Niessen CM.
Tight junctions/adherens junctions: basic structure and function.
Journal of Investigative Dermatology, Vol 127, No 11, pp 2525-32, 2007

Nilsson EE, Kezele P, Skinner MK.
Leukemia inhibitory factor (LIF) promotes the primordial to primary follicle transition in rat ovaries.
Molecular and Cellular Endocrinology, Vol 188, No 1-2, pp 65-73, 2002

Nilsson E, Parrott JA, Skinner MK.
Basic fibroblast growth factor induces primordial follicle development and initiates folliculogenesis.
Molecular and Cellular Endocrinology, Vol 175, No 1-2, pp 123-30, 2001

Nilsson EE, Skinner MK.
Growth and differentiation factor-9 stimulates progression of early primary but not primordial rat ovarian follicle development.
Biology of Reproduction, Vol 67, No 3, pp 1018-24, 2002

Nilsson EE, Skinner MK.
Bone morphogenetic protein-4 acts as an ovarian follicle survival factor and promotes primordial follicle development.
Biology of Reproduction, Vol 69, No 4, pp 1265-72, 2003

O'Brien M J, Pendola J K, Eppig J J.
A revised protocol for in vitro development of mouse oocytes from primordial follicles dramatically improves their developmental competence.
Biology of Reproduction, Vol 68, No 5, pp 1682-6, 2003

O'Keefe MA, Hetherington CJ, Wang YC, Nelson EC, Turner JH, Kisielowski C, Malm JO, Mueller R, Ringnalda J, Pan M, Thust A.
Sub-Angstrom high-resolution transmission electron microscopy at 300 keV.
Ultramicroscopy, Vol 89, No 4, pp 215-41, 2001

Obata Y, Maeda Y, Hatada I, Kono T.
Long-term effects of in vitro growth of mouse oocytes on their maturation and development.
The Journal of Reproduction and Development, Vol 53, No 6, pp 1183-90, 2007

Oktem O, Oktay K.
Current knowledge in the renewal capability of germ cells in the adult ovary.
Birth Defects Research C Embryo Today, vol 87, pp 90-95, 2009

Onichtchouk D, Chen YG, Dosch R, Gawantka V, Delius H, Massagué J, Niehrs C.
Silencing of TGF-beta signalling by the pseudoreceptor BAMBI.
Nature, Vol 401, No 6752, pp 480-5, 1999

Packer AI, Hsu YC, Besmer P, Bachvarova RF.
The ligand of the c-kit receptor promotes oocyte growth.
Developmental Biology, Vol 161, No 1, pp 194-205, 1994

Pakkenberg B, Gundersen HJ.
Total number of neurons and glial cells in human brain nuclei estimated by the disector and the fractionator.
Journal of Microscopy, Vol 150, No 1, pp 1-20, 1988

Pangas SA, Jorgez CJ, Matzuk MM.
Growth differentiation factor 9 regulates expression of the bone morphogenetic protein antagonist gremlin.
Journal of Biological Chemistry, Vol 279, No 31, pp 32281-6, 2004

Parrott JA, Skinner MK.
Kit-ligand/stem cell factor induces primordial follicle development and initiates folliculogenesis.
Endocrinology, Vol 140, No 9, pp 4262-71, 1999.

Parrott JA, Vigne JL, Chu BZ, Skinner MK.
Mesenchymal-epithelial interactions in the ovarian follicle involve keratinocyte and hepatocyte growth factor production by thecal cells and their action on granulosa cells.
Endocrinology, Vol 135, No 2, pp 569-75, 1994.

Pawley J. B.
Handbook of Biological Confocal Microscopy
Third Edition, ©2006, 1995, 1989 Springer Science+Business Media, LLC

Pedersen T, Peters H.
Proposal for a classification of oocytes and follicles in the mouse ovary.
Journal of Reproduction and Fertility, Vol 17, No 3, pp 555-7, 1968.

Pepling ME.
From primordial germ cell to primordial follicle: mammalian female germ cell development.
Genesis, Vol 44, No 12, pp 622-32, 2006.

Pepling M and Spradling C A.
Mouse Ovarian Germ Cell Cysts Undergo Programmed Breakdown to form Primordial Follicles.
Developmental Biology, vol 234, pp 339-351, 2001.

Pepling ME, Sundman EA, Patterson NL, Gephardt GW, Medico L Jr, Wilson KI.
Differences in oocyte development and estradiol sensitivity among mouse strains.
Reproduction, Vol 139, No 2, pp 349-57, 2010

Perez I G, Knudson M, Leykin L, Korsmeyer J S, Tilly L J.
Apoptosis – associated signaling pathways are required for chemotherapy – mediated female germ cell destruction.
Nature Medicine, Vol 3, No 11, November 1997

Picton H, Briggs D, Gosden R.
The molecular basis of oocyte growth and development.
Molecular and Cellular Endocrinology, Vol 145, No 1-2, pp 27-37, 1998

Picton H M.
Activation of follicle development: The Primordial Follicle.
Theriogenology 55:1193-1210, 2001.

Picton H M, Harris S E, Muruvi W, Chambers E L.
The in vitro growth and maturation of follicles.
Reproduction, Vol 136, No 6, pp 703-15, 2008.

Potocnik B and Zazula D.
Automated analysis of a sequence of ovarian ultrasound images. Part I: Segmentation of single 2D images.
Image and Vision Computing, Vol 20, pp 217-225, 2002.

Potter S M.
Vital imaging: two photons are better than one.
Current Biology, Vol 6, No 12, pp 1595-8, 1996

Potter S M, Wang C M, Garrity P A, Fraser S E.
Intravital imaging of green fluorescent protein using two-photon laser-scanning microscopy.
Gene, No 173, pp 25-31, 1996

Pratt W K
Digital Image Processing
ISBN: 978-0-471-76777, Fourth Edition, J. Wiley & Sons, 2007

Press H W, Teukolsky A S, Vetterling T W, Flannery P B.
Numerical Recipes: The Art of Scientific Computing.
ISBN-10: 0521880688, 3rd Edition, ©2007 Cambridge Univeristy Press

Ratts VS, Flaws JA, Kolp R, Sorenson CM, Tilly JL.
Ablation of bcl-2 gene expression decreases the numbers of oocytes and primordial follicles established in the post-natal female mouse gonad.
Endocrinology, Vol, 136, No 8, pp 3665-8, 1995

Reddy P, Adhikari D, Zheng W, Liang S, Hämäläinen T, Tohonen V, Ogawa W, Noda T, Volarevic S, Huhtaniemi I, Liu K.
PDK1 signaling in oocytes controls reproductive aging and lifespan by manipulating the survival of primordial follicles.
Human Molecular Genetics, Vol 18, No 15, pp 2813-24, 2009.

Reddy P, Liu L, Adhikari D, Jagarlamudi K, Rajareddy S, Shen Y, Du S, Tang W, Hämäläinen T, Peng S L, Lan Z J, Cooney A J, Huhtaniemi I and Liu K.
Oocyte-Specific Deletion of Pten Causes Premature Activation of the Primordial Follicle Pool.
Science, Vol 319 pp 611–613, 2008

Reddy P, Shen L, Ren C, Boman K, Lundin E, Ottander U, Lindgren P, Liu Y X, Sun Q Y, Liu K.
Activation of Akt (PKB) and suppression of FKHRL1 in mouse and rat oocytes by stem cell factor during follicular activation and development.
Developmental Biology, Vol 281, No 2, pp 160-70, 2005.

Richardson S J, Senikas V, Nelson J F.
Follicular depletion during the menopausal transition: evidence for accelerated loss and ultimate exhaustion.
Journal of Clinical Endocrinology and Metabolism, Vol 65, No 6, pp 1231-7, 1987

Roberts R, Iatropoulou A, Ciantar D, Stark J, Becker DL, Franks S, Hardy K.
Follicle-stimulating hormone affects metaphase I chromosome alignment and increases aneuploidy in mouse oocytes matured in vitro.
Biology of Reproduction, Vol 72, No 1, pp 107-18, 2005

Rodgers RJ, Irving-Rodgers HF, Russell DL.
Extracellular matrix of the developing ovarian follicle.
Reproduction, Vol 126, No 4, pp 415-24, 2003

Roerdink J and Meijster A.
The Watershed Transform: Definitions, Algorithms and Parallelization Strategies
Fundamenta Informaticae, vol 41, pp 187–228, 2001

Rossner M, Yamada K M.
What's in a picture? The temptation of image manipulation.
Journal of Cell Biology, Vol 166, No 1, pp 11-5, 2004

Rucker EB 3rd, Dierisseau P, Wagner KU, Garrett L, Wynshaw-Boris A, Flaws JA, Hennighausen L.
Bcl-x and Bax regulate mouse primordial germ cell survival and apoptosis during embryogenesis.
Molecular Endocrinology, Vol 14, No 7, pp 1038-52, 2000

Russ J C
Image Processing Handbook
ISBN: 978-0-8493-7254-2, Fifth Edition, CRC Press, 2007

Sadeu J C, Adriaenssens T, Smitz J.
Expression of growth differentiation factor 9, bone morphogenetic protein 15, and anti-Müllerian hormone in cultured mouse primary follicles
Reproduction, Vol 136, pp 195-203, 2008

Saha S, Shimizu M, Geshi M, Izaike Y.
In vitro culture of bovine preantral follicles.
Animal Reproduction Science, Vol 63, No 1-2, pp 27-39, 2000

Santos M, Marcos R, Santos N, Malhão F, Monteiro R A, Rocha E.
An unbiased stereological study on subpopulations of rat liver macrophages and on their numerical relation with the hepatocytes and stellate cells.
Journal of Anatomy, Vol 214, no 5, pp 744-751, 2009

Sforza C, Vizzotto L, Ferrario V F, Forabosco A.
Position of follicles in normal human ovary during definitive histogenesis.
Early Human Development, Vol 74, No 1, pp 27-35, 2003

Shapiro L G and Stockman C G.
Computer Vision
ISBN: 0-13-030796-3, © Prentice-Hall, 2001

Sharpe J.
Optical projection tomography as a new tool for studying embryo anatomy.
Journal of Anatomy, Vol 202, No 2, pp 175-8, 2003

Sharpe J.
Optical projection tomography.
Annual Review of Biomedical Engineering, Vol 6, pp 209-28, 2004

Shimasaki S, Zachow RJ, Li D, Kim H, Iemura S, Ueno N, Sampath K, Chang RJ, Erickson GF.
A functional bone morphogenetic protein system in the ovary.
Procceedings of the National Academy of Sciences of the United States of America, Vol 96, No 13, pp 7282-7, 1999.

Shneider NA, Brown MN, Smith CA, Pickel J, Alvarez FJ.
Gamma motor neurons express distinct genetic markers at birth and require muscle spindle-derived GDNF for postnatal survival.
Neural Development, 4:42, 2009

Sick S, Reinker S, Timmer J, Schlake T
WNT and DKK determine hair follicle spacing through a reaction-diffusion mechanism.
Science, Vol 314, no 5804, pp 1447–1450, 2006

Skinner K M.
Regulation of primordial follicle assembly and development.
Human Reproduction Update, Vol. 11, No.5 p 461-471, 2005

Smith BJ, Plowchalk DR, Sipes IG, Mattison DR.
Comparison of random and serial sections in assessment of ovarian toxicity.
Reproduction and Toxicology, Vol 5, No 4, pp 379-83, 1991

Soille P.
Morphological Image Analysis: Principles and Applications
Springer-Verlag, pp. 170-171, 1999

Solloway MJ, Dudley AT, Bikoff EK, Lyons KM, Hogan BL, Robertson EJ.
Mice lacking Bmp6 function.
Developmental Genetics, Vol 22, No 4, pp 321-39, 1998

Solovei I, Cavallo A, Schermelleh L, Jaunin F, Scasselati C, Cmarko D, Cremer C, Fakan S and Cremer T.
Spatial Preservation of 3D Chromatin Architecture during Three-Dimensional Fluorescence in Situ Hybridization (3D-FISH).
Experimental Cell Research, Vol 276, pp 10-23, 2002

Soriano J, Rüdiger S, Pullarkat P, Ott A.
Mechanogenetic coupling of Hydra symmetry breaking and driven Turing instability model.
Biophysical Journal, Vol 96, No 4, pp 1649-60, 2009

Soutter WP, Diakomanolis E, Lyons D, Ghaem-Maghami S, Ajala T, Haidopoulos D, Doumplis D, Kalpaktsoglou C, Sakellaropoulos G, Soliman S, Perryman K, Hird V, Buckley CH, Pavlakis K, Markaki S, Dina R, Healy V, Balas C.
Dynamic spectral imaging: improving colposcopy.
Clinical Cancer Research, Vol 15, No 5, pp 1814-20, 2009

Spears N, Boland NI, Murray AA, Gosden RG.
Mouse oocytes derived from in vitro grown primary ovarian follicles are fertile.
Human Reproduction, Vol 9, No 3, pp 527-32, 1994.

Sterio D C
The unbiased estimation of number and sizes of arbitrary particles using the disector.
The Journal of Microscopy, Vol 134, no 2, pp 127-136, 1984

Stubbs S A, Hardy K, Da Silva-Buttkus P, Stark J, Webber L J, Flanagan A M, Themmen A P N, Visser J A, Groome N P and Frank S.
Anti-Mullerian Hormone Protein Expression is Reduced during the Initial Stages of Follicle Development in Human Polycystic Ovaries.
The Journal of Clinical Endocrinology & Metabolism 90(10):5536 – 5543, 2005

Stubbs S A, Stark J, Dilworth M S, Franks S, and Hardy K.
Abnormal Preantral Folliculogenesis in Polycystic Ovaries Is Associated with Increased Granulosa Cell Division.
The Journal of Clinical Endocrinology & Metabolism 92(11):4418 – 4426, 2007

Summerbell D.
The effect of local application of retinoic acid to the anterior margin of the developing chick limb.
Journal of Embryology and Experimental Morphology, Vol 78, pp 269-89, 1983.

Supatto W, McMahon A, Fraser S E, Stathopoulos A.
Quantitative imaging of collective cell migration during Drosophila gastrulation: multiphoton microscopy and computational analysis.
Nature Protocols, Vol 4, No 10, pp 1397-412, 2009

Tarumi W, Suzuki N, Takahashi N, Kobayashi Y, Kiguchi K, Sato K and Ishizuka B.
Ovarian toxicity of paclitaxel and effect on fertility in the rat
Jounral of Obstetrics and Gynaecology, Vol. 35, no 3, pp 414–420, 2009

Thatcher S S.
PCOS: Polycystic ovary syndrome: The hidden epidemic
Perspective Press, ISBN: 0-944934-25-0

Tilly J L, Johnson J.
Recent arguments against germ cell renewal in the adult human ovary: is an absence of marker gene expression really acceptable evidence of an absence of oogenesis?
Cell Cycle, Vol 6, No 8, pp 879-83, 2007

Tingen C M, Bristol-Gould S K, Kiesewetter S E, Wellington J T, Shea L, Woodruff T K.
Prepubertal primordial follicle loss in mice is not due to classical apoptotic pathways.
Biology of Reproduction, Vol 81, pp 16-25, 2009

Tingen C M, Kim A, Woodruff T K.
The primordial pool of follicles and nest breakdown in mammalian ovaries.
Mol. Hum. Reprod. Advance Access published on August 26, 2009

Tomic D, Brodie SG, Deng C, Hickey RJ, Babus JK, Malkas LH, Flaws JA.
Smad 3 may regulate follicular growth in the mouse ovary.
Biology of Reproduction, Vol 66, No 4, pp 917-23, 2002

Torrance C, Telfer E, Gosden RG.
Quantitative study of the development of isolated mouse pre-antral follicles in collagen gel culture.
Journal of Reproduction and Fertility, Vol 87, No 1, pp 367-74, 1989

Toyooka Y, Tsunekawa N, Takahashi Y, Matsui Y, Satoh M, Noce T.
Expression and intracellular localization of mouse Vasa-homologue protein during germ cell development.
Mechanism of Development, Vol 93, No 1-2, pp 139-49, 2000

Trigo F, Corrie J, Ogden D.
Laser photolysis of caged compounds at 405 nm: Photochemical advantages, localisation, phototoxicity and methods for calibration.
Journal of Neuroscience Methods, Vol 180, pp 9–21, 2009

Turing, A. M.
The chemical basis of morphogenesis
Philosophicals Transactions of the Royal Society of London B, Vol 237, No 641, pp 37-72, 1952

Urbanek M, Sam S, Legro RS, Dunaif A.
Identification of a polycystic ovary syndrome susceptibility variant in fibrillin-3 and association with a metabolic phenotype.
Journal of Clinical Endocrinology and Metabolism, Vol 92, No 11, pp 4191-8, 2007

Vanhecke D, Studer D, Ochs M.
Stereology meets electron tomography: Towards quantitative 3D electron microscopy
Journal of Structural Biology, Vol 159, pp 443-450, 2007

Viher B, Dobnikar A and Zazula D.
Cellular automata and follicle recognition problem and possibilities of using cellular automata for image recognition purposes.
International Journal of Medical Informatics, Vol 49, pp 231-241, 1998

Virant-Klun I, Rozman P, Cvjeticanin B, Vrtacnik-Bokal E, Novakovic S, Rülicke T, Dovc P, Meden-Vrtovec H.
Parthenogenetic embryo-like structures in the human ovarian surface epithelium cell culture in postmenopausal women with no naturally present follicles and oocytes.
Stem Cells and Development, Vol 18, No 1, pp 137-50, 2009

Vlahos CJ, Matter WF, Hui KY, Brown RF.
A specific inhibitor of phosphatidylinositol 3-kinase, 2-(4-morpholinyl)-8-phenyl-4H-1-benzopyran-4-one (LY294002).
Journal of Biological Chemistry, Vol 269, No 7, pp 5241-8, 1994

Wandji SA, Wood TL, Crawford J, Levison SW, Hammond JM.
Expression of mouse ovarian insulin growth factor system components during follicular development and atresia.
Endocrinology Vol 139, No 12, pp 5205-14, 1998

Wang Y, Shyy JY, Chien S.
Fluorescence proteins, live-cell imaging, and mechanobiology: seeing is believing.
Annual Review in Biomedical Engineering.Vol 10, pp 1-38, 2008

Webber LJ, Stubbs SA, Stark J, Margara RA, Trew GH, Lavery SA, Hardy K, Franks S.
Prolonged survival in culture of preantral follicles from polycystic ovaries.
The Journal of Clinical Endocrinology and Metabolism, Vol 92, No 5, pp 1975-8, 2007

Webber L J, Stubbs S, Stark J, Trew G H, Margara R, Hardy K, Franks S.
Formation and early development of follicles in the polycystic ovary
The Lancet, Vol 362, September 27, 2003

West M J, Slomianka L, Gundersen H J.
Unbiased stereological estimation of the total number of neurons in the subdivisions of the rat hippocampus using the optical fractionator.
The Anatomical Record, Vol 231, no 4, pp 482-497, 1991

West ER, Xu M, Woodruff TK, Shea LD.
Physical properties of alginate hydrogels and their effects on in vitro follicle development.
Biomaterials, Vol 28, No 30, pp 4439-48, 2007

Willis D, Mason H, Gilling-Smith C, Franks S.
Modulation by insulin of follicle-stimulating hormone and luteinizing hormone actions in human granulosa cells of normal and polycystic ovaries.
The Journal of Clinical Endocrinology and Metabolism, Vol 81, No 1, pp 302-9, 1996.

Wordinger R, Sutton J, Brun-Zinkernagel AM.
Ultrastructure of oocyte migration through the mouse ovarian surface epithelium during neonatal development.
Anatomical Record, Vol 227, No 2, pp 187-98, 1990

Wright C S, Hovatta O, Margara R, Trew G, Winston R M, Franks S, Hardy K.
Effects of follicle-stimulating hormone and serum substitution on the in-vitro growth of human ovarian follicles.
Human Reproduction, Vol 14, No 6, pp 1555-62, 1999.

Wu Q, Merchant F, Castleman K R
Microscope Image Processing
ISBN: 978-0-12-372578-3, © Elsevier Inc 2008

Xu M, Kreeger K P, Shea D L, Woodruff T.
Tissue-Engineered Follicles Produce Live, Fertile Offspring
Tissue engineering, Volume 12, Number 10, 2006

Xu M, West E, Shea LD, Woodruff TK.
Identification of a stage-specific permissive in vitro culture environment for follicle growth and oocyte development.
Biology of Reproduction, Vol 75, No 6, pp 916-23, 2006.

Yamamoto S, Konishi I, Nanbu K, Komatsu T, Mandai M, Kuroda H, Matsushita K, Mori T.
Immunohistochemical localization of basic fibroblast growth factor (bFGF) during folliculogenesis in the human ovary.
Gynecological Endocrinology, Vol 11, No 4, pp 223-30, 1997.

Yan C, Wang P, DeMayo J, DeMayo FJ, Elvin JA, Carino C, Prasad SV, Skinner SS, Dunbar BS, Dube JL, Celeste AJ, Matzuk MM.
Synergistic roles of bone morphogenetic protein 15 and growth differentiation factor 9 in ovarian function.
Molecular Endocrinology, Vol 15, No 6, pp 854-66, 2001

Young T I, Gerbrands J J, van Vliet J L.
Fundamentals of Image Processing.
Copyright © 1995, 1997, 1998 by I.T. Young, J.J. Gerbrands and L.J. van Vliet,
ISBN 90–75691–01–7

Yu N, Roy SK.
Development of primordial and prenatal follicles from undifferentiated somatic cells and oocytes in the hamster prenatal ovary in vitro: effect of insulin.
Biology of Reproduction, Vol 61, No 6, pp 1558-67, 1999.

Zhivov A, Stachs O, Stave J, Guthoff R F.
In vivo three-dimensional confocal laser scanning microscopy of corneal surface and epithelium.
British Journal of Ophthalmology, Vol 93, No 5, pp 667-72, 2009.

Zou K, Yuan Z, Yang Z, Luo H, Sun K, Zhou L, Xiang J, Shi L, Yu Q, Zhang Y, Hou R, Wu J.
Production of offspring from a germline stem cell line derived from neonatal ovaries.
Nature Cell Biology, Vol 11, No 5, pp 631-6, 2009

Zucker R M.
Whole insect and mammalian embryo imaging with confocal microscopy: morphology and apoptosis.
Cytometry part A, Vol 69, No 11, pp 1143-52, 2006.

Zucker M R, Jeffay C S.
Confocal laser Scanning Microscopy of Whole Mouse Ovaries: Excellent Morphology, Apoptosis Detection and Spectroscopy.
Cytometry Part A, Vol 69A, pp 930–939, 2006.

Zucker M R, Keshaviah P A, Price T O, Goldman M J.
Confocal Laser Scanning Microscopy of Rat Follicle Development.
The Journal of Histochemistry & Cytochemistry, Vol 48, No 6, pp 781–791, 2000

Zuckerman S.
The number of oocytes in the mature ovary.
Recent Progress in Hormone Research, vol 6, pp 63–109, 1951